



**HAL**  
open science

## Developments in preclinical arterial spin labeling

Lydiane Hirschler

► **To cite this version:**

Lydiane Hirschler. Developments in preclinical arterial spin labeling. Biological Physics [physics.bioph]. Université Grenoble Alpes, 2017. English. NNT : 2017GREAY014 . tel-01648165

**HAL Id: tel-01648165**

**<https://theses.hal.science/tel-01648165>**

Submitted on 24 Nov 2017

**HAL** is a multi-disciplinary open access archive for the deposit and dissemination of scientific research documents, whether they are published or not. The documents may come from teaching and research institutions in France or abroad, or from public or private research centers.

L'archive ouverte pluridisciplinaire **HAL**, est destinée au dépôt et à la diffusion de documents scientifiques de niveau recherche, publiés ou non, émanant des établissements d'enseignement et de recherche français ou étrangers, des laboratoires publics ou privés.

## THÈSE

Pour obtenir le grade de

**DOCTEUR DE la Communauté UNIVERSITÉ  
GRENOBLE ALPES**

Spécialité : **Physique pour les Sciences du Vivant**

Arrêté ministériel : 7 Août 2006

Présentée par

**Lydiane HIRSCHLER**

Thèse dirigée par **Emmanuel BARBIER**  
et codirigée par **Jan WARNKING**

préparée au sein **Grenoble Institut des Neurosciences - INSERM U1216/**  
**Université Grenoble Alpes**  
et de **Ecole Doctorale de Physique**

# Developments in Preclinical Arterial Spin Labeling

Thèse soutenue publiquement le **31 mars 2017**,  
devant le jury composé de :

**Pr, Franz BRUCKERT**

Professeur, Grenoble INP, Président

**Dr, Luisa CIOBANU**

Ingénieur E5, CEA, Rapporteur

**Pr, Matthias GÜNTHER**

Professor, Universität Bremen, Rapporteur

**Dr, Sascha KÖHLER**

Head of PCI Method Development, Bruker Biospin MRI, Examinateur

**Pr, Jean-François PAYEN**

Professeur, CHU de Grenoble, Examinateur

**Dr, David THOMAS**

Principal Research Associate, University College London, Examinateur





# Acknowledgments

Je souhaite tout d'abord remercier avec beaucoup de gratitude mes deux directeurs de thèse Emmanuel Barbier et Jan Warnking. Merci de m'avoir encadrée avec tant de disponibilité et de patience (et d'avoir supporté mes nombreuses tentatives de numérologie !) Merci aussi pour vos multiples corrections lors de la rédaction de ce manuscrit de thèse et pour vos précieux conseils concernant l'après-thèse ! C'est votre passion pour la recherche qui m'a motivée à poursuivre dans ce domaine.

I would like to sincerely thank all the jury members and particularly Luisa Ciobanu and Matthias Günther for reviewing this manuscript.

Ein ganz herzlicher Dank geht an alle Kollegen von Bruker, sei es von der Methoden-, Applikation-, oder Softwaregruppe, für eure wertvolle Hilfe mit dem Paravisionprogrammieren. Sascha, vielen Dank für Deine Hilfe und Umrahmung, ich wünsche dem CASL-Package viel Erfolg! Un grand merci également à Jérôme et Didier pour votre aide lors des manips et de la programmation.

Je souhaite aussi remercier vivement Franek Hennel pour les discussions stimulantes et ses précieux conseils !

I would like to acknowledge the EU COST-action for the scientific short-term mission stipend that triggered the collaboration with the LUMC in Leiden. I would particularly like to thank Matthias van Osch for the opportunity he has given me to come to Leiden for a visit. Many thanks to you and Wouter Teeuwisse for sharing your knowledge on time-encoded ASL. And of course, a biiig (with the French accent of course!) thank you to Leon for this great and fun collaboration!

Un grand merci à tous les membres de l'équipe à Grenoble, pour avoir rendu ma thèse si agréable. Je n'oublierai jamais tous ces bons moments passés au sein de l'équipe 5 du GIN ! Merci Clément de m'avoir initiée à l'ASL et de m'avoir motivée à faire une thèse ! Je ne regrette absolument pas ! Merci aux responsables plateforme, Vasile, Olivier et Hervé, pour votre aide précieuse. Merci à mon correspondant plateforme Vasile, de m'avoir aidée à multiples reprises lors de mes manips, quand le bain ne voulait plus chauffer, quand Paravision ou même l'IRM plantait et même quand ma super tasse s'est cassée. Je tiens également à remercier vivement Nora et Ligia pour leur aide lors des chirurgies. Un grand merci également à Agathe d'avoir contribué à ce travail. Merci

---

Marie-Claude pour ta super bonne humeur et surtout ta patience (l'attente des papiers de retour de mission a parfois été longue) ...

A mes chers colocs de bureau, je vous dis un grand « Cimer Albert ! » pour avoir supporté mes blagues nulles aussi longtemps. Un merci tout particulier à Emma, Ligia, Ivy et Roxane ! Merci pour votre amitié, sans laquelle ces années de thèse auraient été bien moins drôles. Et puis Ivy, n'oublies pas si jamais t'en as marre, il y a Hadamard !

Un énorme merci à Aurélie et Gauthier pour leur aide précieuse lors de la mise en forme du manuscrit final !

Merci à tous mes chers amis grenoblois, alsaciens et valentinois pour tous les supers moments passés ensemble. Merci à mes chères colocs qui m'ont entourées lors de mes premières années de thèse.

Loïs, Jonathan, Aurélie et Adeline, merci pour votre amitié, votre soutien moral infal-  
liblé et les discussions sans fin ! Un énorme merci mes parents qui m'ont soutenu tout au  
long de mes études (enfin terminées !), de m'avoir chouchoutée à la maison pendant les  
deux demi-années que j'ai passées chez Bruker. Merci pour tout ce support inestimable !

# Contents

<b>1. General introduction</b>	<b>1</b>
1.1. Why measure perfusion?	2
1.2. Physiological parameters describing perfusion	5
1.2.1. Parameters related to baseline perfusion	5
1.2.2. Parameters related to oxygen and nutrient delivery	6
1.2.3. Parameters related to functional changes in perfusion	7
1.2.4. Multiparametric perfusion imaging	8
1.3. CBF measurement methods	9
1.4. Arterial spin labeling methods	11
1.4.1. How can blood be used as a tracer?	11
1.4.2. Labeling schemes	15
1.4.2.1. Pulsed Arterial Spin Labeling (PASL)	15
1.4.2.2. Continuous Arterial Spin Labeling (CASL)	17
1.4.2.3. Pseudo-Continuous Arterial Spin Labeling (pCASL)	20
1.4.2.4. Velocity Selective Arterial Spin Labeling (vsASL)	22
1.4.2.5. Consensus Paper	23
1.4.3. Post-labeling delay (PLD)	23
1.4.3.1. Arterial transit time	24
1.4.3.2. Tissue transit time	25
1.4.4. Time encoded ASL	27
1.4.4.1. Multi-PLD ASL	27
1.4.4.2. Hadamard encoded ASL	28
1.4.4.3. Dynamic ASL	30
1.4.5. CBF quantification	31
1.4.5.1. ASL data at different timepoints	31
1.4.5.2. ASL data acquired at a single timepoint	31
1.5. ASL issues at high magnetic field	33
1.5.1. pCASL labeling efficiency at high magnetic field	33
1.5.1.1. Why does labeling fail in some cases?	33
1.5.1.2. Existing strategies to correct for off-resonance effects	34
1.5.2. Heating issues encountered in ASL at high magnetic field	36
1.5.2.1. MR safety	36
1.5.2.2. Influence of MR parameters on heating	37
1.5.2.3. MR safety standards	39
1.6. Objectives of this thesis	40
1.6.1. Industrial Project	40
1.6.2. Research Project	40

<b>2. CASL implementation in Paravision 6</b>	<b>43</b>
2.1. Overview of the developed tools & Workflow	43
2.1.1. Workflow overview - Labeling with the volume coil	44
2.1.2. Workflow overview - Labeling with a separate ASL coil	45
2.2. Technical details of the inversion efficiency measurement (CASL-FcFLASH method)	47
2.2.1. Before running CASL-FcFLASH	47
2.2.2. IE map reconstruction	50
2.2.3. Mean IE value calculation	50
2.2.4. IE measurement execution report	53
2.3. Technical details of the residual MT effect correction (adjustment of the CASL-EPI method)	54
2.3.1. Presentation of the built-in MT correction method	54
2.3.2. Data acquisition	54
2.3.3. Automatic brain extraction	55
2.3.4. Optimal control frequency calculation	56
2.3.5. MT correction execution report	57
2.4. Technical details of the CBF measurement (CASL-EPI method)	58
2.4.1. Before running the CASL-EPI sequence	58
2.4.2. Perfusion data reconstruction	58
2.4.3. CBF measurement execution report	60
2.5. Tests and validation of the developed tools	60
2.5.1. Inversion efficiency	60
2.5.2. MT correction	63
2.5.3. Relative and quantitative perfusion reconstruction	63
2.6. Perspectives	63
<b>3. Simulations</b>	<b>65</b>
3.1. Implementation	65
3.2. pCASL labeling parameter optimization	68
<b>4. Development of robust pCASL labeling</b>	<b>71</b>
4.1. Introduction	71
4.2. Theory	72
4.3. Methods	72
4.3.1. Animals	72
4.3.2. MR sequences	73
4.3.3. Data Processing	74
4.3.4. Experimental Protocols	76
4.3.5. Simulations	78
4.3.6. Statistical analysis	79
4.4. Results	79
4.4.1. Experiment 1	79
4.4.2. Experiment 2	81

4.4.3. Experiment 3 . . . . .	81
4.5. Discussion . . . . .	85
4.6. Conclusion . . . . .	91
<b>5. Time encoded ASL implementation and application in mice</b>	<b>93</b>
5.1. Introduction . . . . .	93
5.2. Methods . . . . .	95
5.2.1. Animals . . . . .	95
5.2.2. MR sequences and experiments . . . . .	95
5.2.3. Post-processing . . . . .	96
5.3. Results . . . . .	98
5.3.1. te-pCASL signal time-course . . . . .	98
5.3.2. Fit to the te-pCASL data . . . . .	100
5.3.3. ATT and CBF maps . . . . .	101
5.3.4. Effect of left carotid occlusion . . . . .	102
5.3.5. Effects of age and brain region on ATT and CBF . . . . .	102
5.3.6. te-pCASL CBF versus standard pCASL CBF . . . . .	102
5.4. Discussion . . . . .	103
5.5. Conclusion . . . . .	109
<b>6. SAR comparison between CASL and pCASL at high magnetic field. Evaluation of the benefit of a separate labeling coil.</b>	<b>111</b>
6.1. Introduction . . . . .	111
6.2. Methods . . . . .	112
6.2.1. Animals . . . . .	112
6.2.2. MR experiments . . . . .	113
6.2.2.1. <i>In vivo</i> temperature measurements . . . . .	114
6.2.2.2. Inversion efficiency measurements . . . . .	116
6.2.2.3. Coil temperature measurements . . . . .	116
6.2.3. Data Processing . . . . .	117
6.3. Results . . . . .	120
6.3.1. $B_{1RMS}$ . . . . .	120
6.3.2. Global temperature time-course . . . . .	120
6.3.3. In-vivo $SAR_{app}$ across sequences . . . . .	122
6.3.4. Heat induced in absence of RF emission . . . . .	126
6.3.5. In-vivo $Q_{dec}$ and $SAR_{RF}$ . . . . .	126
6.3.6. CBF values . . . . .	130
6.3.7. Inversion efficiency . . . . .	131
6.4. Discussion . . . . .	131
6.5. Conclusion . . . . .	134
<b>7. General conclusion &amp; perspectives</b>	<b>135</b>
7.1. Conclusion . . . . .	135
7.2. Perspectives . . . . .	137

<b>APPENDICES</b>	<b>141</b>
<b>A. CASL Reports</b>	<b>141</b>
A.1. Inversion efficiency report (CASL-FcFLASH) . . . . .	141
A.2. MT correction adjustment report (adjustement of CASL-EPI) . . . . .	145
A.3. CBF measurement report (CASL-EPI) . . . . .	149
<b>B. 3D Arterial Spin Labeling</b>	<b>155</b>
B.1. 3D Arterial Spin Labeling Optimization . . . . .	155
B.2. Combined 3D perfusion and diffusion MRI to phenotype the mouse brain: Evaluation and application to a model of schizophrenia . . . . .	158
B.3. 3D Dynamic Arterial Spin Labeling (DASL) in mice . . . . .	165
<b>C. Curriculum Vitae</b>	<b>169</b>
<b>Bibliography</b>	<b>173</b>

# Nomenclature

AD	Alzheimer's Disease
ADC	Apparent Diffusion Coefficient
ASL	Arterial Spin Labeling
ATT	Arterial Transit Time
AUC	Area Under the signal enhancement Curve
BBB	Blood Brain Barrier
BW	BandWidth
CASL	Continuous Arterial Spin Labeling
CBF	Cerebral Blood Flow
CBV	Cerebral Blood Volume
CMRO2	Cerebral Metabolic Rate of Oxygen
CT	Computed Tomography
DASL	Dynamic Arterial Spin Labeling
DSC	Dynamic Susceptibility Contrast
EPI	Echo-Planar Imaging
FcFLASH	Flow-Compensated Fast Low Angle SHot
FLASH	Fast Low Angle SHot
HMPAO	Hexa-Methyl-Propyl-Amine Oxime
ICNIRP	International Commission of Non-Ionizing Radiation Protection
IE	Inversion Efficiency
ISMRM	International Society for Magnetic Resonance in Medicine
MCI	Mild Cognitive Impairment
MRI	Magnetic Resonance Imaging

MT	Magnetization Transfer
MTT	Mean Transit Time
OEF	Oxygen Extraction Fraction
OPT	One Pulse Time
PASL	Pulsed Arterial Spin Labeling
pCASL	Pseudo-Continuous Arterial Spin Labeling
PET	Positron Emission Tomography
PLD	Post-Labeling Delay
RF	Radio-Frequency
RMS	Root Mean Square
ROI	Region Of Interest
SAR	Specific Absorption Rate
SB	Sub-Bolus
SD	Standard Deviation
SNR	Signal to Noise Ratio
SO <sub>2</sub>	Blood Oxygenation Saturation
SPECT	Single Photo Emission Computed Tomography
StO <sub>2</sub>	Tissular Oxygen Saturation
TBI	Traumatic brain injury
te-pCASL	time-encoded pseudo Continuous Arterial Spin Labeling
TI	Inversion Time
Tx/Rx	Transmit/Receive
vsASL	Velocity Selective Arterial Spin Labeling

# 1. General introduction

Perfusion-related parameters such as cerebral blood flow are used in diagnosis and therapeutic follow-up in a large number of diseases to characterize micro-circulation. The first part of this introduction is dedicated to the role of perfusion in clinical neuroimaging. Its relevance in disease detection, treatment and follow-up in humans motivates our interest to further develop tools to estimate perfusion in the context of preclinical studies. Several physiological parameters exist to characterize the microcirculation and are subsequently described in the second part of this introduction. In this thesis, we focused on cerebral blood flow (CBF), which may be measured using numerous approaches [Wintermark et al., 2005]. The most common techniques are described in the third part. In clinical practice, perfusion computed tomography (CT) and dynamic susceptibility contrast (DSC) are the two most widely used techniques to measure CBF. However, both require the injection of a contrast agent and CT uses ionizing radiation. Among all possible methods to measure CBF, the least invasive is arterial spin labeled (ASL) magnetic resonance imaging (MRI): this technique deposits no ionizing radiation and no tracer injection is required [Barbier et al., 2001a]. Instead, arterial water is used as an endogenous tracer within an MRI sequence. To use blood as a tracer, the latter can be magnetically labeled. The labeling's "life-time" lasts only a few seconds, after which the blood magnetization comes back to equilibrium. Taken together with the innocuity of ASL-MRI, this allows measurements to be repeated, providing access to changes in CBF on timescales ranging from seconds to months. Labeling can be achieved through various techniques, described in the fourth part, which differ in the way radio frequency (RF) magnetic fields and magnetic field gradients are used to selectively label inflowing blood. Preclinical scanners operate at higher magnetic fields than human scanners, leading to some undeniable advantages, such as longer longitudinal relaxation times and thus longer label half-life, but which also complicate the use of ASL. Problems encountered at high magnetic field are addressed in the fifth part of this introduction. To finish the chapter, the objectives of the PhD project are described. Even if this thesis focuses on perfusion measurements in rodents, data in humans will be presented as well in the introduction. Basic MR imaging concepts are not developed.

## 1.1. Why measure perfusion?

Cerebral perfusion characterizes the way the brain is irrigated by blood to cover its vital needs in nutrients and oxygen and is an important indicator of function and viability. The micro-vessel's architecture and permeability contribute to the regulation of the exchanges between blood and tissue.

Perfusion varies with cerebral activity, anesthesia, blood oxygenation, capnia, drug intake or other active ingredients, such as caffeine for example, and is altered in a large number of diseases [Telischak et al., 2015]. In many diseases, perfusion assessment allows for diagnosis and therapeutic follow-up to adapt the treatment or to evaluate the treatment quality. It is emerging as a biomarker in neuro-degenerative disorders. This section presents some examples of diseases where a perfusion measurement is helpful for the patient's care. We focus on ASL-MRI applications in the brain, even if, until now, DSC-MRI or Perfusion-CT are more commonly performed, since ASL is just starting to be used outside of research centers.

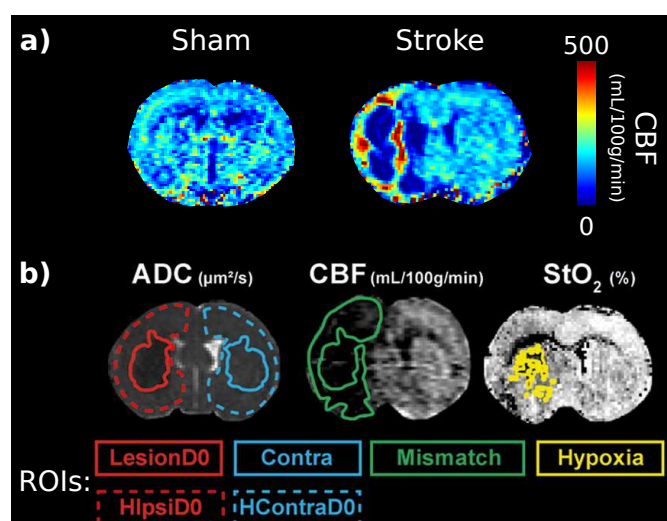


Figure 1.1.: (a) Perfusion scan of a sham rat (left), i.e. that underwent the same surgery as ischaemic rats except the middle cerebral artery occlusion, and of an ischaemic stroke rat before reperfusion (right). (b) Example of standard diffusion (ADC) and perfusion (CBF) maps of an ischaemic rat on which the perfusion-diffusion mismatch was delineated. The hypoxic region is drawn on a brain tissue oxygen saturation (StO<sub>2</sub>) map. Adapted from [Boisserand et al., 2016].

**Stroke** Ischaemic stroke (accounting for around 80% of all stroke cases) is characterized by decreased blood supply in a brain region due to complete or partial occlusion of the supplying vessels. This results in the possible dysfunction of the affected brain area, depending on the lesion's severity. In order to determine the treatment strategy, the so-called penumbra is evaluated [Touzani et al., 2001]. This region is composed of

tissue that remains viable for several hours and is therefore potentially salvageable. If ischaemic stroke is diagnosed rapidly (i.e. up to 6 hours after onset), thrombolysis and/or thrombectomy can be used as treatment to remove or dissolve the clot [Jauch et al., 2013]. Currently in clinical practice, joint perfusion and diffusion MR scans are acquired to detect the presence of such tissue at risk (Fig. 1.1). The penumbra is estimated as the mismatch between the lesion observed on the perfusion scan and that on the diffusion scan [Schlaug et al., 1999]. Correct differentiation between salvageable and irreversibly damaged tissue is crucial since it directly influences the treatment decision. In recent years, the accuracy of penumbra detection by means of perfusion-diffusion mismatch has been contested (mostly due to a lesion overestimation in the diffusion scan). Novel techniques based on multi-parametric MRI [Boisserand et al., 2016] or spectroscopic imaging [Holmes et al., 2012] emerge to refine treatment decisions.

**Tumors** To proliferate, tumors have high needs in oxygen and nutrients, which are supplied by blood flow. High grade malignant tumors (i.e. grade III and IV) are indeed characterized by an angiogenesis leading to increased perfusion (Fig. 1.2). However, when being well oxygenated, tumors also become more radiosensitive: especially when using X-rays as treatment, well oxygenated cells have higher mortality rate than hypoxic cells. Radiation doses are therefore fractionated to allow hypoxic cells to reoxygenate in-between two radiation sessions, to make them more radiosensitive during subsequent radiation doses. As a consequence, perfusion plays an important role in cancer not only for its detection and characterization but also in treatment follow-up [Warmuth et al., 2003; Kimura et al., 2006].

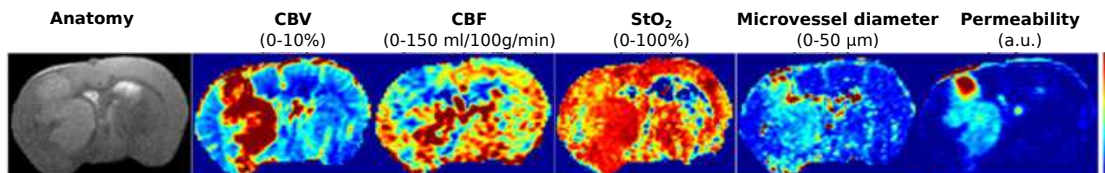


Figure 1.2.: Quantitative perfusion maps of a 9L gliosarcoma rat. Anatomy: T2-weighted image (ventricles in white), CBV: cerebral blood volume; CBF: cerebral blood flow, StO<sub>2</sub>: tissue oxygen saturation, mean microvessel diameter (vessel size index), vessel wall permeability. From Librizzi et al. [2017].

**Traumatic brain injury (TBI)** Perfusion is altered in mild and severe TBI but in a more moderate range than in stroke. ASL-MRI has been shown to be able to identify hypoperfused regions that were not detected with standard MRI or CT scans in mild TBI patients [Lin et al., 2016]. A correlation was found between CBF and post-concussive symptoms. However, it is often difficult to transport TBI patients to MRI scanners due to their fragile state and the monitoring and life-support equipment many of these patients require, the equipment being often not MR-compatible. In a study performed

on diffuse TBI in rats, oxygenation was found to be affected and related to alterations of the micro-circulation and cell edema [Bouzat et al., 2013].

**Dementia** Perfusion is an emerging biomarker in dementia. In early stages of dementia, and in particular in Alzheimer’s disease, perfusion alterations have indeed been measured in brain regions before structural changes occur [Dai et al., 2009; Chao et al., 2010; Wolk and Detre, 2012] (Fig. 1.3).

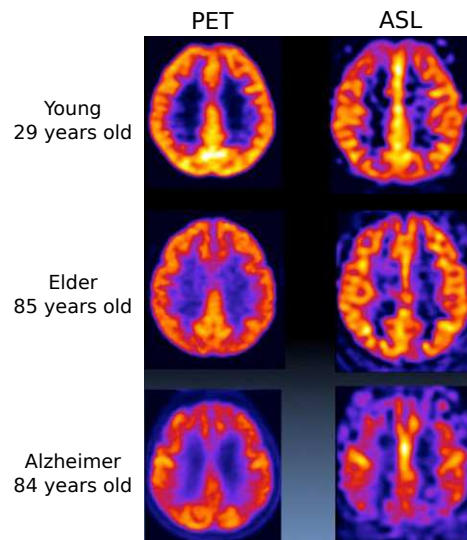


Figure 1.3.: ASL-MRI versus positron emission tomography (PET) perfusion images in a young subject, (top row), an elderly subject (middle row) and in an Alzheimer patient (bottom row) [Hernandez Tamames].

**Epilepsy** Alterations in perfusion parameters, and especially in cerebral blood flow were measured in epileptic seizure [Pizzini et al., 2013; Wu et al., 1999]. Moreover, epileptic seizure also induces vascular remodeling in given brain regions that could be characterized through perfusion assessment [Librizzi et al., 2017].

**Schizophrenia** Altered neuronal activity in schizophrenia leads to perfusion variations [Homan et al., 2013]. Perfusion patterns depend on the brain region, the disease type and stage, the taken medication or treatment. Although cerebral blood flow measurement in schizophrenia is usually performed by means of positron emission tomography (PET) [Liddle et al., 1992; Sabri et al., 1997; Lahti et al., 2006], several ASL-MRI studies were conducted as well [Homan et al., 2013; Scheef et al., 2010; Pinkham et al., 2011] since MRI’s non-invasiveness allows for repeated examinations.

**Other diseases** Table 1.1 shows more diseases where perfusion, and especially cerebral blood flow, is altered. Again, it focuses on ASL-MRI applications [Telischak et al., 2015].

Table 1.1.: Summary of CBF variations in disease from [Telischak et al. \[2015\]](#).

CBF decrease	CBF increase	Mixed CBF
Acute ischaemic stroke	Tumor (primary brain tumors, some metastases)	Seizure
Moyamoya disease	Cerebritis	Migraine
Acute hydrocephalus	Vascular shunts	Hypoxic ischaemic injury
Neurodegenerative disorders	Loss of autoregulation (e.g. hypoxic-ischaemic injury)	Posterior reversible encephalopathy syndrome (PRES)
Sturge-Weber	Hypercapnia	Schizophrenia

To conclude, perfusion is altered in a large number of diseases, which explains why it is routinely assessed in clinical practice in disease detection and treatment follow-up.

## 1.2. Physiological parameters describing perfusion

Perfusion is a complex process and cannot be reduced to a single parameter, even if the term is often used to refer to cerebral blood flow only. This section presents the most common parameters used to describe the micro-circulation in the brain.

### 1.2.1. Parameters related to baseline perfusion

**Cerebral Blood Flow (CBF)** CBF refers to the rate of blood delivered through the local capillary bed of a mass of cerebral tissue. CBF is usually expressed in units of blood volume delivered per unit time to a given mass of tissue (mL/100 g/min).

**Cerebral Blood Volume (CBV)** Describing the volume of brain tissue that is occupied by blood vessels, CBV is expressed in units of volume per tissue mass (mL/100g or  $\mu\text{L/g}$ ), or sometimes as volume fraction (%). This parameter is commonly used for angiogenesis detection in tumors.

**Mean Transit Time (MTT)** Defined as the time a water molecule or contrast agent particle spends in the voxel's vasculature, MTT is related to CBF and CBV as follows:

$$MTT = \frac{CBV}{CBF}.$$

MTT is measured in seconds.

### 1.2.2. Parameters related to oxygen and nutrient delivery

Since perfusion enables oxygen delivery, it directly influences the following oxygenation parameters:

**Blood Oxygenation Saturation (SO<sub>2</sub>)** SO<sub>2</sub> is defined as the fraction of hemoglobin in a vessel that is oxygenated:

$$SO_2 = \frac{[HbO_2]}{[dHb] + [HbO_2]},$$

where [HbO<sub>2</sub>] and [dHb] are respectively the concentrations of oxy- and deoxyhemoglobin.

**Oxygen Extraction Fraction (OEF)** OEF is defined as the fraction of oxygen removed from the blood by the tissue while flowing through the capillary bed. It is calculated as the relative difference between arterial and venous oxygen saturations.

**Cerebral Metabolic Rate of Oxygen (CMRO<sub>2</sub>)** CMRO<sub>2</sub> is the tissue oxygen consumption defined as:

$$CMRO_2 = OEF \times CBF \times CaO_2,$$

where CaO<sub>2</sub> is the arterial oxygen concentration. CMRO<sub>2</sub> varies in presence of disorders but also with neuronal activity.

Joint CBF, OEF and CMRO<sub>2</sub> assessment allows for better understanding of the brain's physio-(patho)logical state.

**Blood Brain Barrier (BBB) permeability** The cerebral tissue is separated from the microvasculature by the blood brain barrier (BBB) composed of tightly interconnected brain endothelial cells. The BBB aims to protect the brain from pathogens and reduces the exchanges from the capillaries to the brain tissue: ~98% of all small molecules are not transported across the BBB [Pardridge, 2012]. This high selectivity is illustrated in Fig. 1.4: small 111 Da histamine particles were injected to a mouse 5 minutes before its euthanasia and the distribution of the particles throughout the organism was subsequently visualized using autoradiography. It can be clearly seen that histamine extravasates in all organs but the brain. In disease, such as tumors, multiple sclerosis or stroke, the BBB becomes more permeable. Such BBB permeability disturbances and changes in its integrity can be measured quantitatively with contrast agents [Tofts and Kermode, 1991; Schwarzbauer et al., 1997; Barbier et al., 2002] and help to characterize the pathology stage: Depending on the contrast agent's size and/or on the presence of pathology, the tracer's ability to extravasate changes. BBB permeability to water can also vary, and thereby impact water-based perfusion measurements.



Figure 1.4.: Whole body autoradiogram of a mouse euthanized 5 minutes after the intravenous injection of small 111 Da molecules ( $[^{14}\text{C}]$ -histamine): extravasation occurs in all organs but the brain. From [Pardridge \[2012\]](#).

**Microvessel architecture** The vessel size (in  $\mu\text{m}$ ) and density (in  $\text{mm}^{-2}$  or  $\text{mm}^{-3}$ ) can be estimated to provide information on the underlying brain's microvasculature and therefore on the perfusion's origin [[Tropès et al., 2015](#)]. Mapping these vessel parameters allows also to better characterize lesions. For instance, in tumors, the blood volume may remain unchanged, whereas the vessel size increases [[Pannetier et al., 2012](#)].

### 1.2.3. Parameters related to functional changes in perfusion

Perfusion, and especially CBF, is actively regulated through an autoregulation mechanism and is constantly adapted to the brain's needs through neurovascular coupling and vasoreactivity. These functional perfusion regulation mechanisms may be altered in some disease, inducing improper brain supply in vital needs. For example, the neurovascular coupling is altered in aging and Alzheimer's disease [[D'Esposito et al., 2003](#)]; hypotension may lead to improper autoregulation inducing loss of consciousness. Each of these functional mechanisms are now shortly defined:

**Autoregulation** CBF is autoregulated to remain constant within a given range of blood and intra-cranial pressures, to provide constant oxygen and nutrient delivery to the brain independently of perfusion pressure. This is done by adapting the vascular tone leading to vessel dilatation or constriction, as shown on Fig. 1.5 from [[Pires et al., 2013](#)].

**Neurovascular coupling** The neurovascular coupling is a mechanism that modifies CBF in response to changes in neuronal activity in order to yield appropriate supply in oxygen in the presence of changing metabolic needs.

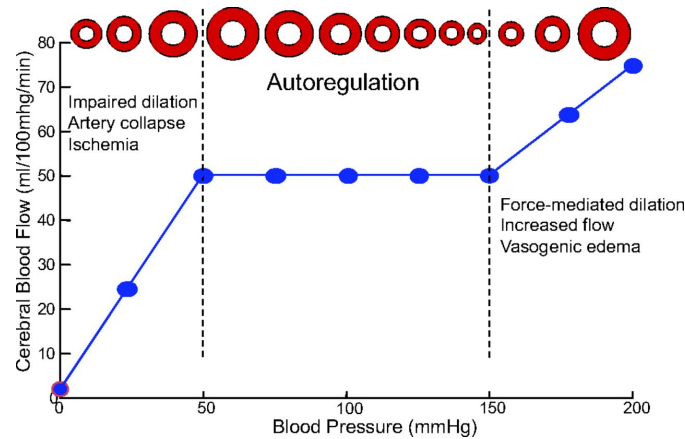


Figure 1.5.: Cerebral blood flow in relation to artery lumen diameter. Dotted lines represent the lower and upper limits of cerebral blood flow autoregulation. Red circles represent the cerebral arteries, and blue line represents the cerebral blood flow. From [Pires et al., 2013].

**Vasoreactivity** Vasoreactivity characterizes the vessel's response to the levels of oxygen and  $\text{CO}_2$  concentrations in the circulating blood. For example, in the brain, a high  $\text{CO}_2$  blood concentration dilates the vessels and induces a CBF increase [Kety and Schmidt, 1948]. A  $\text{CO}_2$  challenge is a way to estimate the vessel's capacity to dilate and therefore provides a means to study neurovascular pathologies [Cantin et al., 2011], as illustrated in Fig. 1.6.

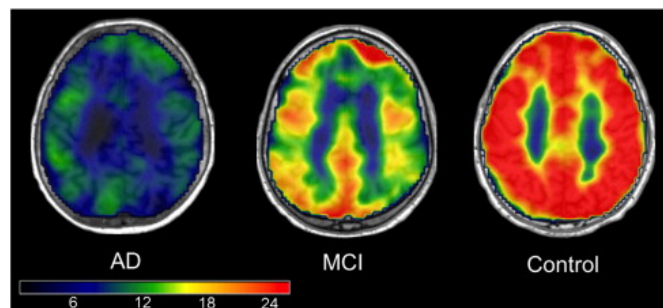


Figure 1.6.: BOLD response to carbogen (95% oxygen / 5%  $\text{CO}_2$ ) inhalation in control subjects (right), in mild cognitive impairment (MCI, middle) and Alzheimer's disease (AD, left) patients. One can observe that vasoreactivity is impaired in MCI and AD patients. From Cantin et al. [2011].

#### 1.2.4. Multiparametric perfusion imaging

As we have seen, perfusion is characterized by and depends on various parameters. *In vivo*, the technique that gives access to most of these parameters and thus allows the most exhaustive perfusion characterization is MRI. An example of maps obtained with multiparametric MRI is shown in Figs. 1.2 and 1.7. In the study of Fig. 1.7, the authors

show the potential of multiparametric MRI to obtain extensive information about tissues that was previously only accessible ex-vivo via histology [Coquery et al., 2014].

CBF is a key parameter of perfusion and in this thesis, we focused on the measurement of this perfusion parameter.

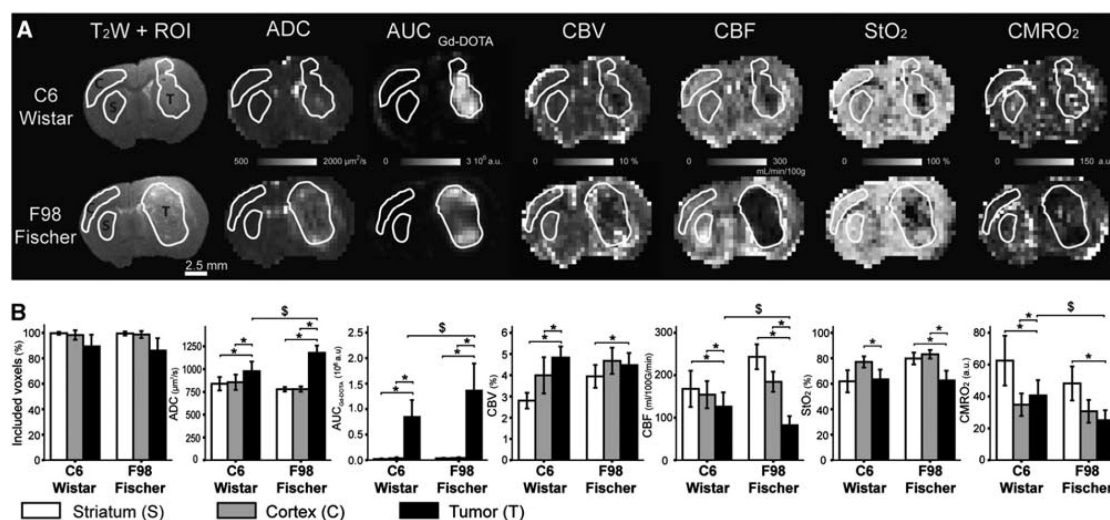


Figure 1.7.: Multiparametric MRI in rat models of glioma Coquery et al. [2014]: anatomical scan ( $T_{2w}$ ), diffusion (ADC), vessel wall permeability ( $AUC_{Gd-DOTA}$ ), CBF, CBV, tissular oxygen saturation ( $StO_2$ ) and  $CMRO_2$ . One can observe that perfusion parameters are not homogeneous and not equally distributed within the tumor. To integrate the multiparametric information and obtain a summary map of tissue types based on perfusion parameters, the authors used a clustering approach (not shown).

### 1.3. CBF measurement methods

Cerebral blood flow measurement techniques rely on the detection and tracking of tracers, which are distributed in the tissue of interest through blood flow. Different types of tracers exist, which differ in their distribution properties:

- **Intravascular** tracers remain in the blood vessels.
- **Extracellular** tracers freely pass through the vessel walls and spread in the extracellular tissue space without entering the cells.
- **Freely diffusible** tracers, such as radioactive tracers or endogenous water molecules, distribute in all tissue compartments and can enter the cells.

These tracers are used in various techniques. Their characterization is organ dependent: for instance, a gadolinium chelate can be considered as an extracellular tracer for the

breast but remains intravascular in the healthy brain, due to the presence of the blood-brain barrier. If gadolinium extravasates in the brain, this shows that the BBB is leaky, indicating the presence of pathology.

The principal techniques used to measure CBF are shortly outlined below [Wintermark et al., 2005].

**Autoradiography** This early method is based on the injection of a radioactive tracer in the animal's veins. The tracer's arterial concentration is sampled during 30 to 45 seconds after injection. Then, the animal is decapitated, the brain quickly removed, frozen and cut into thin slices to quantify the radiolabeled tracer contained in the brain tissue. From the measured arterial input function and the regional tracer concentration, the CBF can then be calculated (Landau et al. [1955]; Sakurada et al. [1978]). Autoradiography is a technique that yields quantitative CBF values [Baskerville et al., 2012]. However its use is not compatible with longitudinal perfusion studies since it requires the animal's euthanasia.

**Single Photon Emission Computed Tomography (SPECT)** This technique uses HMPAO (hexa-methyl-propyl-amine oxime), usually labeled with  $^{99m}\text{Tc}$ . At equilibrium, the accumulation of HMPAO in the brain is related to CBF. This approach is not considered quantitative.

**Positron Emission Tomography (PET)** This technique uses  $^{15}\text{O}$  labeled water as a flow tracer and is considered as the "gold standard" for CBF quantification [Zhang et al., 2014]. However, the use of PET imaging remains limited in practice by its high cost, relative invasiveness, radiation exposure and limited availability. Recently, Wolk and Detre [2012] reviewed that in Alzheimer's disease studies, ASL-MRI may provide similar information as PET.

**Computed Tomography (CT)** Widely used in clinical practice, CT-based perfusion imaging relies on the tissue's X-ray attenuation measurement. It requires the injection or inhalation of an exogenous tracer such as iodine or xenon.

**Magnetic Resonance Imaging (MRI)** MRI is particularly interesting since it does not use any ionizing radiation. CBF measurement by means of MR can be done through two main techniques:

- Dynamic Susceptibility Contrast (DSC) - DSC perfusion imaging tracks the passage of a contrast agent (e.g. gadolinium chelates) in the voxel of interest. A series of images are acquired to sample the MR signal changes produced by the passage of the bolus of contrast agent in the microvasculature. The passage of

gadolinium influences the relaxation times of the voxel such as  $T_2^*$ . By fitting the observed signal intensity-vs.-time curve to a gamma-variate function, relative CBV, CBF and MTT can be calculated. However, quantitative values for CBF are only obtained if a deconvolution of the tissue response with the arterial input function is performed [Willats and Calamante, 2013]. Moreover, repeated usage of gadolinium may harm patients with kidney problems since it has been shown to trigger the development of nephrogenic systemic fibrosis [Grobner, 2006]. Recently some gadolinium accumulation in brain regions were reported as well [McDonald et al., 2015; Zhang et al., 2017].

- Arterial spin labeling (ASL) - Arterial spin labeled perfusion MRI permits quantification of blood flow without using any exogenous contrast agent. Instead, it uses blood water as an endogenous tracer [Detre et al., 1992; Williams et al., 1992; Kim, 1995; Alsop and Detre, 1996]. This noninvasiveness makes ASL especially appealing in pediatric populations, for patients with renal dysfunction or when repeated measurements are required. Moreover, ASL gives access to quantitative CBF values and therefore allows for comparison of perfusion over time (e.g. comparison between pre vs. post treatment states) and for better recognition of global perfusion variations such as hypercapnia or hypoxic/anoxic brain injury states [Pollock et al., 2009]. As an illustration, Fig. 1.8 (adapted from McGehee et al. [2012]) shows perfusion data acquired both with DSC and ASL MRI for a high-grade glioma patient after tumor resection. In the top row, images from baseline are represented and the bottom row shows images acquired 10 weeks later. Since DSC enables to measure only relative values, this explains the different scaling and contrasts on the rCBV map. On the other hand, CBF maps from ASL-MRI scans show stability across exams and allow to clearly identify a hyperperfused spot that cannot be detected on the DSC maps (arrowheads). Subsequent scans confirmed the tumor's recurrence.

However, ASL suffered from a long methodological maturation. A consensus paper in 2015 and progress in hardware made this technique more appealing nowadays.

We now focus on how arterial blood can be used as a tracer and describe the different methods used to magnetically label the water spins in MRI.

## 1.4. Arterial spin labeling methods

### 1.4.1. How can blood be used as a tracer?

Assuming that water is a freely diffusible tracer, arterial spin labeled MRI permits to quantify blood flow without any need for contrast agent injection or radiation [Williams et al., 1992; Detre et al., 1992]. The MR signal originates from the magnetization of the

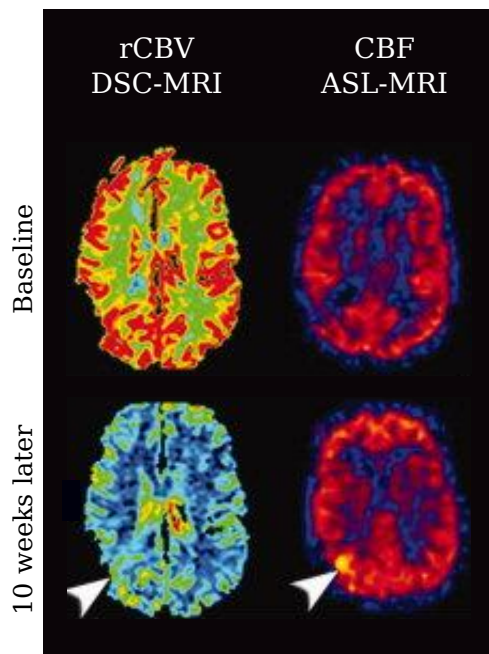


Figure 1.8.: rCBV (left) and CBF (right) maps from baseline (top row) and roughly 10 weeks later (bottom row) for a patient after post high-grade glioma resection with several stable follow-up exams. rCBV maps were acquired by means of DSC and CBF maps with ASL. Adapted from [McGehee et al. \[2012\]](#)

nuclear spin of hydrogen in water molecules. Therefore, by changing the longitudinal magnetization of the proton spins in arterial blood water before it flows into the organ of interest, and thereby labeling the blood, regions that are perfused with labeled blood will see an MR signal change proportional to blood flow. To eliminate signal from static spins in tissue water, pairs of images are acquired: From the difference in MR signal between one image acquired after labeling arterial blood and one “control” image acquired without labeling, perfusion can be measured (Fig. 1.9).

All arterial spin labeling methods basically rely on the same three steps: first, the blood water spins are labeled, and after a delay allowing the labeled spins to perfuse the tissue of interest, an image is acquired. A control image is generated as well, using the same steps, but leaving the water spins unaffected (or by affecting them differently as in flow-sensitive alternating inversion recovery (FAIR), cf. below). The ASL signal results from the difference between the label and the control images. Since ASL yields a weak perfusion signal often close to the noise level (i.e.  $\sim 1-7\%$  of the signal intensity from static spins), averaging of several label-control pairs is required ( $\sim 20-30$ ) to obtain a usable perfusion map.

Labeling is achieved by applying specific radio-frequency (RF) pulses affecting the magnetization of the blood’s spins. In ASL, this results in inverting their, by default  $B_0$ -aligned, magnetization. Several techniques exist to invert the spin’s magnetization.

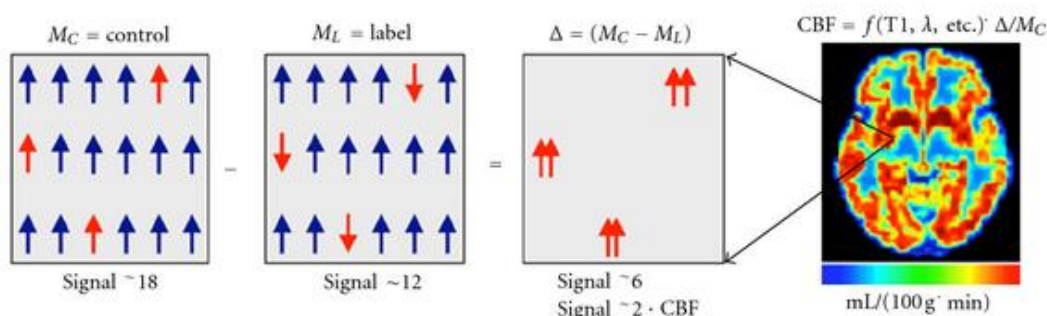


Figure 1.9.: Arterial spin labeling principle. The three first panels represent the signal from a single voxel that originates from a control condition (left), a label condition (middle) and the resulting control-label difference (right): after subtraction, only the labeled spins yield signal. The contribution of all other non-labeled spins cancel out. A CBF map is shown on the last panel on the right. From Borogovac and Asllani [2012]

### Classic inversion

A classic inversion is achieved by applying an RF pulse at a frequency equal to the target spin's Larmor frequency and in a direction perpendicular to the magnetic field  $B_0$ . The flip angle is proportional to the integral of the RF amplitude  $B_1$  over the pulse duration  $T$ , according to following equation:

$$\theta = \gamma \int_0^T B_1(t) dt. \quad (1.1)$$

A flip angle of  $180^\circ$  leads to perfect inversion of magnetization. However, this inversion technique is very sensitive to  $B_1$  inhomogeneities, causing unwanted spatial flip angle variations. The quality of an inversion pulse is measured by its inversion efficiency ( $IE = (1 - \cos \theta) / 2$ ), defined as the relative change in longitudinal magnetization it provokes, with respect to an ideal inversion pulse. In the context of ASL, the difference in the inversion efficiencies of the label and control pulses is also referred to as the inversion efficiency of the label or the label efficiency [Zhang et al., 1993]:

$$IE = \left| \frac{M_{C,c} - M_{L,c}}{2M_{C,c}} \right|, \quad (1.2)$$

where  $M_{C,c}$  and  $M_{L,c}$  are respectively the complex signals from the control and the label experiments. Since the label efficiency of classic inversion pulses is not robust to  $B_1$  variations and may in practice often be low, they are not used in ASL to label the blood spins.

**Adiabatic inversion**

The flip angle of an adiabatic inversion depends on the temporal variation in amplitude and frequency of the RF pulse: spins get inverted in presence of pulses modulated in frequency and amplitude over time. Adiabatic inversions have the advantage to reduce the sensitivity to  $B_1$  inhomogeneities.

**Flow-induced adiabatic inversion**

The blood spins are often labeled in the carotids, i.e. prior to their arrival in the brain region of interest [Dixon et al., 1986]. In this case, the spins to label are flowing in the carotids. Thus, by applying a magnetic field gradient  $G$  in the flow direction and, at the same time, an RF-pulse with constant  $B_1$  amplitude and frequency in time, the moving spins experience a variable magnetic field [Williams et al., 1992]. Indeed, when moving along the vessel, the resulting magnetic field (gradient + RF) is varying with the position, and the Larmor frequency of the flowing spins varies accordingly. Varying Larmor frequency at fixed RF frequency is equivalent to subjecting static spins with fixed Larmor frequency to an adiabatic RF pulse with variable frequency. Blood spins are inverted if their velocity ( $v$ ), longitudinal (resp. transverse) relaxation times  $T_1$  (resp.  $T_2$ ) and the applied labeling parameters meet the following adiabaticity condition:

$$\frac{1}{T_1}, \frac{1}{T_2} \ll G \cdot \frac{v}{B_1} \ll \gamma B_1. \quad (1.3)$$

A flow induced adiabatic inversion is represented Fig. 1.10. The spin's magnetization  $M_z$  is gradually inverted when moving and crossing the labeling plane thanks to the applied constant gradient and RF pulse. The magnetization follows the direction of a so-called effective magnetic field  $\overrightarrow{B_{eff}}$  in a reference frame rotating at the RF frequency:

$$\overrightarrow{B_{eff}} = B_1 \overrightarrow{x} + 2\pi \frac{f_{RF} - f(p)}{\gamma} \overrightarrow{z}, \quad (1.4)$$

where  $f_{RF}$  is the RF resonance frequency,  $f(p)$  the current spin's frequency at position  $p$ ,  $\overrightarrow{x}$  the unitary vector aligned with the  $B_1$  field in the rotating frame and  $\overrightarrow{z}$  the unitary vector pointing in the main magnetic field direction.

**Region 1** When the spins are located far away and before the labeling plane, their frequency is much lower than the applied RF frequency: the first term of equation 1.4 is negligible, the blood magnetization is aligned along the +z-axis.

**Region 2** When moving towards the labeling plane, the spin's frequency gets gradually closer to the RF frequency: the term  $f_{RF} - f$  converges to 0. At the labeling plane

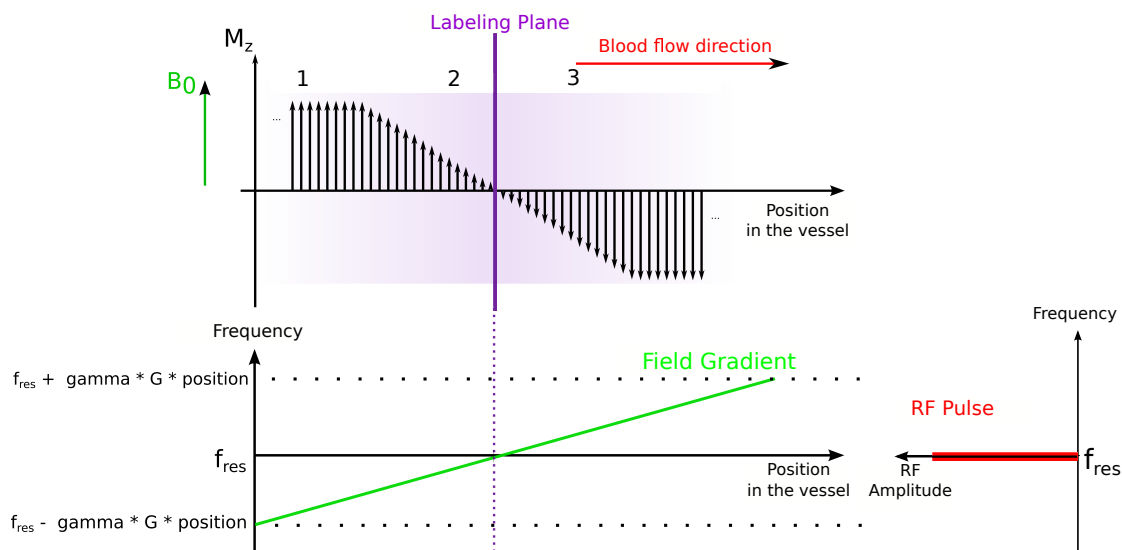


Figure 1.10.: Flow-driven adiabatic inversion scheme.

$f$  is equal to  $f_{RF}$ : the longitudinal component cancels out, the blood magnetization is flipped in the transverse plane.

**Region 3** When moving away from the labeling plane, the spin's frequency increases, the term  $f_{RF} - f$  becomes negative: the blood magnetization is along  $-z$ , i.e. inverted.

Hence, this labeling technique only inverts spins that are moving in a given direction, leaving static spins unaffected, except those located at the labeling plane. The latter experience an arbitrary and very large flip angle, since they are on resonance, which has no effect on the labeled bolus.

The inversion techniques described above are used within various labeling schemes, which are detailed in the next subsection.

## 1.4.2. Labeling schemes

Numerous labeling schemes have been developed in the past twenty five years [Barbier et al., 2001a; Alsop et al., 2015]. They can be divided in three main categories: pulsed, continuous and velocity-selective ASL. The continuous ASL technique has a variant called pseudo-continuous ASL, which is the recommended technique for clinical studies. These labeling schemes are now presented from a preclinical application point of view.

### 1.4.2.1. Pulsed Arterial Spin Labeling (PASL)

In pulsed ASL (PASL), labeling is achieved by inverting a large slab of blood by means of a short adiabatic RF pulse. In order to obtain the best defined blood bolus (i.e. thick slab with sharp edges) with high inversion efficiency that is robust to variations

in  $B_1$  field strength, adiabatic pulses, and more precisely hyperbolic secant pulses, are commonly used. Various PASL schemes have been developed; in preclinical studies, flow-sensitive alternating inversion recovery (FAIR) developed by Kim [1995] and Kwong et al. [1995] is the most frequently used technique (Fig. 1.11). To produce the label and control conditions, images are acquired after a slice-selective inversion and a non-selective inversion (global inversion) respectively. The pulse is followed by a so called post-labeling delay (PLD).

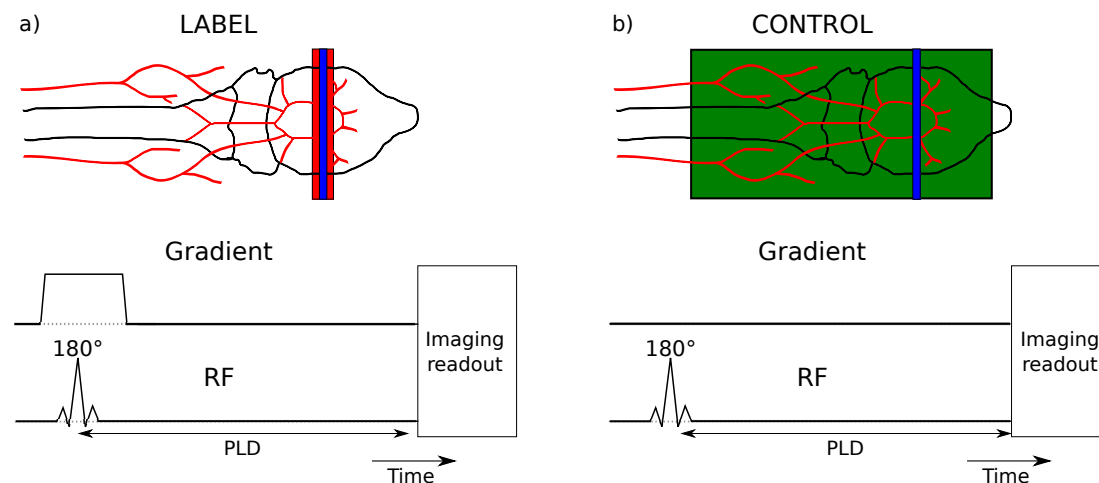


Figure 1.11.: (a) Label and (b) control diagrams for FAIR. The vessel architecture supplying the brain is illustrated in red and has been adapted from Engel et al. [2011]. The labeling (resp. control) slices are represented with a red (resp. green) box. The imaged slice is displayed in blue. The corresponding gradient and RF amplitude timecourses are shown as well.

### Advantages

- Since only a single RF pulse is needed for labeling, PASL has the advantage to deposit lower RF energy than CASL and pCASL.

### Drawbacks

- Even if adiabatic pulses are used to label, the resulting inverted blood slab - and therefore the temporal width of the labeling bolus - remains unknown because it depends on the blood flow velocity and on the pulse profile.
- Since the achievable duration of the bolus of labeled blood is much lower than the bolus used in continuous labeling, the perfusion signal to noise ratio (SNR) is generally lower in pulsed ASL [Chen et al., 2011]. The amount of labeled spins is limited by the transmit coil's size and the labeling bolus has to be contained in the homogeneous part of the volume coil.

On clinical scanners, more refined techniques exist, with additional saturation pulses, enabling especially a better control of the labeled blood bolus duration. Warnking and Pike [2006] introduced bandwidth-modulated selective saturation and inversion (BASSI) RF pulses in PASL that achieve uniform and highly selective profiles at any flip angle. However, since these techniques are not commercially available on preclinical (Bruker) scanners, and because they yield lower SNR than continuous ASL techniques, we are not going into more details about pulsed ASL techniques in this thesis.

#### 1.4.2.2. Continuous Arterial Spin Labeling (CASL)

In continuous ASL (CASL), spins are continuously inverted while flowing through the labeling plane by means of a flow-driven adiabatic inversion. The labeling plane is usually located where carotids are approximately parallel to the animal's head-foot direction (i.e. the magnet's z direction), before the separation of the common carotid in external and internal carotids [Debacker et al., 2016]. In mice, this is located about 1 cm upstream the center of the brain; in rats, at 2 cm.

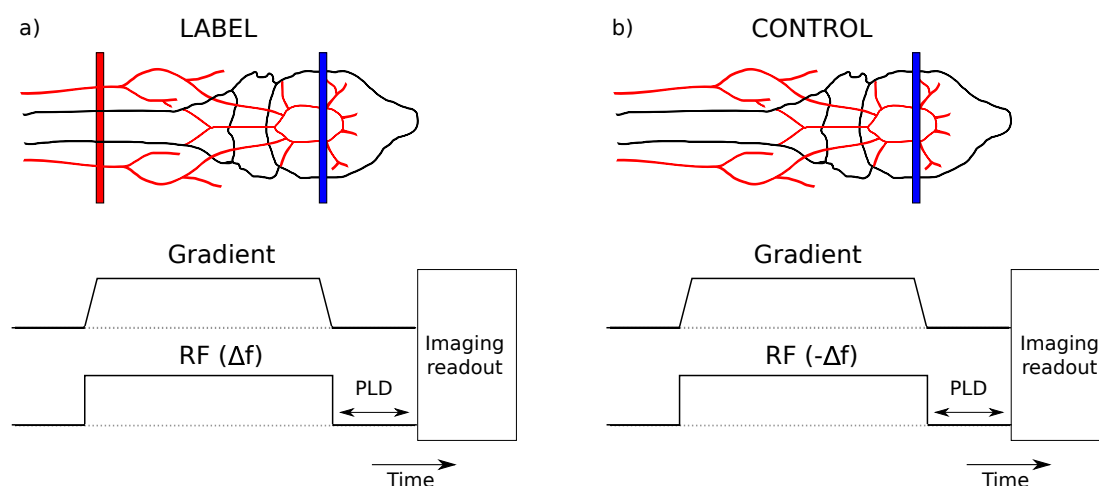


Figure 1.12.: (a) Label and (b) control diagrams for CASL. The vessel architecture supplying the brain is illustrated in red and has been adapted from Engel et al. [2011]. The labeling (resp. control) slices are represented with a red (resp. green) box. The imaged slice is displayed in blue. The corresponding gradient and RF amplitude timecourses are shown as well. PLD stands for post-labeling delay.

**RF & Gradients** The CASL labeling scheme consists of a continuous constant RF pulse applied during several seconds in presence of a constant gradient to generate a labeled blood bolus (Fig. 1.12). In practice, when labeling with a whole body volume coil, this long continuous labeling pulse inverts not only on-resonance spins in the labeling plane but saturates also macromolecules that have a broad spectrum making them sensitive to off-resonance RF pulses. Cross-relaxation of macromolecules with brain tissue wa-

ter changes the latter's magnetization. This phenomenon is called the magnetization transfer (MT) effect [Henkelman et al., 2001]. Therefore, the magnetization reduction measured in the label image is not only due to labeled blood but is also contaminated by MT effects. To compensate for these effects, which are generally larger than that of perfusion, a similar perturbation can be applied before acquiring the control image, so that, when subtracting the label and the control images, MT effects cancel out. Assuming that the macromolecules' spectrum is symmetrical, this compensation can be achieved by applying the same RF pulse as during labeling but with an opposite offset frequency ( $-\Delta f$ ) to avoid labeling [Zhang et al., 1992]. This strategy reduces the number of slices to a single slice.

Pekar et al. [1996] showed that the macromolecules' spectrum was not perfectly symmetrical and that residual MT effects remain after control-label subtraction. Hua et al. [2007] found that the negative offset side produced statistically significant lower intensities than the positive side ( $P < 0.001$ ) (Fig. 1.13a). This explains why in dead rats, CASL still produces a positive control-label signal when labeling with an negative offset frequency and when the control pulse is applied with an opposite offset frequency with respect to the label frequency [Debacker, 2014]. To describe MT effects, the magnetization transfer ratio (MTR) can be calculated as:

$$MTR = \frac{M_z - M_0}{M_0}, \quad (1.5)$$

where  $M_z$  and  $M_0$  are respectively the longitudinal magnetizations with and without applying an off-resonance RF pulse. Fig. 1.13b reports the MT asymmetry, calculated as the difference between the MTR values at the positive offsets and the corresponding negative offsets with respect to water: the higher the offset frequency, the lower the residual MT effects. Conversely, the higher the applied  $B_1$  amplitude, the higher the measured MT effects (Fig. 1.13a) and MT asymmetry (Fig. 1.13b). Moreover, the amplitude of such residual MT effects increases with the magnetic field.

Several strategies exist to compensate residual MT effects and therefore to avoid a CBF bias:

- Pekar et al. [1996] investigated several combinations of label and control gradients to correct for asymmetric MT effects, such as reversing the labeling gradient's polarity while applying the same RF pulse than during labeling. The authors also show that when the gradient is flipped, the magnetic field is not always the same as without flipping it. As the gradient slightly modifies the MT spectrum, this strategy could be limited to an imaging slice located at the isocenter.
- Pekar et al. [1996] and Barbier et al. [1999] suggested to sweep the control frequency during a prescan around its theoretical value  $-\Delta f$  in order to find the optimal control frequency that cancels residual MT effects out after control-label subtraction. More

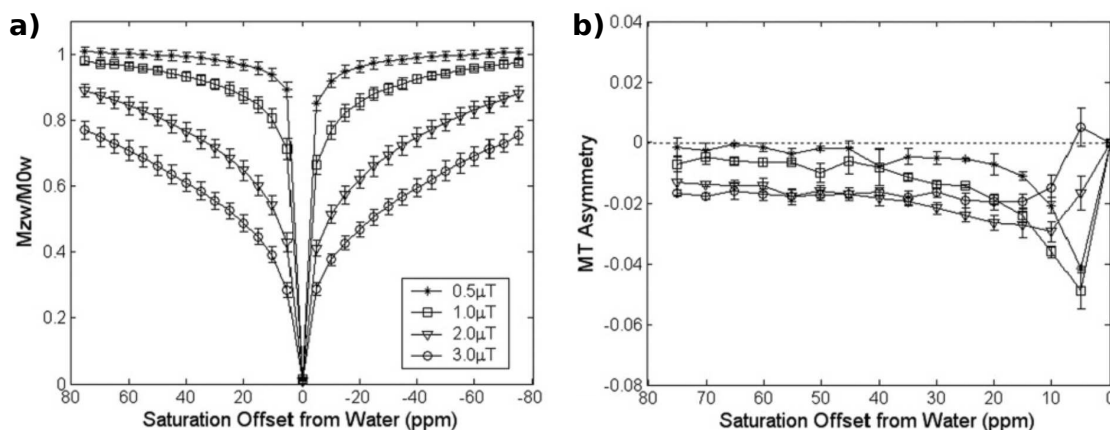


Figure 1.13.: (a) z-spectra (i.e.  $(1 - \text{MTR})$ ) as a function of the frequency offset of the RF irradiation) of white matter in healthy human brains at 3 T ( $N = 5$ ). The z-spectra are asymmetric with the negative offset side having statistically significant lower intensities ( $P < 0.001$ ). Datasets with  $B_1$  amplitudes of 0.5, 1, 2, and 3  $\mu\text{T}$  are displayed. (b) MTR asymmetry spectra. The magnitude of MTR asymmetry depends on both RF saturation power and offset. From Hua et al. [2007].

details about this technique are given in Chapter 2.3. This approach is limited to single slice imaging.

- An amplitude modulated RF field can be applied to invert the spins in the carotids twice in the control condition [Alsop and Detre, 1998]. This approach allows multi-slice imaging. However, it reduces the inversion efficiency (the double inversion is not perfect).
- An amplitude modulated RF field can be applied to invert simultaneously the spins in two planes, proximal and distal to the area of interest. This generates a flat MT saturation profile in the center frequency. Such a simultaneous proximal and distal irradiation (SPDI) is applied in presence of a gradient for label and in absence of a gradient in the control condition [Talagala et al., 1998]. This approach allows multi-slice imaging but in a limited spatial range and increases the SAR as well.

The restriction of CASL to a single slice due to residual MT effects can be overcome by using a dedicated small labeling coil placed under the animal's neck and whose field of view does not overlap the brain area of interest [Silva et al., 1995]. In this case, spins located in the imaged slice do not "see" the long continuous CASL RF pulse and there is therefore no saturation of the macromolecules magnetization [Talagala et al., 2004].

### Advantages

- Spins are inverted continuously, yielding high inversion efficiency (IE) for a large velocity range [Maccotta et al., 1997].

- A long and temporally well-defined bolus of labeled blood is generated [Alsop and Detre, 1996; Wong et al., 1998].
- Higher SNR than PASL is obtained, since more spins are labeled.

### Drawbacks

- In absence of a dedicated ASL coil, residual magnetization transfer effects bias the CBF measurement if no correction is performed. These undesired effects increase with the amplitude of MT effects and therefore with the magnetic field strength [Pohmann et al., 2011].
- Multiple slice measurement with high IE is only possible if a labeling coil is available. Other existing multi-slice strategies result in reduced inversion efficiency.

#### 1.4.2.3. Pseudo-Continuous Arterial Spin Labeling (pCASL)

Pseudo-continuous ASL (pCASL) has been introduced to overcome technical limitations encountered in CASL, such as continuous RF power application on clinical scanners. Moreover, its labeling RF and gradient scheme enables the measurement of multiple slices.

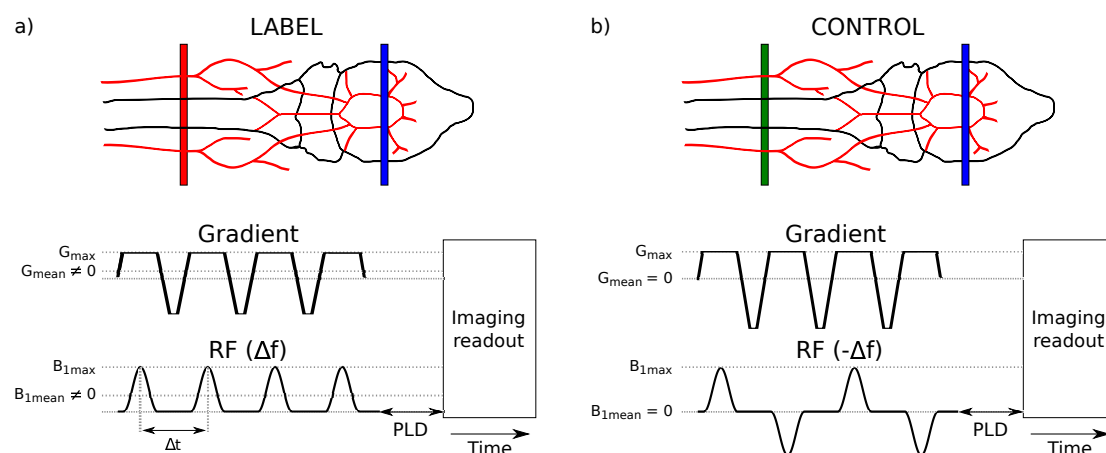


Figure 1.14.: (a) Label and (b) control diagrams for unbalanced pCASL. The vessel architecture supplying the brain is illustrated in red and has been adapted from Engel et al. [2011]. The labeling (resp. control) slices are represented with a red (resp. green) box. The imaged slice is displayed in blue. The corresponding gradient and RF amplitude timecourses are shown as well.

**RF & Gradients** pCASL imitates CASL's long continuous RF pulse by applying a series of short RF pulses in rapid succession, as shown in Fig. 1.14. To match the phase evolution of the flowing spins during labeling, an interpulse phase increment ( $\Delta\varphi_{th,L}$ ) has to be applied [Dai et al., 2008]:

$$\Delta\varphi_{th} = \gamma G_{mean}\Delta z\Delta t,$$

where  $\gamma$  is the gyromagnetic ratio,  $G_{mean}$  the mean gradient,  $\Delta z$  the labeling slice offset and  $\Delta t$  the time interval between two RF pulses. In CASL, we saw that the control pulse frequency needs to be opposite to that of label to induce (approximately) the same MT effects in the brain tissue during control as during labeling while avoiding spin labeling (if no labeling coil is available). Contrary to CASL, the RF pulse train scheme of pCASL allows keeping the same frequency for the label and the control pulse. Indeed in pCASL, the interpulse phase increment during control ( $\Delta\varphi_{th,C}$ ) can be shifted by  $180^\circ$  relatively to the one used in the label condition ( $\Delta\varphi_{th,L}$ ): this avoids labeling while inducing exactly the same MT effects in the brain region of interest during control than during label.

Concerning the applied labeling gradients, CASL's long constant gradient is split as well: to avoid aliasing planes, the gradient is increased during the RF pulse application (Fig. 1.15). Aliasing planes are well suppressed, if  $G_{max}/G_{mean} \gg \Delta t/OPT$ , where OPT is the duration of one individual RF pulse [Dai et al., 2008]. Moreover, this larger gradient amplitude during labeling increases the frequency difference between that of protons at the labeling plane and that of macromolecules in the brain tissue, and therefore reduces MT effects (cf. Fig. 1.13). To reach the same average gradient during labeling than in CASL, the gradient in-between two pCASL-RF pulses is set to a minimal value (Fig. 1.14a). For the control experiment, two different gradient conditions are commonly used:

- Balanced pCASL, with similar mean gradient for label and control conditions. Therefore, in balanced pCASL,  $\Delta\varphi_{th,C} = \Delta\varphi_{th,L} + 180^\circ$ .
- Unbalanced pCASL, with null mean gradient during control. The minimum gradient is increased, while keeping the same maximum gradient as during labeling (Fig. 1.14b). The unbalanced method is known to be less sensitive to off-resonance effects [Wu et al., 2007]. For unbalanced pCASL, since the mean gradient during control is zero,  $\Delta\varphi_{th,C} = 180^\circ$ . Simulations of the inversion obtained by means of unbalanced pCASL, based on which we optimized the pCASL gradients and RF parameters for this thesis, are shown in Chapter 3.

### Advantages

- No residual MT effects since the labeling and control slices are located exactly at the same place (pulses applied at the same frequency and during the same gradient).
- Multi-slice imaging is possible without an additional ASL coil.

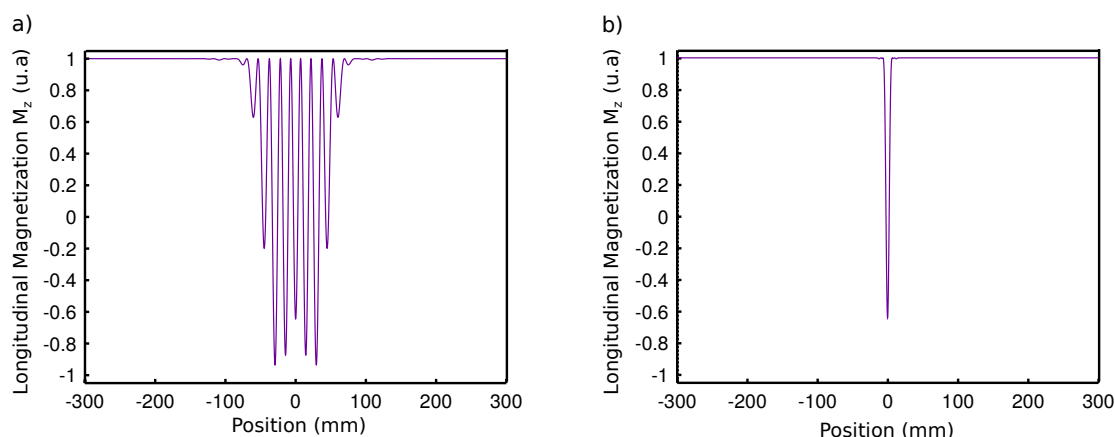


Figure 1.15.: Suppression of aliased labeling planes in a large field of view (600 mm) when increasing the gradient during RF pulse emission. (a) Magnetization profile obtained when applying a constant labeling gradient of 1 mT/m. (b) Profile obtained when increasing the labeling gradient to 9 mT/m during the RF pulse application, while keeping a mean gradient of 1 mT/m. Other pCASL parameters were set to:  $B_{1\text{ave}} = 5 \mu\text{T}$ ,  $\text{OPT} = 500 \mu\text{s}$ ,  $\Delta t = 1500 \mu\text{s}$ , labeling duration = 3 ms. The flow velocity was set to 0 mm/s for visualization reasons and relaxation was neglected (cf. Chapter 3 for simulation algorithm details).

### Drawbacks

- pCASL is very sensitive to field inhomogeneities that are present at the labeling plane. This effect increases with the magnetic field and currently limits its use on human high field systems (7T and above). More details about pCASL labeling issues at high magnetic field are given later and a correction strategy is proposed in Chapter 4.
- At equal average  $B_1$  labeling amplitude and inversion efficiency (e.g.  $5 \mu\text{T}$ ), pCASL yields a higher specific absorption rate (SAR) than CASL (cf. Chapter 6).

#### 1.4.2.4. Velocity Selective Arterial Spin Labeling (vsASL)

In velocity selective ASL (vsASL), the blood is labeled depending on its velocity. In this type of labeling method, a velocity selective pulse train (RF pulses with crusher gradients) is first applied to saturate blood flowing above a chosen cutoff velocity. After a post-labeling delay, a second velocity selective pulse module with the same cutoff velocity is applied either within or prior to the imaging readout. Thus, only signals from spins that have decelerated from above the cutoff velocity to below the cutoff velocity are measured in the final image, which provides selectivity for arterial delivery, as blood on the venous side of the circulation generally accelerates with time (Fig. 1.16) [Wong et al., 2006]. One advantage of this method is that the velocity selective saturation is usually spatially non-selective, and can even be within the imaging volume. Therefore,

velocity selective labeling is not sensitive to vascular transit time variations in the brain. However, the resulting SNR is lower than in other ASL techniques and a proper cutoff velocity selection remains difficult.

This method has so far been exclusively implemented on human scanners: no publication on animals can be found.

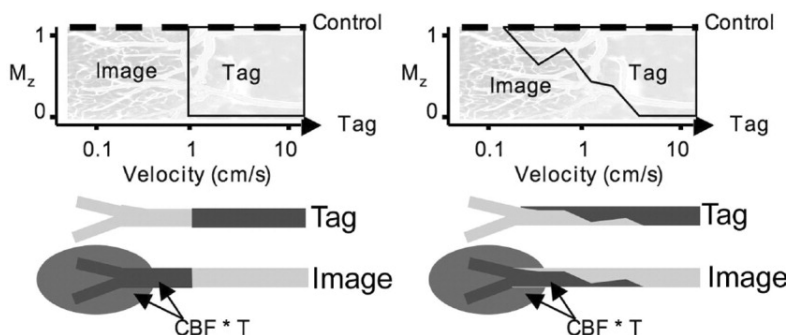


Figure 1.16.: Left: Ideal velocity cutoff. Right: Imperfect velocity cutoff. In either case the total amount of tagged blood appearing in the image is  $TI \cdot CBF$ . From [Wong et al., 2006].

#### 1.4.2.5. Consensus Paper

In order to encourage the use of ASL and to improve its utility, the perfusion community (ISMRM<sup>1</sup> perfusion study group and the European ASL in dementia consortium) recently agreed on recommended implementations of ASL for clinical applications [Alsop et al., 2015]. In summary, the recommended labeling scheme is unbalanced pCASL with inclusion of a background suppression strategy to remove static tissue signal, segmented 3D-readout without vascular crushing gradients. These proposed recommendations are for clinical use at 1.5 T and 3 T. Unlike on human scanners, the pCASL labeling scheme is not currently commercially available on preclinical systems.

#### 1.4.3. Post-labeling delay (PLD)

After being labeled in the carotids, the arterial blood water travels in the different vessels supplying the brain (Fig. 1.17). Once it reaches the voxel it perfuses, the water spins contained in the blood exchange with that of the tissue compartment. Depending on the compartment in which the water spins are located, the longitudinal and transverse relaxation times are different, which impacts the measured ASL signal [Debacker et al., 2016; Wells et al., 2009]. We now describe the different compartments and explain how they affect the ASL signal.

<sup>1</sup>International Society for Magnetic Resonance in Medicine.

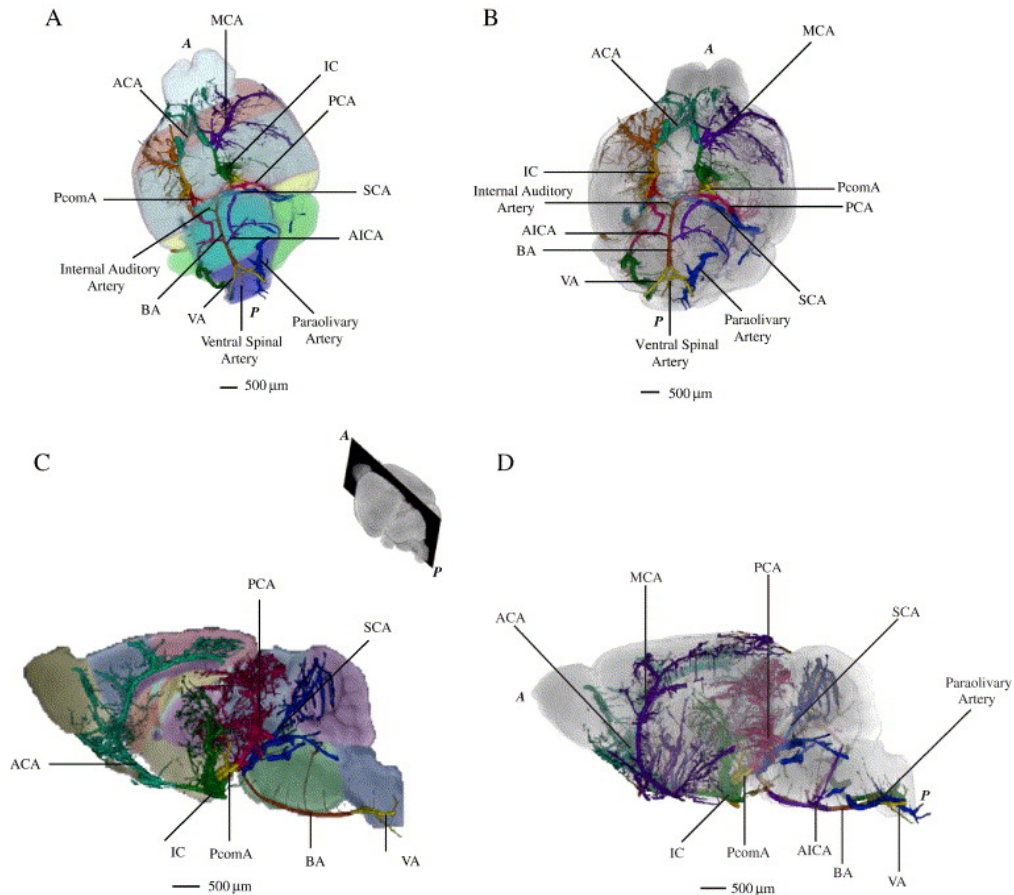


Figure 1.17.: Different views of the circle of Willis on mouse brain surface, showing the anterior cerebral artery (ACA), the anterior choroid artery (AchA), the basilar artery (BA), internal carotid (IC) middle cerebral artery (MCA), posterior cerebral artery (PCA), posterior communicating artery (PcomA), the superior cerebellar artery (SCA) and their branches. The insert represents the level at which the slice was taken. The MCA is excluded from panel (C) to allow better viewing of the internal arteries. From [Dorr et al. \[2007\]](#).

#### 1.4.3.1. Arterial transit time

After labeling, the blood needs some time to travel from the labeling plane to the imaged brain region. This time is called arterial transit time (ATT). If imaging was performed directly after labeling, CBF misestimation would occur: first, in some regions, not all the labeled blood would have arrived when the image is acquired, leading to CBF underestimation. And second, other regions may contain intravascular labeled blood that is meant to perfuse other parts of the brain, yielding overestimated CBF.

Therefore, after labeling, a delay called post-labeling delay (PLD) is introduced before image acquisition in order to reduce the ASL's signal sensitivity to ATT and to allow labeled arterial water to reach the microcirculation [[Alsop and Detre, 1996](#)]. To obtain a CBF measurement that is unbiased by incomplete labeling bolus delivery, a PLD

just longer than the longest ATT value is optimal, since unnecessarily long PLD values induce signal loss by relaxation without any further gain in quantification accuracy [Buxton et al., 1998]. The consensus paper on ASL [Alsop et al., 2015] recommends specific values to be used for ASL in humans (Fig. 1.18).

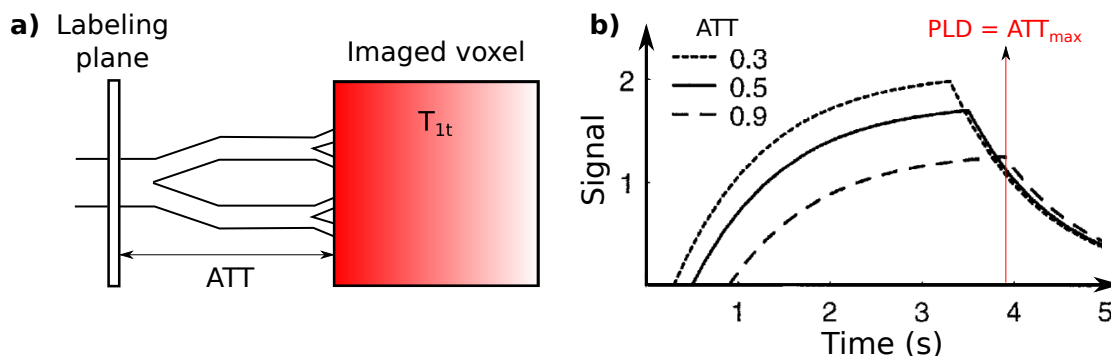


Figure 1.18.: (a) Illustration of a single-compartment perfusion model at  $t = ATT$ : once the labeled blood arrived in the imaged voxel, the blood-tissue exchange is supposed instantaneous. (b) Signal time-course in the imaging slice during a (p)CASL experiment for different ATTs. The labeling duration is 3 s, CBF 0.8 mL/min-mL and  $T_1$  1.0 s. By inserting a PLD longer than the longest ATT ( $ATT_{max}$ ), the measured signal becomes less sensitive to ATT. Adapted from Buxton et al. [1998] and Liu et al. [2011].

ATT is also an interesting parameter in itself, since it may reflect underlying vascular pathologies such as increased vessel tortuosity or occlusion [Hendrikse et al., 2004]. It also varies with the distance between the labeling and imaging planes. Moreover, depending on the vessels that supply the considered brain region and their length (Fig. 1.17), the measured ATT is affected as a consequence (cf. Chapter 5). In rats, ATT was shown to be in the range of 100 and 500 ms, depending on the considered brain region. The mean brain ATT in rats is around 200-300 ms [Barbier et al., 2001b; Thomas et al., 2006; Wells et al., 2010].

ATT can be measured by varying the PLD to sample the blood inflow in the tissue of interest (multi-PLD ASL): the ASL signal increases once the labeled blood reached the imaged brain region. More details about such MR sequences and how they can be made more time-efficient are provided later, in section 1.4.4.

### 1.4.3.2. Tissue transit time

Once arrived in the imaged voxel, the labeled water spins exchange from the vessel compartment to the tissue compartment. The time the water spins take to travel from the labeling plane to reach the tissue compartment (Fig. 1.19) is called tissue transit time ( $\delta$ ). When assuming a single compartment model, which is usually the case when quantifying CBF in the literature, this exchange duration between the blood and the tissue is supposed instantaneous:  $\delta$  is considered to be equal to ATT. However, in

the normal rat cortex, Wells et al. [2013] measured  $\delta$  to be  $ATT + 370 \pm 40$  ms, i.e. approximately twice as long as ATT.

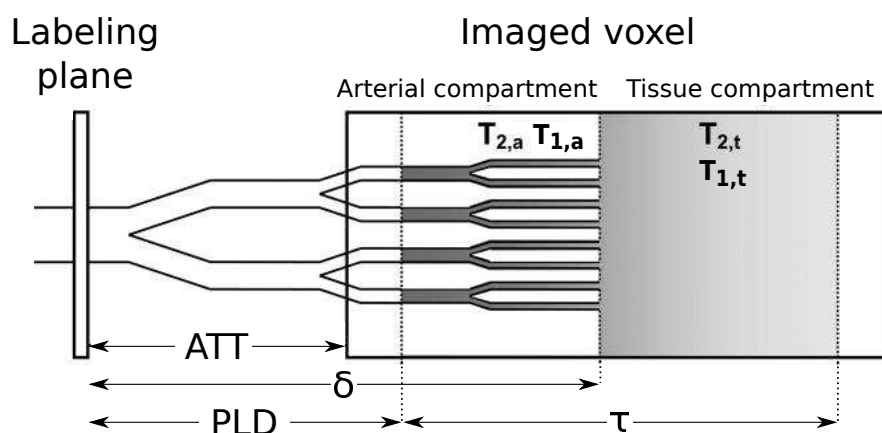


Figure 1.19.: Representative scheme from Liu et al. [2011] of the labeled blood route from the labeling plane to the imaged voxel when assuming a two-compartment model (arterial and tissue compartments) for pCASL at the time of imaging (i.e.  $t = \tau + PLD$ ). The brain feeding arteries, splitting in arterioles and capillaries once they reach the brain, are represented as well.

Depending on the signal's origin, the measured ASL intensity is different. Indeed, the longitudinal relaxation time  $T_1$  is higher for blood than for tissue (e.g. 2.4 s for blood versus 1.7 s at 9.4 T [Nasrallah et al., 2012; Dobre et al., 2007; de Graaf et al., 2006]): at equal measurement timing, intravascular labeled water yields higher signal than water that already passed the BBB, since its relaxation rate is lower. CBF quantification usually assumes that the ASL signal decays with the  $T_1$  of tissue after the ATT. Therefore, when performing (p)CASL at  $PLD = ATT$  and if the blood-tissue exchange is not instantaneous, the ASL signal is still intravascular and causes CBF to be overestimated. To avoid that, diffusion gradients can be used before imaging to crush the remaining arterial signal [Ye et al., 1997]. However, in clinical practice, their use is not recommended when performing standard ASL experiments (i.e. at a single PLD), since they may remove important information on potential disease induced longer ATTs [Alsop et al., 2015]. When using crusher gradients in a multi-PLD ASL experiment,  $\delta$  is measured instead of ATT: an ASL signal increase will only be seen once the signal arrives in the brain tissue, since intravascular signal is spoiled.

Recently, another technique was developed to simultaneously estimate CBF, ATT and  $\delta$ . The measurement method is based on the different transverse relaxation times  $T_2$  of spins contained in intravascular, extracellular or intracellular compartments [Haida et al., 1987; Matsumae et al., 2003; Lascialfari et al., 2005; Wells et al., 2009]. MR sequences can take advantage of this  $T_2$  differences between compartments by making the ASL signal sensitive to the transverse relaxation time [Liu et al., 2011; Wells et al., 2009]. This enables the determination of the compartment (vessel or intra-/extracellular

tissue) in which the labeled water is located during imaging. As a consequence, when encoding such sequences in time, i.e. when measuring the  $T_2$ -weighted ASL signal at different PLDs, tissue transit times can be measured as well [Liu et al., 2011; Wells et al., 2013; Schmid et al., 2015].

#### 1.4.4. Time encoded ASL

Time encoded ASL aims to sample the timing of blood arrival in the brain region of interest. Different strategies exist and are described in this section.

##### 1.4.4.1. Multi-PLD ASL

Multi postlabeling delay ASL is the most intuitive way to measure ATT. The ASL signal is sampled at different post labeling delays in separate acquisitions to detect the blood inflow in the imaged slice of interest (Fig. 1.20). A model (e.g. Eq. 1.9 from Buxton et al. [1998]) can then be fitted to the obtained signal time-course to retrieve ATT and CBF.

If crusher gradients are added before imaging to remove the contribution of arterial signal, the tissue transit time is measured instead of the ATT.

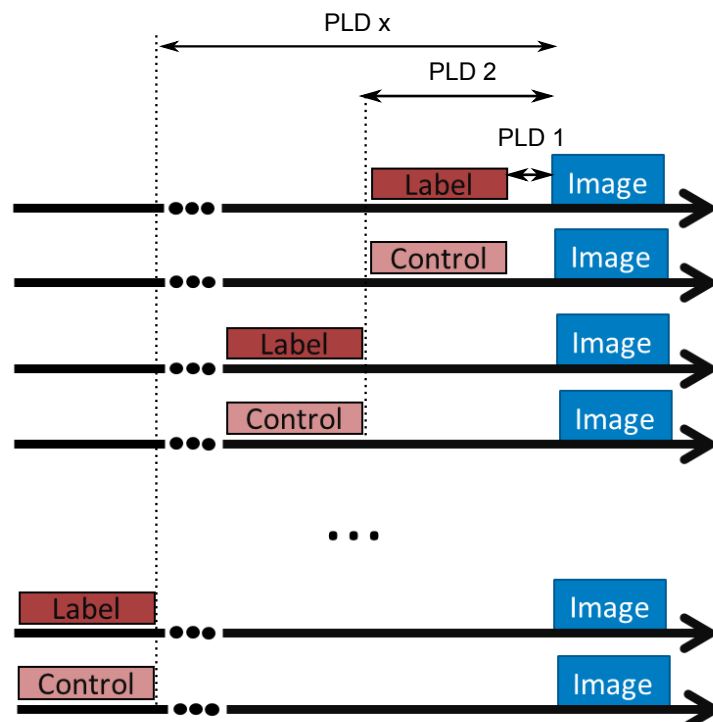


Figure 1.20.: Multi-PLD labeling scheme.

### 1.4.4.2. Hadamard encoded ASL

Multi-PLD ASL is time consuming. Hadamard encoded ASL enables to measure ATT based on the same principle as multi-PLD ASL, except that the labeling is made more time efficient by using a Hadamard matrix [Günther, 2007; Wells et al., 2010; Dai et al., 2013; Teeuwisse et al., 2014a]. This enables to calculate the perfusion signal for the same amount of PLDs as there are blocks in one labeling bolus. Instead of alternating full label and control states as it is done in multi-PLD ASL, this time-encoded strategy alternates between label and control conditions inside one bolus preceding imaging. One bolus is therefore sub-divided into smaller “blocks” or “sub-boli” (SB). The order of the label and control blocks differs over different acquisitions and is altogether played out as a Hadamard matrix. Fig. 1.21a represents such a Hadamard encoded labeling scheme, in which twelve encoded images are acquired.



Figure 1.21.: (a) Hadamard encoded labeling scheme for time-encoded ASL. Label condition is represented in red, control in blue and the imaging readout in green. The signs in the 11<sup>th</sup> sub-bolus (SB) block represent the way the acquired images are subtracted during decoding for this particular SB. (b) Obtained images after decoding across PLDs. Note that the PLD number is reversed compared to the SB number.

Decoding of the Hadamard matrix allows to calculate the perfusion image that would have been measured with a traditional multi-PLD ASL scan with the same labeling duration and PLD as the individual blocks of the Hadamard-matrix and gives therefore access to the ASL signal time-course. Decoding is done as follows: for a particular PLD, PLD<sub>x</sub>, the images with control blocks preceding PLD<sub>x</sub> are added, while the images with

label blocks preceding PLD<sub>x</sub> are subtracted. This yields the CBF-weighted difference of that block, creating an image of a ‘sub-bolus’ with a PLD of PLD<sub>x</sub>.

For example, if we consider the 11<sup>th</sup> sub-bolus (Fig. 1.21a) corresponding to the 1<sup>st</sup> PLD, the signal for this particular block is obtained by combining the acquired images as:

$$\begin{aligned} \Delta M(\text{PLD}_1) = & -\text{Image 1} + \text{Image 2} - \text{Image 3} + \text{Image 4} + \text{Image 5} + \text{Image 6} \\ & -\text{Image 7} - \text{Image 8} - \text{Image 9} + \text{Image 10} - \text{Image 11} + \text{Image 12} \end{aligned} \quad (1.6)$$

When applying this decoding for a particular PLD (here PLD<sub>1</sub>), the signal of all the other PLDs cancels out as a result of the Hadamard matrix property. For example, in our case during decoding of the signal for the 11<sup>th</sup> sub-bolus, the remaining signal produced by the 10<sup>th</sup> sub-bolus (signal from PLD<sub>2</sub>) is:

$$\begin{aligned} \Delta M = & -\text{Label}(\text{PLD}_2) + \text{Label}(\text{PLD}_2) - \text{Control}(\text{PLD}_2) + \text{Control}(\text{PLD}_2) \\ & + \text{Control}(\text{PLD}_2) + \text{Label}(\text{PLD}_2) - \text{Label}(\text{PLD}_2) - \text{Label}(\text{PLD}_2) \\ & - \text{Control}(\text{PLD}_2) + \text{Label}(\text{PLD}_2) - \text{Control}(\text{PLD}_2) + \text{Control}(\text{PLD}_2) \\ = & 0. \end{aligned} \quad (1.7)$$

This is the case for all PLDs, but the 1<sup>st</sup>. Indeed:

$$\begin{aligned} \Delta M(\text{PLD}_1) = & -\text{Label}(\text{PLD}_1) + \text{Control}(\text{PLD}_1) - \text{Label}(\text{PLD}_5) + \text{Control}(\text{PLD}_1) \\ & + \text{Control}(\text{PLD}_1) + \text{Control}(\text{PLD}_1) - \text{Label}(\text{PLD}_1) - \text{Label}(\text{PLD}_1) \\ & - \text{Label}(\text{PLD}_1) + \text{Control}(\text{PLD}_1) - \text{Label}(\text{PLD}_1) + \text{Control}(\text{PLD}_1) \\ = & 6 \times (\text{Control}(\text{PLD}_1) - \text{Label}(\text{PLD}_1)). \end{aligned} \quad (1.8)$$

In this case, the only sub-bolus that gives signal is the 11<sup>th</sup> subbolus (PLD<sub>1</sub>).

The perfusion signal can be calculated in a similar fashion for all the other PLDs. After decoding, similar information is obtained as in a multi-PLD ASL scan: Fig. 1.21b shows an example of obtained images after decoding across PLDs. A model (e.g. Eq. 1.9 from Buxton *et al.* [1998]) can be fitted voxel-by-voxel to the evolution of the signal timecourse over the separate PLDs to estimate ATT and CBF.

We implemented, optimized and applied such a Hadamard encoded labeling scheme in mice in collaboration with teams of the Leiden University Medical Center in the Netherlands. The obtained results are detailed in Chapter 5.

### 1.4.4.3. Dynamic ASL

In dynamic ASL (DASL), longer labeling sub-boli than in Hadamard encoded ASL are used and organized as a periodic labeling function [Barbier et al., 1999, 2001b]. The tissue magnetization response to this labeling function is sampled at different timepoints, allowing to monitor the inflow of labeled blood. Again, when fitting a model voxel-by-voxel to the evolution of the signal over time, ATT, CBF and the tissue longitudinal relaxation  $T_1$  can be estimated.

Fig. 1.22 represents a DASL labeling scheme, where the signal sampling has been optimized to image with higher temporal resolution (50 ms temporal resolution) around the blood arrival time (i.e. between 0-0.4 s and 2-2.4 s: repetitions 1-9 and 17-25) and with lower temporal resolution (200 ms) otherwise. Imaging, performed at the end of each bolus, has not been represented for readability reasons.

DASL has the advantage to use longer bolus durations than Hadamard encoded ASL, yielding high perfusion SNR per TR, and still allows for high temporal resolution to sample label inflow. The periodic acquisitions eases the use of signal filtering schemes.

We implemented such a DASL scheme with a 3D readout on the 9.4 T scanner in Grenoble. Results are shown in Appendix B.3.

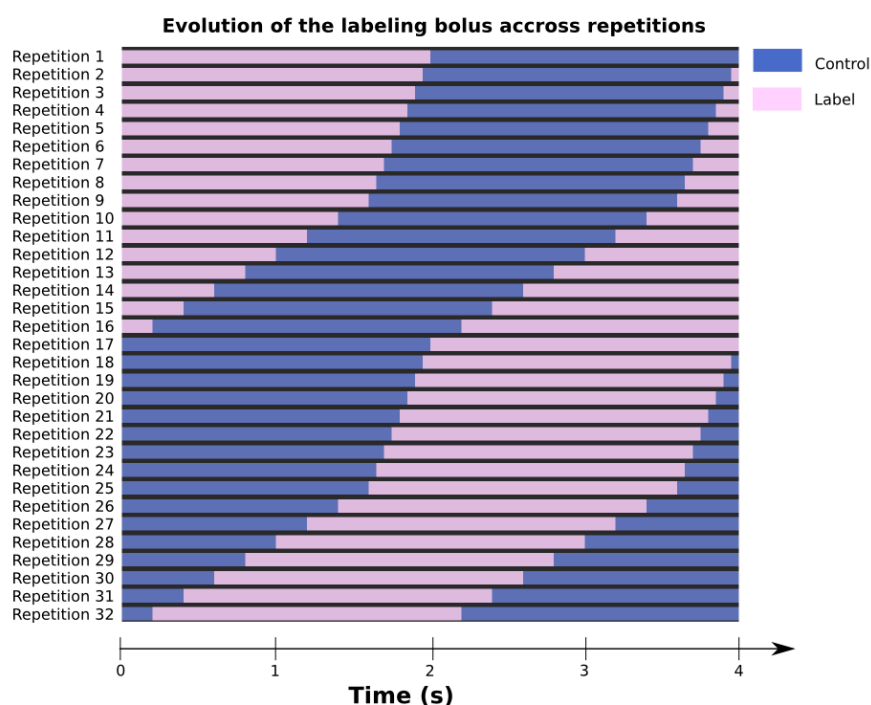


Figure 1.22.: Dynamic ASL labeling scheme. The signal sampling frequency was increased between 0 and 0.4 s (i.e. from repetition 1 to 9) and from 2 to 2.4 s (i.e. from repetition 17 to 25) to more accurately sample the arterial transit time.

### 1.4.5. CBF quantification

In this thesis, we used a single compartment model to quantify CBF from (p)CASL experiments [Buxton et al., 1998]: instantaneous exchange between the blood and the tissue is supposed. In literature, this model is the most commonly used method to quantify CBF and is recommended by the consensus paper on ASL [Alsop et al., 2015]. We first outline Buxton's quantification model used to fit the data acquired with time-encoded image series (i.e. multi-PLD ASL, Hadamard decoded images, etc). In a second time, the recommended CBF quantification equation is expressed.

#### 1.4.5.1. ASL data at different timepoints

From the acquired images, the following model can be fitted to the data to estimate CBF, ATT and the apparent tissue  $T_1$  ( $T_{1app}$ ):

$$\Delta M(t) = \begin{cases} 0 & 0 < t < ATT \\ 2 M_{0b} CBF T_{1app} IE e^{-\frac{ATT}{T_{1b}}} (1 - e^{-\frac{t-ATT}{T_{1app}}}) & ATT < t < \tau + ATT \\ 2 M_{0b} CBF T_{1app} IE e^{-\frac{ATT}{T_{1b}}} e^{-\frac{t-\tau-ATT}{T_{1app}}} (1 - e^{-\frac{\tau}{T_{1app}}}) & \tau + ATT < t \end{cases} \quad (1.9)$$

where  $\Delta M(t)$  is the ASL signal over time;  $t$  is time measured from the start of the label RF pulse;  $T_{1b}$  is the longitudinal relaxation time of blood; IE is the inversion efficiency;  $M_{0b}$  is the equilibrium magnetization of arterial blood, approximated to the equilibrium magnetization of tissue  $M_{0t}$  divided by the partition coefficient of water  $\lambda$  [Detre et al., 1992] and  $\tau$  is the labeling duration.

#### 1.4.5.2. ASL data acquired at a single timepoint

When acquiring pairs of label and control images at a single post-labeling delay ( $\omega$ ) that is just longer than the longest ATT in the subject (i.e. the entire labeled bolus has been delivered to the tissue), Eq. 1.9 comes down to the following quantification equation:

$$CBF = \frac{\lambda \Delta M e^{\frac{\omega}{T_{1b}}}}{2 IE T_{1app} M_{0t} (1 - e^{-\frac{\tau}{T_{1app}}})}, \quad (1.10)$$

with the same notations as in Eq. 1.9.

Validation of the obtained CBF values remains difficult. In animals, external parameters, such as the anesthesia procedure for example (chosen agent, anesthesia dose), introduce potential confounds [Petrinovic et al., 2016]: anesthesia directly influences the heart and breath rates, the vessel diameters, and has an effects on the neurovascular coupling. For example, isoflurane induces dose-dependent vaso-dilatation that increases basal CBF [Masamoto et al., 2009].

Table 1.2 presents average brain CBF values measured in rodents by means of different techniques. The measured CBF is highly variable across techniques, even in identical species and with the same anesthetic agent.

Table 1.2.: Comparison of CBF values in rodents obtained by means of different acquisition techniques. Unless mentioned otherwise, mean brain values in mL/100g/min, mean  $\pm$  standard deviation are shown. They are globally ordered by acquisition method and magnetic field strength for MRI techniques. The number of animals used in each study is indicated in between brackets in the CBF column. Note the high variability between CBF estimates; GM: gray matter. Adapted from [Debacker \[2014\]](#).

Species	Strain	Anesthesia	Acquisition method	CBF	Reference
Rat	Wistar	N <sub>2</sub> O	PET	171 $\pm$ 86 (n=8)	<a href="#">Takagi et al. [1987]</a>
	Sprague-Dawley	Halotane	Autoradiography	181 $\pm$ 9 (n=10)	<a href="#">Bereczki et al. [1993]</a>
	Sprague-Dawley	Isoflurane	DSC - 7T	93 $\pm$ 10 (n=6)	<a href="#">Tanaka et al. [2011]</a>
	Wistar	Isoflurane	FAIR - 3T	103 $\pm$ 10 (n=5)	<a href="#">Wegener et al. [2007]</a>
	Sprague-Dawley	Isoflurane	FAIR - 7T	152 $\pm$ 6 (GM, n=6)	<a href="#">Esparza-Coss et al. [2010]</a>
	Sprague-Dawley	Halotane	CASL - 2.35T	241 (n=12)	<a href="#">Thomas et al. [2006]</a>
	Sprague-Dawley	Halotane	CASL - 2.35T	303 (cortex, n=3)	<a href="#">Wells et al. [2010]</a>
	Sprague-Dawley	Isoflurane	CASL - 4.7T	418 $\pm$ 100 (n=4)	<a href="#">Hendrich et al. [1999]</a>
	Sprague-Dawley	Isoflurane	CASL - 4.7T	120 (n=4)	<a href="#">Petrinovic et al. [2016]</a>
	Sprague-Dawley	Etomidate	CASL - 4.7T	40 - 80 (n=4)	<a href="#">Petrinovic et al. [2016]</a>
	Wistar	Isoflurane	CASL - 4.7T	121 $\pm$ 37 (n=43)	<a href="#">Debacker et al. [2015]</a>
	Wistar	Isoflurane	CASL - 7T	126 $\pm$ 32 (n=43)	<a href="#">Debacker et al. [2015]</a>
	Sprague-Dawley	Isoflurane	CASL - 7T	84 $\pm$ 3 (n=6)	<a href="#">Tanaka et al. [2011]</a>
	Wistar	Isoflurane	CASL - 11.7T	101 $\pm$ 28 (n=43)	<a href="#">Debacker et al. [2015]</a>
	Sprague-Dawley	Isoflurane	DASL - 4.7T	530 $\pm$ 60 (n=8)	<a href="#">Barbier et al. [2001b]</a>
	Sprague-Dawley	Halotane	H-CASL - 2.35T	310 (cortex, n=3)	<a href="#">Wells et al. [2010]</a>
Mouse	C57BL/6J, CD1, BTBR T+tf/J	Isoflurane	CASL - 9.4T	120 - 165 (n=32)	<a href="#">Petrinovic et al. [2016]</a>
	C57BL/6J	Medetomidine	CASL - 9.4T	165 (n=30)	<a href="#">Petrinovic et al. [2016]</a>
	C57BL/6J, CD1, BTBR T+tf/J	Etomidate	CASL - 9.4T	40 - 80 (n=34)	<a href="#">Petrinovic et al. [2016]</a>

However, [Baskerville et al. \[2012\]](#) compared CBF values obtained with a pCASL-like sequence to autoradiography in a rat stroke model. Good agreement was found between both measurement methods (Fig. 1.23). CBF values obtained with ASL were slightly lower than those retrieved with autoradiography only in an ROI covering both the caudate nucleus and the putamen.

In this thesis, we chose to work with CASL and pCASL labeling schemes. Animal scanners operate usually at higher magnetic fields than those available in clinical practice, providing undeniable advantages, such as higher SNR. However, they also lead to several issues, that are introduced now.

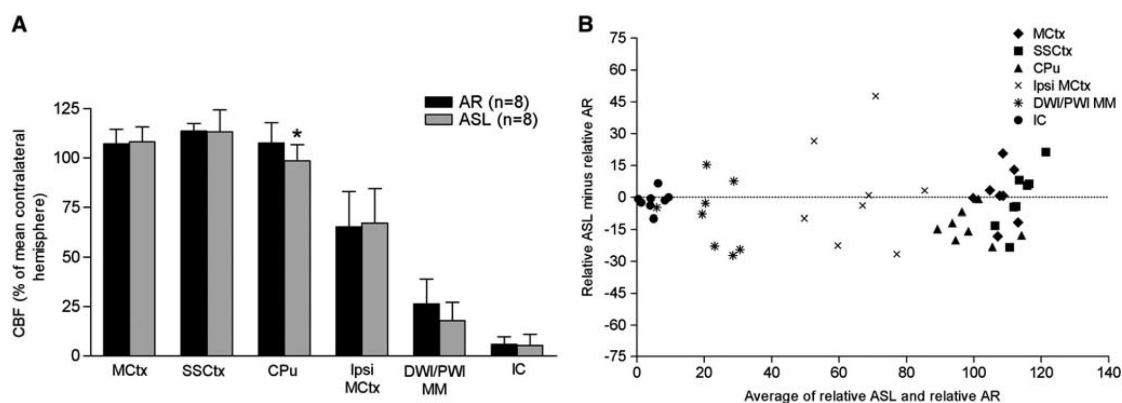


Figure 1.23.: (A) CBF values measured with autoradiography (AR) and pseudo-pCASL in six ROIs (mean  $\pm$  s.d.). Blood flow measurements were only significantly different between AR and ASL in the caudate putamen (CPu). Two-tailed paired Student's t-test: contralateral motor cortex (Mctx),  $P = 0.83$ ; sensorimotor cortex (SSctx),  $P = 0.93$ ; CPu,  $*P = 0.014$ ; ipsilateral motor cortex (ipsi Mctx),  $P = 0.83$ ; diffusion/perfusion mismatch (DWI/PWI MM),  $P = 0.17$ ; IC,  $P = 0.35$ . (B) There is broad agreement between AR and ASL measurements on the Bland Altman plot (data averaged across slices), although ASL values tend to be slightly lower than AR values. From Baskerville et al. [2012].

## 1.5. ASL issues at high magnetic field

At higher magnetic fields, ASL benefits from both higher signal-to-noise ratio and longer  $T_1$  ( $T_1 \sim \omega^{1/3}$ [Lu et al., 2004]) resulting in a slower label decay but is also impacted by several issues. Longer  $T_1$  values lead indeed to outflow of labeled blood. Moreover, with increasing magnetic field,  $T_2^*$  values decrease, which induces variations in the contribution of the different compartments (arterioles, capillaries and venules), and impacts the measured MR signal. All these effects affect ASL quantification. Furthermore, at higher field, field inhomogeneities in the labeling plane tend to be more severe and can significantly impact the labeling efficiency of the pCASL labeling scheme. In addition, more energy is deposited in the scanned subject, causing unwanted heating. In this thesis we addressed the two last issues more specifically and introduce them now.

### 1.5.1. pCASL labeling efficiency at high magnetic field

#### 1.5.1.1. Why does labeling fail in some cases?

At higher magnetic fields,  $B_0$  inhomogeneities at the labeling plane, away from the isocenter, increase and affect the spins' phase. Such off-resonance effects can originate from poor shims at the tagging plane and/or patient geometry. Since air spaces cavities (i.e. throat, esophagus and mouth cavities) are located very closely to the labeling slice in rodents, susceptibility artifacts are even more pronounced in preclinical studies. Moreover, to reduce brain distortions in the image, a second-order shim is usually

performed on the brain, which further degrades the field homogeneity in the neck.

These inhomogeneities cause the theoretical label and control interpulse phase increments  $\Delta\varphi_{th,L}$  and  $\Delta\varphi_{th,C}$  to be non-optimal: during labeling arterial blood magnetization may not be fully inverted and during control some inversion may occur. Altogether, this lowers the inversion efficiency (IE) and yields instable ASL signal across subjects (lower relative ASL signal, inter-hemispherical asymmetry).

This effect was observed at different magnetic fields in human and animal studies:

- 3 T: Wu et al. [2007], Jung et al. [2010], Jahanian et al. [2011], Shin et al. [2012], Teeuwisse et al. [2014b]
- 7 T: Teeuwisse et al. [2010], Luh et al. [2013]
- 9.4 T: Larkin et al. [2016]
- 11.7 T: Debacker et al. [2015].

Ghariq et al. [2012] showed that pCASL at 7 T is not trivial and very challenging although ASL measurements at 7T remain possible.

Placing the labeling plane at the isocenter is a way to obtain high inversion efficiency [Duhamel et al., 2012], but at the cost of image quality, since the readout is no longer located at the isocenter.

### 1.5.1.2. Existing strategies to correct for off-resonance effects

In the past few years, several correction strategies were developed for balanced pCASL and are described in this section. In balanced pCASL, mean gradients are identical and the control phase is therefore always shifted by  $180^\circ$  relative to the labeling phase.

**Dual-shim pCASL** Shimming separately in the labeling and imaging regions to arrange optimal shims for both regions has been tested by Teeuwisse et al. [2014b]. No significant improvement in perfusion signal or left-right asymmetry was experimentally observed with this dual shim-strategy.

**Field map based approach** Jahanian et al. [2011] presented a phase and gradient correction approach based on the measurement of the off-resonance field and the gradient within the labeling slice at 3 T. The RF phase and mean gradient are then adjusted accordingly to correct for the off-resonance fields. The low inversion efficiency observed without correction (mean  $IE \pm SD$ :  $55 \pm 27\%$ ) could be corrected in all five subjects using the proposed method (mean  $IE \pm SD$ :  $77 \pm 3\%$ ). However, this fieldmap based approach may be more difficult to apply at magnetic fields higher than 3 T due to shorter  $T_2^*$  values, especially at the labeling plane [Luh et al., 2013]: in our study at 9.4 T (Chapter 4), measuring such a fieldmap did not yield accurate values in the rat's neck.

**Multiphase pCASL** Instead of measuring only pairs of label-control images (i.e. collecting only two phases: 0 and 180°), images with different pCASL phase offsets are acquired [Jung et al., 2010; Larkin et al., 2016]. The signal is then fitted to a model to retrieve the CBF. However, this method is based on a blood velocity dependent model and yields a lower SNR per unit of acquisition time. Since the perfusion SNR is already small, a multi-phase pCASL-like approach would be more suited as a prescan to estimate the phase error, that could be used in a conventional pCASL scan (cf. next method).

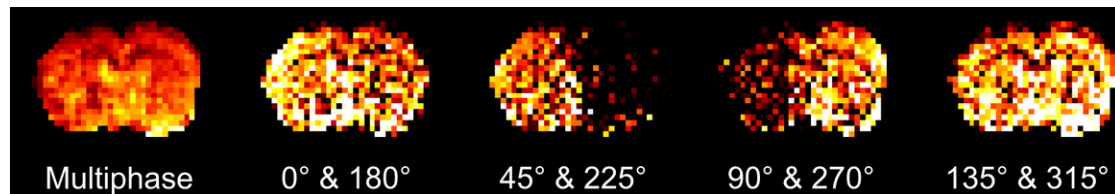


Figure 1.24.: Multiphase single slice analysis with conventional analysis from pairs of label-control images at different phase offsets. From Larkin et al. [2016].

**Prescan approach** Luh et al. [2013] demonstrated for balanced pCASL on humans at 7 T, that varying the phase during a low-resolution prescan to measure the optimal phase increment was a robust way to improve the overall perfusion signal while keeping the imaging plane around the isocenter (Fig. 1.25). To simultaneously compensate for off-resonance effects for all labeled vessels, additional gradients in the X (left-right) and Y (head-foot) directions can be added. The latter step however implies to know the perfusion territories of carotids and vertebral arteries on the brain slice of interest, which is not straightforward in rats or mice. The measured phase error offsets in the seven subjects ranged from -143° to 83° before correction, were  $23.3 \pm 13.4^\circ$  after phase correction and  $8.2 \pm 2.2^\circ$  after both phase and gradient correction.

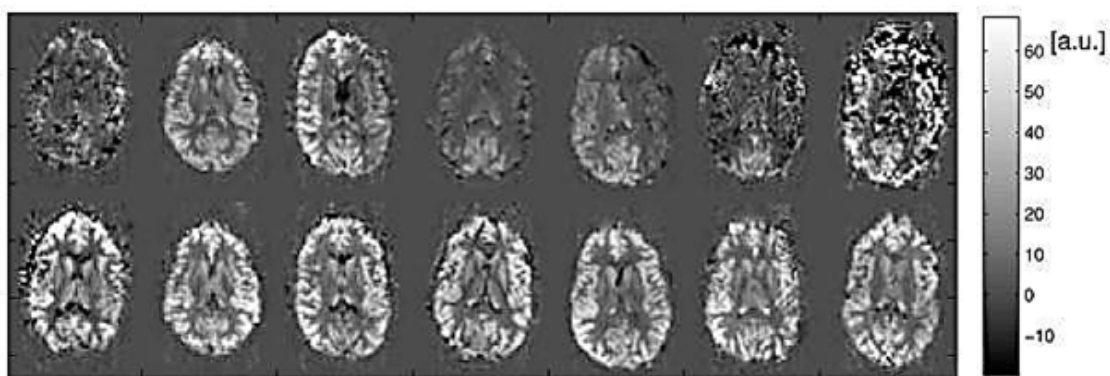


Figure 1.25.: 7T-pCASL images of one slice from 7 subjects before (top row) and after (bottom) correcting for off-resonance effects. From Luh et al. [2013].

We implemented a similar prescan based phase correction approach than Luh et al.

[2013] for unbalanced pCASL on preclinical scanners. We tested its robustness towards suboptimal shims. The results of this study are shown in Chapter 4.

### 1.5.2. Heating issues encountered in ASL at high magnetic field

At higher magnetic fields, ASL suffers from higher RF power deposition and thus temperature increase. The following section is dedicated to address MR safety aspects and to explain the origin of MR heating.

#### 1.5.2.1. MR safety

MRI uses constant and time-varying magnetic fields to interact with the nuclear spins in the sample. Of the time-varying magnetic fields used in MRI, only the radio-frequency fields (at frequencies of hundreds of MHz) are usually relevant in terms of induced heating, since gradient switching takes place at frequencies that are orders of magnitude lower (kHz). The RF magnetic fields induce electric fields and eddy currents in electrically conducting samples. These induced currents lead to a power deposition in the exposed tissues, which may lead to heating. Moreover, the RF coils designed to produce only RF magnetic fields are often imperfect and simultaneously generate RF electric fields that can extend to the sample and directly induce RF heating. The amount of energy deposited in a biological tissue by a time-varying electric field is quantified by the specific absorption rate (SAR), which represents the energy absorbed by a mass of tissue per unit time [Vaughan and Griffiths, 2012]:

$$SAR = \sigma \frac{\vec{E}^2}{\rho}, \quad (1.11)$$

where  $\sigma$  is the electric conductivity of tissue,  $\vec{E}$  is the effective (i.e. root mean square (RMS)) electric field and  $\rho$  is the mass density of the tissue.

The absorbed energy leads to a change in sample temperature. In living organisms, tissue temperature is dependent on the metabolic rate, on the heat exchange with the surroundings and on the cooling effect of perfusion. The temperature changes with respect to this steady state ( $\Delta T$ ) due to energy deposited by an electromagnetic field are described by the bioheat equation [Pennes, 1948]:

$$c \frac{d\Delta T}{dt} = \frac{k}{\rho} \nabla^2 T - f c_b \rho_b \Delta T + SAR, \quad (1.12)$$

where  $c$  is the specific heat capacity and  $k$  the thermal conductivity of the tissue,  $c_b$  and  $\rho_b$  are the specific heat capacity and mass density of blood and  $f$  is blood flow. A typical example of temperature change across time due to RF heating is shown in Fig. 1.26. Temperature first increases linearly and subsequently reaches an asymptotic

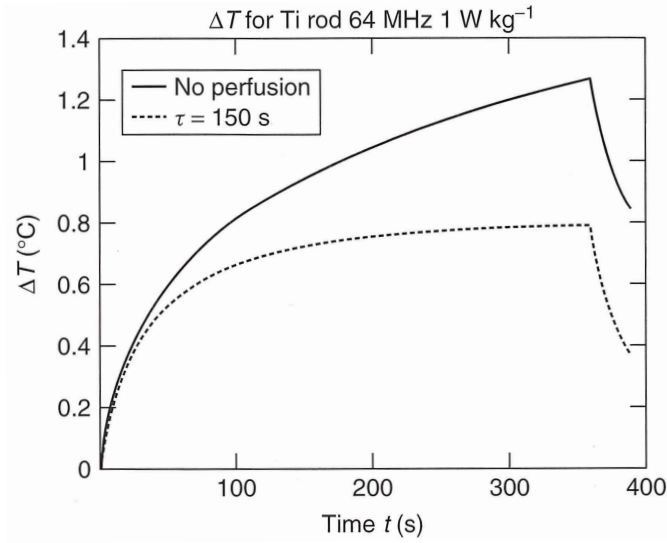


Figure 1.26.: Calculated temperature versus time in a titanium rod, without perfusion and with a perfusion time-constant of 150 ms. The RF is turned off at  $t = 360$  s. From Vaughan and Griffiths [2012].

value where the heating by SAR is counterbalanced by the cooling effect of perfusion. For rapid and mostly uniform heating, the SAR can be measured from the initial slope of the temperature change, neglecting the first two terms in Eq. 1.12:

$$\Delta T = \frac{SAR \times t}{c}, \quad (1.13)$$

where  $t$  is the time over which the temperature rise  $\Delta T$  was measured.

Often, neither the electric fields at the origin of RF heating nor the SAR can be measured directly, especially if heating in living organisms is to be investigated. In these cases, indirect measurements of RF heating via thermometry is a convenient method. Other methods include coupled numerical electromagnetic and thermal simulations [Bouldi, 2014]. These simulations are however difficult to set up and complex to perform.

### 1.5.2.2. Influence of MR parameters on heating

**Magnetic field** As can be seen from Eq. 1.11, the amount of heating depends on the strength of the electric field and on the tissue conductivity. Both, the induced electric field due to the time-varying magnetic field, and the tissue conductivity increase with RF frequency [Duck, 1991]. As a consequence, RF heating strongly increases with main magnetic field due to the corresponding increase in Larmor frequency. This tends to increase the problems related to RF deposition in preclinical MRI, with respect to human MRI.

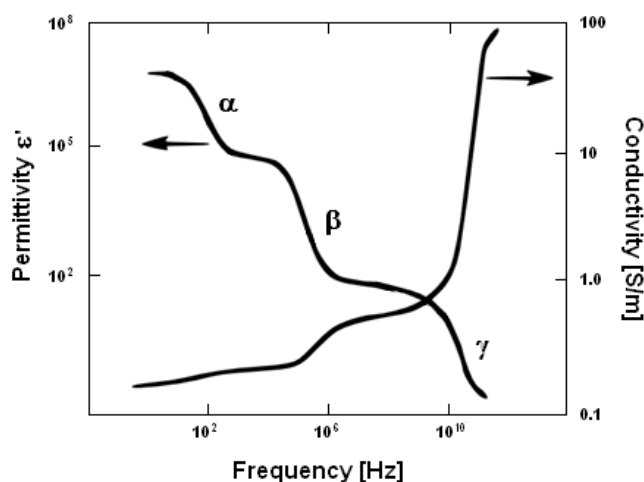


Figure 1.27.: Permittivity and conductivity dependence on frequency. From Duck [1991].

**Sample geometry** The RF eddy currents are mainly induced at the sample perimeter. Therefore, energy deposited increases supra-linearly with sample volume. For example, for a spherical sample exposed to a uniform  $B_1$ -field, the dissipated power  $P$  increases with the fifth power of the sample radius  $r$  and the square of the RF frequency  $\omega_0$ :

$$P \propto \frac{\omega_0^2 B_1^2 r^5}{\sigma}.$$

The small samples in preclinical MRI thus allow the use of relatively high RF field strengths, despite the high frequency.

**RF pulse shape** The instantaneous power deposition is proportional to the square of the instantaneous  $B_1$ -field strength. The time-averaged SAR is thus proportional to  $B_{1\text{RMS}}^2$  and not to  $B_{1\text{mean}}^2$ : two MR sequences with equal mean applied  $B_1$  ( $B_{1\text{mean}}$ ), i.e. equal flip angle, can yield different SAR if other parameters, e.g. pulse shape, pulse spacing or repetition time (TR), are different.

This is what happens when comparing CASL to pCASL. At equal mean applied  $B_1$  ( $B_{1\text{mean}}$ ), i.e. at equal flip angle, pCASL yields higher  $B_{1\text{RMS}}$  than CASL and leads therefore theoretically to higher SAR. For example, let's assume a 3-s CASL RF pulse with an amplitude of 5  $\mu\text{T}$  and thus a  $B_{1\text{RMS}}^2$  of 25  $\mu\text{T}^2$  (if only the labeling pulse is considered, without PLD and imaging, TR = 3 s). To reach the same  $B_{1\text{mean}}$  in pCASL, if we assume 400- $\mu\text{s}$  Hanning window shaped RF pulses repeated every 800  $\mu\text{s}$  during 3 s, the maximum  $B_1$  sent during pCASL has to be 20  $\mu\text{T}$ , leading to a  $B_{1\text{RMS}}^2$  of 75  $\mu\text{T}^2$ . We investigated such SAR issues *in vivo* during application of standard CASL and pCASL sequences and show the obtained results in Chapter 6.

Table 1.3.: Mass in kg and basal metabolic rate (BMR) in different animals. The ratio between both values is shown in the last column. Adapted from Kleiber [1932].

Animal	Mass (in kg)	Basal Metabolic Rate (BMR, in W)	BMR/Mass (in W/kg)
Dove	0.16	0.97	6.06
Rat	0.26	1.45	5.58
Pigeon	0.3	1.55	5.17
Hen	2	4.8	2.4
Dog (female)	11	14.5	1.32
Dog (male)	16	20	1.25
Sheep	45	50	1.11
Woman	60	68	1.13
Man	70	87	1.24
Cow	400	266	0.67
Steer	680	411	0.60

### 1.5.2.3. MR safety standards

SAR safety standards exist for humans (International Commission of Non-Ionizing Radiation Protection (ICNIRP) IEC 60601-2-33 [2010]). Basically, the safety criteria are based on the following principles:

- Induced temperature increases below  $0.5^{\circ}\text{C}$  are considered safe.
- The deposited energy should not exceed 2.5 times the energy produced by the resting body.
- The organ's perfusion and their capacity to evacuate heat has to be taken into account.

This leads to following SAR restrictions (SAR estimated during 6 minutes): 0.08 W/kg whole body average SAR, 2 W/kg for local (i.e. in 10 g of tissue) SAR in the head or the trunk, and 4 W/kg for local SAR in the limbs (ICNIRP 2005).

There are no agreed SAR exposure limits for animals. In order to put human limitations in proportion to animal physiology, one can compare the baseline metabolic rates across species (Table 1.3). The metabolic rate of rats is between 4 and 5 times that of human. Therefore, in theory, the SAR limit could be pushed from 2 W/kg to at least 8 W/kg. From a perfusion point of view, brain perfusion in rodents anesthetized with isoflurane (120 ml/100g/min) is at least 1.5 times that of human (80 ml/100g/min). This would allow, in theory, to use higher SAR than in humans. Regarding the elevation of tissue temperature, the surface/volume ratio of rodents is more favorable than that of humans to evacuate heat. However, the fur of rodents limits heat evacuation. Altogether, these data suggest that higher SAR might be tolerated by rodents, but the SAR limit remains to be determined.

## 1.6. Objectives of this thesis

This doctoral research focuses on CBF measurement in rodents by means of arterial spin labeling (ASL) at high magnetic field. It was conducted within a CIFRE (Convention Industrielle de Formation par la REcherche) agreement between the Grenoble Institute of Neuroscience (GIN), a research structure, and Bruker Biospin, a manufacturer of preclinical MR systems. This PhD was supervised by Pr. Emmanuel Barbier and Dr. Jan Warnking. The global objective of this PhD project was to increase the performance and to facilitate the use of continuous and pseudo-continuous ASL tools in preclinical studies.

This three-year project was split into two parts: one year ( $2 \times 6$  months) was spent at Bruker Biospin in Germany, at the scanner constructor's site to work on the industrial part of the project (a requirement of the CIFRE program) and two years were dedicated to the research aspect of the PhD in Grenoble.

### 1.6.1. Industrial Project

The industrial part of the project was to develop, in collaboration with Bruker, a user-friendly workflow to map CBF based on CASL. Indeed, quantitative CBF mapping currently requires several optimization, acquisition and post-processing steps that limit the use of ASL on preclinical scanners. The package includes inversion efficiency measurement, control frequency optimization to compensate for residual MT effects and the perfusion measurement itself with a relative or absolute quantification. Details about this implementation are described in Chapter 2.

### 1.6.2. Research Project

The research part focused on three main topics:

- The first topic was the robust optimization of the unbalanced pseudo continuous ASL (pCASL) labeling sequence for preclinical studies at high magnetic fields. After a pCASL parameter optimization based on simulations (chapter 3), a prescan based phase correction strategy was developed and evaluated at 9.4 T *in vivo*, its robustness with respect to sub-optimal shim conditions was tested and the optimized label and control phases were linked to the  $B_0$  at the labeling plane (chapter 4). This methodological work led to an abstract presented at the ISMRM in Toronto (2015) and at the COST meeting dedicated to ASL<sup>2</sup>. A manuscript has been published in the journal *Magnetic Resonance in Medicine*. A pCASL-package consisting of three sequences (phase optimization prescan, inversion efficiency evaluation

---

<sup>2</sup>European COST Action BM1103: ASL Initiative in Dementia (AID) <http://www.aslindementia.org/>, led by Pr. Xavier Golay and Pr. Matthias Günther.

and perfusion measurement) developed in the Paravision 6 software environment as well as a protocol for rat brain imaging has been shared with 10 other institutes worldwide. Several abstracts showing various applications were submitted (cf. Appendix C).

- The second topic consisted in the development of time-encoded pCASL in mice (chapter 5) and was performed in collaboration with teams of the Leiden University Medical Center (LUMC) in the Netherlands (Pr. Matthias van Osch and Pr. Louise van der Weerd's groups). This work led to an abstract presented at the ISMRM in Singapore (2016), awarded the ISMRM Magna Cum Laude-award 2016, and an abstract at the ISMRM in Hawaii (2017). A manuscript is in preparation. For this project, I received a short-term scientific mission (STSM) stipend from the aforementioned ASL COST network.
- Since the labeling process leads to heating, especially at higher magnetic fields, the third topic of this work was an in-depth evaluation of the specific absorption ratio (SAR) in rats for different labeling sequences and coil setups at 9.4 T: heating induced by CASL and pCASL labeling sequences was compared *in vivo* using implanted fiber-optic temperature probes and the benefit of a separate labeling coil was evaluated (chapter 6). This work led to an abstract presented at the ISMRM in Singapore (2016). A manuscript is in preparation.

Additional small projects, such as 3D-ASL-EPI optimization (Appendix B.1), combined DTI and ASL imaging in mice (Appendix B.2), 3D dynamic ASL (Appendix B.3), were conducted and are briefly exposed in Appendix B. These works also led to two abstracts presented at the ISMRM in Hawaii (2017).



## 2. CASL implementation in Paravision 6

The goal of this industrial part of the PhD project was to develop, in collaboration with Bruker, a user-friendly workflow to map blood flow in rodents, and more specifically cerebral blood flow (CBF) based on CASL. Indeed, quantitative CBF mapping currently requires several optimizations, acquisitions and post-processing steps that limit the use of ASL on preclinical scanners. The developed package includes inversion efficiency measurement, control frequency optimization to compensate for residual MT effects when labeling without a dedicated coil and the perfusion measurement itself with either a relative or an absolute quantification. A year, split in two 6-months periods, was spent in Ettlingen in Germany, at the company's site, to work on this part of the PhD project. This work was supervised by Dr. Sascha Köhler, head of Bruker's method development team. I programmed a prototype in Paravision, on which Bruker is basing a product.

### 2.1. Overview of the developed tools & Workflow

Originally, the implemented ASL method on Bruker MR systems included a CASL labeling sequence with an echo-planar-imaging (EPI) readout. At the end of the scan, the raw EPI images were provided to the users without any additional post-processing. We completed this existing method with following optimization, acquisition and reconstruction steps:

- An inversion efficiency (IE) method to measure the effective labeling quality. This sequence consists of a CASL labeling module followed by a flow-compensated FLASH imaging sequence (CASL-FcFLASH). At the end of the scan, a mean inversion efficiency value is calculated, which can be used to quantify absolute CBF maps.
- An adjustment scan in the CASL-EPI method to calculate the optimal control frequency that compensates the residual MT effects. This step is required when labeling with a volume coil, i.e. in absence of a dedicated labeling coil.
- A reconstruction menu in the CASL-EPI method, where the user can choose between different reconstruction types: default (i.e. raw EPI images), relative or quantitative CBF map.

Technical details about the developed steps and tools are described later, in sections 2.2, 2.3 and 2.4. First, we present an overview of the workflow from the user point of view. This workflow depends on the coil used for spin labeling:

- If no specific ASL coil is available, labeling will be performed with a volume coil. When using the Bruker CASL in this coil configuration, only a single slice can be acquired, because, due to MT effects, the control frequency has to be symmetrical to the labeling frequency with respect to the imaging slice frequency [Zhang et al., 1992]. This coil configuration has however the advantage of using a standard animal setup, since no additional ASL coil needs to be taken into account.
- Labeling with a separate ASL coil positioned directly under the animal's neck presents several advantages compared to labeling with the volume coil. Multi-slice imaging is possible since the spins of the imaged slice are not in the labeling coil's field of view and therefore do not experience MT effects during the labeling RF pulse. Another advantage is the lower induced SAR of this method (cf. Chapter 6). Using a separate ASL coil requires additional positioning and adjustment steps to correctly localize the coil and to calibrate its reference transmit power.

A workflow overview adapted to either coil configuration is described. Steps preceded by the sign  $\diamond$  are coil configuration specific. For each workflow, we assume that all standard measurements, usually done at the beginning of each MRI session, have already been performed: acquisition of a standard so-called "localizer" scan (FLASH sequence) to check the animal's position (Fig. 2.1a) during which all standard adjustments (i.e. basic frequency, shimming, reference power adjustment for the volume transmit RF coil, etc.) are automatically performed. This scan can be followed by an anatomical acquisition (e.g. T2-TurboRARE) if necessary.

### 2.1.1. Workflow overview - Labeling with the volume coil

Here we consider a standard 2-coil configuration, composed of a volume coil and of a surface head coil. The workflow is also valid if only a single volume coil is available. Once all standard adjustments and the "localizer" scan have been performed, the following scans can be started:

- Images to localize the vessels to label (i.e. carotids and sometimes vertebral arteries)
  - This can be done using a Bruker multi-slice FLASH (flow-compensated) sequence. Fig. 2.1a shows a planning example of such a scan. The obtained images are shown in Fig. 2.1b. To obtain more signal in the neck, the volume coil was used in transmit-receive (Tx/Rx) mode.

- Inversion efficiency measurement (CASL-FcFLASH method)
  - Position labeling and imaging slices, using the previously acquired vessel localization scan (Fig. 2.1b).
  - Choose the number of regions of interest (ROI, default number is 2) and position them roughly on the arteries of interest, as shown in Fig. 2.1b. These ROI will be used to measure the inversion efficiency (cf. section 2.2).
- Perfusion measurement (CASL-EPI method)
  - Position labeling and imaging slices. The labeling slice has to be at the same position than the one used during the CASL-FcFLASH scan.
  - $\diamond$  Start the MT correction adjustment (measurement of the optimal control frequency, cf. section 2.3) in the adjustment platform.
  - Choose the reconstruction mode: raw CASL images, relative or quantitative CBF maps (cf. section 2.4).

### 2.1.2. Workflow overview - Labeling with a separate ASL coil

Here we consider a 3-coil configuration, composed of a volume coil, a surface head coil and an ASL coil. This workflow is also valid without the surface head coil. Once all standard adjustments and acquisitions have been performed, the following scans can be started:

- Images to localize the vessels to label
  - This can be done using a Bruker multi-slice FLASH sequence acquired in Tx Volume/Rx ASL coil configuration. This coil configuration enables to view the labeling coil's position before adjusting its reference power. Fig. 2.1a shows an example of planing such a scan. The corresponding acquired images are shown in Fig. 2.1c. The labeling coil's position has to be checked at the end of the scan to ensure that the ASL coil covers correctly the labeling plane without overlapping the brain area, where the CBF will be measured. Thereby, one avoids MT effects in the brain tissue of interest.
- Inversion efficiency measurement (CASL-FcFLASH method)
  - Position labeling and imaging slices, using the previously acquired vessel localization scan (Fig. 2.1c).
  - $\diamond$  ASL coil reference power adjustment: run the  $B_1$  map adjustment in the adjustment platform.

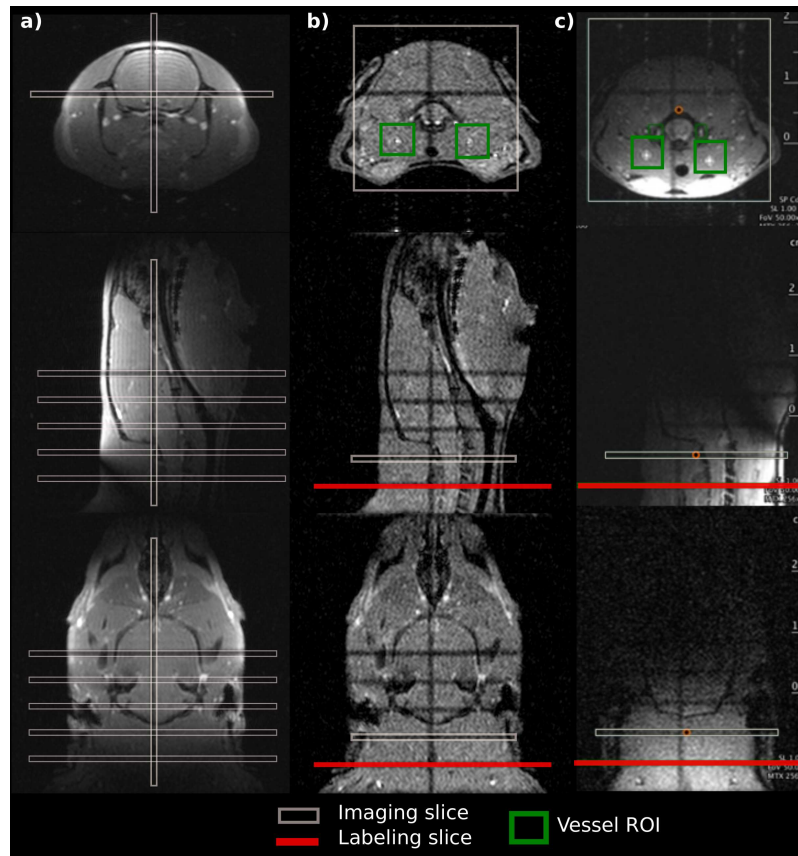


Figure 2.1.: (a) Localizer images to check the animal’s position. The white boxes represent the planned slices to be acquired during the multi-slice FLASH sequence. (b+c) Images of the multi-slice FLASH scan to visualize the vessels to label. The boxes represent the planned imaging (white) and labeling (red) slices for CASL-FcFLASH. The vessel ROIs are positioned on the chosen imaging slice for CASL-FcFLASH (top row, green boxes). The signal was received with the volume coil for the images shown in panel (b), and with the ASL coil in panel (c).

- Choose the number of regions of interest (default number is 2) and position them roughly on the arteries of interest (cf. section 2.2) that will be used to measure the IE. An example of ROI positioning is shown in Fig. 2.1c.
- Perfusion measurement (CASL-EPI method)
  - Position labeling and imaging slices. The labeling slice has to be at the same position than the one used during the CASL-FcFLASH scan.
  - Choose the reconstruction mode: raw CASL images, relative or quantitative CBF maps (cf. section 2.4).

To facilitate the use of the described workflow, a so-called ”scan program” (Fig. 2.2) will be delivered with the perfusion package. It consists of a list of scans, where all parameters, except the animal-dependent steps described in the workflow, are set to

pre-optimized values. Therefore, the user only needs to add this scan program to the current scan list, and to follow the steps described in the above workflow overview to obtain CBF maps. So far, this optimization has been done in rats using the following coils in a 2- or 3-coil configuration (i.e. with or without using the ASL coil):

- a transmit-receive quadrature volume coil (86 mm inner diameter) for imaging and labeling,
- a receive-only surface phased-array, (4-channel) rat head coil,
- a transmit-receive single loop ASL coil (diameter 23 mm) placed under the animal's neck for labeling.

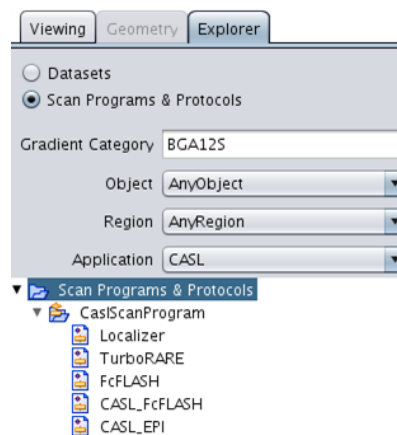


Figure 2.2.: Screen-shot of the CASL scan program proposed to the user.

Fig. 2.3 gives a general overview of all manual and automatic steps described in the next sections and views the links between the different sequence inputs and outputs.

## 2.2. Technical details of the inversion efficiency measurement (CASL-FcFLASH method)

This section details all steps mentioned in the workflow overview for the CASL-FcFLASH method and the automatic tasks performed by Paravision are detailed.

### 2.2.1. Before running CASL-FcFLASH

**Slice positioning** Labeling and imaging slices have to be positioned first, e.g. based on the multi-slice flow-compensated FLASH images, as shown on Fig. 2.1b and c. To maximize the adiabatic flow-induced inversion and minimize the presence of turbulent flow, the labeling slice should be located in an area where the vessels are approximately

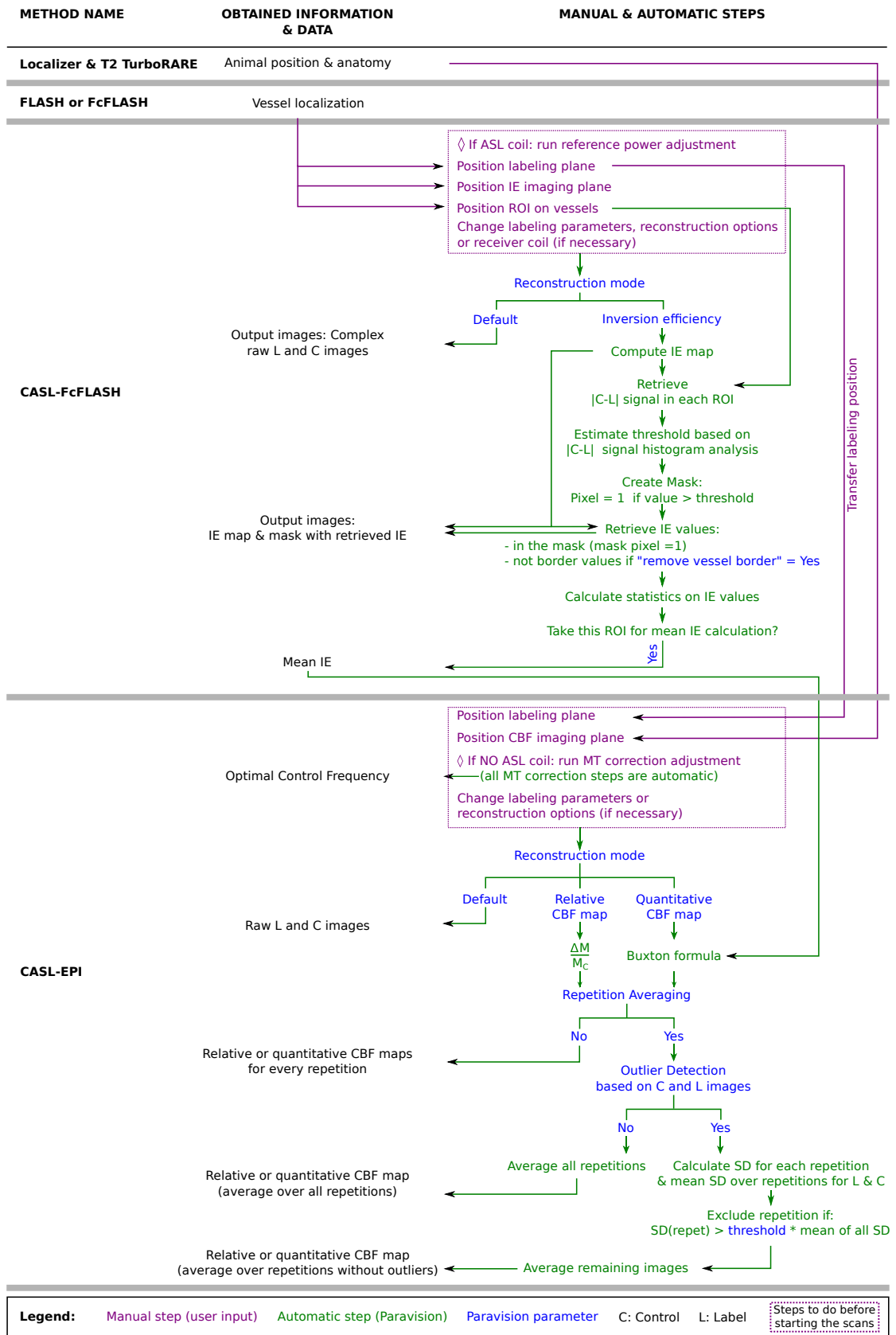


Figure 2.3.: General overview of the perfusion package.

parallel to the head-foot direction and before the separation of the common carotids in internal and external carotids. The imaging slice should be positioned in the vessels as well, few millimeters downstream the labeling plane to avoid the transition area where spin inversion occurs. In the rat protocol, this distance is set to 5 mm. The method limits the imaging slice number to a single slice.

◇ **ASL coil reference power** If an ASL coil is available, its reference power needs to be adjusted. This can be done based on a  $B_1$  map acquired with the ASL coil as transmit/receive in the so-called "adjustment platform" (cf. Fig. 2.4). The ASL coil's reference power ( $\text{Ref}_{\text{Pow}}$ ) is then calculated by Paravision in a volume of interest positioned by the user in the vessel area at the labeling plane, as the power needed to produce a  $90^\circ$  flip angle using a hard, 1 ms long, RF pulse.

**Vessel ROI positioning** Large ROIs are automatically displayed inside the CASL-FcFLASH imaging plane. The user has to roughly place them on each vessel of interest (Figs. 2.1b and c) and to run the scan: the ROI does not need to be adapted to precisely delineate the vessel, since this segmentation step is done by Paravision during reconstruction. The size and the number of ROIs can be modified. This ROI positioning step has to be performed before acquiring the data.

**Information about the CASL labeling parameters** Fig. 2.4 shows the CASL-FcFLASH labeling parameter menu. The labeling power is automatically derived from the labeling pulse  $B_1$  amplitude instruction (blue box) and from the reference power of the transmit coil used to label ( $\text{Ref}_{\text{Pow}}$ ), as:

$$\text{Labeling Power} = \text{Ref}_{\text{Pow}} \left( \frac{B_1}{B_{1\text{ref}}} \right)^2, \quad (2.1)$$

where  $B_{1\text{ref}}$  is the  $B_1$  strength generating a  $90^\circ$  pulse during 1 ms, i.e.  $B_{1\text{ref}} = 5.87 \mu\text{T}$ .

IE is measured close to the labeling plane and the average blood velocity in the carotids is about  $9.79 \pm 2.2$  cm/s in rats and  $12.6 \pm 1.7$  cm/s in mice [Kreis et al., 2011]. A short 200-ms labeled blood bolus is therefore sufficient to allow the labeled blood to travel across more than one centimeter and thus to renew the blood magnetization in the studied slice. No post-labeling delay is introduced to directly measure the blood magnetization inside the vessels. The labeling gradient has to be the same as the one applied during the perfusion measurement in the CASL-EPI method.

**Receiver coil** Since complex data will be reconstructed, the signal receiver has to be a single-channel coil in the current version of Paravision (PV 6.0.1). For example, in our 3-coil configuration, the volume and the ASL coils are suited to receive the signal,

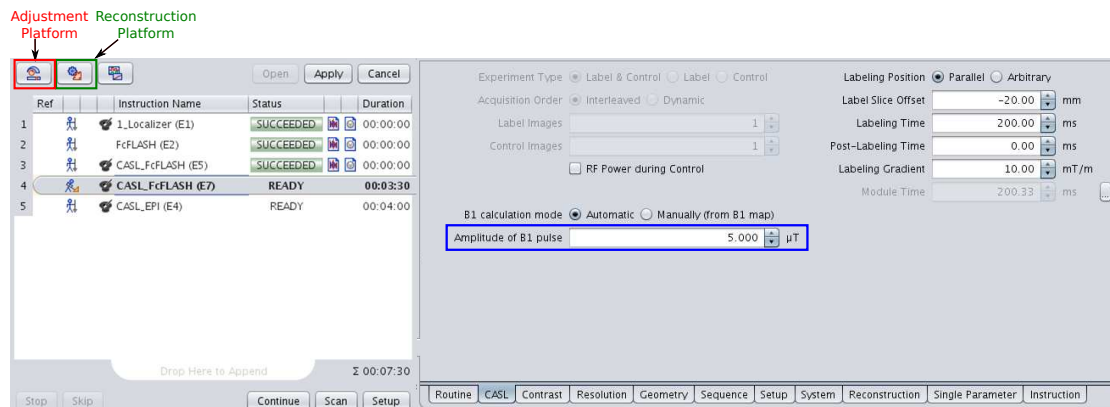


Figure 2.4.: CASL labeling menu of the CASL-FcFLASH method.

contrary to the 4-channel phased array coil, for which this complex reconstruction would fail.

In absence of an ASL coil and if the surface head coil has a single channel, a test has to be performed to determine the coil that yields the best SNR in the CASL-FcFLASH imaging area: acquiring the data with the volume coil yields sometimes higher SNR than with a surface head coil, whose sensitivity can be decreased in the vessels of interest, located too far away.

### 2.2.2. IE map reconstruction

At the end of the acquisition, two complex images are obtained: a label and a control image. An IE map is calculated using the following expression pixel by pixel (step 1a in Fig. 2.5) [Zhang et al., 1993; Debacker et al., 2016]:

$$IE = \left| \frac{M_{C,c} - M_{L,c}}{2M_{C,c}} \right|, \quad (2.2)$$

where  $M_{C,c}$  and  $M_{L,c}$  are respectively the complex signals from the control and the label experiments.

### 2.2.3. Mean IE value calculation

In order to avoid a time-consuming fine manual drawing of small ROIs on the vessels to retrieve the IE values within each carotid and/or vertebral artery, a semi-automatic algorithm was built-in: based on the large ROIs positioned by the user, the vessels are segmented, the IE values in the vessels retrieved, and the mean IE calculated. This algorithm is now detailed.

An automatic detection of the vessels based on the IE map is complicated, since the map can be very noisy. Conversely, the control-label difference image brings out only the labeled vessels and reduces the intensity of other non-labeled areas (step 1b in Fig. 2.5).

Therefore, we based the vessel segmentation on this difference image. For each ROI that roughly delineates a vessel, the following algorithm is applied:

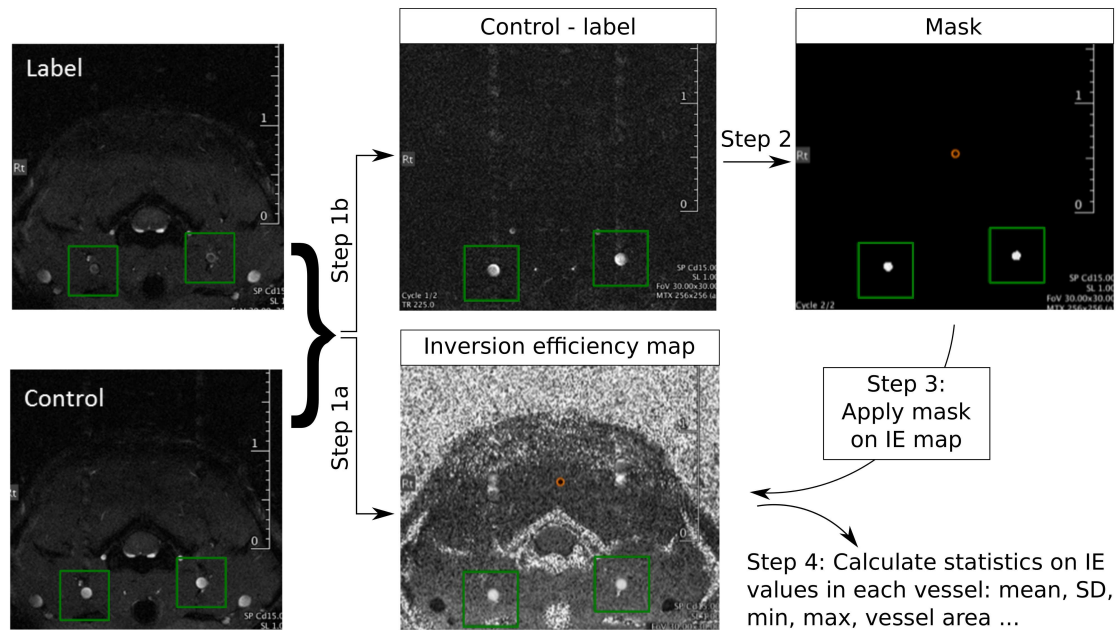


Figure 2.5.: CASL-FcFLASH reconstruction steps.

- Mask creation (step 2 in Fig. 2.5)
  - Extraction of the absolute value of the control-label difference ( $|M_{C,c} - M_{L,c}|$ ) for every pixel contained in the ROI.
  - Based on an histogram analysis [Otsu, 1975] of the  $|M_{C,c} - M_{L,c}|$  signal, a threshold that segments the vessels from the background is calculated.
  - Creation of a mask: pixels, where  $|M_{C,c} - M_{L,c}|$  is higher than the threshold are set to 1. All other pixels are set to 0.
- Retrieve IE values (step 3 in Fig. 2.5) that are:
  - In the mask
  - Not border values (ie. not contiguous with pixels where mask values are 0) if the option "Remove vessel border" is ticked (cf. Fig. 2.6b and c: red "1"s would be removed). This option allows excluding possible isolated high intensity noise pixels as well as pixels at the vessel border where blood may not reach the brain due to its low velocity.
- Calculate statistics (step 4 in Fig. 2.5), i.e. mean, standard deviation (SD), maximum, minimum IE values, vessel surface area, etc., on the selected IE values. All these values are stored and displayed in the reconstruction menu, as shown in Fig. 2.7c.

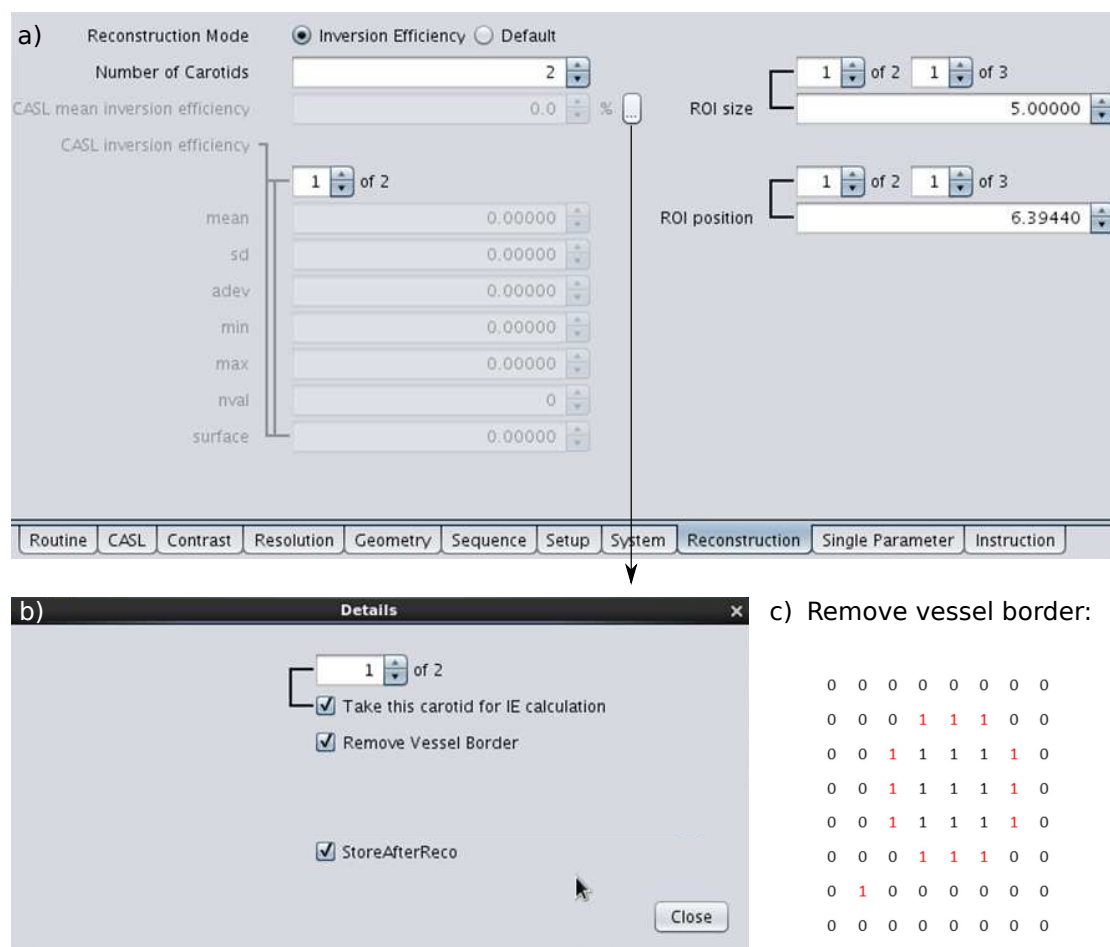


Figure 2.6.: (a) CASL-FcFLASH reconstruction menu before acquisition. (b) Reconstruction options. This windows pops up when clicking on the three dots shown on panel a. (c) In red, example of pixels that would be excluded when the option "Remove Vessel Border" is checked.

Once these steps are completed for each ROI, the mean IE value over all ROIs is calculated. If necessary, ROIs can be removed from this average calculation by unticking the corresponding "Use this carotid for IE calculation" box (cf. Fig. 2.6b).

The output image at the end of the CASL-FcFLASH post-processing is composed of two frames: one contains the entire IE map (Fig. 2.7a) and another frame contains only the IE pixels used to calculate the "CASL inversion efficiency" statistics (Fig. 2.7b).

Note that the ROI position and size can not be modified anymore after the acquisition. This is due to the way geometry objects are handled inside Paravision. However, other reconstruction options (cf. Fig. 2.6b) can be changed in a duplicated reconstruction. For example, ROIs can still be excluded from the mean IE calculation by unticking the corresponding "Take this carotid for IE calculation" box. Anyways, in the worst case, i.e. if the ROIs have not been placed on the vessels, the user can delineate them manually on the IE map, which is available as image output.

## 2.2. Technical details of the inversion efficiency measurement (CASL-FcFLASH method)

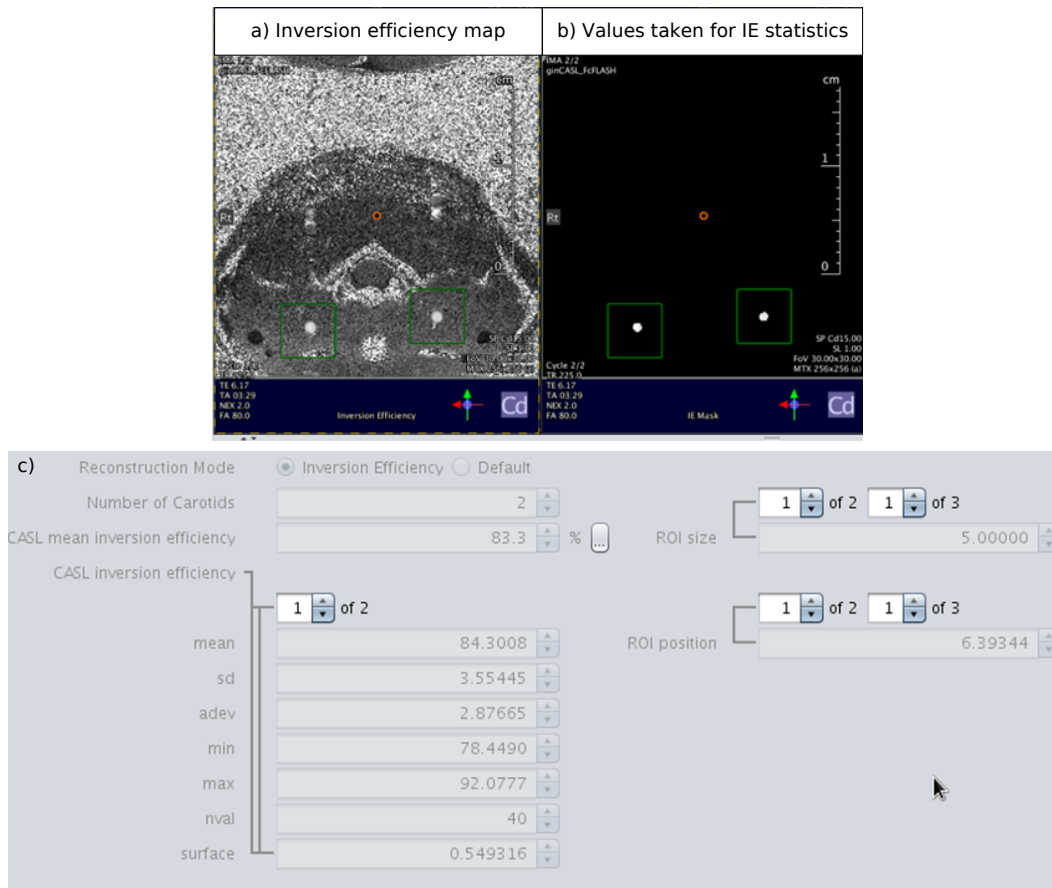


Figure 2.7.: CASL-FcFLASH output frames: (a) Whole IE map and (b) masked IE map, which contains only the values that were used to calculate IE statistics (step 4). (c) CASL-FcFLASH reconstruction menu. The statistics (mean, SD, etc.) are available after acquisition and reconstruction.

Raw label and control images can be obtained by choosing the "default" reconstruction mode.

The mean IE value is automatically stored and transferred to the CASL-EPI method.

### 2.2.4. IE measurement execution report

A template that enables an easy reporting of all acquisition and reconstruction parameters has been created for the CASL-FcFLASH method. A PDF file can therefore be generated in few clicks and helps the user to keep track of his experiments. The obtained results are also reported: the final mean IE over ROI is stored as well as all calculated statistics for each individual ROI. At the end of the report, images of the total IE map and of the "mask" containing only the segmented vessels can be found. An example of such a report is shown in Appendix A1.

## 2.3. Technical details of the residual MT effect correction (adjustment of the CASL-EPI method)

If no dedicated labeling coil is available, the long continuous labeling pulse induces MT effects in the brain tissue and contaminates the label image. In order to compensate for these effects, the same perturbation has to be applied before acquiring the control image, so that, when subtracting the label and the control images, MT effects cancel out. Assuming that the macromolecules' spectrum is symmetrical, this compensation can be achieved by applying the same RF pulse as during labeling but with an opposite offset frequency ( $-\Delta f$ ) to avoid labeling [Zhang et al., 1992]. However, the macromolecules' spectrum is not perfectly symmetrical [Pekar et al., 1996] and therefore residual MT effects remain after control-label subtraction.

In this section, the automatic steps performed during the residual MT effect correction are detailed.

### 2.3.1. Presentation of the built-in MT correction method

We implemented a method to optimize the control offset frequency to better compensate for MT effects [Pekar et al., 1996; Barbier et al., 1999]. The technique consists in sweeping the control frequency offset around its theoretical value  $-\Delta f$ , while maintaining the label frequency constant at  $\Delta f$ , to find the control frequency that induces the same perturbation on macromolecules than the labeling pulse. The labeling gradient is set to 0 mT/m during this experiment so that the measured signal is only dependent on MT effects and not on perfusion. After each label or control RF pulse, an image of the brain slice of interest (i.e. where the CBF will be measured) is acquired. The control-label difference tissue magnetization is plotted against the applied control frequencies and fitted to a straight line. The optimal control frequency is obtained as the one yielding a null difference between the label and the control signals.

We implemented such a control frequency optimization as an adjustment of the CASL-EPI method in Paravision. It can be found in the adjustment platform and is performed on-demand by the user before starting the CASL-EPI scan (i.e. the adjustment does not start automatically at the beginning of a CASL-EPI measurement). Besides the acquisition parameters that may be changed by the user, note that none of the reconstruction steps need user-input and start automatically once the data are acquired.

### 2.3.2. Data acquisition

Parameters that can be modified to adapt the MT correction are found in a dedicated "parameter card" shown in Fig. 2.8. Here we chose to perform 2 label and 5 control images ( $N_{\text{Control}}$ ). For the  $i^{\text{th}}$  control image, the applied control offset frequency  $f_{\text{control}(i)}$

### 2.3. Technical details of the residual MT effect correction (adjustment of the CASL-EPI method)

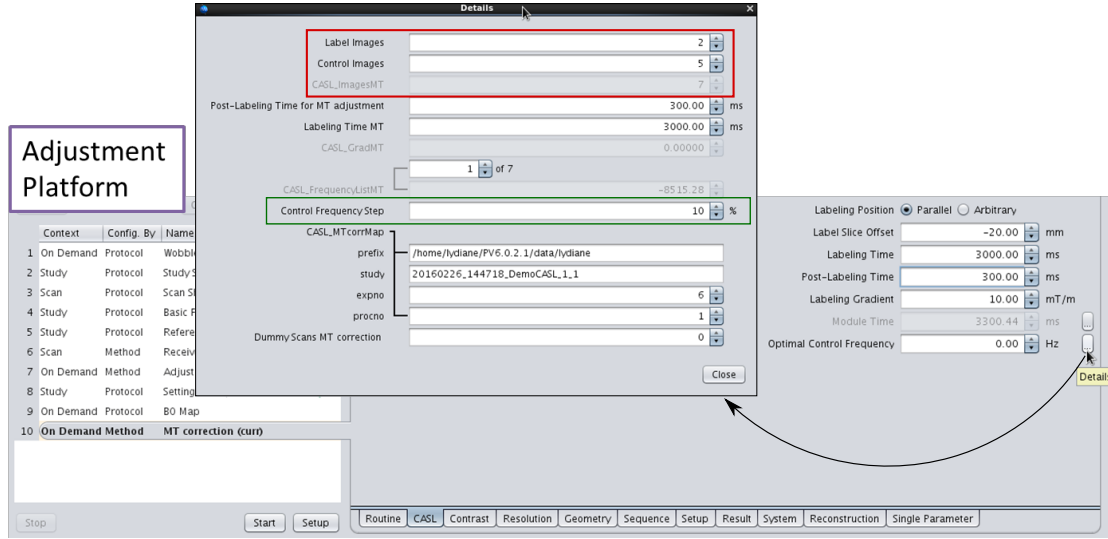


Figure 2.8.: MT correction optimization menu opened in the adjustment platform.

is calculated from the "control frequency step" (cf. parameter card) and from the theoretical control frequency  $-\Delta f$  as  $f_{\text{control}}(i) = \left[1 + \frac{\text{step}}{100} (i - \text{floor}(\frac{\text{NbControl}}{2}))\right] \times -\Delta f$ , where floor is the integer part function and step the control frequency step (in %).

Here, the control frequency step is 10 % (cf. green box in Fig. 2.8), and the labeling frequency  $\Delta f$  is -8515 Hz. Therefore the 5 control frequencies are:

- 6812 Hz, i.e.  $(1 - 2*10\%) \times -\Delta f$
- 7664 Hz, i.e.  $(1 - 10\%) \times -\Delta f$
- 8515 Hz, the "theoretical" control frequency  $-\Delta f$ , i.e. the opposite label offset frequency with respect to the image frequency. The image is located at the isocenter in our example.
- 9367 Hz, i.e.  $(1 + 10\%) \times -\Delta f$
- 10218 Hz, i.e.  $(1 + 2*10\%) \times -\Delta f$ .

#### 2.3.3. Automatic brain extraction

To correct for MT effects within the brain and not in the surrounding muscle or noise, an automatic brain segmentation has been implemented. The algorithm runs as follows (Fig. 2.9):

- To increase the SNR of the image on which the brain segmentation is based, an average of all raw EPI images is calculated and used to perform the following steps.
- To segment the brain from the surrounding structures, a threshold is generated, based on an histogram analysis of the average image [Li and Lee, 1993]. Values

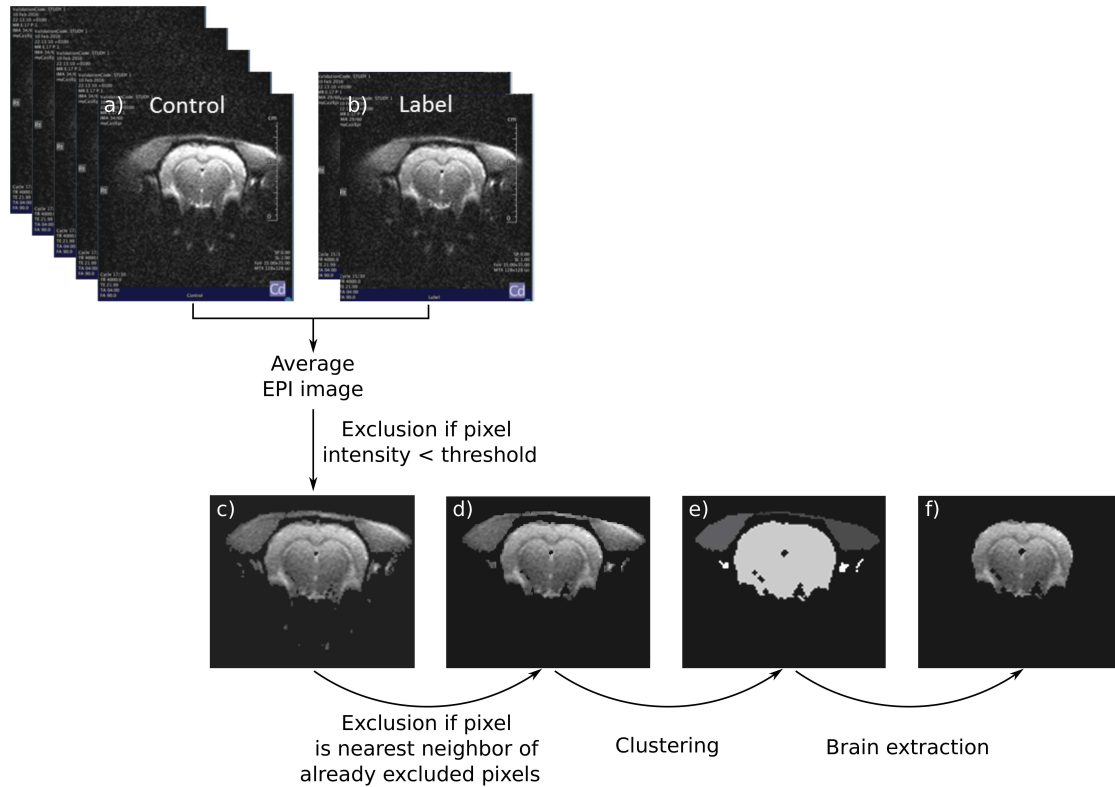


Figure 2.9.: Brain extraction steps.

below the threshold are mostly pixels in the background noise and pixels from the skull. This allows to isolate the brain (Fig. 2.9b). However, muscles yield high intensity values as well and are therefore not excluded during this first step.

- To increase the gap between the muscle and the brain and to eliminate isolated remaining noise pixels, first neighbors of already excluded pixels are removed as well (cf. step 3 of previous subsection 2.2.3).
- Remaining pixels can now be clustered in different well separated regions as shown in Fig. 2.9e: the gray-scale indicates to which cluster each pixel belongs. The brain region robustly has the largest number of pixels. This enables to identify the brain and to create a mask, that can be applied on all individual label and control images.

### 2.3.4. Optimal control frequency calculation

After brain extraction, the two label images are averaged together. Then, this label and the individual control images are spatially averaged. The difference between each of the 5 control and the average label values is calculated, plotted across the control frequencies and fitted to a straight line (Fig. 2.10). Remember that no labeling gradient was applied:

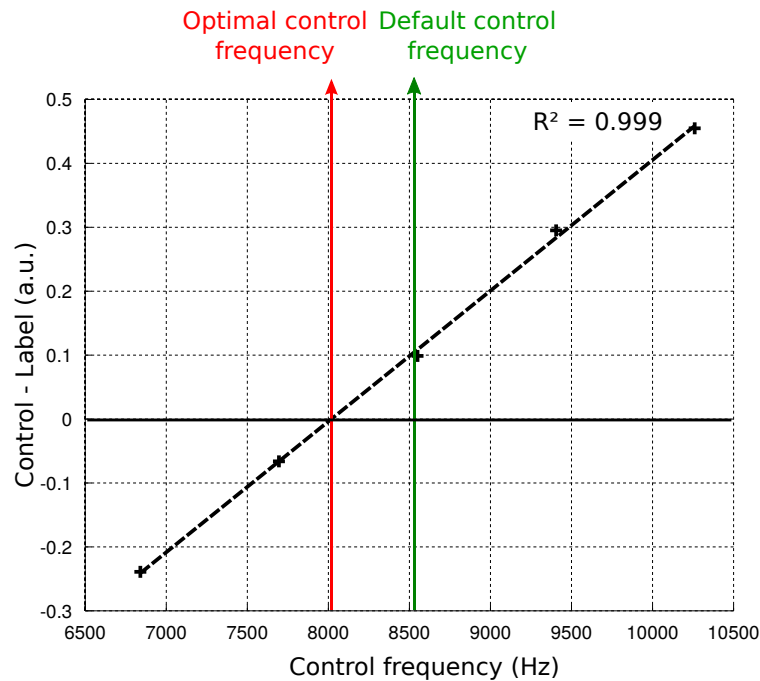


Figure 2.10.: Control-label difference across control frequencies (Hz). The dashed line represents a linear fit to the data.

the observed signal is only due to residual MT effects. Therefore, the optimal control frequency is derived as being the one leading to a null control-label difference. Fig. 2.10 shows that for this particular animal, the optimal control frequency is 8017 Hz instead of the theoretical 8515 Hz.

The optimal control frequency is stored to be used when starting the CASL-EPI scan.

### 2.3.5. MT correction execution report

A report can be generated to specifically document the MT correction. Besides the acquisition parameters, the PDF file contains a graph similar to Fig. 2.10, where the control-label values are plotted across control frequencies. The linear fit to the data is represented as well. The brain mask is found at the end of the report. An example of such a report is shown in Appendix A2. Generating this report enables the user to check the quality of the MT correction. It might be useful to warn the user if the optimized control frequency is very different from the theoretical offset frequency. For example a warning could be given if the optimized frequency exceeds 10% of the theoretical frequency, or if the correlation coefficient of the fitted curve to the data is lower than 0.6.

## 2.4. Technical details of the CBF measurement (CASL-EPI method)

In this section, we develop the steps mentioned in the workflow overview for the CASL-EPI method and detail the tasks performed by Paravision.

### 2.4.1. Before running the CASL-EPI sequence

Labeling and imaging slices first need to be positioned. The labeling slice geometry used during the IE measurement can be easily transferred to the CASL-EPI protocol: the user selects the original scan (CASL-FcFLASH) and drag-and-drops it on the target scan (CASL-EPI). A window pops up to choose the geometry that should be transferred, which is the labeling slice geometry in our case (Fig. 2.11).

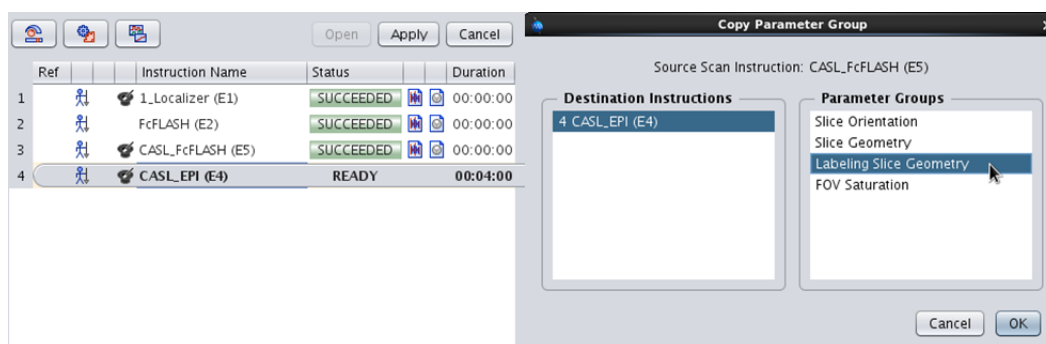


Figure 2.11.: Labeling slice geometry transfer from CASL-FcFLASH to CASL-EPI.

In absence of a dedicated ASL coil, the control frequency can be optimized in the adjustment platform, as described in section 2.3. When returning to the main menu, the optimized control frequency is automatically transferred and used during the perfusion measurement (Fig. 2.12a, blue box).

The CASL-EPI reconstruction mode can be chosen before running the scan (Fig. 2.12b), but all reconstruction parameters can be modified again once the data are acquired.

### 2.4.2. Perfusion data reconstruction

Three reconstruction modes were implemented (Fig. 2.12b, green box):

- "Default": raw label and control image reconstruction.
- "Relative CBF": calculates the relative ASL signal as

$$\text{relative CBF} = \frac{\Delta M}{M_C} \times 100, \quad (2.3)$$

where  $\Delta M$  is the magnitude difference between control and label images and  $M_C$  the magnitude image from the control experiment.

## 2.4. Technical details of the CBF measurement (CASL-EPI method)

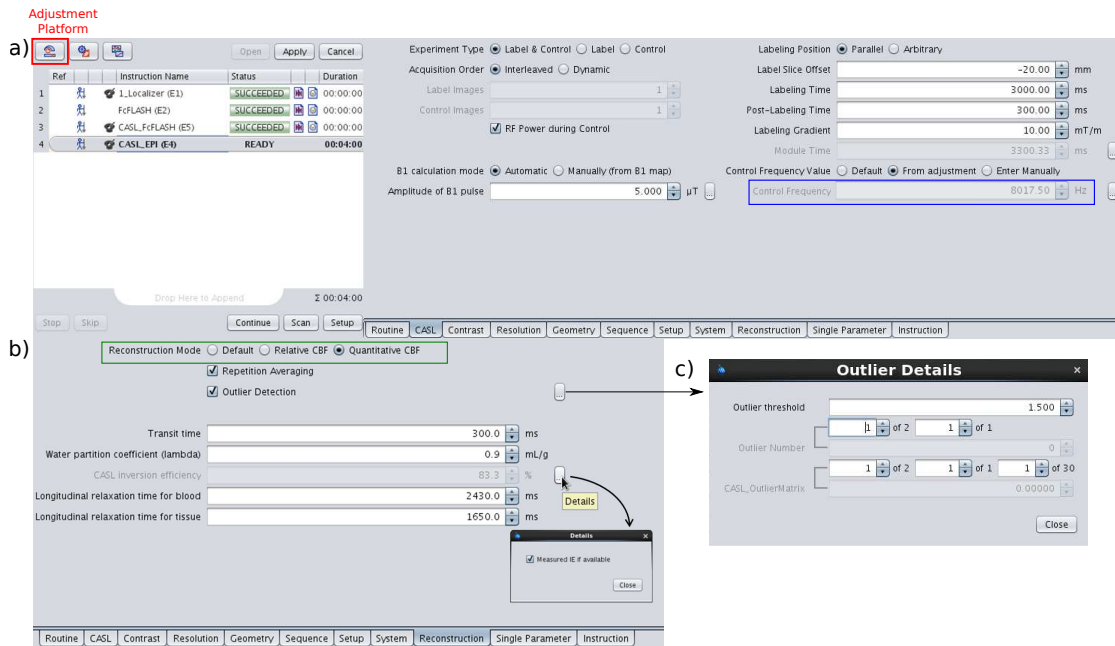


Figure 2.12.: (a) CASL and (b) reconstruction menus of the CASL-EPI method. (c) Detailed parameter card for outliers.

- "Quantitative CBF": calculates CBF based on the model developed by Buxton et al. [1998] (cf. Equation 1.10). The different parameters can be modified in the interface. By default, the longitudinal relaxation times of blood ( $T_{1b}$ ) and of tissue ( $T_{1app}$ ) are set to values measured experimentally or from literature (3 T: [Lu et al., 2004; Stanisiz et al., 2005], 4.7 T and 7 T: [Dobre et al., 2007], 9.4 T: [Nasrallah et al., 2012], 11.7 T: [Lin et al., 2012]) and are automatically adapted to the magnetic field of the system. The values shown in Fig. 2.12b are those used at 9.4 T. If IE has previously been measured (CASL-FcFLASH scan), its value has been transferred to this reconstruction menu. IE can also be entered manually by unchecking "Measured IE if available". Then the "CASL inversion efficiency" field becomes editable.

The two last reconstruction modes (relative and quantitative CBF) have additional options:

- "Repetition averaging": interleaved control and label images can only be acquired by means of repetitions. In order to obtain a single CBF map per slice, this option can be chosen.
- "Outlier detection" (appears only if the first option ("Repetition averaging") is checked): This tool enables the detection and exclusion of images with abnormal pixel intensities (e.g. with stripes) before averaging all repetitions together [Tan et al., 2009]. Such unwanted signal variations may appear due to RF spikes during

image acquisition (e.g. unexpected electrical discharges or presence of poorly-fixed metallic objects). ASL intrinsically yields low perfusion SNR and is therefore highly affected by such acquisition artifacts. Thus, images that have a spatial standard deviation (SD) exceeding a given limit value are excluded from the mean relative or quantitative CBF calculation. The limit value is calculated as the average SD across repetitions times the parameter "Outlier threshold" (Fig. 2.12c), that can be entered manually.

### 2.4.3. CBF measurement execution report

A template that enables an easy reporting of all acquisition and reconstruction parameters has been created for the CASL-EPI method: a PDF file can be generated in few clicks and helps the user to keep track of his experiments.

If the control frequency was optimized during an MT correction adjustment, the report includes a section dedicated to the MT correction, where all MT correction parameters can be found with a graph similar to Fig. 2.10. However, no image of the brain mask is provided in this CBF measurement execution report. A report has to be made directly from the MT adjustment scan to visualize the brain mask (cf. section 2.3).

The result of the outlier detection is reported as well (if performed): the number of excluded images as well as a graph of the data SD across repetitions are shown for each acquired slice. The limit, over which the images were considered as outliers, is plotted on the same graph.

If a quantitative CBF map was generated, all parameters used to quantify CBF, such as the IE value,  $T_{1b}$ ,  $T_{1app}$ , etc. can be found in the report. An example of such a report is shown in Appendix A3.

## 2.5. Tests and validation of the developed tools

The results produced by Paravision were compared to those obtained using an in-house built software coded in MATLAB, that is commonly used in the team in Grenoble to post-process IE and CBF maps. ROIs were delineated manually when using the MATLAB script.

### 2.5.1. Inversion efficiency

Fig. 2.13 shows IE maps and their corresponding vessel segmentation performed with Paravision in two animals (a rat and a mouse). In the rat, the vessel segmentation was challenged by decreasing the labeling  $B_1$  amplitude from 5  $\mu\text{T}$  down to 1.5  $\mu\text{T}$  and by using different coils to label (ASL and volume coil). The data were taken from the SAR study (Chapter 6) and from the time-encoded ASL study (Chapter 5). This vessel

extraction algorithm has been tested on data from 13 animals. Carotids are always correctly segmented, even for low IE. Vertebral artery segmentation is however more challenging due do the small vessel size.

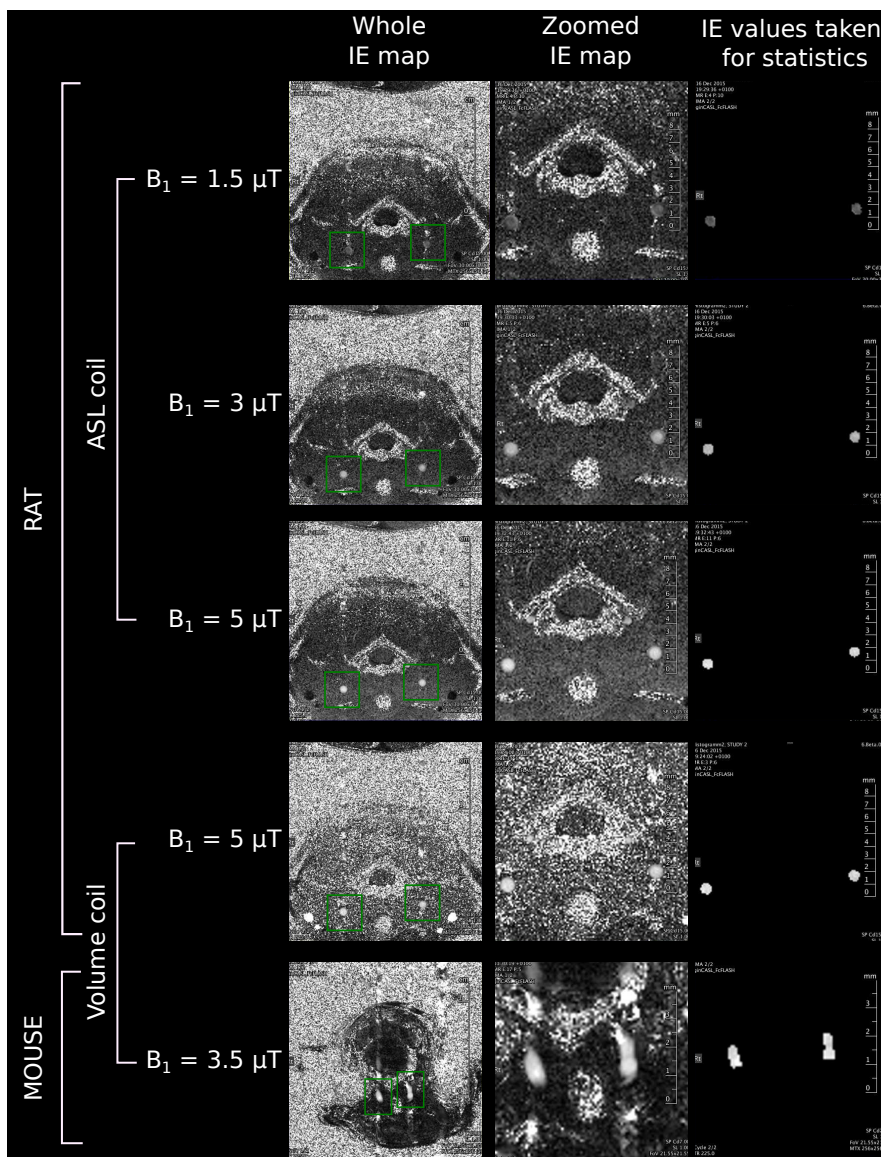


Figure 2.13.: Inversion efficiency maps and final carotid segmentation (i.e. IE values taken to calculate statistics in each vessel) for different animals, labeling coils and  $B_1$  amplitudes.

IE values obtained through Paravision's semi-automatic segmentation were compared to those retrieved after manual carotid delineation in MATLAB by calculating the relative difference between IE values as:

$$\text{Difference} = \frac{\text{IE from Paravision} - \text{IE from Matlab}}{\text{IE from Matlab}} \times 100. \quad (2.4)$$

This comparison was performed on 20 datasets obtained in 10 animals as follows:

- IE scans with different labeling  $B_1$  amplitudes (1.5, 3, 5 and 7  $\mu\text{T}$ ), labeling coil configurations (volume or ASL coil) and labeling schemes (CASL or pCASL; for pCASL the labeling was done with the volume coil) from one rat (Fig. 2.14a). These 11 datasets were taken from the SAR study (Chapter 6).
- IE scans with  $B_1 = 3.5 \mu\text{T}$  from five mice (Fig. 2.14c). These data were taken from the time-encoded ASL study (Chapter 5).
- IE scans with  $B_1 = 5 \mu\text{T}$  from four rats at 4.7 T (Fig. 2.14b). These data were collected specifically to test the final developed CASL-FcFLASH method *in vivo*.

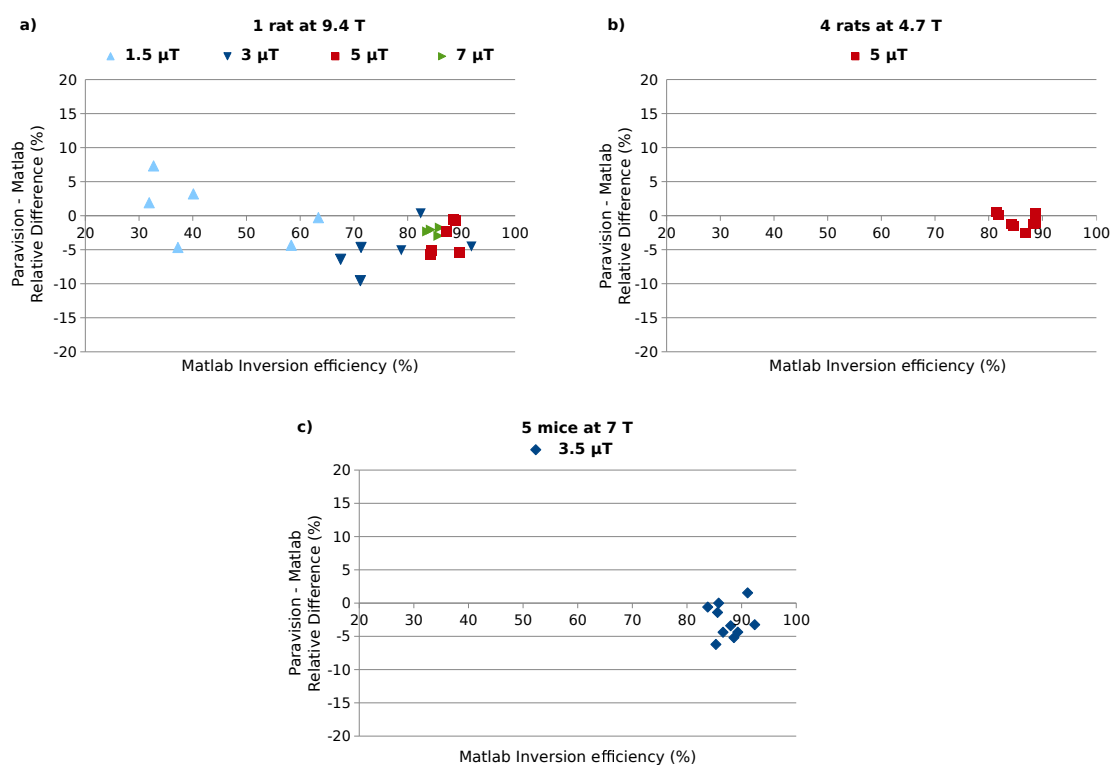


Figure 2.14.: Relative IE difference between the values extracted by Paravision and those measured with MATLAB as a function of the IE measured with MATLAB for following data: (a) in one rat at different labeling  $B_1$  values and coil configurations at 9.4 T; (b) in 4 rats at a single labeling  $B_1$  amplitude at 4.7 T; (c) in 5 mice at a single labeling  $B_1$  amplitude at 7 T. Each data point represents IE values in one carotid. IE in both carotids are plotted for each animal.

For all animals,  $B_1$  amplitudes, coil configurations and labeling schemes, the difference between a semi-automatic and a manual vessel delineation is lower than 10% (Fig. 2.14). In rats, the difference between the two segmentations does not exceed 6% when the labeling efficiency is acceptable (5  $\mu\text{T}$  or 7  $\mu\text{T}$ ) but becomes larger for 1.5  $\mu\text{T}$  and

3  $\mu$ T. For low  $B_1$  amplitudes, IE values are more heterogeneous in the vessels. When drawing the ROIs manually, I focused more on IE values in the vessel center, whereas Paravision's algorithm takes the whole labeled vessel, which may explain the observed difference between segmentation methods (paired t-test Paravision vs. MATLAB  $< 10^{-5}$  and correlation coefficient  $> 0.99$ ).

### 2.5.2. MT correction

The brain extraction algorithm has been tested on six rats, and it succeeded in all cases.

So far, the control frequency retrieved by Paravision has been compared to that obtained using the MATLAB script for one animal. The latter gave a frequency of 8017 Hz and Paravision 8035 Hz. This 18 Hz-difference is small compared to the difference between the optimized control frequencies and the theoretical 8515 Hz. It may be explained by the distinct ways of brain delineation: to run the MATLAB script, an ROI was manually drawn to delineate the brain whereas Paravision automatically extracted the brain signal; therefore not exactly the same pixels may have been taken into account for the calculation. Even if this first try has been successful, the MT correction algorithm needs to be further validated on more animals and for different imaging slice offsets.

### 2.5.3. Relative and quantitative perfusion reconstruction

Paravision's relative and quantitative CBF map reconstruction with repetition averaging were compared to the in-house developed MATLAB script as well (Fig. 2.15). Both are in good agreement, as shown by the obtained CBF values and by the difference maps. This test was performed on one animal.

The outlier detection has not been deeply tested yet: the algorithm detects and excludes images, whose SD exceeds a given threshold, but no test was performed on *in vivo* datasets.

## 2.6. Perspectives

The developed prototypes have now been integrated as Bruker methods into Paravision by Dr. Sascha Köhler. The final CASL-FcFLASH method has successfully been tested in four rats (cf. Fig. 2.14b). As shown in 4.4.1, MT corrected CASL and pCASL yield similar CBF maps. Steps of the CASL-EPI method, such as the MT correction for slices not located at the isocenter and the outlier detection, need to be further validated *in vivo*. The implemented MT correction could be compared to a second technique, where gradients are reversed during control and to CASL with a dedicated labeling coil, especially for slices that are not at the isocenter. The implemented outlier detection

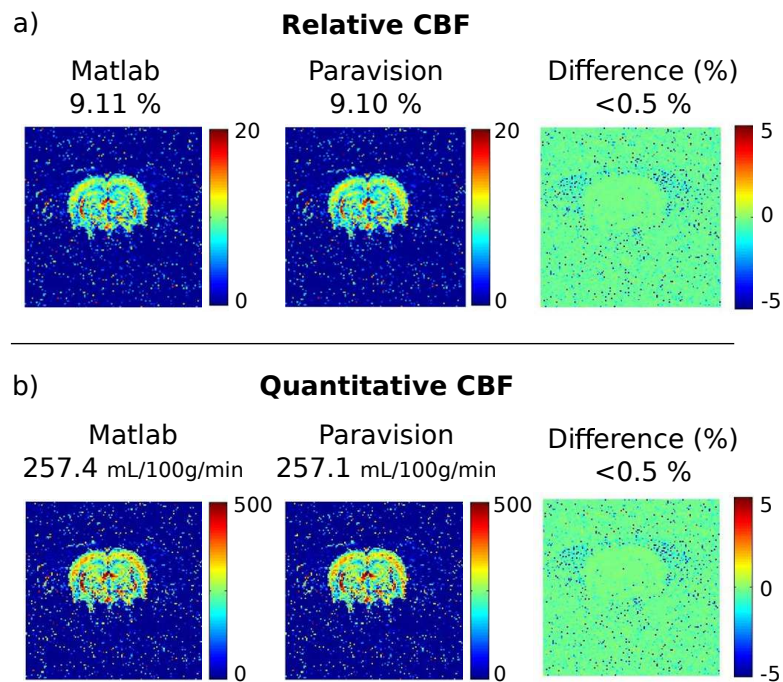


Figure 2.15.: Comparison between (a) Relative (%) and (b) quantitative CBF (mL/100g/min) maps generated by MATLAB (first column) and Paravision (second column). The third column contains the relative difference map between both scripts. Values above each image represents mean values inside the brain.

could also be improved, by calculating a threshold automatically based on statistics (e.g. [Thompson, 1935]).

Since the animals are anesthetized, movement in the images is usually negligible, which makes the developed technique usable in most cases. Still, it is undeniable that registration would further improve the use of this perfusion tool and enable its application in other organs, such as kidney for example.

This prototype demonstrates the potential of integrating automated adjustments and reconstruction steps in Paravision 6.

## 3. Simulations

This brief simulation work aimed to determine the spatial magnetization profile induced by a flow-driven adiabatic inversion in the context of a pCASL sequence in our experimental conditions. From the obtained magnetization profile, the labeling efficiency can be retrieved and optimized by varying the different pCASL parameters. One could also derive the inversion distance, i.e. the distance along which spins become inverted. Similar simulations were performed by Maccotta et al. [1997], Dai et al. [2008] and Wu et al. [2007]. However, the latter were applied with parameters suited to clinical scanners and human physiology. This explains our motivation to implement such a simulation tool to optimize pCASL labeling parameters for preclinical scanners, that have different gradient capabilities and less stringent SAR limitations (cf. section 1.5.2). Moreover, the average blood velocity in rodents may be lower, around 100 mm/s [Kreis et al., 2011] compared to 400 mm/s in humans [Maccotta et al., 1997].

This chapter outlines the implementation of the simulation tool and details the optimization of the pCASL parameters for a preclinical use. Part of this work was developed during the final-year project of my engineering studies, under the supervision of Clément Debacker and Emmanuel Barbier, and has further been completed during this PhD.

### 3.1. Implementation

A moving magnetization vector in presence of a pCASL sequence was simulated in MATLAB and monitored while crossing the labeling plane. To this end, I used a set of routines initially developed by Brian Hargraeves<sup>1</sup> and further adapted by Jan Warnking<sup>2</sup>. The tool finely discretizes a sequence of arbitrary RF and gradient pulses and numerically integrates the Bloch equations over periods with piecewise constant RF, gradient amplitudes and phases for static spins. I adapted this simulation tool to a pCASL labeling scheme and added the velocity component to simulate flowing spins (moving at constant velocity  $v$ ).

The equations of motion are integrated by performing successive rotations in the rotating frame of the applied RF around the effective field  $B_{eff}$ . The algorithm can be subdivided into several steps: first, pCASL gradient and RF pulse trains are generated

---

<sup>1</sup>Stanford University, <http://www-mrsrl.stanford.edu/~brian/bloch>

<sup>2</sup>Grenoble Institut des Neurosciences, Inserm / Université Grenoble Alpes

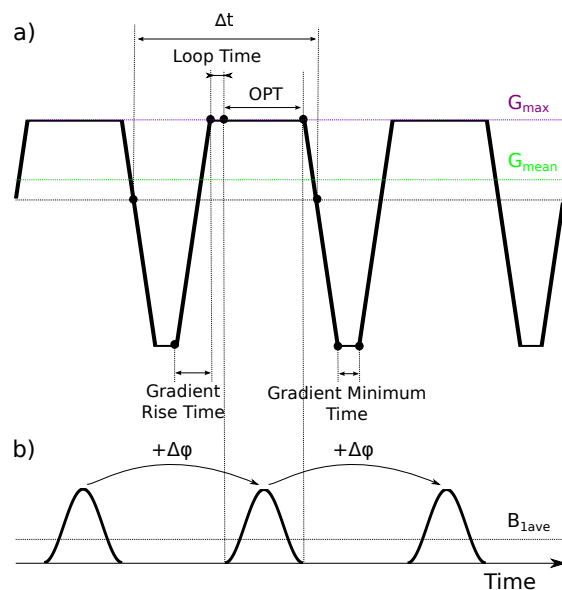


Figure 3.1.: Extract of pCASL (a) gradient and (b) RF time-courses; OPT: one pulse time;  $\Delta t$  = time between the onset of two RF pulses, loop time = software loop delay (10 $\mu$ s),  $G_{\max}$ (resp.  $G_{\text{mean}}$ ) = maximum (resp. mean) ASL gradient over time,  $B_{1\text{ave}}$  = mean ASL  $B_1$  over time.

(Fig. 3.1, [Dai et al., 2008]). Then, at each temporal step  $dt$ , the magnetization, initially parallel to the main  $B_0$  field (+z-axis), may be subjected to:

- Dephasing due to the applied field gradient during  $dt$ ,
- $T_1$  and  $T_2$  relaxation,
- Application of the RF pulse,
- Spin position shifting of  $dt \cdot v$  to simulate blood flow.

All presented simulations were performed using a temporal step  $dt$  of 1  $\mu$ s, a  $T_1$  of 2430 ms (i.e. that of blood at 9.4T [Dobre et al., 2007]) and  $T_2 = 100$  ms. The algorithm calculates the gradient minimum time and amplitude from the  $G_{\max}$  and  $G_{\text{mean}}$  instructions. The gradient rise time was set to the system's gradient rise time: 147  $\mu$ s.

When simulating a pCASL label pulse without flow, the profile shown in Fig. 3.2a is obtained. Only spins located at the labeling plane are on resonance and experience a magnetization change. When repeating the simulation with the same pCASL parameters, but in presence of a spin velocity of 400 mm/s, the magnetization profile shown in Fig. 3.2b is obtained. This profile is similar to the illustration in Fig. 1.10: before reaching the labeling plane, the spins are aligned along the main  $B_0$  field (+z-axis). When getting closer to the labeling plane, the longitudinal magnetization decreases, until canceling out at the labeling plane: spins are on resonance, the magnetization is along  $B_{1\text{ave}}^{\rightarrow}$

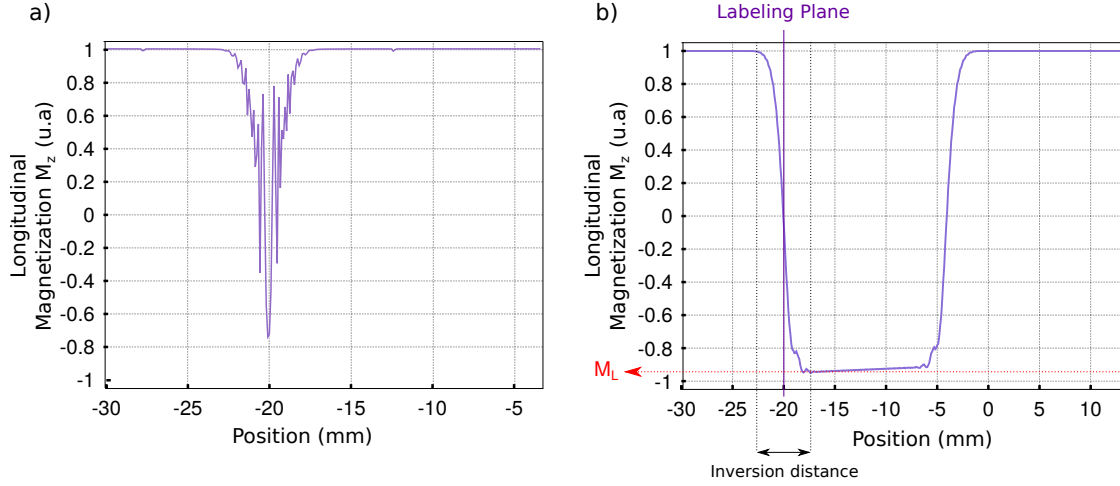


Figure 3.2.: Magnetization inversion profiles obtained after 40 ms of labeling at an off-center position of -20 mm (a) in absence of flow and (b) for a flow velocity of 400 mm/s. pCASL parameters were set to:  $G_{\max} = 45$  mT/m,  $G_{\text{mean}} = 5$  mT/m,  $B_{1\text{ave}} = 5$   $\mu$ T,  $\text{OPT} = 300$   $\mu$ s,  $\Delta t = 600$   $\mu$ s.

(cf. Eq. 1.4), i.e. in the transverse plane. When leaving the labeling plane, the effective magnetic field stays along the  $-z$ -axis: spins that flowed through the labeling plane are inverted.

From such profiles, we calculate the inversion efficiency as:

$$IE = \frac{M_0 - M_L}{2M_0}, \quad (3.1)$$

where  $M_0$  is the equilibrium magnetization, i.e.  $M_0 = 1$ , and  $M_L$  the magnetization after labeling. After inversion, the magnetization sometimes oscillates before reaching a stable value (cf. Fig. 3.2b). Therefore  $M_L$  is obtained as the mean magnetization value of the seven first minima occurring after the labeling plane. If the relative difference between the two first minima is larger than 0.03, the first minimum is ignored. For the profile shown in Fig. 3.2b, IE is 97%. Fig. 3.3 shows magnetization profiles obtained with identical pCASL labeling parameters but for different velocities. As expected, the bolus width is dependent on the spin velocity. Inversion efficiency depends on velocity as well. Unlike humans, for whom the blood speed in the carotids is  $342 \pm 48$  mm/s [Ferrara et al., 1995], the average velocity in the rat carotids is  $97.9 \pm 22$  mm/s [Kreis et al., 2011]. In mice, the blood speed is  $126 \pm 17$  mm/s and may reach up to  $374 \pm 41$  mm/s [Williams et al., 2007]. Moreover, this speed varies with the animal's physiology and especially with the heart rate [Kreis et al., 2011] and therefore with anesthesia type and depth. Given these high velocity ranges in rodents, pCASL parameters have to be optimized in such a way that the inversion efficiency is the least affected by blood flow. The pCASL parameter optimization is the topic of the next section.

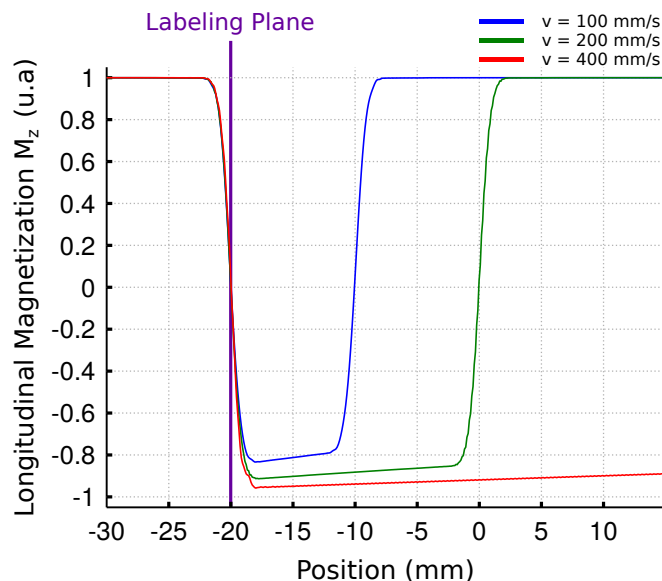


Figure 3.3.: Magnetization inversion profiles obtained after a 100 ms labeling at an off-center position of -20 mm for different flow velocities: 100 mm/s (blue), 200 mm/s (green), 400 mm/s (red). Other pCASL parameters were set to:  $G_{\max} = 45$  mT/m,  $G_{\text{mean}} = 5$  mT/m,  $B_{1\text{ave}} = 5$   $\mu$ T,  $\text{OPT} = 400$   $\mu$ s,  $\Delta t = 800$   $\mu$ s.

### 3.2. pCASL labeling parameter optimization

Magnetization profiles were generated for different maximum and average gradients ( $G_{\max}$ ,  $G_{\text{mean}}$ ), mean RF amplitudes ( $B_{1\text{ave}}$ ), velocities and pulse timings (duration of a Hanning-shaped RF pulse ( $\text{OPT}$ ), pulse spacing  $\Delta t$ ), as shown in Table 3.1. The labeling duration was set to 100 ms, which is the minimal time to measure inversion efficiency with sufficient accuracy, and which was chosen to limit the duration of the simulations. From the obtained profiles, the inversion efficiency was calculated and plotted across the different pCASL parameter values in order to optimize them.

Table 3.1.: Different pCASL parameters ranges applied to optimize the labeling.

pCASL parameter	Applied range
$G_{\max}/G_{\text{mean}}$	[2, 6, 9, 15]
$G_{\text{mean}}$ (mT/m)	[1, 2, 3, 4, 5, 10, 15]
$B_{1\text{ave}}$ ( $\mu$ T)	[1, 2, 3, 4, 5, 7, 8]
velocity (mm/s)	[30, 50, 100, 200, 300, 400, 500, 700, 1000]
$\text{OPT}$ ( $\mu$ s)	[300, 400, 500, 600]
$\Delta t$ ( $\mu$ s)	[800, 1000, 1200]

The choice of  $\text{OPT}$  and  $\Delta t$  also depends on the MR hardware. On our system, the use of  $\text{OPT}/\Delta t = 400/800$   $\mu$ s was an acceptable combination for the hardware, while keeping the interpulse delay minimal, to avoid too much phase accumulation (data not shown).

We now focus on the choices of gradient strengths and  $B_{1\text{ave}}$  amplitudes. Fig. 3.4 shows the inversion efficiency as a function of  $G_{\text{max}}/G_{\text{mean}}$  and  $G_{\text{mean}}$  for four different blood flow velocities. Again, it can be observed that the optimal pCASL parameters are highly dependent on the spin velocity. Globally, for a given  $G_{\text{mean}}$ , increasing  $G_{\text{max}}$  increases IE as well. A minimal  $G_{\text{mean}}$  of 4 mT/m is needed to reach at least 80% inversion efficiency for all flow velocities. Panels (a) and (b), suggest that, for a  $G_{\text{max}}/G_{\text{mean}}$  of 9, choosing higher mean gradient values would increase IE. However, for higher speeds, this is not true anymore (panels (c) and (d)). Note that for very low values of  $G_{\text{max}}/G_{\text{mean}}$ , aliasing planes may have occurred in these simulations within the simulated spatial domain, and the obtained IE values may not be reliable.

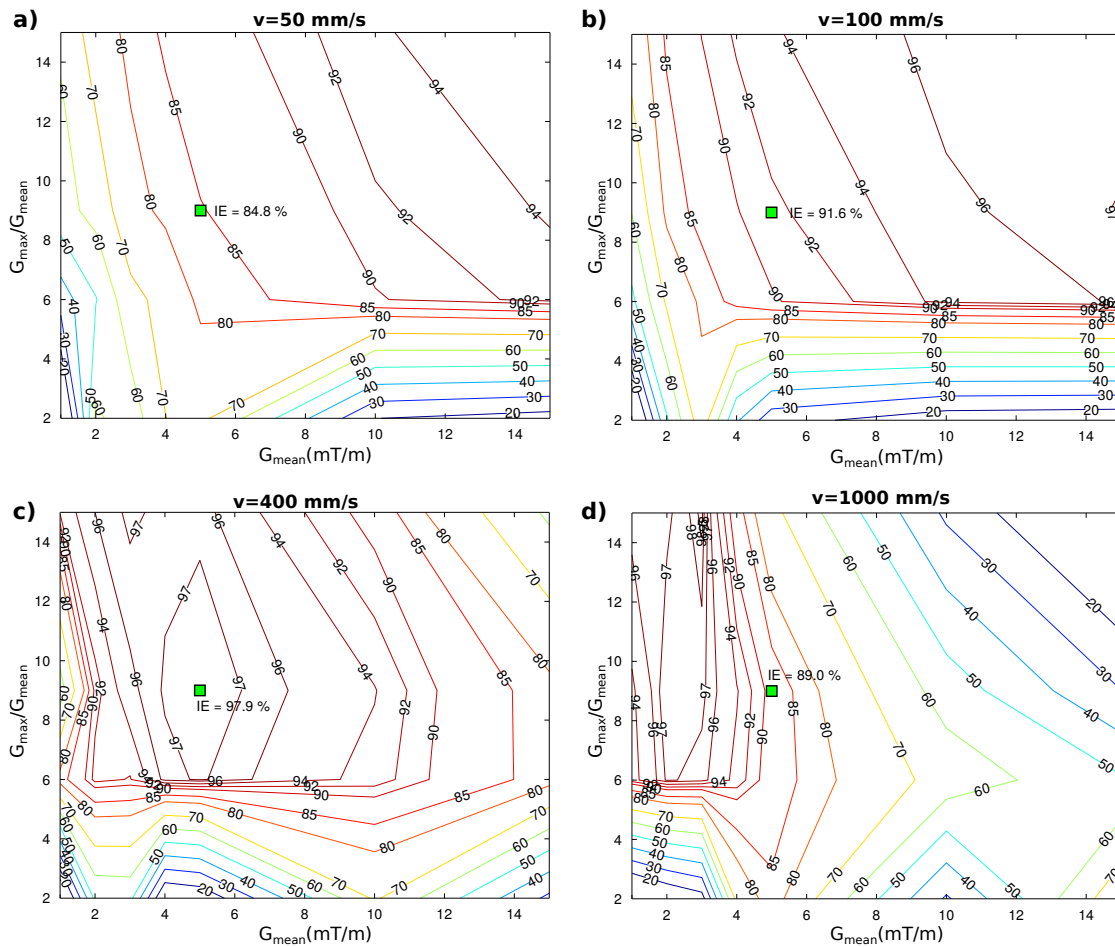


Figure 3.4.: Simulated labeling efficiency as a function of  $G_{\text{max}}/G_{\text{mean}}$  and  $G_{\text{mean}}$  for different flow velocities: (a) 50 mm/s, (b) 100 mm/s, (c) 400 mm/s and (d) 1000 mm/s. Other pCASL parameters were set to:  $B_{1\text{ave}} = 5 \mu\text{T}$ ,  $\text{OPT} = 400 \mu\text{s}$ ,  $\Delta t = 800 \mu\text{s}$ , labeling duration = 100 ms. The green squares show the IE measured for  $G_{\text{max}} = 45$  mT/m and  $G_{\text{mean}} = 5$  mT/m.

Fig. 3.5 shows the IE dependence on the applied RF amplitude,  $B_{1\text{ave}}$ , as a function of the spin velocity for four different gradient conditions. Generally, the higher the

applied  $B_{1\text{ave}}$ , the higher the IE, as is expected from the adiabaticity criterion. However, increasing  $B_{1\text{ave}}$  also increases the SAR (cf. Chapter 6). For a given  $B_{1\text{ave}}$ , IE gets more and more dependent on velocity when applying stronger gradients. For reasonable  $B_{1\text{ave}}$  values (i.e. 5  $\mu\text{T}$  for instance), the best compromise is panel (a), with a  $G_{\text{max}}/G_{\text{mean}}$  of 9 and a  $G_{\text{mean}}$  of 5 mT/m. For these parameters, a IE value of 92% is theoretically obtained.

Magnetization profiles were also generated in presence of a frequency offset in order to evaluate the impact of such offsets on the measured pCASL signal. The results of these simulations are presented in the following chapter.

Altogether, these simulations led us to use a pulse duration of 400  $\mu\text{s}$ , a  $\Delta t$  of 800  $\mu\text{s}$ , a  $G_{\text{max}}$  of 45 mT/m, a  $G_{\text{mean}}$  of 5 mT/m and a  $B_{1\text{ave}}$  of 5  $\mu\text{T}$  for the subsequent pCASL experiments performed in this thesis.

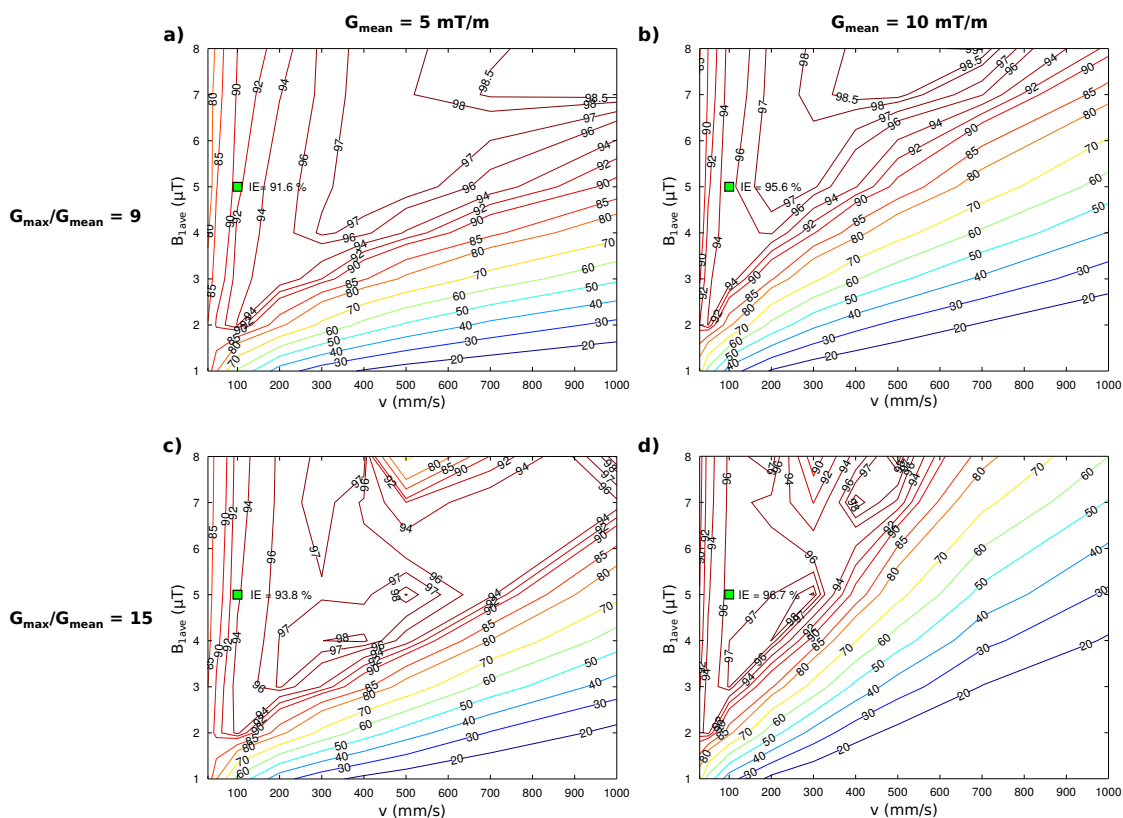


Figure 3.5.: Simulated labeling efficiency as a function of  $B_{1\text{ave}}$  and velocity for different  $G_{\text{max}}/G_{\text{mean}}$  (value of 9 in the first row and 15 in the second row) and  $G_{\text{mean}}$  values (5 mT/m in the left column and 10 mT/m in the right column). Other pCASL parameters were set to:  $\text{OPT} = 400 \mu\text{s}$ ,  $\Delta t = 800 \mu\text{s}$ , labeling duration = 100 ms. The green squares show the IE measured for  $B_{1\text{ave}} = 5 \mu\text{T}$  and  $v = 100 \text{ mm/s}$ .

## 4. Development of robust pCASL labeling

The purpose of this study was to implement a robust pCASL sequence to measure CBF in rats. I first transferred the pCASL-sequences coded in Paravision 5 by Clément Debacker during his PhD to Paravision 6. The work presented in this chapter is the evaluation of a prescan-based radio-frequency (RF) phase correction strategy for unbalanced pseudo-continuous arterial spin labeling (pCASL) at 9.4 T *in vivo* and tests of its robustness towards sub-optimal shim conditions. The measured phase correction was linked to the frequency in the carotids at the labeling plane. A manuscript has been published in the journal *Magnetic Resonance in Medicine* [Hirschler et al., 2017]. Here the manuscript has been adapted and completed with additional figures in the results and the discussion.

### 4.1. Introduction

The pseudo-continuous labeling technique imitates continuous ASL (CASL) by applying a train of short RF pulses in rapid succession [Dai et al., 2008]. To match the phase evolution of the flowing spins during labeling, a theoretical interpulse phase increment ( $\Delta\phi_{th,L}$ ) is applied:

$$\Delta\phi_{th,L} = \gamma G_{\text{mean}} \Delta z \Delta t, \quad (4.1)$$

where  $\gamma$  is the gyromagnetic ratio,  $G_{\text{mean}}$  the mean gradient,  $\Delta z$  the labeling slice offset and  $\Delta t$  the time interval between two pCASL RF pulses. Two different gradient schemes have been proposed for the control experiment [Wu et al., 2007]: balanced pCASL, with similar mean gradient for label and control conditions, and unbalanced pCASL, with null mean gradient during control. For standard pCASL measurements, the unbalanced method is recommended [Alsop et al., 2015; Duhamel et al., 2012] since it is known to be less sensitive to off-resonance effects [Wu et al., 2007]. The theoretical interpulse phase increment during control ( $\Delta\phi_{th,C}$ ) is shifted by  $180^\circ$  relative to the one used in the label condition to avoid labeling. For unbalanced pCASL, since the mean gradient is zero,  $\Delta\phi_{th,C} = 180^\circ$ .

At higher magnetic fields,  $B_0$  inhomogeneities in the labeling plane, away from the isocenter, increase and affect the spins' phase. Thereby, the theoretical interpulse phase increments  $\Delta\phi_{th,L}$  and  $\Delta\phi_{th,C}$  may not be optimal anymore. In this condition, arterial blood magnetization may not be fully inverted during labeling, and some inversion may

occur during control. Altogether, this lowers the inversion efficiency and the relative ASL signal, yields instable ASL signals across subjects and leads to inter-hemispheric asymmetry at high magnetic fields [Teeuwisse et al., 2010; Ghariq et al., 2012; Luh et al., 2008; Teeuwisse et al., 2014b].

Several strategies were developed for balanced pCASL (cf. Introduction Chapter 1.5.1). Unbalanced pCASL with a separate optimization of the control phase has not been evaluated. Here, we investigate a phase optimization prescan approach for unbalanced pCASL on rats at 9.4 T. We analyzed the effect of separately optimizing the label and the control interpulse phases on the relative ASL signal and on its inter-hemispherical symmetry. We challenged the robustness of this phase correction approach by manually changing the shims. In a second time, the dependence of the obtained optimal phase values on the shim settings and on the Larmor frequency at the location of the carotids in the labeling plane was evaluated.

## 4.2. Theory

The presence of an off-resonance frequency offset  $\Delta f$  introduces an additional phase accumulation of  $2\pi \Delta f \Delta t$  in between two successive pCASL RF pulses and shifts the real tagging location by  $-2\pi\Delta f/(\gamma G_{\max})$ , where  $G_{\max}$  is the gradient applied during the RF pulse. Altogether, when adding these modifications to Eq. 4.1, the expected total interpulse phase to apply is:

$$\Delta\phi = \gamma G_{\text{mean}} \left( \Delta z - \frac{2\pi\Delta f}{\gamma G_{\max}} \right) \Delta t + 2\pi\Delta f \Delta t. \quad (4.2)$$

As a consequence, the phase correction  $\Delta\phi_{\text{corr}}$  to add to the theoretical phase  $\Delta\phi_{\text{th}}$  should be:

$$\Delta\phi_{\text{corr}} = 2\pi\Delta f \Delta t \left( 1 - \frac{G_{\text{mean}}}{G_{\max}} \right). \quad (4.3)$$

For the control condition, since  $G_{\text{mean}}$  is 0 mT/m, the expected control phase correction  $\Delta\phi_{\text{corr},C}$  is  $2\pi \Delta f \Delta t$ .

In the following, these theoretical interpulse phases obtained in presence of a frequency offset at the labeling plane are compared to the experimentally measured values.

## 4.3. Methods

### 4.3.1. Animals

A total of 21 healthy rats (Sprague Dawley male rats, 6-8 weeks old, weight: 200-300 g, Charles Rivers, France) were used. All experiments were approved by the local ethics committee and were performed in full compliance with the guidelines of the European

community (EUVD 86/609/EEC) for the care and use of the laboratory animals. Experiments were performed under permits (n°380945 for EB and A3851610008 for experimental and animal care facilities) from the French Ministry of Agriculture. All procedures were performed under isoflurane anesthesia (IsoFlo, Axience, France, 5 % for induction, 2 % for maintenance). Respiration rate, heart rate, oxygen saturation and rectal temperature were monitored and maintained within the following ranges: 40-60 brpm, 400-500 bpm, 98-100 % and 36-37 °C respectively.

### 4.3.2. MR sequences

Experiments were performed on a 9.4 T horizontal scanner (Avance III-HD, Bruker Biospec, Ettlingen, Germany; IRMaGe MRI facility, La Tronche, France) with a quadrature volume transmit and a phased-array surface receive coil configuration.

We first detail all MR sequences that were used in this study and describe the protocols in a second time (cf. “Experimental protocols” subsection below).

**EPI** All EPI-based sequences (i.e. ASL and  $T_1$  maps) were acquired with the following readout parameters: TE/TR = 22/4000 ms (unless mentioned otherwise), single-shot spin-echo EPI, 340 kHz bandwidth, in-plane resolution =  $234 \times 234 \mu\text{m}^2$ , one 1-mm thick slice.

**Labeling** Unless mentioned otherwise, unbalanced pCASL labeling was applied in the rat’s neck (at  $\Delta z = -2$  cm from the isocenter) during  $\tau = 3$  s, followed by a 300 ms post-labeling delay ( $\omega$ ). The labeling pulse train consisted of 400- $\mu\text{s}$  Hanning window shaped RF pulses repeated every 800  $\mu\text{s}$  and scaled to an average  $B_1$  amplitude of 5  $\mu\text{T}$  during the RF pulse train.  $G_{\text{max}}/G_{\text{mean}}$  were set to 45/5 mT/m.

The following sequences were used in this study, but not all for each animal (cf. “Experimental protocols” subsection below for more details):

- Anatomical  $T_2$ -weighted ( $T_{2w}$ ) images were obtained through a spin-echo sequence (TR/TE = 3346/33 ms, resolution =  $0.137 \times 0.137 \times 0.8 \text{ mm}^3$ , number of average (NA) = 2, acquisition time  $T_{\text{acq}} = 3 \text{ min } 34 \text{ s}$ ).
- A  $T_1$  map was acquired for cerebral blood flow (CBF) quantification [Debacker et al., 2016] using a non-selective inversion recovery sequence (TR = 10 s, TE = 19 ms, 18 inversion times (TI) between 30 and 10000 ms,  $T_{\text{acq}} = 4 \text{ min}$ ). Other EPI parameters were identical to the aforementioned ones.
- Label phase optimization prescan ( $T_{\text{acq}} = 100 \text{ s}$ ). During this scan, perfusion images were measured with the previously described EPI readout and pCASL-labeling parameters, except that the labeling duration was reduced to 1.5 s and

that the acquisition slice thickness was set to 4 mm (single slice, TR = 2 s). To quickly measure the labeling efficiency and to characterize interhemispheric asymmetry, relative cerebral perfusion weighted EPI images were acquired. A total of 25 label-control pairs, each with a different label interpulse phase, were obtained: the phase was swept from 0° correction ( $\Delta\phi_{th,L} + 0^\circ$ ) to 360° correction ( $\Delta\phi_{th,L} + 360^\circ$ ) in steps of 15°. The interpulse phase increment of the control experiment was set to 180° ( $\Delta\phi_{th,C}$ ). From this scan, the optimal label interpulse phase correction  $\Delta\phi_{corr,L}$  was extracted (cf. “Data Processing” subsection below).

- Control phase optimization prescan ( $T_{acq} = 100$  s). This time, the label phase increment was fixed to the optimized label phase increment ( $\Delta\phi_{th,L} + \Delta\phi_{corr,L}$ ) and the control interpulse phase increment was swept from 0° correction ( $\Delta\phi_{th,C} + 0^\circ$ ) to 360° correction ( $\Delta\phi_{th,C} + 360^\circ$ ) in steps of 15°. All other parameters were the same as for the label phase prescan. From this scan, the optimal control interpulse phase correction  $\Delta\phi_{corr,C}$  was extracted.
- pCASL perfusion scan ( $T_{acq} = 4$  min): 30 label-control pairs of pCASL-EPI experiments were acquired with the previously described labeling and EPI parameters. The label and control phase increments were set as described in the experimental protocol (cf. below).
- MT corrected CASL-EPI scans were acquired with the previously described EPI parameters ( $T_{acq} = 4$  min). The labeling parameters were the same as for the pCASL sequence except that the labeling gradient was set to 10 mT/m. To correct for the asymmetrical spectrum of the macromolecules, the control frequency of the CASL experiment was optimized prior to the CASL-EPI acquisition, as described in Barbier et al. [1999].
- Inversion efficiency values were measured 5 mm downstream of the labeling plane for CBF quantification with a flow-compensated gradient-echo sequence (TR/TE = 225/5.6 ms, resolution =  $0.117 \times 0.117$  mm<sup>2</sup>, 1 mm slice thickness, NA = 2,  $T_{acq} = 3$  min 30 s). Optimized label and control phases were applied. Sequence specific labeling parameters were:  $\tau = 200$  ms and  $\omega = 0$  ms (other labeling parameters were the same than that of the pCASL).
- The water frequency along the carotids was measured by means of a PRESS sequence with outer volume suppression and without water suppression module:  $2 \times 2 \times 2$  mm<sup>3</sup> voxel size, TR = 2500 ms, TE = 13 ms, NA = 12,  $T_{acq} = 30$  s.

### 4.3.3. Data Processing

MRI data were analyzed using software developed in-house in the MATLAB environment (The MathWorks Inc., Natick, MA).

**T<sub>1</sub>map** T<sub>1</sub> maps were obtained by fitting the following equation to the signal from each pixel using a Levenberg-Marquardt algorithm:

$$M_z(\text{TI}) = M_0(1 - 2\kappa e^{-\text{TI}/T_1}), \quad (4.4)$$

where  $M_z(\text{TI})$  is the MR signal collected at each TI,  $M_0$  the magnetization at thermal equilibrium,  $T_1$  the longitudinal relaxation time constant of tissue and  $\kappa$  the inversion efficiency.  $M_0$ ,  $T_1$  and  $\kappa$  are the fitted parameters.

**Inversion efficiency** The IE was derived from a complex reconstruction of the (p)CASL-FcFLASH sequence as follows:

$$\text{IE} = \left| \frac{M_{C,c} - M_{L,c}}{2M_{C,c}} \right|, \quad (4.5)$$

where  $M_{C,c}$  and  $M_{L,c}$  are the complex signals from the control and the label experiments, respectively. A region of interest (ROI) was manually drawn on each carotid. The IE was obtained as the mean IE across both carotids.

**Phase optimization** To derive the phase correction, ROIs were manually drawn to delineate the left and right brain hemispheres (Fig. 4.1 F1). The relative perfusion signal in both hemispheres ( $r\text{ASL}_{\text{left}}$  and  $r\text{ASL}_{\text{right}}$ ) in percent was calculated as

$$r\text{ASL} = \frac{\Delta M}{M_C} \times 100, \quad (4.6)$$

where  $\Delta M$  is the magnitude difference between control and label acquisitions and  $M_C$  the magnitude from the control experiment.  $r\text{ASL}_{\text{left}}$  and  $r\text{ASL}_{\text{right}}$  were plotted as a function of the label (resp. control) phase values.  $\Delta\phi_{\text{corr},L}$  was determined by visual inspection to be the center of the plateau yielding close to maximal  $r\text{ASL}$  on the label phase optimization graph (Fig. 4.1B).  $\Delta\phi_{\text{corr},C}$  was defined as the phase that is the furthest away from the dip of the control phase optimization graph: control minimum + 180° (Fig. 4.1C).

To evaluate the quality of the phase optimization, the mean ( $r\text{ASL}_{\text{mean}}$ ) and the difference in ASL magnitude between hemispheres ( $r\text{ASL}_{\text{asymmetry}}$ ) were computed as

$$r\text{ASL}_{\text{asymmetry}} = \frac{|r\text{ASL}_{\text{left}} - r\text{ASL}_{\text{right}}|}{|r\text{ASL}_{\text{left}}| + |r\text{ASL}_{\text{right}}|} \times 100 \quad (4.7)$$

$$r\text{ASL}_{\text{mean}} = \frac{|r\text{ASL}_{\text{left}} + r\text{ASL}_{\text{right}}|}{2}. \quad (4.8)$$

**Quantitative CBF maps** To calculate quantitative CBF maps, we assumed a single compartment and used the standard kinetic model developed by Buxton et al. [1998].

Assuming that the arterial transit time is equal to the post-labeling delay and that  $M_{0b}$ , the magnetization of arterial blood at thermal equilibrium, may be approximated by  $M_{0t}/\lambda$ , where  $M_{0t}$  is the magnetization of tissue at thermal equilibrium and  $\lambda$  the blood-brain partition coefficient of water (0.9 mL/g [Herscovitch and Raichle, 1985]), we used the following equation to quantify CBF [Alsop et al., 2015; Buxton et al., 1998; Debacker et al., 2016]:

$$CBF = \frac{\lambda \Delta M e^{\frac{\omega}{T_{1b}}}}{2 \text{IE } T_{1app} M_{0t} (1 - e^{\frac{-\tau}{T_{1app}}})}, \quad (4.9)$$

where  $\Delta M$  is the signal difference between control and label acquisitions averaged over repetitions;  $T_{1app}$  is the apparent  $T_1$  of tissue obtained from the  $T_1$  map;  $T_{1b}$  is the longitudinal relaxation time of blood (2430 ms at 9.4 T [Nasrallah et al., 2012; Dobre et al., 2007; de Graaf et al., 2006]).  $M_{0t}$  is the control image intensity of the ASL experiment multiplied by  $[1 - \exp(-TR/T_{1app})]^{-1}$  to correct for incomplete  $T_1$  relaxation during the 4-s TR.

#### 4.3.4. Experimental Protocols

**Experiment 1** This experiment (n = 8 animals) was designed to evaluate the impact of correcting label and/or control interpulse phase increments on the perfusion signal. The following MR scans were performed with axial slice orientation after a standard global first order shim (called ‘study shim’). The details of each sequence are provided in the ‘MR sequences’ subsection above.

- Anatomical  $T_{2w}$  scan
- $T_1$  map
- Label and control optimization prescans, from which the label and control interpulse phase corrections (resp.  $\Delta\phi_{corr,L}$  and  $\Delta\phi_{corr,C}$ ) were extracted.
- Three pCASL-EPI perfusion scans: one without any phase optimization (#0, using  $\Delta\phi_{th,L}$  and  $\Delta\phi_{th,C}$ ), one with an optimized label phase increment and a theoretical control phase increment (#1, using  $\Delta\phi_{th,L} + \Delta\phi_{corr,L}$  and  $\Delta\phi_{th,C}$ ) and one with both optimized label and control phase increments (#2, using  $\Delta\phi_{th,L} + \Delta\phi_{corr,L}$  and  $\Delta\phi_{th,C} + \Delta\phi_{corr,C}$ ).
- A CASL-EPI perfusion scan, acquired in a sub-set of animals (n = 5) to compare with the pCASL experiments. This sequence was chosen because the IE of CASL is not as sensitive to  $B_0$  inhomogeneities as that of pCASL.
- Inversion efficiency, which was measured for CBF quantification both for CASL and pCASL without optimized phases and with an optimized label phase. The

IE values with both optimized label and control phases for pCASL were measured separately in three animals.

**Experiment 2** This experiment ( $n = 5$  animals) was designed to evaluate the robustness of the phase optimization in the presence of different magnetic field distributions and to evaluate its limits. Field (in)homogeneity was changed in a controlled fashion by modifying study shim values manually to introduce asymmetry between carotids, to change the frequency profile along the vessels and to evaluate the impact of second-order shims, which may often be necessary to optimize image quality. We explored shim amplitudes up to the maximum shim values that still allowed sufficient image quality for the analysis (i.e. up to four times the study shim values). The shims were changed as follows:

- Study shim. The average  $\pm$  standard deviation shim values across five animals were: X ( $34 \pm 91$ ) Hz/cm, Y ( $-312 \pm 277$ ) Hz/cm, Z ( $610 \pm 545$ ) Hz/cm,  $Z^2 = 0$  Hz/cm<sup>2</sup>.
- The initial X (left-right direction) shim value was multiplied by -2, 0, 2 and 4 (max: 233 Hz/cm, min: -116 Hz/cm). These shim conditions were called -2X, 0X, 2X and 4X.
- The initial Y (ventro-dorsal direction) shim value was multiplied by 2, 1.5, 0.5 and 0 (max: 0 Hz/cm, min: -784 Hz/cm). These shim conditions were called 2Y, 1.5Y, 0.5Y and 0Y.
- The initial Z (head-foot direction) shim value was multiplied by 2, 1.5, 0.5 and 0 (max: 1626 Hz/cm, min: 0 Hz/cm). These shim conditions were called 2Z, 1.5Z, 0.5Z and 0Z.
- Four different values for the  $Z^2$  shim were applied between -300 Hz/cm<sup>2</sup> (called -2Z<sup>2</sup>) and 300 Hz/cm<sup>2</sup> (2Z<sup>2</sup>). These values are in the range of values obtained after a second order shim on the rat brain in our system.

Shims were changed one at a time, the other values were set to the initial study shim values. Label and control phase optimization prescans were acquired for each shim situation. From the label phase optimization graph,  $\Delta\phi_{corr,L}$  and the relative perfusion value without any phase optimization were extracted (#0).  $\Delta\phi_{corr,C}$  and the relative ASL signal with both optimized phases (#2) were obtained from the control phase optimization graph. The relative ASL signal with the optimized label phase only (#1) was obtained from both label and control optimization graphs and the reported value is the average of both extracted values.

**Experiment 3** To evaluate the dependence of the optimized phase value on the resonance frequency measured at and around the labeling plane, the following experiments were performed:

- a) In a first group of animals ( $n = 3$ ), frequency profiles were measured along each carotid and the optimized label and control phases were derived after a second order shim and in 11 additional Z-shim conditions: First, the Z-shim component was modified to null the observed gradient along the carotids, measured over 4 mm (cf. simulations) around the labeling plane. From this nulled gradient condition, -1000 Hz/cm to +1000 Hz/cm with a 200 Hz/cm step were added to the Z-shim. Profiles were measured with the PRESS sequence at 13 positions between  $z = -25$  mm and -10 mm. From the obtained frequency profiles, the gradient around the labeling plane was derived (linear fit over 4 mm) and the frequency at -20 mm retrieved. The data from the phase optimization graphs were fitted to an *ad hoc* model, where the phase of the maximum signal, the duty cycle, the transition width and the signal amplitude were the estimated parameters.
- b) For a second group of animals ( $n = 5$ ), we optimized the label and control interpulse phases with the prescans and measured the frequency with the PRESS sequence in both carotids at the labeling plane. An IE scan was acquired using optimized label and control phases. This entire experiment was performed using a global first-order shim and a local (brain) second-order shim.

#### 4.3.5. Simulations

To evaluate the distance over which the inversion of arterial blood magnetization occurs and to confirm the control and label phase dependence on frequency, a moving magnetization vector in presence of a pCASL sequence was simulated in MATLAB and followed while crossing the labeling plane. Bloch equations were integrated with a step size of  $1 \mu\text{s}$  (cf. Chapter 3). Parameters for the pCASL labeling were identical to the ones used *in vivo*, except the labeling duration, which was set to 200 ms. The blood flow velocity was set to the average blood velocity in the rat's carotids, i.e. 10 cm/s [Kreis et al., 2011]. The inversion distance was measured as the distance over which the magnetization varies from 0.5% to maximum inversion (cf. Fig. 3.2).

Phase optimization experiments were simulated by repeating the inversion simulation for different RF interpulse phase increments. The longitudinal magnetization intensity after inversion was retrieved and plotted against the applied interpulse phase increment to determine the phase that yields the best inversion for label and no inversion for

control. Such simulated phase optimization experiments were also performed when the resonance frequency of the spins was offset with respect to the RF carrier.

### 4.3.6. Statistical analysis

Paired t-tests were performed to evaluate the difference in ASL signal between hemispheres, and to compare quantitative CBF values obtained from the phase-optimized pCASL with the ones from the CASL experiment. A value of  $P < 0.01$  was considered significant. All data are expressed as mean  $\pm$  SD.

## 4.4. Results

### 4.4.1. Experiment 1

An example of a phase optimization experiment is shown in Fig. 4.1: rASL is drawn as a function of the interpulse phase increment correction for label (Fig. 4.1A) and control (Fig. 4.1B) experiments. For this particular rat, the interpulse phase needed a correction of  $90^\circ$  for labeling and of  $160^\circ$  for control. As these corrections differed between rats,  $\Delta\phi_{corr,L}$  and  $\Delta\phi_{corr,C}$  were measured for each animal. The relative perfusion signal  $rASL_{mean}$  improves when applying the optimal phases (Fig. 4.1D and F): optimizing the label phase increases the ASL signal by more than a factor 2. When adding an optimal control phase, another 50% increase is gained. Without any optimization,  $rASL_{mean}$  is lower than the standard deviation across rats (Fig. 4.1D), meaning that the perfusion measurement is very unstable. These inter-subject variations are corrected when applying the optimized label and control phases.

If no optimization is performed or only the label phase is optimized, the ASL signal differs significantly between hemispheres (Fig. 4.1E), as determined by a paired t-test (#0  $P = 0.004$ , #1  $P = 0.005$ ). This asymmetry is reduced to  $4 \pm 3\%$  when both label and control phases are optimized (#2  $P = 0.12$ ).

We compared the quantitative CBF maps obtained with pCASL for each labeling condition (Fig. 4.1F 2-4) to a CASL acquisition performed on the same animal during the same MRI session (Fig. 4.1F 5). When only one or no phase is optimized, quantitative CBF maps obtained via pCASL are significantly different from the ones obtained with the CASL sequence (paired t-test for CASL vs. pCASL #0:  $P = 0.001$ , CASL vs. pCASL #1:  $P = 0.006$ ). If both label and control phases are optimized (Fig. 4.1F 4), pCASL scans yield CBF maps comparable to those from CASL (paired t-test CASL vs. pCASL #2:  $P = 0.21$ ). Remaining differences between CASL and pCASL ( $-4 \pm 6\%$  relative change) may be ascribed to physiological perfusion fluctuations. For the animal shown in Fig. 4.1F, the CASL scan was acquired 13 minutes after the pCASL scan, which can explain the observed CBF variations. Still, the observed contrast on both CASL and



pCASL (#2) CBF maps is similar, with higher cortical and thalamic perfusion values compared to white matter CBF (corpus callosum). The average brain CBF (from #2 pCASL) was  $153 \pm 25$  mL/100g/min, which is comparable to values from literature obtained in Sprague-Dawley rats under isoflurane anesthesia [Petrinovic et al., 2016; Kim and Kim, 2005; Esparza-Coss et al., 2010; Hansen et al., 1988].

This experiment shows that optimizing both label and control phases dramatically improves relative perfusion signal obtained with unbalanced pCASL, corrects asymmetry arising when labeling far from the isocenter at high field and preserves high image quality at the same time.

#### 4.4.2. Experiment 2

This experiment investigated the robustness of the phase optimization to different magnetic field inhomogeneities. Fig. 4.2A shows the difference between the measured left and right optimized label phase values for all shim conditions. As expected, when increasing the frequency difference between carotids (i.e. changing the X-shim), asymmetry arises in  $\Delta\phi_{corr,L}$  as well. However, for all situations, optimizing both label and control phases leads to maximum and stable ASL signal (Fig. 4.2B), with minimal signal loss at degraded X-shims, whereas without any optimization or only an optimal label phase, the ASL signal is lower and unstable. The asymmetry observed in absence of optimized phases was reduced to  $1 \pm 3$  % when performing both optimizations in all shim conditions (Fig. 4.2C), i.e. up to four times the observed study shim values.

#### 4.4.3. Experiment 3

We evaluated the relation between the frequency profile around the labeling plane and the optimized phase values.

According to our simulations, inversion occurs over a distance of 3.8 mm (represented as a gray band on Fig.4.3A-C). Varying the Z-shim changes the gradient around the labeling plane, the frequency at the labeling plane and the label and control phase optimization graphs (Fig. 4.3). Fig. 4.4A-B shows that the phase correction values are strongly correlated to the frequency measured at the center of the labeling plane. A small difference can be observed between the expected and measured phase values, leading to a slope of the linear fit  $\sim 11\%$  smaller than expected. Fig. 4.4C-D show that this phase difference (noted “residual  $\Delta\phi_{corr}$ ”) does not depend on the gradient around the labeling plane. This gradient however slightly impacts the duty cycle of the label phase optimization graph (Fig. 4.4E-F). This duty cycle is independent of the frequency at the labeling plane (data not shown). Fig. 4.4G-H show that the rASL signal amplitude becomes less dependent on the gradient around the labeling plane when both corrections are performed.

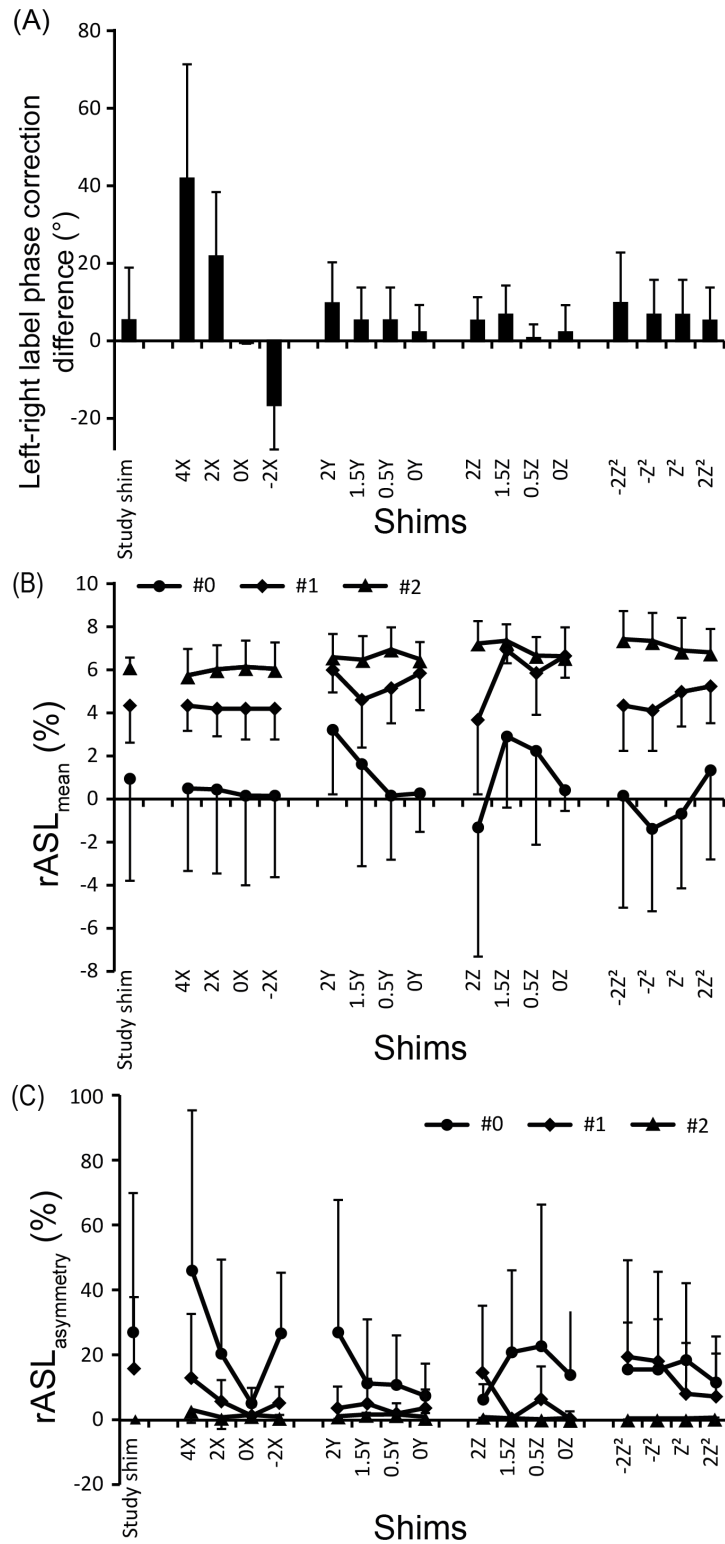


Figure 4.2.: Effect of phase correction on perfusion signal for different shim conditions (5 animals): (A) Left-right label phase correction difference across shims. (B) Relative perfusion signal and (C) asymmetry across hemispheres without phase correction (#0), with label phase correction only (#1) and with both label and control phase corrections (#2). Data expressed as mean  $\pm$  SD.

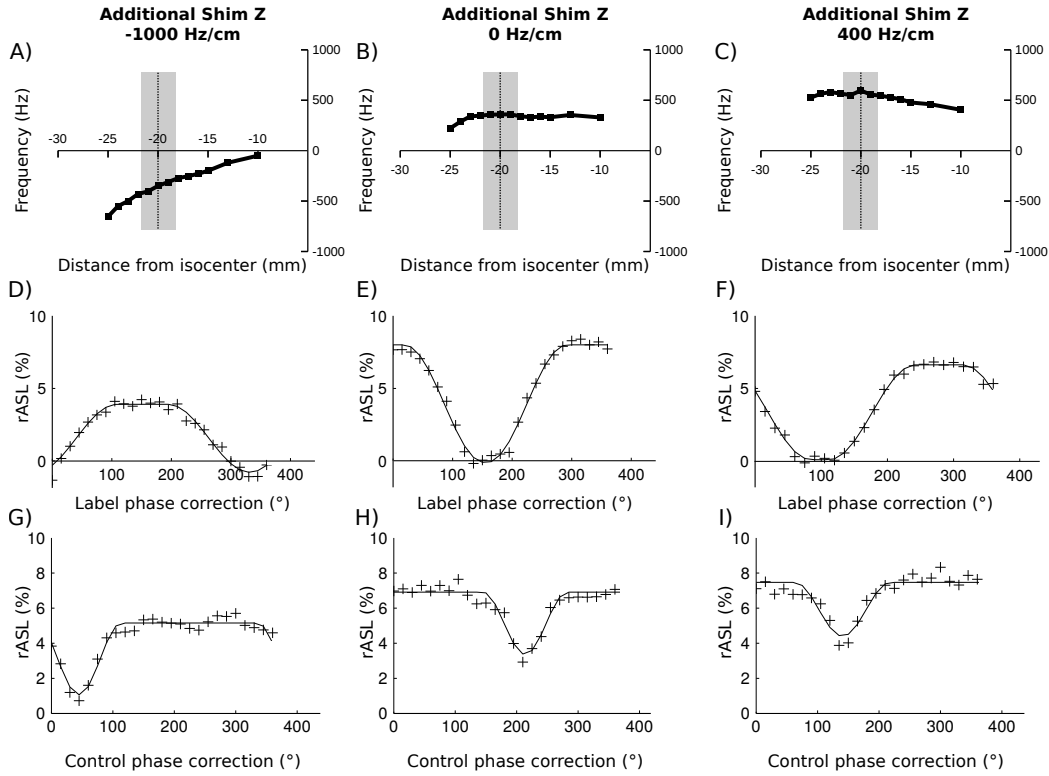


Figure 4.3.: Examples of frequency profiles along the left carotid for three shim conditions in one animal: from the situation with a compensated gradient around the labeling plane (B), additional Z-shims were added. Here we show two out of the 11 additional Z-shims: with an additional shim of -1000 Hz/cm (A) and 400 Hz/cm (C). Note that the actual additional gradient as measured with the PRESS sequence does not correspond to the nominal shim setting, suggesting an error in the shim unit conversion on our system. The labeling plane position is indicated by the black dashed lines and the transition width, derived from the simulations, by the gray boxes. The label (D-F) and control (G-I) phase optimization graphs change depending on the shim condition. The full lines in (D-I) represent an *ad hoc* model fit to the data.

To further explore the dependence of optimized phase increments on the resonance frequency at the labeling plane under standard imaging conditions, Fig. 4.6 shows data obtained using first and second order shims optimized for imaging. Whether a first or a second order shim is performed, the optimized phases  $\Delta\phi_{corr,L}$  and  $\Delta\phi_{corr,C}$  are strongly linearly correlated to the frequency  $f$  at the labeling plane (Fig. 4.6) as predicted by Eq. 4.3: the slope of the linear relation between  $\Delta\phi_{corr,L}$  and the resonance frequency is now  $0.26^\circ/\text{Hz}$ , i.e.  $(1 - G_{mean}/G_{max}) \Delta t \cdot 360$ , as expected; for control,  $\Delta\phi_{corr,C}$  is linearly related to  $f$  with a slope of  $0.29^\circ/\text{Hz}$  ( $= \Delta t \cdot 360$ ). The simulated phase optimization experiments confirmed these results: an example is shown in Fig. 4.5. In presence of a -600 Hz frequency offset, the retrieved phase corrections are  $210^\circ$  for label and  $180^\circ$  for control. When calculating the phases from Eq. 4.3,  $206^\circ$  correction is obtained for label and  $187^\circ$  for control. Application of these phase corrections (Fig. 4.5e

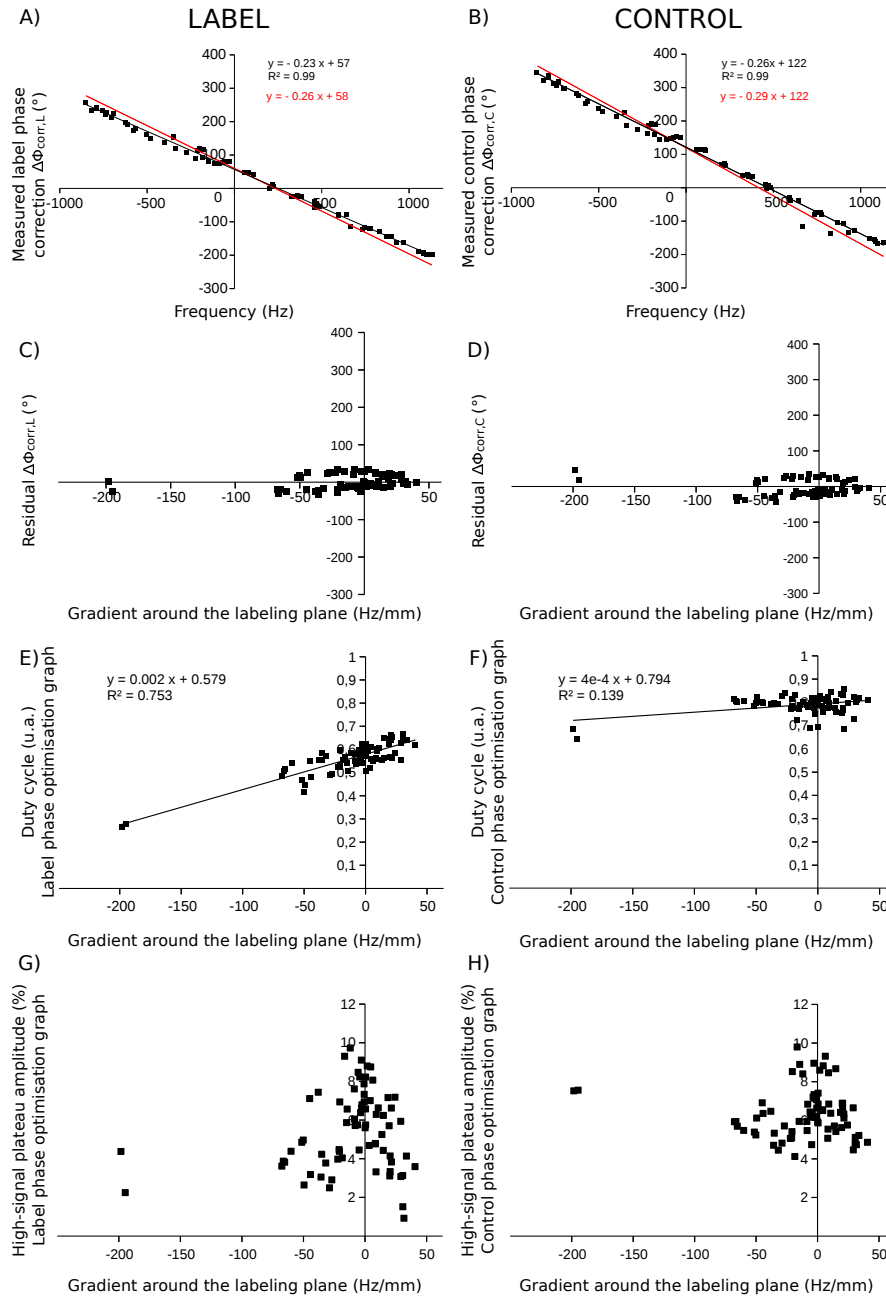


Figure 4.4.: Label (A) and control (B) phase corrections as a function of the resonance frequency measured at the labeling plane for all 12 shim conditions of Experiment 3a. Each data point corresponds to the optimized phase correction measured in one hemisphere and the frequency measured in the corresponding carotid, in one shim condition. The black line corresponds to the linear fit to the data and the red line to the expected values. The slope of the red line was calculated according to Eq. 4.3 and the offset was derived from Experiment 3b (cf. Fig. 4.6). (C) and (D) represent the residual phase correction, i.e. the difference between the data points in (A) and (B) and the expected values. (E-F): Dependence of the duty cycle of the label and control phase optimization graphs on the gradient around the labeling plane. The duty cycle was obtained as the proportion of the high-signal plateau (full-width half maximum) in the full phase cycle. (G-H): Amplitude of the high-signal plateau, measured from the label and control phase optimization graphs, as a function of the gradient around the labeling plane. Note that, in one animal, the initial gradient around the labeling plane was much higher ( $\sim 200$  Hz/mm) than those observed in other animals.

and f, red curves) restores a magnetization profile very close to that obtained in absence of frequency offset (blue curves).

Unexpected offsets of the curves are however observed in vivo (Fig. 4.6): At 0 Hz (no off-resonance effect), one would expect no need for phase correction; instead, a correction of  $58^\circ$  is required for labeling ( $\text{offset}_L$ ) and  $122^\circ$  for control ( $\text{offset}_C$ ). These offsets are stable across animals: The results shown in Fig. 4.6 originate from five animals and match those observed in Experiment 3a.

For all five animals, after both label and control phase optimizations, IE was at  $89 \pm 2\%$  and remained stable whether a second order shim was performed or not: The IE difference between first vs. second order shim was  $0 \pm 3\%$ .

## 4.5. Discussion

In this study, we described and evaluated a method to obtain stable pCASL perfusion maps in rats at 9.4 T using unbalanced pCASL. Optimizing both label and control phases of unbalanced pCASL by means of prescans yields robust ASL signal and the obtained quantitative CBF maps are comparable to those from CASL, a method less sensitive to  $B_0$  inhomogeneities. Optimized phase values vary across animals and depend on shim parameters; therefore it appears necessary to measure  $\Delta\phi_{\text{corr},L}$  and  $\Delta\phi_{\text{corr},C}$  for each animal. Applying a separate control phase correction (i.e. applying not necessarily the same  $\Delta\phi_{\text{corr},C}$  as  $\Delta\phi_{\text{corr},L}$ ) further improves the ASL signal and yields stable results across large shim and frequency-offset ranges (i.e. up to 1000 Hz). Perfusion asymmetry between hemispheres, which could be as high as 100 % without phase optimization, could be corrected with the proposed workflow, down to  $1 \pm 3$ . (mean $\pm$ SD value for Experiments 1 and 2).

Each proposed prescan acquisition lasts 100 s. Data processing involves extracting the brain-average ASL signal as a function of RF phase increment and determining the optimized phase, which is easily performed using simple off-line tools. In total, the proposed optimization adds approximately 5 minutes to ASL protocols, which is acceptable in most preclinical animal studies.

Accounting for the loss in the inversion efficiency when quantifying the CBF values should yield constant CBF, in theory. We however observed global CBF to be  $66 \pm 68$  mL/100g/min in our group of animals (n=8) without correction,  $105 \pm 40$  mL/100g/min with a label correction only, and  $153 \pm 25$  mL/100g/min with both corrections. According to common practice, IE is calculated using Eq. 4.5, leading to an always positive value, even when the ASL signal, and hence the actual IE, is negative. In case of negative IE in one or both carotids, the actual mean IE is overestimated leading to an underestimation of global CBF. Moreover, the contribution of each carotid to the perfusion is not necessarily equal in each brain region. Reliable CBF quantification may thus only be

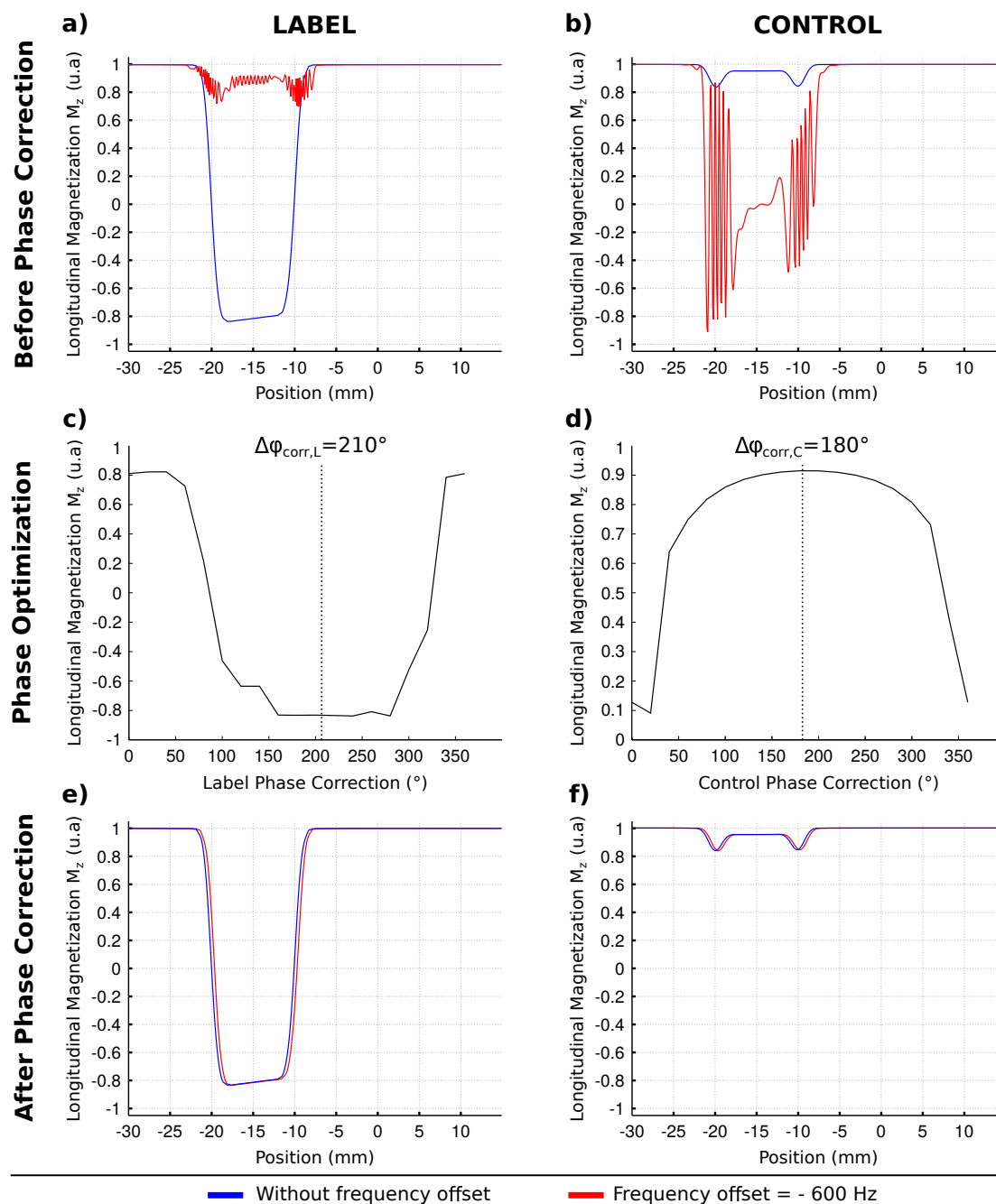


Figure 4.5.: Simulated phase correction. Longitudinal magnetization profiles for (a) label and (b) control obtained in presence of a -600 Hz frequency offset (red curves). Reference profiles generated without frequency offset (blue curves) are shown as well. Simulated label (c) and control (d) phase optimization graphs in presence of a -600 Hz frequency offset. Note that the represented values are the longitudinal magnetizations and not rASL values. Therefore, for label, the optimal phase is the phase that yields the lowest values (maximal inversion) and for control the phase that yields the values closest to 1 (no inversion). In practice, the phase of the middle of each plateau was chosen, as shown with the dashed lines. Magnetization profiles in presence of a -600 Hz frequency offset (red curves), but with corrected phases for (e) label and (f) control. Profiles in absence of frequency offset are superimposed as a reference (blue curves).

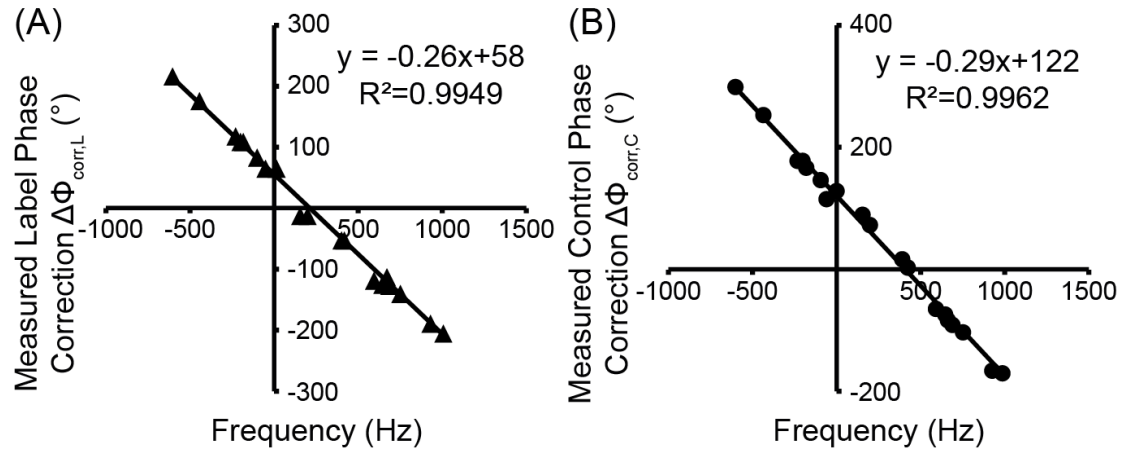


Figure 4.6.: Label (A) and control (B) phase corrections as a function of the resonance frequency measured at the labeling plane, located -20 mm from the isocenter. Each of the 20 data points corresponds to a phase correction measured in one hemisphere and a frequency measured in the corresponding carotid. The 20 data points result from the measurements in the 2 carotids of 5 animals under a first and a second order shim. All phase corrections were measured with a phase optimization prescan. The equation corresponds to the linear fit to the data.

obtained when the actual IE is positive and similar in both carotids (i.e. when both phases are optimized).

Varying the shim settings in Experiment 2 changed the labeling and imaging slice positions and thicknesses - less than 5% for labeling and 20% for imaging - and distorted the images. This may have biased the ASL signal estimation and could have contributed to the variations of mean rASL values across shim settings (Fig. 4.2B). However, these variations were only moderate. The mean rASL<sub>mean</sub> for #2 across shim settings was  $6.6 \pm 0.5\%$ , a SD comparable to that obtained between animals for one shim setting. These residual variations in rASL between shims could also be due to changes in perfusion as the physiological status of the animal may have evolved during the experiment (the total scan time for one animal was around 5 h). Despite these variations, the fully optimized rASL signal (i.e #2) is always higher than the non-optimized ones (#0 and #1).

The measured phase corrections ( $\Delta\phi_{corr,L}$  and  $\Delta\phi_{corr,C}$ ) are strongly ( $R^2 > 0.99$ ) correlated with the resonance frequency at the labeling plane measured with the PRESS sequence. In Experiment 3a, under manually degraded shim conditions, both slopes differ from the expected ones (Eq. 4.3). This is no longer true in Experiment 3b when shims optimized for imaging are used. This suggests that the slope difference observed in Experiment 3a may arise from shifts and/or distortions of the labeling and/or imaging planes. Note that the frequency ranges in both experiments are similar. Fig. 4.4 shows that the gradient around the labeling plane does not impact the optimized phase values

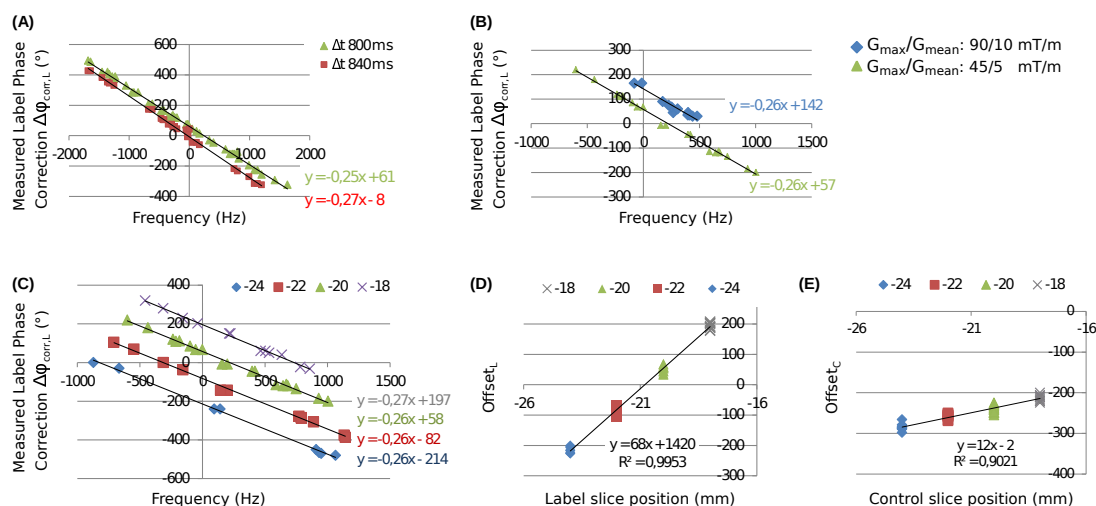


Figure 4.7.: Impact of pCASL labeling parameters on the phase correction dependence to frequency: different pulse spacings  $\Delta t$  (A), maximum and average gradients (B) and labeling slice positions (C).  $\text{Offset}_L$  (D) and  $\text{offset}_C$  (E) for different labeling slice positions.

but has a small effect on the duty cycle of the label phase optimization graph. The blood velocity may also influence the shape of the phase optimization graph [Zhao et al., 2016].

To further understand why a phase correction was needed in absence of frequency offset at the labeling plane (Figs. 4.4A-B and Fig. 4.6), we evaluated the impact of different pCASL parameters on  $\text{offset}_L$  and  $\text{offset}_C$  by repeating Experiment 3b for different pulse spacing durations, maximum and mean gradients and labeling slice positions. For all explored parameters, the curve's slope followed Eq. 4.3. The measured  $\text{offset}_L$  and  $\text{offset}_C$ , however, varied when changing the sequence parameters (Fig. 4.7). The offset variation across pCASL parameters is different in label and in control: for example the dependence to the labeling slice offset is not the same for  $\text{offset}_L$  than for  $\text{offset}_C$  (Fig. 4.7D and E).

The presence of these offsets may stem either from sequence or from hardware issues, since the offsets stayed stable across animals for a given pCASL parameter set. To investigate the offsets' origin, pCASL gradient waveforms were measured on a water tube: by calculating the derivative of the MR signal phase difference between two slices over time while the pCASL gradients are played out, the effective gradient waveform can be obtained [Beaumont et al., 2007]. These *in situ* gradient measurements confirmed that the effective average gradient seen by the spins is indeed following the pulse program's instructions (Fig. 4.8). The phase shift due to imperfections in the gradient waveform was estimated to be below  $10^\circ$ . Therefore, errors in gradient execution leading to large phase accumulation offsets may be excluded.

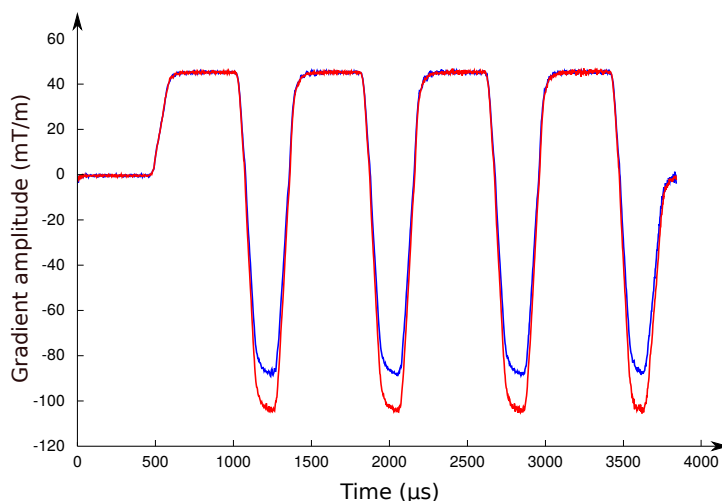


Figure 4.8.: Label (blue) and control (red) pCASL gradients measured on a water tube.

The way the RF pulses are generated and played out from the pulse program may be another possible explanation for the presence of the phase offsets (Fig. 4.9). Indeed, depending on the way off-resonance RF pulses are produced, additional phase shifts appear [Hennel, 2014].

Unfortunately, we could not test how our system controls the frequency and phase at the hardware level to check if an extra phase offset exists and explain the observed  $\text{offset}_L$  and  $\text{offset}_C$ . Such phase offsets could also be present on other MRI scanners developed by other companies, but we have not investigated this.

Several improvements may be discussed. Combining the label and control phase optimization scans in one single acquisition is possible and would accelerate this adjustment step. Prediction of optimal phases from the frequency at the labeling plane is also an option. In presence of additional hardware offsets as observed on our system,  $\text{offset}_L$  and  $\text{offset}_C$  have to be measured once for a particular set of pCASL parameters (labeling gradients, slice position, interpulse delay, etc.) and these values can then be combined with the frequency at the labeling plane measured in each animal to derive the optimal phase corrections. A phase correction based on the frequency measurement is particularly interesting for measuring perfusion in animals with low CBF: if the signal to noise ratio in the prescans becomes low, the optimal values of  $\Delta\phi_{corr,L}$  and  $\Delta\phi_{corr,C}$  may no longer be accurately detected.

In our experimental conditions, measuring the frequency at the labeling plane by means of a field map yielded unstable frequency values (data not shown). This is most probably due to the short  $T_2^*$  values at 9.4 T (the carotid area was not shimmed). Since frequency gradients along the carotids do not affect the optimal phase values (Fig. 4.4) and only the frequency at the labeling plane is required to calculate the optimal phases, a PRESS sequence, allowing a frequency measurement at the labeling plane on each

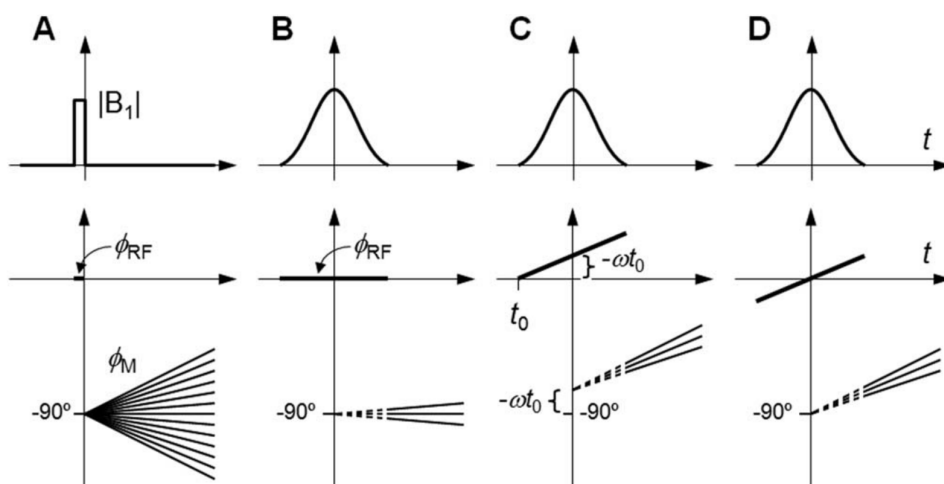


Figure 4.9.: Excitation with a hard pulse and with selective pulses of different phase ramps. The upper plots show the RF pulse amplitude, and the lower plots show the phase of the RF and of the excited transverse magnetization. The hard pulse (A) applied with phase 0 excites all spins of different frequency offsets; their phase evolution starts at  $-90^\circ$ . A selective pulse on resonance (B) excites only a few spins with offsets within the pulse band. For these spins, after the pulse, the evolution is identical with that of the hard pulse. The same pulse applied off-resonance, that is, with a phase ramp (C) excites a different group of spins. Their evolution is equivalent to what a phase-shifted hard pulse would produce; the phase shift depends on the frequency offset and the zero-crossing time point of the ramp. When the zero-crossing coincides with the shape's focus (D), the selective pulse is equivalent to the hard pulse disregarding its frequency offset. This figure was taken from [Hennel, 2014].

carotid with accuracy, is more appropriate. Moreover, the PRESS sequence yields an absolute frequency while reconstruction algorithms used to post-process a  $B_0$  map may center the distribution of frequencies and thereby introduce a frequency shift.

If the difference between optimal phases for the left and the right carotids is too large, a case not encountered in the present study despite strong shim changes, the proposed approach will no longer yield optimized pCASL labeling in both carotids. In these conditions, a dual-shim approach, i.e. application of different shim settings during labeling and during imaging, could be helpful to restore a more homogeneous magnetic field at the labeling plane. While dual shim alone did not seem sufficient to optimize pCASL in humans [Teeuwisse et al., 2014b], combining this approach with the phase optimization step should yield an optimal phase correction value for both vessels, based on our results.

The phase optimization graphs in unbalanced pCASL differ between the label and control conditions, as a result of the difference in the pCASL gradient. This would not be observed in case of balanced pCASL, for which the control optimization graph is a simple  $180^\circ$  shift of the label optimization graph. As the control phase optimization graph has a high-signal plateau larger than  $180^\circ$ , there exists always a joint optimized

control phase for both carotids. This makes unbalanced pCASL more robust to  $B_0$  inhomogeneities than balanced pCASL.

This study focused on the labeling of the blood flowing in the carotids. When using the optimized label and control phases, the mean IE in the vertebral arteries across six animals was  $74\pm 7\%$ , values smaller than those measured in the carotids for these animals ( $90\pm 1\%$ , data not shown). To properly optimize the label and control phases specifically for the vertebral arteries, better knowledge of the vascular territories perfused by the vertebrals in rodents would be necessary. However, given the observed IE, and since vertebrals in rodents preferentially perfuse the cerebellum and much less the cerebral hemispheres [Dorr et al., 2007], the proposed approach should provide near-optimal signal for most preclinical ASL studies.

In humans, carotid and vertebral arteries are separated by a greater distance and may therefore be subject to greater frequency differences. In this case, finding a compromise phase correction value for all four arteries could be more difficult. A dual-shim approach could be helpful to restore a more homogeneous field at the labeling plane, permitting optimal phase correction values for all vessels.

## 4.6. Conclusion

This study shows that performing both label and control phase correction improves relative perfusion signal, corrects asymmetry arising when labeling far from isocenter at high field and preserves high image quality at the same time. This correction approach yields stable results, also when the shim in the animal's neck is degraded, or if strong off-resonance effects are present. The phase correction values are strongly correlated to the measured frequency in the carotids. The prediction of the phase correction from the frequency measurement in the carotids is therefore possible if calibration steps to estimate  $\text{offset}_L$  and  $\text{offset}_C$  are done beforehand. Finally, in addition to the measurements presented in this work performed at 9.4T, the label and control phase correction approach has also been successfully applied at ultra-high field (17.2 T [Ciobanu et al., 2015]) as well as on different scanners and animals (Pharmascan 7 T (Chapter 5), Biospec 11.7 T [Debacker et al., 2015]). This approach is expected to be beneficial also in human studies performed at high magnetic field for which unbalanced pCASL is recommended [Alsop et al., 2015].



## 5. Time encoded ASL implementation and application in mice

This chapter results from a collaboration with teams of the Leiden University Medical Center (LUMC) in the Netherlands (groups led by Pr. Matthias van Osch and Pr. Louise van der Weerd). The collaboration was discussed during a COST meeting dedicated to ASL in early 2015<sup>1</sup> and started as a short-term scientific mission (STSM, April 2015). Thanks to a stipend from that COST action, I had the opportunity to spend two weeks in Leiden to learn more about Hadamard encoded ASL and to share our pCASL package. Together we optimized a time-encoded pCASL-EPI sequence on mice. The following study was performed with Leon Munting, a PhD student of Pr. van der Weerd's group working on imaging of neurovascular dysfunction and therapeutic response in cerebral amyloid angiopathy. The developed sequence was applied in young and old mice to evaluate whether a change in CBF and/or ATT is observed in aging. A manuscript is in preparation.

### 5.1. Introduction

Currently, there is a lack of functional disease biomarkers for the diagnosis of neurovascular dysfunction in patients and animal models. This hampers the prediction of clinical events such as a vessel rupture or cognitive impairment. Cerebral Blood Flow (CBF) as measured by Arterial Spin Labeling (ASL) MRI has shown the potential to develop into such a biomarker [Wolk and Detre, 2012]. However, CBF quantification is influenced by the arterial transit time (ATT), the time it takes for the blood to travel from the labeling slice to the brain slice of interest. Taking the ATT into account therefore reduces potential bias when comparing CBF between groups [Alsop and Detre, 1996]. Furthermore, ATT is interesting in itself, as it may reflect underlying pathologies such as increased vessel tortuosity or occlusion [Hendrikse et al., 2004]. No optimized MRI sequence exists at the moment to measure ATT in mice.

ATT maps can be obtained using multi-delay ASL [Thomas et al., 2006]. However, these scans are time consuming, as each acquisition provides information at a single

---

<sup>1</sup>COST Action BM1103: ASL Initiative in Dementia (AID) <http://www.aslindementia.org/>, led by Pr. Xavier Golay and Pr. Matthias Günther.

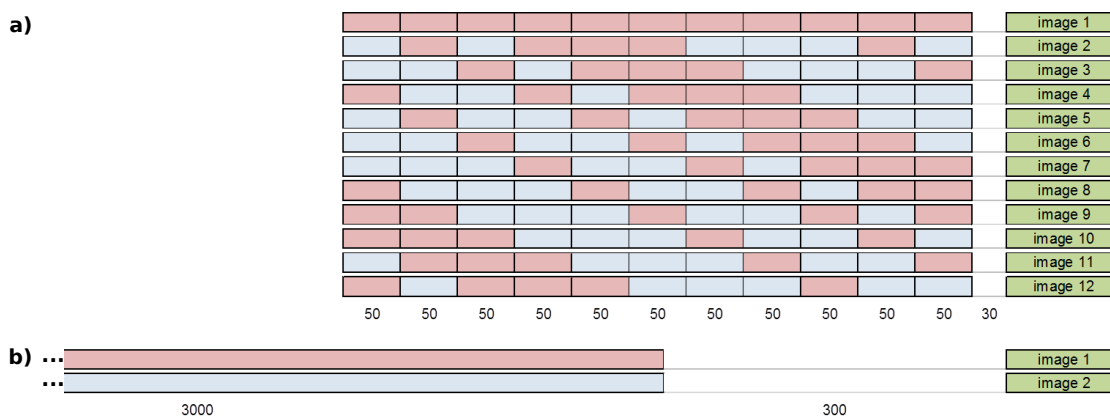


Figure 5.1.: (a) te-pCASL and (b) pCASL labeling schemes. Label (resp. control) sub-boli are represented in red (resp. blue), and the imaging readout in green. The duration of every sub-bolus for te-pCASL was 50 ms and a final PLD of 30 ms was added between the end of the last sub-bolus and the EPI-acquisition. The labeling duration for standard pCASL was 3 s followed by a 300 ms PLD.

post-label delay (PLD) only. Recently, time-encoded labeling schemes have been implemented in rats and men, enabling ATT mapping with higher SNR and lower scan time [Günther, 2007; Wells et al., 2010; Dai et al., 2013; Teeuwisse et al., 2014a]. The basis of this technique is the sub-division of the labeling period into “blocks” or “sub-boli” and the alternation between labeling and control states during the label period in each acquisition. The order of the label and control blocks differs over different acquisitions and is altogether played out as a Hadamard matrix (Figure 5.1). Decoding of the Hadamard matrix enables to calculate perfusion images from the individual blocks of the Hadamard matrix. Thereby, time-encoded ASL provides the possibility to monitor the evolution of the signal over the separate PLDs from which the ATT can be estimated as well as the shape of the label inflow curve. Each individual perfusion image from a sub-bolus provides similar information and SNR as a traditional ASL scan with the same labeling duration, total scan time, TR, and PLD. Since time-encoded ASL allows the measurement of multiple ASL images within the same scan time without SNR penalty, it provides a more effective manner to obtain similar information as in a multi-PLD ASL scan.

In this study, we show that ATT estimation by time-encoded ASL is also feasible in mice. Furthermore, we demonstrate that the sequence is sensitive to mechanically induced ATT changes and that wildtype mice have preserved CBF and ATT up to 25 months of age.

## 5.2. Methods

### 5.2.1. Animals

All experiments were approved by the local ethics committee and were performed in full compliance with the guidelines of the European community (EUVD 86/609/ EEC) for the care and use of the laboratory animals. Experiments were performed under DEC permit 12065 of the Leiden University Medical Center.

Two groups of wild-type (WT) mice were studied: one group of young mice ( $n = 8$ ; 50% female; mean $\pm$ SD age of  $5.8\pm 0.40$  months) and one group of old mice ( $n = 8$ ; 50% female; mean age of  $25.5\pm 1.2$  months). From the group of old mice, two mice (both male) needed to be excluded due to insufficient data quality due to severe movements during the scan. All mice were on a mixed C57BL/6J and C3H/HeJ background, further referred to as B6 C3 mice.

All procedures were performed under isoflurane anesthesia (3.5% for induction, 1.5-2% for maintenance in air:O<sub>2</sub> 1:1). During scans, respiration rate and rectal temperature were monitored and maintained at around 100 bpm and 37°C respectively.

One additional B6 C3 young mouse (6 months old; male) was used for a carotid occlusion experiment to evaluate the sensitivity of the implemented method to measure ATT variations. After anesthesia induction with isoflurane, a medial cut was made along the chest and the left carotid was disjointed from the surrounding mesenchyme. After, a stitch was used to fully occlude the artery. Then the wound was closed and the animal was scanned immediately; the time from wound closure to the first ASL scan was approximately 30 minutes. The animals were not allowed to recover after the experiments and the brains were collected for future experiments.

### 5.2.2. MR sequences and experiments

Experiments were performed in Leiden on a horizontal 7-T preclinical MRI scanner (PharmaScan, Bruker, Ettlingen, Germany) with a mouse transmit-receive 23 mm volume coil. Anatomical T<sub>2</sub>-weighted (T<sub>2w</sub>) images were obtained through a spin-echo sequence (TR/TE = 2500/35 ms, in-plane resolution  $84\times 84\ \mu\text{m}^2$ , 0.7-mm slice thickness, RARE-factor = 8, acquisition time T<sub>acq</sub> = 80 s). Two ASL labeling schemes were implemented: a standard pseudo-continuous ASL (pCASL) labeling scheme [Dai et al., 2008] to measure CBF and a time-encoded pCASL (te-pCASL) labeling scheme optimized for ATT measurements (Fig. 5.1). Both were followed by identical axial single-shot spin-echo EPI acquisitions of the brain (TE = 17 ms, in-plane resolution =  $224\times 224\ \mu\text{m}^2$ , slice thickness 1.5 mm, slice gap 1 mm, three slices with the center of the most posterior slice at approximately -3 mm from the bregma and the middle slice located at the isocenter of the bore). Since pCASL is known to be sensitive to off-resonance effects [Jahani et al., 2011; Luh et al., 2013], the entire study was performed with a global first-order shim

and the pCASL interpulse phase increase was optimized during a prescan as described before (cf. Chapter 4). Labeling pulses were applied in the neck, at 10 mm from the isocenter with the following sequence-specific parameters:

- For pCASL, a label duration of 3 seconds was followed by 300 ms PLD (Figure 5.1b). 60 pairs of label/control images were acquired within 7 minutes (TR = 3498 ms).
- For te-pCASL, a Hadamard-12 matrix was used as labeling scheme (Fig. 5.1a). pCASL RF pulses and gradients were similar to that used in Chapter 4. The duration of every sub-bolus was 50 ms and a final PLD of 30 ms was added at the end of the scheme. This resulted in 11 effective PLDs (30, 80, 130 ... 530 ms). The scheme was repeated 45 times (TR = 778 ms,  $T_{\text{acq}} = 7$  min).

For CBF quantification, maps of the apparent tissue  $T_1$  ( $T_{1\text{app}}$ ) were acquired with an inversion recovery spin-echo EPI sequence (TR/TE = 10000/19 ms, 18 inversion times (TI) between 30 ms and 10000 ms,  $T_{\text{acq}} = 4$  min) and labeling efficiency was measured 3 mm downstream of the labeling plane with a flow-compensated, ASL-encoded FLASH (TR/TE = 225/5.6 ms, 84  $\mu\text{m}$  isotropic in-plane resolution, 1 mm slice thickness, NA = 2,  $T_{\text{acq}} = 3$  min 30 s) for each animal.

### 5.2.3. Post-processing

**Inversion efficiency** The inversion efficiency (IE) was derived from a complex reconstruction of the pCASL-FcFLASH sequence as follows (cf. previous chapters):

$$IE = \left| \frac{M_{C,c} - M_{L,c}}{2M_{C,c}} \right|, \quad (5.1)$$

where  $M_{C,c}$  and  $M_{L,c}$  are respectively the complex signals from the control and the label experiments. A region of interest (ROI) was manually drawn on each common carotid. The inversion efficiency IE was obtained as the mean of the inversion efficiencies measured independently in each of the two carotids.

**Scan registration and brain region delineation** This scan registration step was performed by Artem Khmelinskii (LUMC) as follows.

To compensate for possible motion during standard pCASL and te-pCASL acquisitions, all repetitions were registered to the first EPI acquisition. ROIs for the auditory/visual cortex, hippocampus, motor cortex, sensory cortex, striatum and thalamus were delineated manually on an anatomical  $T_{2w}$  image of a randomly selected animal (reference  $T_{2w}$  image) based on the Franklin & Paxinos mouse brain atlas [Franklin and Paxinos, 2007] (Figure 5.7). The  $T_{2w}$  images of the remaining animals were registered to the above-mentioned reference  $T_{2w}$  and all ROIs were propagated to each

animal’s correspondent  $T_{2w}$  image. For each animal, all sequences (te-pCASL,  $T_{1app}$  map,  $T_{2w}$  images) were registered to the standard pCASL space. The registration of the  $T_{2w}$  images to the standard pCASL space allowed propagating the anatomical ROIs to all the remaining MRI sequences. Two independent observers verified the quality of the registration by visual inspection. The registration was performed using the open source image registration toolbox Elastix [Klein et al., 2010] and was performed in a coarse-to-fine process.

**Tissue  $T_1$  map** The  $T_{1app}$  map was obtained by fitting the following equation to the signal from each pixel using a Levenberg-Marquardt algorithm:

$$M_z(TI) = M_0(1 - 2\kappa e^{-TI/T_{1app}}), \quad (5.2)$$

where  $M_z$  is the MR signal collected at each TI,  $M_0$  is the magnetization at thermal equilibrium,  $T_{1app}$  is the longitudinal relaxation time constant of tissue and  $\kappa$  is the inversion efficiency.  $M_0$ ,  $T_{1app}$  and  $\kappa$  are the fitted parameters.

**ASL maps - te-pCASL post-processing** After averaging the 45 raw te-pCASL-EPI repetitions together, the twelve Hadamard-encoded images were combined to obtain eleven perfusion-weighted images at different PLDs. Buxton’s general kinetic perfusion model [Buxton et al., 1998] was fitted voxel-by-voxel to the ASL signal intensity over time using a Levenberg-Marquardt algorithm, where ATT, CBF and  $T_{1app}$  were the estimated parameters. This perfusion model consists of three parts (Figures 5.3 and 5.4): in the first part, the labeled blood has not arrived yet, therefore the signal intensity is zero. The second part is the rising part of the curve, which represents the inflow of label, while accounting of longitudinal relaxation of the label. During the third and last part, the signal declines, reflecting only relaxation of the label (outflow is neglected in this model). The equation describing the model is provided in Eq. 1.9. To quantify CBF from te-pCASL, the fit’s peak height ( $\Delta M$ ) was retrieved and the CBF was calculated as described below. Voxels that showed very low transit times ( $< 30$  ms) and/or very high longitudinal relaxation rates ( $T_{1app} < 100$  ms), which are expected to mainly reflect voxels largely composed of arterial blood, were excluded when calculating the average values over the ROIs.

**ASL maps - CBF quantification** Assuming that  $M_{0b}$ , the magnetization of arterial blood at thermal equilibrium, may be approximated by  $M_{0t}/\lambda$ , where  $M_{0t}$  is the magnetization of tissue at thermal equilibrium and  $\lambda$  the blood-brain partition coefficient of water (0.9 mL/g [Herscovitch and Raichle, 1985]), we used the following equation to quantify CBF [Alsop et al., 2015; Buxton et al., 1998]:

$$CBF = \frac{\lambda \Delta M e^{\frac{\omega}{T_{1b}}}}{2 IE T_{1app} M_0 (1 - e^{\frac{-\tau}{T_{1app}}})}, \quad (5.3)$$

where  $\Delta M$  is either the peak-height for te-pCASL or the averaged signal difference between control and label acquisitions for standard pCASL;  $T_{1app}$  is the apparent tissue  $T_1$  taken from the  $T_{1app}$  map;  $T_{1b}$  is the longitudinal relaxation time of blood (2230 ms at 7T [Dobre et al., 2007]);  $M_0$  is the magnetization of tissue obtained from the IR experiment's  $M_0$  map. For standard pCASL, we assumed that the arterial transit time was equal to the PLD.

**Statistical analysis** A mixed ANOVA was performed to analyze the effect of age, brain region and the interaction of age and brain region on the measured parameters ATT, CBF measured with te-pCASL and CBF measured with standard pCASL. Since Mauchly's test of sphericity was significant for all of the three parameters, the degrees of freedom for the F-distribution were corrected. The Greenhouse-Geisser-estimate of  $\varepsilon$  was 0.478 for ATT measurements, 0.413 for CBF measurements with te-pCASL, and 0.354 for CBF measurements with standard pCASL. A post-hoc Bonferroni-corrected pairwise comparison was performed when the ANOVA showed that there was a significant difference. All statistical analyses were conducted with the IBM SPSS statistics 23 software.

## 5.3. Results

### 5.3.1. te-pCASL signal time-course

By decoding the Hadamard-encoded ASL signal [Günther, 2007; Teeuwisse et al., 2014a], individual sub-bolus images were obtained from the te-pCASL measurements for each slice (Figure 5.2). At the early time points after labeling, single bright voxels can be seen, indicating the arrival of signal in the larger arteries. Quickly thereafter, the ASL signal arrives in larger groups of voxels, representing the spread of the labeled blood through smaller vessels. Lastly, the signal enters the capillaries and exchanges with the tissue magnetization. On top of these tracer kinetics, the signal continuously decays due to longitudinal relaxation.

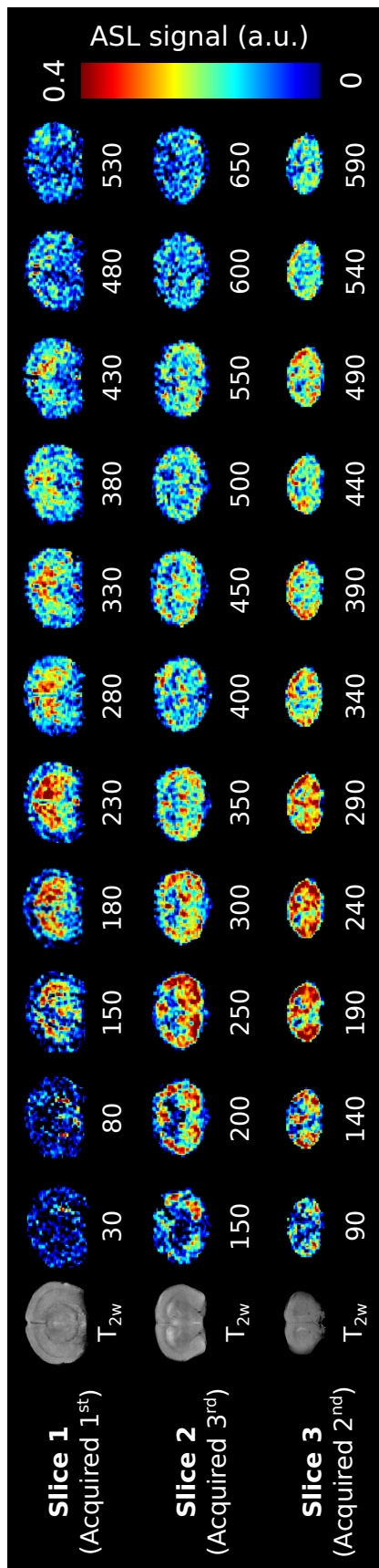


Figure 5.2.: Example of perfusion-weighted images (arbitrary units) obtained after Hadamard-decoding, and the corresponding anatomical images ( $T_{2w}$ ). The number below each map indicates the effective post-labeling delay (PLD) in milliseconds. Note that the slices were acquired in interleaved order (i.e. slice 1 - slice 3 - slice 2).

## 5.3.2. Fit to the te-pCASL data

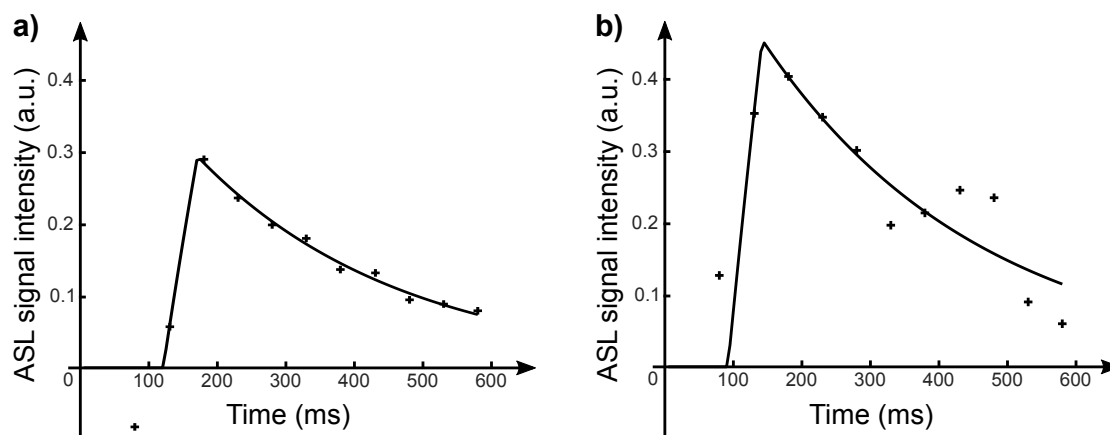


Figure 5.3.: Two examples of the signal intensity (i.e. decoded Hadamard-encoded ASL-signal) time-courses (crosses) with their corresponding model fits (full lines). The two voxels are taken from the same mouse and the same brain region (hippocampus). The estimated parameters for the first voxel (a) are ATT 121 ms, CBF 284 mL/100g/min and  $T_{1app}$  296 ms and the model seems to fit the data. For the second voxel (b), the estimated parameters are ATT 92 ms, CBF 472 mL/100g/min and  $T_{1app}$  319 ms, but the model does not fit the data well.

Figure 5.3 shows examples of the Buxton model fitted to the te-pCASL signal time-course from two individual voxels. The estimated parameters for the first voxel were: ATT 121 ms, CBF 284 mL/100g/min and  $T_{1app}$  296 ms and visual inspection confirms that the model fits the data. For the second voxel, the estimated parameters were ATT 92 ms, CBF 472 mL/100g/min and  $T_{1app}$  319 ms, but visual inspection reveals that the model fits the data poorly, as the measured ASL signal seems to show a second wave of arrival of labeled blood. Figure 5.4a shows the time-courses averaged over all young mice in the auditory/visual cortex and in the hippocampus, which represent the ROIs with highest ( $284 \pm 16$  ms) and lowest ATT ( $169 \pm 11$  ms) respectively. A fit to the experimental data is displayed in the same figure. In Figure 5.4b, these fits are then compared to theoretical Buxton curves, derived from the CBF value from standard pCASL,  $T_{1app}$  from the inversion recovery experiment and the ATT from te-pCASL (from now on referred to as theoretical Buxton curves). In the hippocampus, the  $\Delta M$  values from te-pCASL reach markedly higher values than the  $\Delta M$  from the theoretical Buxton curves. In contrast, in the auditory/visual cortex, the  $\Delta M$  values from both curves reach about the same height. In both brain regions, the decay after the peak is faster in the te-pCASL data than in the theoretical Buxton curves: mean decay values retrieved from the fit to the te-pCASL data are between 300 ms and 500 ms instead of the 1600-1700 ms measured with the IR sequence.

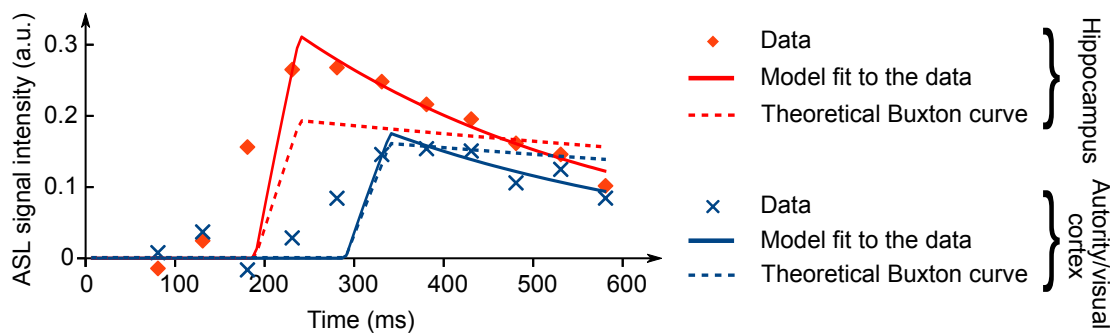


Figure 5.4.: Signal time-courses of the ASL signal. *te*-pCASL  $\Delta M$  values in the sub-boli are averaged over all young mice for two brain regions (crosses) and displayed together with the fit to the data (full lines). Dashed lines represent theoretical Buxton curves with CBF values from standard pCASL,  $T_{1app}$  values from the inversion recovery experiment and ATTs from *te*-pCASL. The auditory/visual cortex are depicted in blue and the hippocampus in red.

### 5.3.3. ATT and CBF maps

Figure 5.5 shows the CBF and ATT maps of a representative mouse. Next to the CBF maps determined with *te*-pCASL (second row), maps acquired with standard pCASL are also shown (first row). In both CBF maps, a clear contrast is observed between grey and white matter (corpus callosum), with grey matter showing higher values. However, it can also be noticed that CBF values are higher in the *te*-pCASL measurement as compared to those measured with standard pCASL.

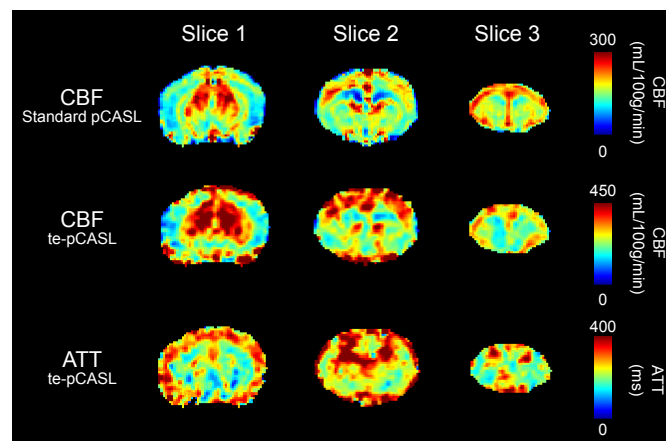


Figure 5.5.: CBF maps obtained in one mouse (3 slices) with a standard pCASL acquisition (first row) and a voxel-by-voxel fit to the *te*-pCASL data (second row). Note the difference in color scale. The third row shows the ATT as obtained from *te*-pCASL.

### 5.3.4. Effect of left carotid occlusion

Both the ATT and the CBF maps measured in the mouse with a left carotid occlusion are affected by the occlusion (Figure 5.6). When comparing the ROIs drawn in the hemisphere ipsilateral to the occlusion with their respective contralateral ROIs, ATT was found to be slightly increased (11% on average), whereas CBF was markedly lower (47% for standard pCASL CBF and 33% for te-pCASL CBF on average).

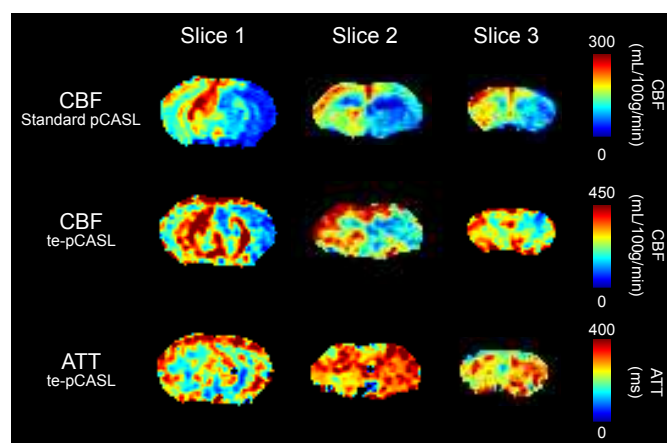


Figure 5.6.: CBF maps from standard pCASL (first row) and from te-pCASL (second row) and ATT maps (bottom row) obtained on a mouse with a left carotid occlusion (3 slices). Note that the images are represented in radiological convention.

### 5.3.5. Effects of age and brain region on ATT and CBF

No significant effects of age were observed for the ATT ( $F [1,12] = 0.056$ ), the CBF measured with te-pCASL ( $F [1,12] = 0.220$ ) nor for the CBF measured with standard pCASL ( $F [1,12] = 0.484$ ) (Figure 5.7).

A significant effect of the brain region on ATT,  $p < 0.001$  ( $F [2.388, 28.658] = 92.335$ ) was found, with 22 out of the 30 post-hoc brain region comparisons showing statistically significant differences. No additional effects of interaction between age and brain region were observed on the ATT ( $F [2.388, 28.658] = 0.264$ ), te-pCASL CBF ( $F [2.064, 24.768] = 0.399$ ) or standard pCASL CBF ( $F [1.770, 21.237] = 0.454$ ).

### 5.3.6. te-pCASL CBF versus standard pCASL CBF

CBF estimations as measured with the te-pCASL and the standard pCASL sequences in all the 14 animals and all the brain regions were compared in a Bland-Altman plot. The te-pCASL sequence shows a consistently higher estimated CBF than the standard pCASL sequence (Figure 5.8). Furthermore, the difference between the two measurements increases with the mean CBF value.

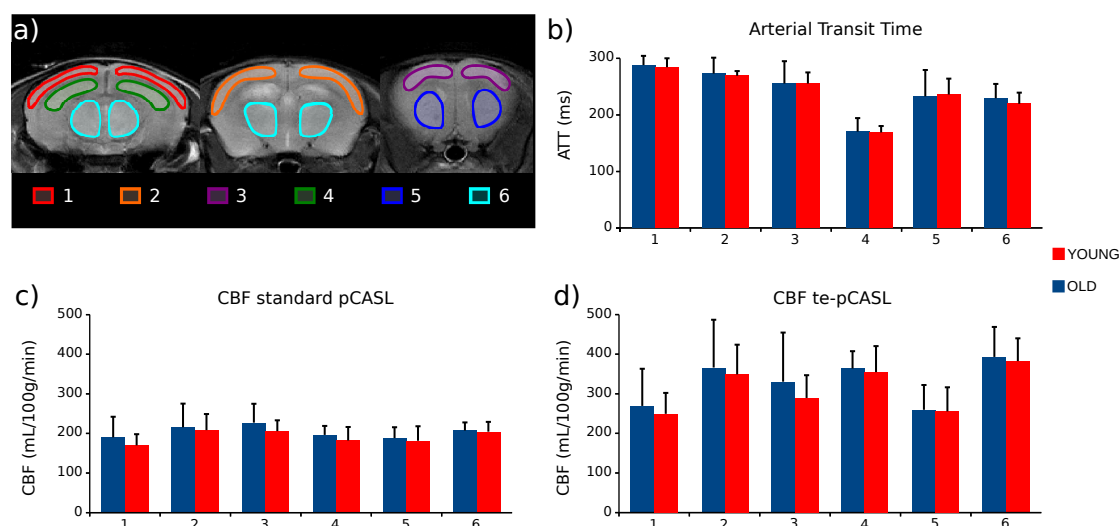


Figure 5.7.: (a) Example of anatomical  $T_{2w}$  images with ROIs: 1- Auditory/visual cortex, 2- Sensory cortex, 3- Motor cortex, 4- Hippocampus, 5- Striatum, 6- Thalamus. (b) Comparison between young (red) and old (blue) mice in different brain regions for ATT, (c) CBF from standard pCASL and (d) CBF from te-pCASL. Bars show mean values  $\pm$ SD.

## 5.4. Discussion

This study demonstrated that the implementation of a time-encoded ASL approach enables ATT measurements in mice. Since inflow times in the mouse brain are short and the brain regions are small compared to human anatomy, high spatial and temporal resolutions are required, which severely limits the perfusion signal-to-noise ratio (SNR). The above described te-pCASL sequence was optimized to keep a balance between spatial resolution, temporal resolution and perfusion SNR. The high amount of averaging was a prerequisite for this trade-off (note that one Hadamard scheme is already equivalent to 6 averages of standard multi-PLD pCASL performed with a label duration equal to the sub-bolus duration [Günther, 2007]). This also made it preferable to split the perfusion imaging and the ATT measurement into two separate sequences. A “free-lunch-approach” in which ATT-measurement blocks are played out during the PLD of a traditional pCASL scan would either lead to too low SNR for the ATT measurement to allow accurate ATT measurements or to too long scan times.

The measured ATT values were different across brain regions. Average ATT values in young mice varied from 169 ms (hippocampus) to 284 ms (auditory-visual cortex). To the best of our knowledge, only one other study acquired Hadamard-encoded ASL-MRI data in animals, which were obtained with CASL in rats [Wells et al., 2010]. In that study, ATT was measured in cortical regions of three rats to be between 190 and 310 ms. The values from the time-encoded sequence and those from the multi-PLD CASL sequence acquired in the same animals were well in accordance with each other.

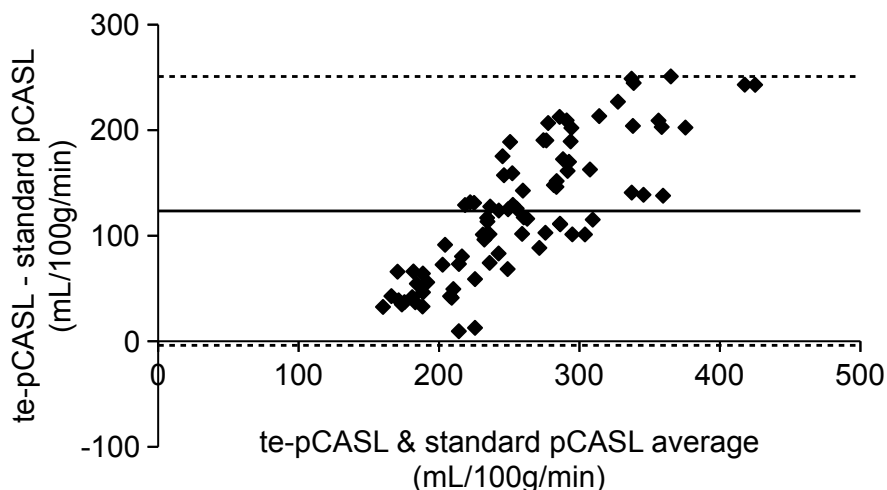


Figure 5.8.: Bland-Altman plot comparing CBF values from te-pCASL and standard pCASL. All 14 animals and all the brain regions are represented. The central line represents the mean of all values and the two dashed lines are offset by  $2\pm\text{SD}$  from that mean.

In an earlier study, ATT estimates for the whole rat brain measured with multi-PLD ASL in a group of 12 rats ranged from 100 to 500 ms [Thomas et al., 2006]. Using a dynamic ASL scheme (DASL), another study reported ATT values in rats of around 200 ms [Barbier et al., 2001b]. Also, a pCASL optimization study in mice, which may not have been intended to estimate ATT, does provide a rough estimation of ATT in mice [Duhamel et al., 2012]: the authors optimized a pCASL sequence by varying several parameters settings, including the PLD, and analyzed the resulting SNR in the perfusion images. Regarding the PLD, they concluded that it ideally should be between 200 and 400 ms, since the perfusion signal is highest between these points. Hence, the values found in this study are in agreement with previously reported ATT values.

Furthermore, the animal with a unilateral carotid occlusion showed increased ATTs in the ipsilateral hemisphere, suggesting on the one hand that the sequence is capable of capturing ATT changes due to macrovascular pathologies. On the other hand, the ATT difference between the ipsilateral and contralateral hemispheres was not very large (11%), especially compared to the major difference in CBF measured in the same scans. It can thus be questioned whether ATT measurements in mice would be suitable to detect milder pathology, such as partial occlusion, or increased vessel tortuosity with the setup used in this study.

In all mice, cortical regions showed longer transit times than subcortical regions. This is consistent with the anatomy of the murine cerebral circulation Dorr et al. [2007] (Fig. 5.9 and Fig. 1.17). The major blood supply of the murine cerebrum comes from the internal carotid arteries, which end in the circle of Willis, located ventrally to the brain. From there, several arteries sprout, which supply blood to the different brain

regions. Subcortical tissue is supplied with blood through arteries such as the posterior cerebral artery (PCA) and the anterior choroidal artery (AchA), which directly penetrate the brain tissue from the circle of Willis. The mouse cerebral cortex on the other hand, is mostly supplied by the anterior and middle cerebral arteries (ACA and MCA respectively), which first curve around the cerebrum before they penetrate the brain tissue. In the posterior part of the cerebrum, this cortical-subcortical difference is the most profound. The posterior parts of the cortex is fed by the most distal parts of the ACA and MCA, which wrap around the frontal and medial cortex. On the other hand, the PCA and AchA penetrate directly into the subcortical regions in the posterior part of the cerebrum, with a much smaller distance to the internal carotids. This could explain the large difference in ATT between the cortical and subcortical regions on the most posterior slice in Figure 5.5. Furthermore, it could explain the fact that the hippocampus, located posteriorly and subcortically, showed the lowest transit times from the regions analyzed in this study (Fig. 5.7b). It would be of interest to image perfusion territories in mice using ASL to confirm our analysis of ATT distributions across brain regions.

In all six brain regions analyzed, the mean ATT was smaller than 300 ms. This indicates that the PLD-choice of the standard pCASL, 300 ms, was appropriate to reduce contamination of the ASL signal from the major arteries and to limit the sensitivity of pCASL to ATT heterogeneity [Alsop and Detre, 1996]. However, on the microscale (arterioles, capillaries, parenchyma and venules), it remains elusive in which compartment the label resides at the moment of detection, both for the CBF measured with standard pCASL, as well as for CBF measured with te-pCASL. At the chosen PLD of 300 ms, smaller vessels may still contain labeled blood that ultimately moves on to perfuse tissue in a different voxel. Previously, distinctions have been made between vascular and tissue transit times [Alsop and Detre, 1996; Wang et al., 2003]. The te-pCASL sequence used here was optimized to see the inflow-phase of the label, and thus corresponds to the aforementioned vascular transit time. Due to the fact that ATT is mainly influenced by the macro-vasculature, measurement of the *tissue* transit time may provide additional useful information on the microvascular status. The exact definition of tissue transit time, whether it indicates arrival of labeled spins in the extravascular space, in the capillaries or in the microvasculature that only feeds tissue located within a distance smaller than the size of an imaging voxel, varies among studies. In order to measure transit times to the microvasculature, vascular crushers can be used to crush the signal coming from flowing spins in the arteries just before the imaging read-out [Ye et al., 1997] with the strength of the crushers determining how far down the vascular tree the ASL signal is suppressed. However, this approach further lowers SNR, as part of the perfusion signal is also attenuated due to the diffusion-weighting of the crushers. Another method exploits the measurement of the T2 of the ASL signal, since the T2 of the

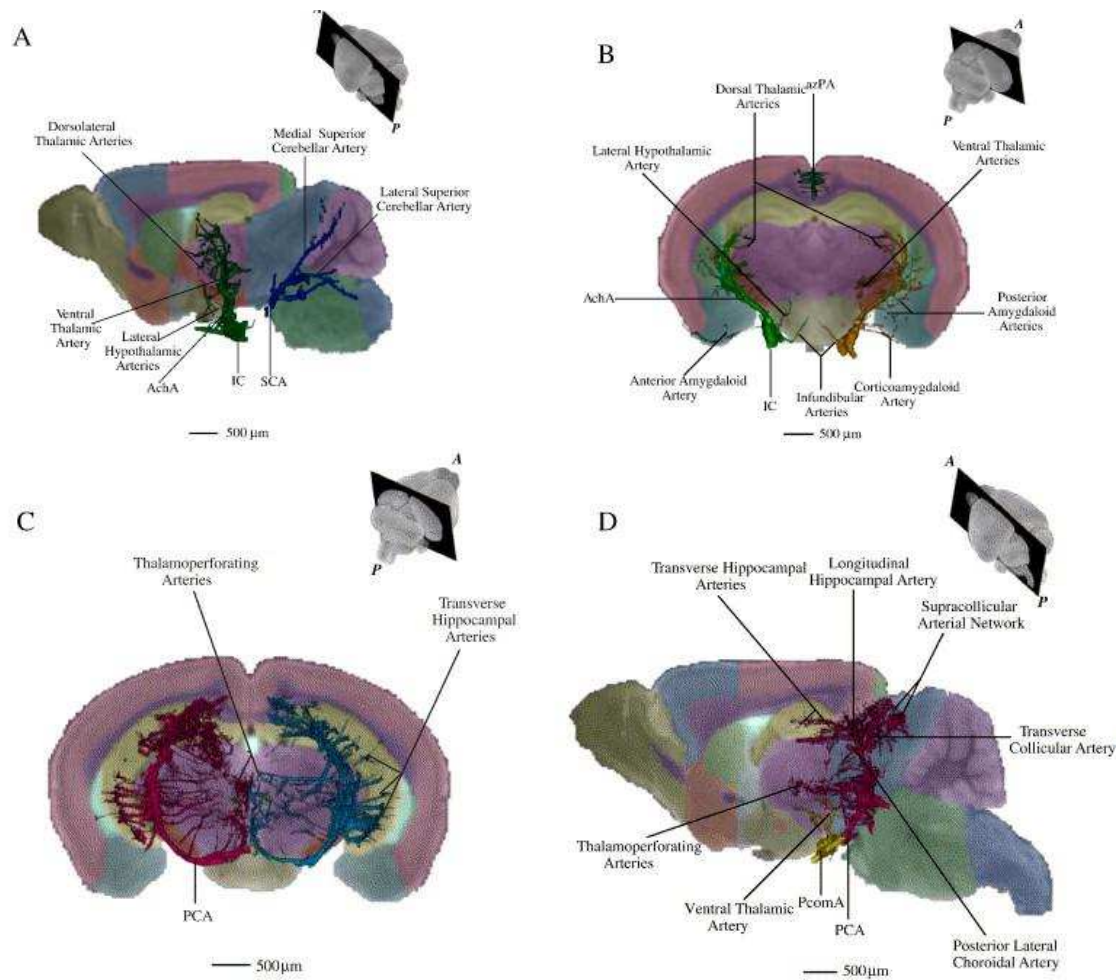


Figure 5.9.: Internal carotid (IC), superior cerebellar artery (SCA), posterior cerebral artery (PCA) and their branches superimposed on slice planes at or near the anatomical location of the artery of interest, where slices were chosen to best show the majority of the artery. Inserts represent the level at which the slice of interest was taken. From Dorr et al. [2007].

label depends on whether it is intra- or extravascular [Wells et al., 2009; Liu et al., 2011; Wells et al., 2013; Schmid et al., 2015]. This approach has the potential to distinguish between labeled spins in vascular and extravascular spaces, but has to deal with the difficulties inherent in separating the components in biexponential transverse relaxation signals. In rats, the measured transit time of labeled spins to the extravascular space was about  $370 \pm 40$  ms longer than the ATT [Wells et al., 2013], providing a ballpark estimate of what could be expected in mice. The transit time to the moment labeled spins arrive in vessels that are small enough to only feed local tissue, which would be the time of interest to choose the PLD, is likely situated between the ATT measured here and this tissue transit time.

The te-pCASL sequence may be improved in several ways. Tissue transit times are

longer than the longest effective PLD used in the te-pCASL labeling scheme of this study. It might therefore be useful to adapt the temporal encoding scheme to cover later time points. Furthermore, given the low SNR of the te-pCASL measurements in mice, the te-pCASL sequence should probably be adapted in combination with higher field strengths and/or more sensitive receive coils in order to measure tissue transit times. A second technical limitation of the current sequence was the limited number of slices (three). This was caused by the long readout time per slice: extending the number of imaging slices to four (or more), would result in poor determination of the ATT in the additional slices, since the label would already have arrived. This limitation can be overcome by using a 3D readout, a multiband readout, or stronger and faster gradients. In Appendix B.3, we show first results of ATT and CBF maps obtained in mice with a time encoded ASL 3D-EPI scan with a dynamic ASL (DASL) labeling scheme.

The ASL signal of the te-pCASL data decreased faster than the  $T_{1app}$  measured with the inversion-recovery (IR) sequence. This is also the reason why CBF values from the te-pCASL experiment were quantified from the fit's peak height ( $\Delta M$ ), instead of directly using the CBF value provided by the fit. There may be explanations at both sides of the signal profile from the te-pCASL data. Since the te-pCASL sequence is optimized to see the inflow-phase of the label, it will be contaminated by vascular signal. This may lead to higher values at the early part of the signal profile. This explanation is supported by Figure 5.3b and Figure 5.4. In Figure 5.3b, the first peak most probably represents the passage of a bolus through arteries feeding more distal brain regions, whereas the second peak would represent true perfusion of the voxel, identical to what has been described by Chappell et al. [2010]. Nevertheless, after averaging signals across voxels in the cortical ROI and across animals this pattern was not visible anymore (Figure 5.4), and thus further research is necessary to document these effects. Moreover, a higher signal was measured in the hippocampal ROI for the earlier time-points after labeling for the te-pCASL data (Figure 5.4). Labeled spins detected in these time-points may be located in the larger vessels that surround and penetrate the hippocampus [Dorr et al., 2007], but may go on to perfuse a different voxel in the later time-points. The signal in the auditory/visual cortex, containing less of these large vessels, show comparable peak signal in the te-pCASL data curve and the theoretical Buxton curve, which was obtained from the traditional pCASL perfusion scan.

At the late part of the time profile of the te-pCASL signal, there may be influence by venous outflow, which was not taken into account in this study. Underestimation due to venous outflow becomes of particular importance with high blood flow [Parkes and Tofts, 2002] and high blood  $T_1$  [Dobre et al., 2007]. In humans, this may be less of a problem than in rodents, which have higher CBF and are imaged at higher magnetic fields with therefore prolonged blood  $T_1$ . In rats, using a multi-TI FAIR approach, significant outflow of labeled blood from the imaging slice leading to accelerated ASL

signal decrease was shown for CBF values higher than 100 mL/100g/min [Wegener et al., 2007]. In a previous DASL study in rats, the authors also measured higher CBF and faster signal decay in voxels containing mostly arterial signal Barbier et al. [2001b].

The different designs of the standard pCASL and the te-pCASL sequence ultimately resulted in differences between the measured CBF values, which can probably be explained by the above described vascular artefacts and venous outflow. Additionally, it should be noted that the standard pCASL sequence, with its long labeling duration (3 s), may be particularly sensitive to the outflow effect, especially in regions with high flow rates. This may lead to underestimation of the CBF and can be an additional explanation for the different CBF values between standard pCASL and te-pCASL.

The labeling durations in the te-pCASL and standard pCASL sequences differed to a great extent: 50 ms versus 3000 ms. This resulted in a large raw ASL signal difference between the te-pCASL data and the standard pCASL data: Figure 5.10 shows a comparison of the ASL signals measured with te-pCASL and with standard pCASL. The mean ASL signal obtained in the hippocampus of one mouse after Hadamard decoding of the te-pCASL images is represented (green diamonds) and the corresponding fit to the data is drawn in pink. To compare, the ASL signal obtained after control-label subtraction of standard pCASL (blue star) is shown on the same graph. The black line represents how the signal evolution would have been with a CBF value of 181 mL/100g/min (i.e. the CBF value measured with standard pCASL in this particular region), an ATT of 140 ms (i.e. the ATT value obtained from te-pCASL in this particular region) and a  $T_{1app}$  of 1.6 s (i.e. from the inversion recovery  $T_{1app}$  map). The signal intensity difference yielded by the two methods can be clearly observed; Standard pCASL yields signal around 24 times higher than te-pCASL. Noisy MRI data can be biased by the Rician distribution of the noise, but when the SNR is higher than 2, the noise distribution is nearly Gaussian [Gudbjartsson and Patz, 1995]. Therefore, to ensure that the te-pCASL signal is not subjected to a noise dependent bias, we quantified the noise in the decoded Hadamard images. The whole-brain average ASL SNR was higher than 2 for all time-points after arrival of the label (data not shown), which allows to confirm the normal distribution of decoded te-pCASL data. This implies that the ATT as obtained by fitting the Buxton-model can be trusted, even though the SNR of decoded te-pCASL data ( $<5$ ) was much lower than that of standard pCASL data ( $\sim 38$ ). Another improvement that could be made is to fit a Buxton model extended with dispersion of the blood arrival times [Hrabe and Lewis, 2004]. This would probably lead to a better fit of the rising part of the curve.

With aging, CBF in the human brain has been shown to decrease, also with imaging modalities different from MRI [Leenders et al., 1990; Pagani et al., 2002; Liu et al., 2012; Maier et al., 2014]. In case of neurological disease, such as Alzheimer's disease, CBF is even further reduced [Wolk and Detre, 2012]. Even though the evidence is less strong, both vascular and tissue transit times have been shown to increase with age [Liu et al.,

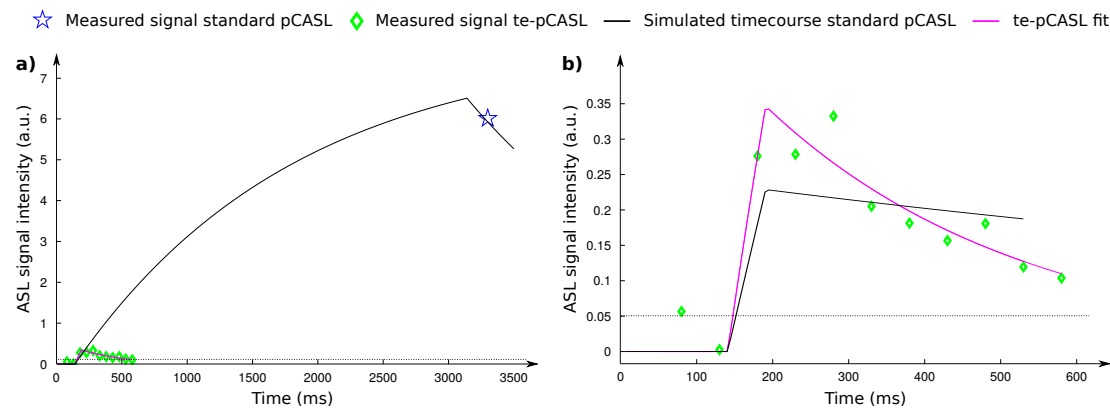


Figure 5.10.: (a) Mean hippocampal ASL signal from standard pCASL (blue star) and ASL timecourse measured with time-encoded pCASL (green diamonds) in one mouse. The fit to the te-pCASL datapoints is plotted in pink. The black line represents how the signal evolution would have been with a CBF value of 181 mL/100g/min (i.e. the CBF value obtained with standard pCASL in this particular region), an ATT of 140 ms (i.e. the ATT value obtained from te-pCASL in this particular region) and a  $T_1$  of 1.6 s (i.e. from the inversion recovery  $T_{1app}$  map), for a label duration of 3 s in panel (a) and 50 ms in panel (b). (b) Zoom in on the 600 first milliseconds of panel (a). The noise level (standard deviation of the noise) measured in a region outside the brain (without artifacts) is represented with dashed lines for standard pCASL on panel (a) and for te-pCASL on panel (b).

2012]. It has already been reported that CBF in WT mice is maintained, as opposed to several mouse models of neurological disease which do show decreased CBF with age [Maier et al., 2014]. Our experiments also did not show an effect of aging on the CBF in WT mice. Additionally, our results indicate that ATT is also preserved with aging in WT mice. Therefore, in future studies it might be of interest to investigate whether there is an age-dependent change in the ATT in mouse models of neurological disease.

## 5.5. Conclusion

This study shows the successful implementation of te-pCASL in mice. For the first time, ATT was measured in mice and changes in ATT as a function of age were assessed. No differences were found in CBF or in ATT between old (25 months) and young (6 months) mice. te-pCASL and standard pCASL CBF values were different, probably due to a vascular contribution and the venous outflow of labeled spins.



## **6. SAR comparison between CASL and pCASL at high magnetic field.**

### **Evaluation of the benefit of a separate labeling coil.**

This chapter is dedicated to evaluate MR safety when using ASL in rats at 9.4 T, and more specifically heating induced by the CASL and pCASL sequences. To this end, temperature probes were implanted at three different locations in the rat and the induced heating during ASL scans was measured. The benefit of a dedicated labeling coil was evaluated as well. A manuscript is in preparation.

#### **6.1. Introduction**

Arterial spin labeling (ASL) is an MR method that enables non-invasive, non-ionizing cerebral blood flow (CBF) measurements without any injection of contrast agents. Its recommended implementation for clinical applications is pseudo-continuous ASL (pCASL), a method based on the application of short rapidly repeated RF pulses to imitate a long continuous RF pulse [Alsop et al., 2015]. In rodents, the use of continuous arterial spin labeling (CASL), where a long continuous RF pulse is used to label the blood, or flow-sensitive alternating inversion recovery (FAIR), where blood is labeled by means of a single short adiabatic pulse, is more common, since pCASL is not a commercially available technique on preclinical systems. Long labeling pulses, in (p)CASL, have the advantage of producing higher perfusion SNR [Chen et al., 2011] and therefore facilitate CBF measurements, especially in pathological cases, where CBF may be low. However, the application of long labeling RF pulse trains makes (p)CASL prone to produce heat in the imaged subject, especially at higher magnetic fields. Heating may not only lead to safety concerns but may also bias the results obtained. Heating in itself impacts the blood flow [Wang et al., 2014; Masuda et al., 2011]. Moreover, in some diseases, such as traumatic brain injury (TBI), stroke or subarachnoid hemorrhage, cerebral temperature increases have shown important impacts on the brain function and may worsen the patient's outcome as a consequence [Mrozek et al., 2012; Busto et al., 1989]. Therefore, temperature fluctuations should be taken into account when using ASL for long scanning

periods or with diseased animals.

Heating due to RF exposure is characterized by the specific absorption rate (SAR, in W/kg, cf. section 1.5.2). The SAR distribution is not homogeneous in the considered subject and depends on various parameters such as the subject's geometry, its composition (tissue type), its localization in the RF field, the RF coil's properties and the MR field strength. Its amplitude depends furthermore on the applied labeling  $B_1$  amplitude. Phantoms and numerical simulations are used to assess heating in humans, for whom MR safety is an important topic. Clinical scanners have built-in SAR restrictions for patient safety reasons: if the estimated SAR exceeds a given threshold, the sequence does not start or sequence parameters are automatically adjusted to meet the limits. Such tools are however not routinely available on preclinical scanners, even if the latter usually present higher magnetic fields and work with higher  $B_1$  amplitudes, and may therefore induce as much or more RF heating despite the much smaller sample size.

Animal phantoms<sup>1</sup> may be used to simulate SAR in animals. However, precise knowledge of the coil's design is needed as well and additional steps to integrate it in the simulation are required. MR thermography is a technique yielding temperature maps and is commonly used for real-time thermal dose monitoring during thermal therapies (e.g. tumor ablation) [de Senneville et al., 2007]. However its ability to accurately measure smaller temperature variations (i.e.  $< 1^\circ\text{C}$ ) remains limited. Moreover, simultaneous acquisition of temperature monitoring by means of MR-thermography and of ASL scans requires specific sequence programming and optimization.

In this study, we addressed SAR issues in animals simply by measuring temperature fluctuations *in situ*, i.e. by implanting fiber-optic temperature probes. This method is of course invasive but is a robust way to estimate RF heating without making any assumptions on the coil's or system's design and takes into account all possible heating sources. SAR has never been measured in rats during ASL sessions. Here we investigated the heating induced by CASL and pCASL sequences *in vivo* at 9.4 T for different labeling  $B_1$  amplitudes and evaluated the benefit of a dedicated labeling coil.

## 6.2. Methods

### 6.2.1. Animals

A total of twelve rats (Sprague Dawley male rats,  $231 \pm 29$  g, Charles Rivers, France) were used. All experiments were approved by the local ethics committee and were performed in full compliance with the guidelines of the European community (EUVD 86/609/ EEC) for the care and use of the laboratory animals. Experiments were performed under permits (n°380945 for EB and A3851610008 for experimental and animal care facilities)

---

<sup>1</sup>[www.itis.ethz.ch/virtual-population/animal-models](http://www.itis.ethz.ch/virtual-population/animal-models)

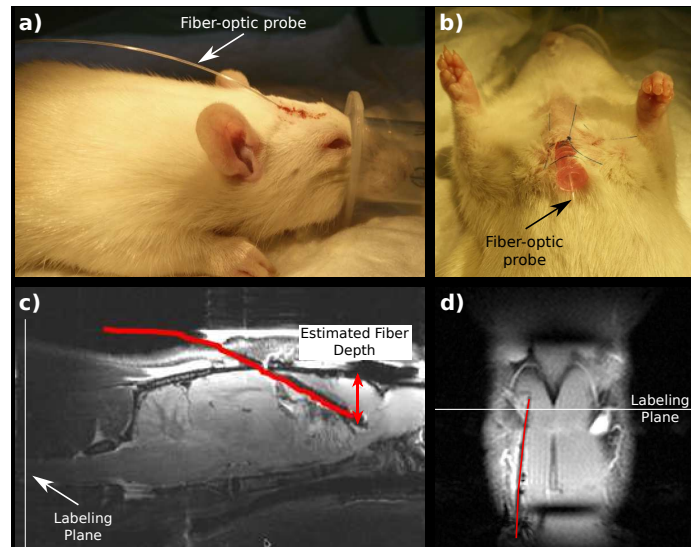


Figure 6.1.: Example of the temperature probe position in the brain (a) and at the carotid level (b). Top row: before installing the animal inside the MR scanner. Bottom row: T2-TurboRARE (left) and FLASH (right) MR images.

from the French Ministry of Agriculture. All procedures were performed under isoflurane anesthesia (IsoFlo, Axience, France, 5% for induction, 2% for maintenance). Respiration rate, heart rate, oxygen saturation were monitored and maintained within the following ranges: 40-60 breaths per minute, 400-500 beats per minute and 98-100% respectively. Temperature was monitored and measured in the animals as follows:

- To measure the heating induced by the applied MR scans, the temperature was continuously measured using fiber-optic temperature probes (model FTP-LTF2-ST-10M, Photon Control, Burnaby, BC, Canada; diameter: 650  $\mu\text{m}$ ; sampling frequency of 10 Hz) implanted at three different locations: (i) inside the brain, (ii) subcutaneously near the labeling plane (between carotids) and (iii) in the rectum (Fig. 6.1). This experiment has been performed in nine rats.
- Three additional rats were used to measure the inversion efficiency of the different sequences (cf. MR experiments subsection). In these animals, the rectal temperature was monitored with a rectal probe and maintained between 36 and 37  $^{\circ}\text{C}$ .

To globally maintain the animal's body temperature, hot water was circulating in the holder, under the animal's body. The rat's head and its neck were outside of the heating range.

### 6.2.2. MR experiments

Experiments were performed on a horizontal 9.4 T scanner (Bruker Biospec, AVIII-HD), using 3 RF coils:

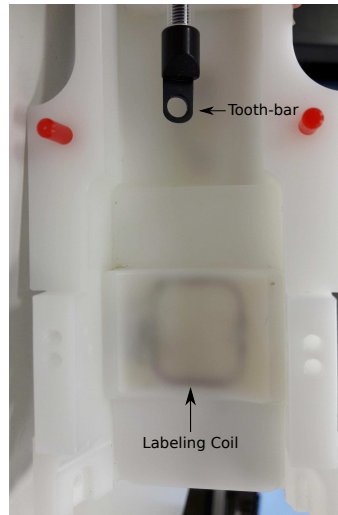


Figure 6.2.: Labeling coil (top view) installed in the rat cradle.

- a transmit-receive volume coil (86 mm inner diameter) for imaging and labeling,
- a receive-only surface phased-array, (4-channel) rat head coil,
- a Bruker prototype of a transmit-receive single loop ASL coil (diameter 23 mm) placed under the animal's throat for labeling (Fig. 6.2). The position of the coil can be manually adjusted in the head-foot direction.

#### 6.2.2.1. *In vivo* temperature measurements

This first experiment was performed on nine rats. Each scanning session consisted of several parts: the session started with adjustments and anatomical scans. The second and longest part consisted of 12 ASL scans with different parameters, each of them followed by the same CBF measurement (CASL<sub>Perfusion</sub>) and a pause. For some animals, ASL scans without RF emission during labeling were acquired as well. During the final part, two additional ASL scans were acquired to evaluate the reproducibility and two anatomical scans were performed to localize the temperature probe. Per animal, the total scan session lasted about 350 minutes. At the end of the session, the rats were euthanized. These scans are now described in detail.

**Adjustments and anatomical scans** At the beginning of the scanning session, the following scans were performed:

- Standard adjustments: volume coil tuning and matching, basic frequency adjustment, standard global first order shim, volume coil RF pulse power calibration and  $B_1$  maps to adjust the ASL coil reference power.

- FLASH scans to visualize the fiber-optic probe's position in the carotids (TR/TE = 120/1.6 ms, resolution 0.195x0.195x0.8 mm<sup>3</sup>, number of averages (NA) = 2, acquisition time T<sub>acq</sub> = 31 s, 20 slices),
- Anatomical axial T2-weighted (T<sub>2w</sub>) images acquired through a spin-echo T2-TurboRARE sequence (RARE factor 8, TR/TE = 3139/33 ms, resolution 0.137x0.137x0.8 mm<sup>3</sup>, NA = 2, T<sub>acq</sub> = 3 min 21 s, 30 slices).

**RF heating during ASL scans** During this second part, four sets of ASL experiments were performed:

- pCASL-EPI sequences using the volume RF coil for labeling (called "pCASL<sub>vol</sub>")
- pCASL-EPI sequences using the ASL coil for labeling (called "pCASL<sub>lab</sub>")
- CASL-EPI sequences using the volume RF coil for labeling (called "CASL<sub>vol</sub>")
- CASL-EPI sequences using the ASL coil for labeling (called "CASL<sub>lab</sub>").

Within each set of experiment, a range of mean label B<sub>1</sub> amplitudes (B<sub>1ave</sub>) was applied: 3, 5 and 7 μT, resulting in 12 individual ASL-scans. These 12 individual ASL-scans were performed in random order. The RF power during the control experiment was turned off for the CASL<sub>lab</sub> and pCASL<sub>lab</sub> scans, since the ASL coil induced no magnetization transfer (MT) effects in the imaged slice.

All labeling pulses were applied in the neck (at 2 cm from the isocenter) during  $\tau = 3$  s followed by a 300-ms post-labeling delay ( $\omega$ ) and a single-shot spin-echo echo-planar imaging (EPI) acquisition (TE/TR = 22/4000 ms, in-plane resolution 234 x 234 μm<sup>2</sup>, one 1-mm thick slice) performed with the volume coil as transmit and the surface array coil as receive. 30 pairs of label/control images were acquired within 4 minutes.

pCASL labeling pulse trains consisted of 400-μs Hanning window shaped RF pulses repeated every 800 μs. G<sub>max</sub>/G<sub>mean</sub> were set to 45/5 mT/m. The CASL gradient was 10 mT/m.

**CBF measurements** To measure CBF over time while avoiding any possible bias due to different inversion efficiency (IE) values, a short 5-μT CASL<sub>lab</sub> scan (called "CASL<sub>Perfusion</sub>", T<sub>acq</sub> = 2 min 40 s) was acquired repeatedly during the imaging session:

- once at the beginning of the scanning session (baseline) before the axial T<sub>2w</sub> scan,
- after the axial T<sub>2w</sub> scan,
- after each of the 12 individual ASL scans,
- after the 3- and 5 μT pCASL<sub>vol</sub> scans repeated at the end of the scanning session (cf. below).

Labeling and imaging parameters for CASL<sub>Perfusion</sub> were identical to the previously described ones, besides the number of slices which was increased to 5 contiguous slices for a better brain coverage and the number of label/control pairs which was reduced to 20 to limit total acquisition time.

Each CASL<sub>Perfusion</sub> scan was followed by an 8-minute cool-down pause.

**B<sub>1ave</sub> = 0  $\mu$ T ASL scans** In three animals, additional ASL-scans were performed without emitting RF during labeling ( $B_{1ave} = 0 \mu\text{T}$ ). In order to evaluate any potential impact of the rapid gradient switching during labeling on the temperature, some of them were acquired twice, i.e. with and without labeling gradients. CASL<sub>Perfusion</sub> scans were acquired with a  $B_{1ave}$  of 0  $\mu\text{T}$  as well, to evaluate the impact of the EPI readout on the temperature: during CASL<sub>Perfusion</sub>, 5 slices are acquired compared to 1 during the other ASL scans. Not all of these scans were acquired in all three animals.

**Reproducibility and anatomical scans** To evaluate the reproducibility, the 3- and 5  $\mu\text{T}$  pCASL<sub>vol</sub> scans were repeated at the end of the scanning session. The second 5- $\mu\text{T}$  pCASL<sub>vol</sub> scan lasted 20 minutes (150 label/control pairs) to evaluate the temperature behavior during longer labeling sessions.

At the end of the scanning session two additional sagittal and coronal anatomical T<sub>2</sub>-TurboRARE scans were acquired to measure the fiber-optic probe's position in the brain. MR parameters for these sagittal (resp. coronal) anatomical scans were the same as for the first T<sub>2w</sub> axial scan, besides TR = 3202 ms, T<sub>acq</sub> = 3 min 24 s and the number of slices that was reduced to 21 (resp. 19).

#### 6.2.2.2. Inversion efficiency measurements

Inversion efficiency was measured in 3 additional animals 5 mm downstream of the labeling plane with a flow-compensated, ASL encoded FLASH sequence for each ASL labeling scheme, each coil setup and  $B_{1ave}$  values of 1.5, 3, 5 and 7  $\mu\text{T}$ . Both label and control interpulse phases were optimized prior to the pCASL IE measurement (cf. Chapter 4). The volume (resp. labeling) coil was used to receive the MR signal in (p)CASL<sub>vol</sub> (resp. (p)CASL<sub>lab</sub>).

#### 6.2.2.3. Coil temperature measurements

RF coils that are present but not used at a given time during the MR sequences are actively decoupled from the other coils using a decoupling circuit. This is notably the case for coils that are not used during transmission of the RF labeling pulses: the volume transmit and surface receive coils during labeling with the ASL coil and the ASL and surface receive coils during labeling with the volume coil. Due to the very long duration of the labeling periods in ASL, the decoupling circuit itself may induce non-negligible

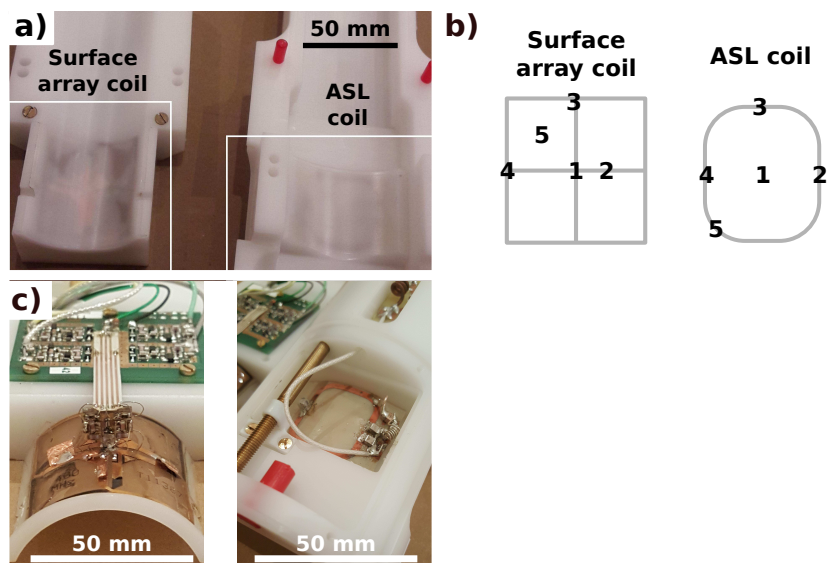


Figure 6.3.: (a) Setup of closed coils and (b) corresponding illustrations with locations of the fiber-optic probes to measure temperature variations. (c) Zoomed images of opened surface array head coil (left) and labeling coil (right). Note that the coils are flipped around after housing opening.

heating. To investigate the heating induced in absence of RF emission, i.e. only during the coils' decoupling, local thermometry at five locations and thermal imaging (FLIR Systems, AB FLIR B60) was performed directly on the phased-array surface coil and the ASL coil during the four sets of ASL experiments (i.e. pCASL<sub>vol</sub>, pCASL<sub>lab</sub>, CASL<sub>vol</sub> and CASL<sub>lab</sub>) without animal and without any labeling and imaging RF power:  $B_{1ave}$  was set to 0  $\mu$ T and the power of both excitation and refocusing EPI pulses was set to 0 W. We also opened the coil's housings to image more precisely localized heating (hot-spots). The setup of the experiments with the thermal camera is shown in Fig. 6.3.

### 6.2.3. Data Processing

**SAR** From the global temperature time-course spanning the entire experiment, each individual, sequence-specific, temperature curve was extracted. Since the 8-min pause, introduced after each CASL<sub>Perfusion</sub> scan, was usually not sufficient to return to an equilibrium temperature value (Fig. 6.4a), the linear temperature drift considered during a 3-min baseline (gray box 1 in Fig. 6.4b) was removed from the temperature time-course. To ensure the measurement of the correct period, a safety margin of 45 s was inserted between the baseline and the temperature increase of interest (box 2 in Fig. 6.4b). A linear curve was then fitted to the next 1.5 minutes of the temperature increase (box 3 in Fig. 6.4b) and the apparent SAR ( $SAR_{app}$ ) was calculated with:

$$SAR_{app} = S_{scan} \cdot C_{tissue} \quad (6.1)$$

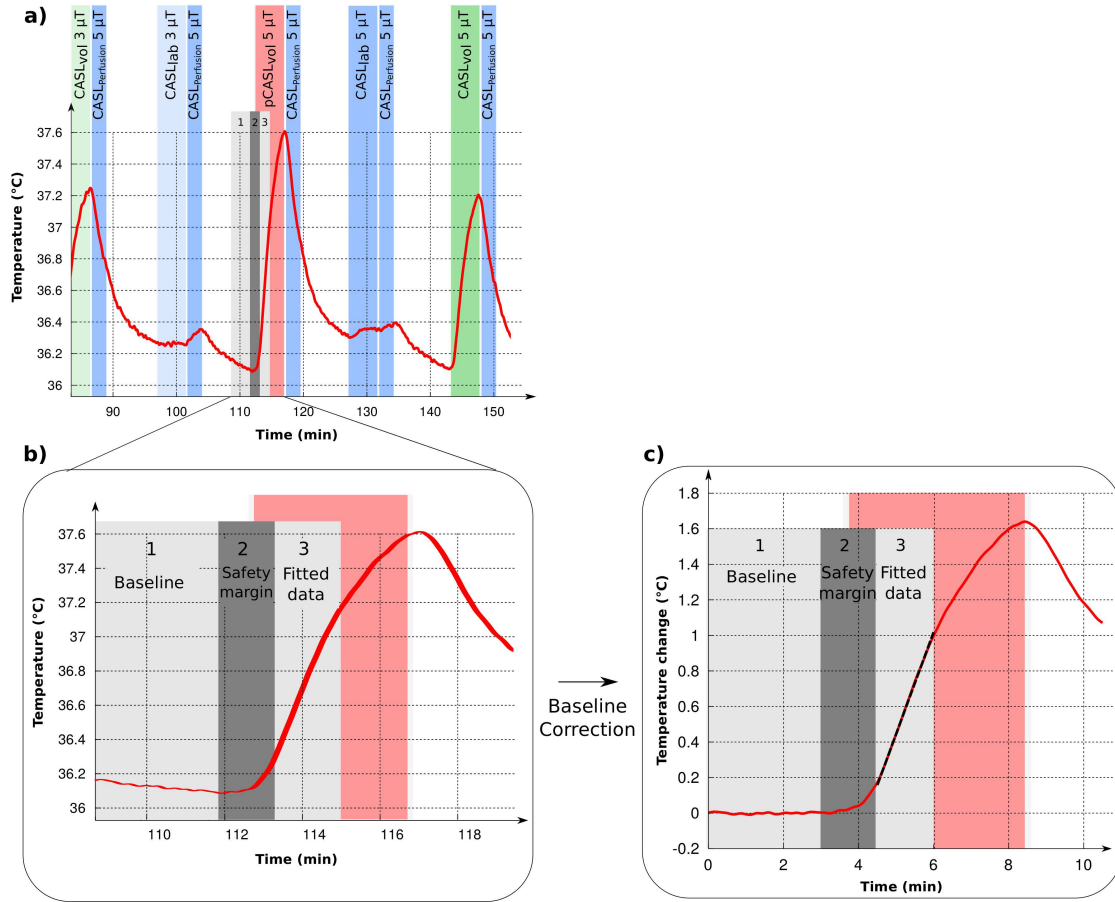


Figure 6.4.: (a) Part of the temperature time-course measured in between the carotids. (b) Zoom on the pCASL<sub>vol</sub> temperature time-course before and (c) after baseline correction.

where  $S_{scan}$  is the fitted slope of the temperature increase and  $C_{tissue}$  the specific heat capacity of tissue ( $3664 \text{ J} \cdot (\text{kg} \cdot \text{K})^{-1}$  [Sotero and Iturria-Medina, 2011]).

In a second step, to better characterize the observed SAR variations,  $SAR_{app}$  was split into two terms:

$$SAR_{app} = SAR_{RF} + Q_{dec} , \quad (6.2)$$

where  $SAR_{RF}$  is the SAR in W/kg generated by RF energy deposition and  $Q_{dec}$  the energy deposition due to external heating from the decoupling circuit in W/kg. To retrieve estimates of  $Q_{dec}$  and  $SAR_{RF}$ , for each animal,  $SAR_{app}$  values were plotted across  $B_{1RMS}^2$  and fitted to a line, which resulted in graphs similar to those from Fig. 6.9 (data not shown). Then for each animal, each probe and each of the four ASL sequences,  $Q_{dec}$  was retrieved as the fitting curve's offset and  $SAR_{RF}$  normalized to  $B_{1RMS}^2$  (i.e.  $SAR_{RF}/B_{1RMS}^2$ ) as the curve's slope.

**Inversion efficiency** The inversion efficiency (IE) was derived from a complex reconstruction of the (p)CASL-FcFLASH sequence as in Chapter 4:

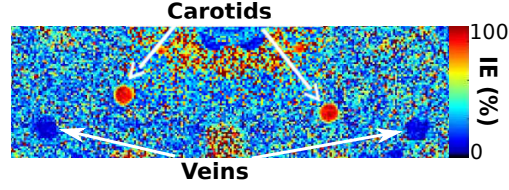


Figure 6.5.: Zoom on an inversion efficiency map example, measured 5 mm downstream of the labeling plane.

$$IE = \left| \frac{M_c - M_L}{2M_C} \right|, \quad (6.3)$$

where  $M_C$  and  $M_L$  are respectively the complex signals from the control and the label experiments. An inversion efficiency map example is shown in Fig. 6.5. Carotids (resp. veins) can clearly be identified as the bright red (resp. dark blue) vessels. A region of interest (ROI) was manually drawn on each carotid. IE was obtained as the mean inversion efficiency across the 2 carotids.

**Quantitative CBF maps** CBF maps were computed as described in Chapter 4. To calculate quantitative CBF maps from  $CASL_{Perfusion}$ , the scan used to monitor CBF over time, we assumed a single compartment and used the standard kinetic model [Buxton et al. \[1998\]](#). Assuming that the arterial transit time is equal to the post labeling delay and that  $M_{0b}$ , the magnetization of arterial blood at thermal equilibrium may be approximated by  $M_{0t}/\lambda$ , where  $M_{0t}$  is the magnetization of tissue at thermal equilibrium and  $\lambda$  the blood-brain partition coefficient of water (0.9 mL/g [[Herscovitch and Raichle, 1985](#)]), we used the following equation to quantify CBF pixel by pixel [[Alsop et al., 2015](#); [Buxton et al., 1998](#)]:

$$CBF = \frac{\lambda \Delta M e^{\frac{\omega}{T_{1b}}}}{2 IE T_{1app} M_{0t} (1 - e^{\frac{-\tau}{T_{1app}}})}, \quad (6.4)$$

where  $\Delta M$  is the signal difference between control and label acquisitions averaged over repetitions;  $T_{1app}$  is the apparent longitudinal relaxation time of tissue (1650 ms at 9.4 T);  $T_{1b}$  is the longitudinal relaxation time of blood (2430 ms at 9.4 T [[Nasrallah et al., 2012](#); [Dobre et al., 2007](#); [de Graaf et al., 2006](#)]);  $M_0$  is the control image intensity of the ASL experiment multiplied by  $[1 - \exp(-TR/T_{1app})]^{-1}$  to correct for incomplete  $T_1$  relaxation during the 4-s TR; IE is the mean IE obtained separately on 3 animals with a  $B_{1ave}$  of 5  $\mu$ T ( $CASL_{Perfusion}$  was acquired with a 5  $\mu$ T labeling amplitude).

The brain was manually delineated on the 5 slices and CBF was obtained as the average brain CBF.

## 6.3. Results

### 6.3.1. $B_{1RMS}$

The root mean square  $B_1$  ( $B_{1RMS}$ ) was calculated from the pulse program for each sequence and each applied  $B_{1ave}$  (Fig. 6.6). The EPI excitation and refocusing pulses were also taken into account, but yielded small values compared to those of the labeling pulses:  $B_{1RMS}$  for a single-slice EPI was  $0.2 \mu T$ . For a given  $B_{1ave}$ , note that  $B_{1RMS}$  is  $\sqrt{3}$  times higher for pCASL than for CASL. The applied  $B_{1RMS}$  is  $\sqrt{2}$  times lower when labeling with the separate ASL coil (CASL<sub>lab</sub> and pCASL<sub>lab</sub>) than with the volume coil (CASL<sub>vol</sub> and pCASL<sub>vol</sub>), since the RF power during the control experiment was turned off when labeling with the ASL coil.

Labeling $B_{1ave}$		CASL <sub>lab</sub>	pCASL <sub>lab</sub>	CASL <sub>vol</sub>	pCASL <sub>vol</sub>
<b>0 <math>\mu T</math></b> (EPI only)	1 slice	0.2 $\mu T$			
	5 slices CASL <sub>Perfusion</sub>	0.5 $\mu T$			
<b>3 <math>\mu T</math></b>	1 slice	1.8 $\mu T$	3.2 $\mu T$	2.6 $\mu T$	4.5 $\mu T$
<b>5 <math>\mu T</math></b>	1 slice	3.1 $\mu T$	5.3 $\mu T$	4.3 $\mu T$	7.5 $\mu T$
	5 slices CASL <sub>Perfusion</sub>	4.3 $\mu T$	-	-	-
<b>7 <math>\mu T</math></b>	1 slice	4.3 $\mu T$	7.4 $\mu T$	6.1 $\mu T$	10.5 $\mu T$

Figure 6.6.: Root mean square  $B_1$  ( $B_{1RMS}$ ) for different labeling amplitudes  $B_{1ave}$ . The shown  $B_{1RMS}$  includes labeling and EPI readout. The 5-slice CASL<sub>Perfusion</sub> scan was used to measure CBF after each ASL scan (cf. Fig. 6.4a).

### 6.3.2. Global temperature time-course

Fig. 6.7a shows an example of the temperature time-course measured in the brain (blue line), in between the carotids (red line) and in the rectum (yellow line) in one particular animal.

Globally, the rectal temperature is lower than that of the brain and the carotids. The temperature variations in the rectum are slow and lower than those observed in the brain or in the carotids.

During adjustments, a significant temperature increase can be observed at the very beginning of the scanning session. This peak was observed when tuning and matching the quadrature volume coil.

Temperature increases in absence of RF labeling power emission as well, as observed

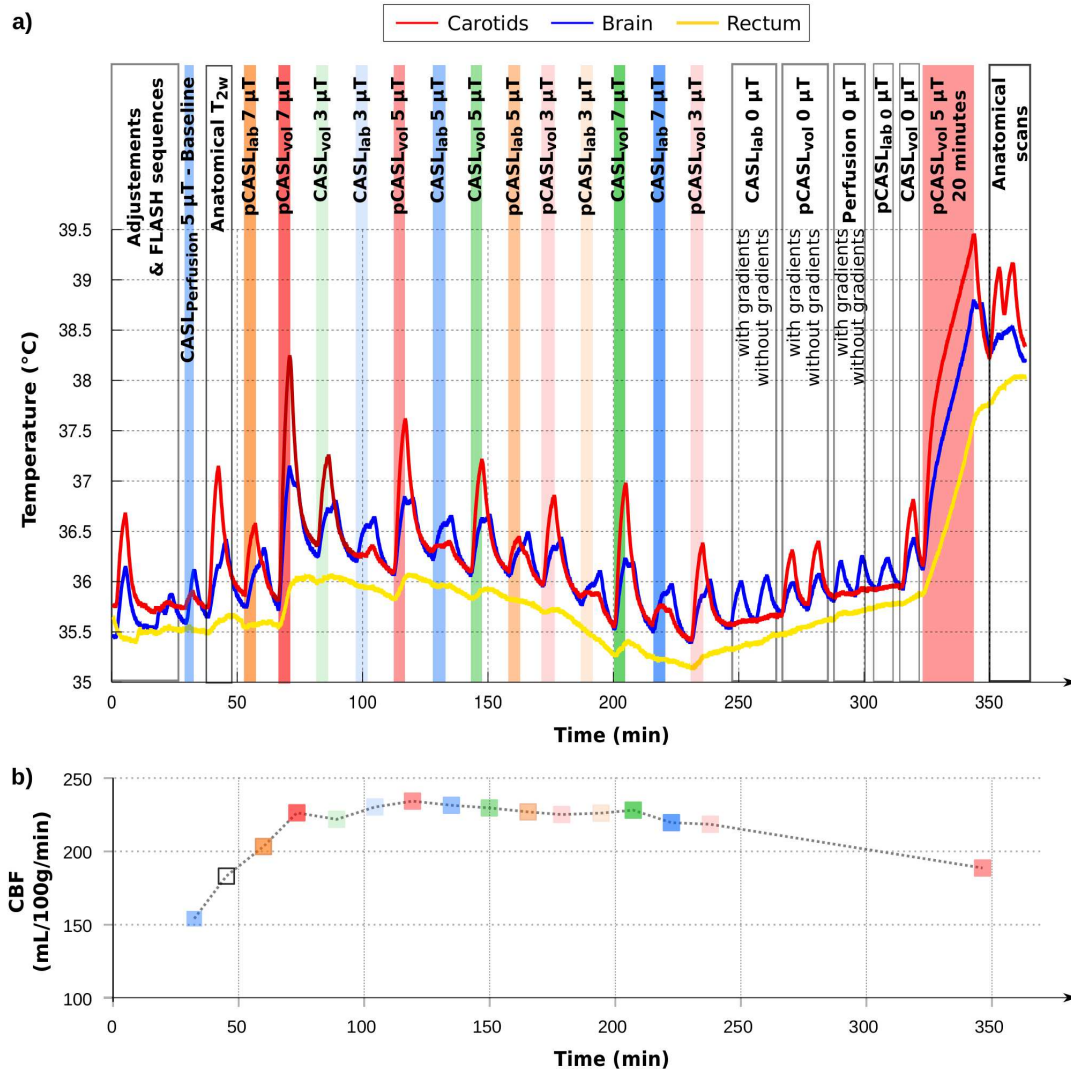


Figure 6.7.: (a) Example of the temperature time-course measured at 3 different locations in one animal while performing ASL scans: in the brain (blue), in between the carotids (red) and in the rectum (yellow). Note that the CASL<sub>Perfusion</sub> scans, repeated after each ASL scan to monitor CBF, have not been color-coded, besides the first one (baseline). (b) CBF in mL/100g/min across time measured after each sequence with CASL<sub>Perfusion</sub> for the rat shown in the first panel of this figure.

The color boxes indicate the sequence type: the box is red for pCASL<sub>vol</sub>, orange for pCASL<sub>lab</sub>, green for CASL<sub>vol</sub> and blue for CASL<sub>lab</sub>. The color's intensity reflects the amplitude of B<sub>1ave</sub>: the stronger the color intensity, the higher the applied B<sub>1ave</sub>.

during the 0  $\mu\text{T}$  ASL scans. Note that no 5- $\mu\text{T}$  CASL<sub>Perfusion</sub> scans were acquired after the 0  $\mu\text{T}$  ASL scans; therefore, the observed temperature increase corresponds to the 0  $\mu\text{T}$  ASL scans only. Contrary to the 0- $\mu\text{T}$  (p)CASL<sub>vol</sub> scans that produce temperature increases in the brain and in the carotids, running the 0  $\mu\text{T}$ -(p)CASL<sub>lab</sub> scans does not heat at the carotids level. Turning the labeling gradients off has no effect on the heating behavior. The EPI-readout does not seem to affect the observed temperature since the temperature variations observed when acquiring 5 slices per TR (i.e. during 0  $\mu\text{T}$ -CASL<sub>Perfusion</sub> scans,  $B_{1\text{RMS}} = 0.5 \mu\text{T}$ , 2 minutes 40 s acquisition) are lower than when acquiring a single slice per TR (i.e. during 0  $\mu\text{T}$ -CASL<sub>lab</sub> scans,  $B_{1\text{RMS}} = 0.2 \mu\text{T}$ , 4 minutes acquisition). The EPI- $B_{1\text{RMS}}$  values are much lower than those applied during other ASL-scans (cf. Fig. 6.6); however, heating in the brain during those scans is of the same order of magnitude than some scans with much higher  $B_{1\text{RMS}}$  (e.g. (p)CASL<sub>lab</sub> scans). Therefore, we concluded that the temperature increases observed during the 0  $\mu\text{T}$ -scans was not due to RF heating. We assumed that it could be ascribed to the coil's decoupling circuits. This hypothesis was validated in subsequent described experiments.

The CASL<sub>Perfusion</sub> scans, acquired after the axial  $T_{2w}$  and after each 3-, 5-, and 7  $\mu\text{T}$  ASL scans, were not color-coded on Fig. 6.7a for readability reasons. However, when looking at the temperature curve of the axial  $T_{2w}$  or of a 3-, 5-, and 7  $\mu\text{T}$  ASL scan, two temperature peaks can be observed within each color-coded block, especially in the brain. The second peak is induced by the CASL<sub>Perfusion</sub> scan. Mean brain CBF values resulting from the CASL<sub>Perfusion</sub> scans for this particular animal are shown in Fig. 6.7b. Note that the observed global CBF is not following the temperature time-course.

The 20-minute long 5  $\mu\text{T}$  pCASL<sub>vol</sub> scan shows that the temperature never reaches an equilibrium value: as long as the scan is running, the temperature increases, even if after approximately 7 minutes, the heating speed slows down a little. In total, for this animal, this long pCASL<sub>vol</sub> scan generated temperature increases of 3.5  $^{\circ}\text{C}$  at the carotids level, 3  $^{\circ}\text{C}$  in the brain and 1.2  $^{\circ}\text{C}$  in the rectum.

### 6.3.3. In-vivo SAR<sub>app</sub> across sequences

Fig. 6.8 shows temperature time-courses for the different ASL labeling techniques at identical  $B_{1\text{ave}} = 5 \mu\text{T}$  and for the anatomical scan (black line). For this animal (the same as in Fig. 6.7), temperature increased up to 0.9  $^{\circ}\text{C}$  in the brain (Fig. 6.8a), 1.6  $^{\circ}\text{C}$  at the carotids' level (Fig. 6.8b) and 0.25  $^{\circ}\text{C}$  in the rectum (Fig. 6.8c) within 4 minutes.

The mean ( $n = 9$  animals) SAR<sub>app</sub> dependence on  $B_{1\text{RMS}}^2$  and on the applied sequences at the different locations is summarized in Fig. 6.9. Different profiles can be observed:

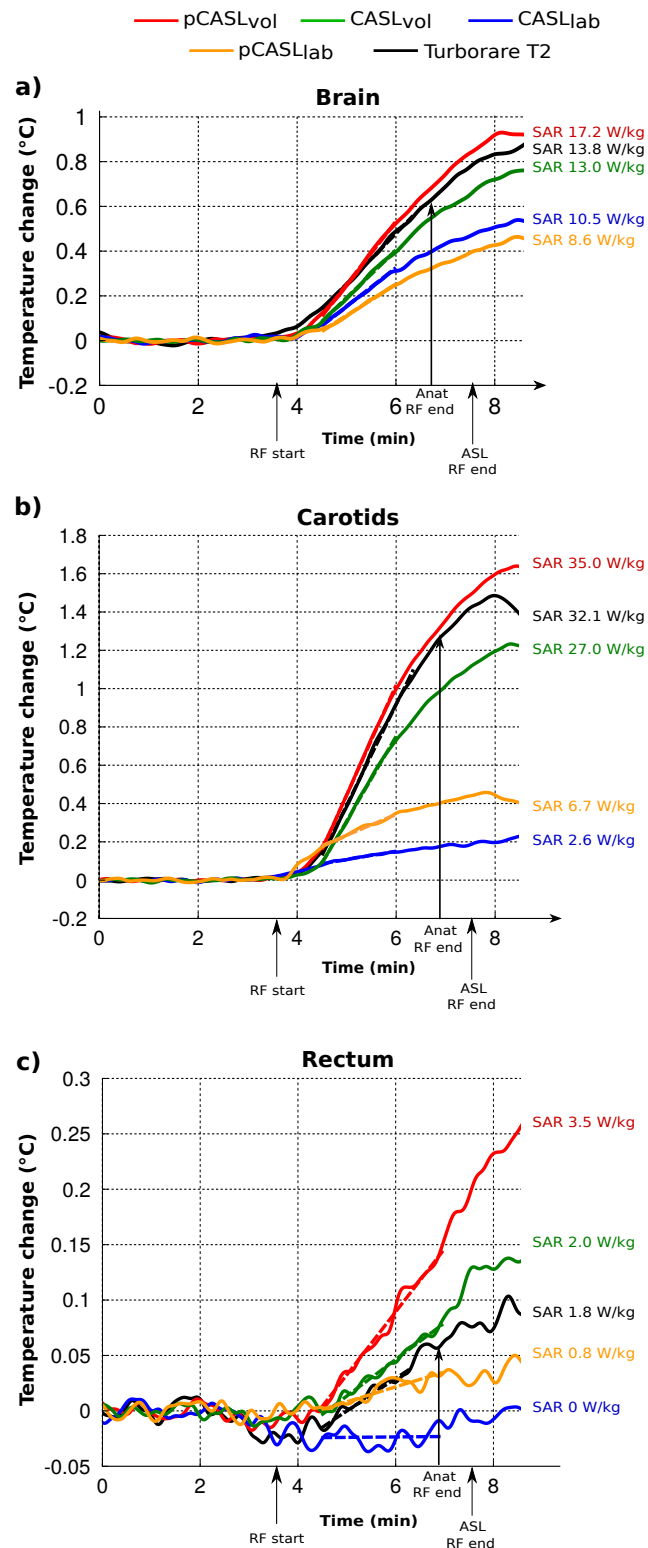


Figure 6.8.: Typical temperature time courses after correction of baseline temperature drift with  $SAR_{app}$  estimation for pCASL<sub>vol</sub> (red), CASL<sub>vol</sub> (green), CASL<sub>lab</sub> (blue) and pCASL<sub>lab</sub> (orange) at  $B_{1ave} = 5 \mu T$  and the anatomical TurboRARE scan (black), in the brain (a), at the labeling plane (b) and in the rectum (c) for the animal shown in Fig. 6.7. Dashed lines represent a linear fit.

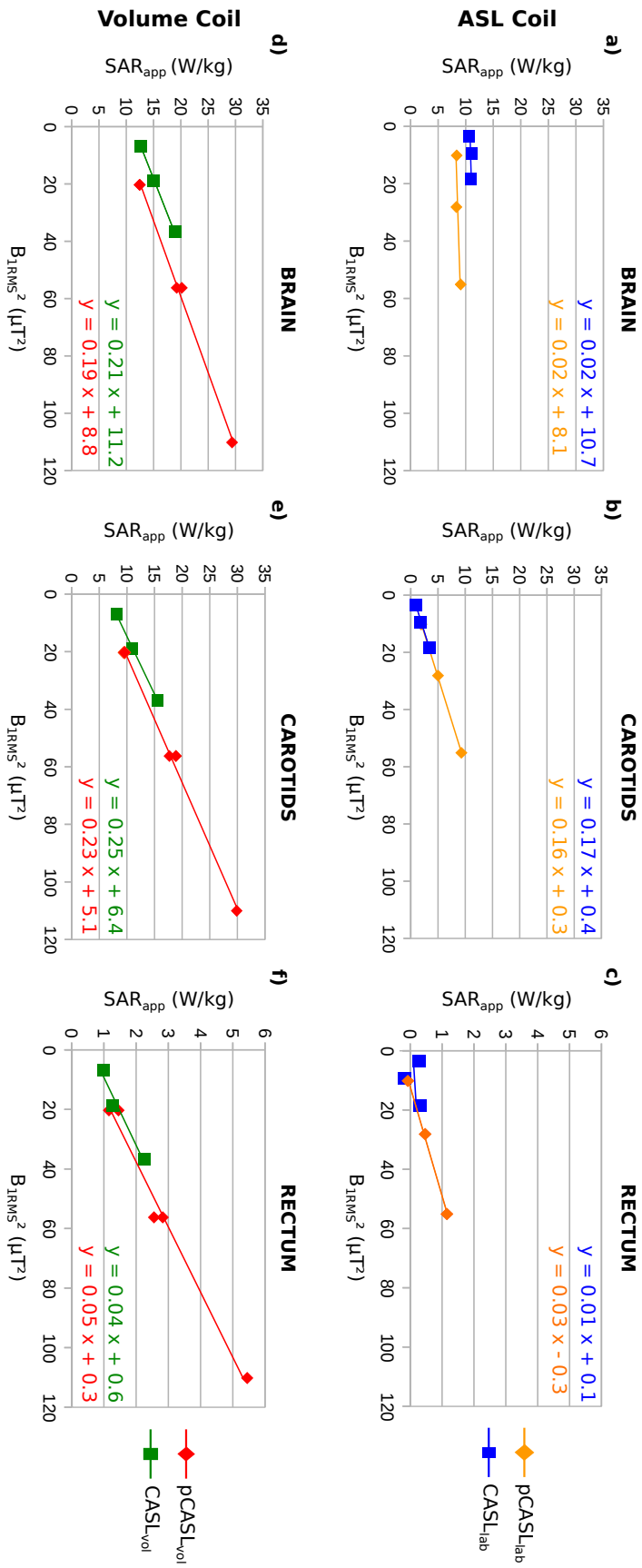


Figure 6.9.: Mean (9 animals)  $SAR_{app}$  versus  $B_{IRMS}^2$  in the brain (a and d), around the labeling plane (b and e) and in the rectum (c and f) for pCASL and CASL. Labeling was performed either with the dedicated ASL labeling coil (a, b and c) or with the volume coil (d, e and f). For comparison, the anatomical T2-TurboRARE scan led to a  $SAR_{app}$  of 13 W/kg in the brain, 15 W/kg in the carotids and 2 W/kg in the rectum. Full lines represent a linear fit to the data.

- **In the brain:**

- When labeling with the **separate ASL coil** (Fig. 6.9a), the measured  $\text{SAR}_{\text{app}}$  depends only very weakly on  $B_{1\text{RMS}}^2$ . This independence with respect to the applied RF labeling power indicates that, as expected, labeling with a separate coil induces very little RF energy deposition in the brain. However, a large non-zero  $\text{SAR}_{\text{app}}$  value is observed: the offset of the curve (which corresponds to  $Q_{\text{dec}}$ ) is 10.7 W/kg for  $\text{CASL}_{\text{lab}}$  (blue squares) and 8.1 W/kg for  $\text{pCASL}_{\text{lab}}$  (orange diamonds). We did not add error bars in Fig. 6.9 for sake of clarity. The values shown in this figure are variable across animals. To estimate this  $\text{SAR}_{\text{app}}$  variability, the standard deviation (SD) across animals was averaged for the different sequences and  $B_{1\text{RMS}}^2$ . In the brain, with the separate ASL coil, this SD was 11.3 W/kg.
- When labeling with the **volume coil** (Fig. 6.9d), the observed  $\text{SAR}_{\text{app}}$  is linearly dependent on  $B_{1\text{RMS}}^2$ , with similar slopes for  $\text{CASL}_{\text{vol}}$  and  $\text{pCASL}_{\text{vol}}$ . A non-zero  $Q_{\text{dec}}$  is observed at 0  $\mu\text{T}^2$ : the offset is 11.2 W/kg for  $\text{CASL}_{\text{vol}}$  (green squares) and 8.8 W/kg for  $\text{pCASL}_{\text{lab}}$  (red diamonds), i.e. values close to those measured in the brain when labeling with the separate labeling coil (Fig. 6.9a). The  $\text{SAR}_{\text{app}}$  variability was 16.2 W/kg.

- **At the labeling plane level (carotids):**

- When labeling with the **separate ASL coil** (Fig. 6.9b), the measured  $\text{SAR}_{\text{app}}$  is directly proportional to  $B_{1\text{RMS}}^2$  and is independent of the sequence type for a given  $B_{1\text{RMS}}^2$ : the same slope is observed for  $\text{CASL}_{\text{lab}}$  and  $\text{pCASL}_{\text{lab}}$ . The standard deviation (SD) across animals averaged for the different sequences was 2.3 W/kg.
- When labeling with the **volume coil** (Fig. 6.9e), the observed  $\text{SAR}_{\text{app}}$  is linearly dependent on  $B_{1\text{RMS}}^2$ , with similar slopes for  $\text{CASL}_{\text{vol}}$  and  $\text{pCASL}_{\text{vol}}$  but again with different non-zero  $Q_{\text{dec}}$  values at 0  $\mu\text{T}^2$ : 6.4 W/kg for  $\text{CASL}_{\text{vol}}$  and 5.1 W/kg for  $\text{pCASL}_{\text{lab}}$ . We note that labeling with the volume coil induces higher  $\text{SAR}_{\text{RF}}$  than labeling with a separate coil: the SAR normalized to  $B_{1\text{RMS}}^2$  (i.e. the curve's slope,  $\text{SAR}_{\text{RF}}/B_{1\text{RMS}}^2$ ) is 0.17 W/kg/ $\mu\text{T}^2$  for (p) $\text{CASL}_{\text{lab}}$  compared to 0.24 W/kg/ $\mu\text{T}^2$  for (p) $\text{CASL}_{\text{vol}}$ . The  $\text{SAR}_{\text{app}}$  variability was 8.1 W/kg.

- **In the rectum (global body temperature measurement):**

- When labeling with the **separate ASL coil** (Fig. 6.9c), small  $\text{SAR}_{\text{app}}$  values are measured: the maximal mean  $\text{SAR}_{\text{app}}$  value is 1 W/kg, obtained with  $\text{pCASL}_{\text{lab}}$  for a  $B_{1\text{ave}}$  of 7  $\mu\text{T}$  ( $B_{1\text{RMS}}^2 = 55 \mu\text{T}^2$ ). The standard deviation (SD) across animals averaged for the different sequences was 0.6 W/kg.

- When labeling with the **volume coil** (Fig. 6.9f), the measured  $\text{SAR}_{\text{app}}$  is higher than when labeling with the separate coil and depends linearly on  $B_{1\text{RMS}}^2$ , with similar slopes for  $\text{CASL}_{\text{vol}}$  and  $\text{pCASL}_{\text{vol}}$ . The  $\text{SAR}_{\text{app}}$  variability was 0.7 W/kg.

All linear fits on Fig. 6.9 had a coefficient of determination  $R^2$  higher than 0.9, except those where  $\text{SAR}_{\text{app}}$  was not dependent on  $B_{1\text{RMS}}^2$  (i.e. in the brain and in the rectum when labeling with the ASL coil). The high observed  $\text{SAR}_{\text{app}}$  variability across animals is addressed in section 6.3.5.

### 6.3.4. Heat induced in absence of RF emission

To understand and validate the non-zero  $Q_{\text{dec}}$  values observed at 0  $\mu\text{T}^2$  in the brain and in between the carotids (Fig. 6.9), the heat intensity induced in absence of RF power emission (i.e. instructions of 0 W were given to the MR system for all labeling and imaging pulses) was characterized for the four ASL sequences (Fig. 6.10): a global view of the coil's temperature at the end of the 4-minute scans is given by the thermal images (Fig. 6.10a) and quantitative values in  $^\circ/\text{min}$  measured with the fiber-optic probes at 5 points (panel b) are given panel c. Following results were observed:

- **The surface array rat head coil** (top row of Fig. 6.10) heats in all situations. The closer to the junction of the four coil elements (point n°1, panel b), the higher the measured temperature increase. For a given labeling scheme, identical temperature variations are observed when labeling with the volume coil or the ASL coil. In average  $\pm$  SD over the 5 probe positions, pCASL heats  $31 \pm 2\%$  less than CASL.
- **ASL coil** (bottom row of Fig. 6.10): heating is observed only when labeling with the volume coil. Again, pCASL<sub>vol</sub> causes  $32 \pm 5\%$  less heating than CASL<sub>vol</sub>. The measured temperature variations are not spatially symmetrical: a hot-spot on the left side of the coil (point n°4, panel b) is observed, which corresponds to the location of electrical components (Fig. 6.11).

### 6.3.5. In-vivo $Q_{\text{dec}}$ and $\text{SAR}_{\text{RF}}$

Fig. 6.9 showed the average  $\text{SAR}_{\text{app}}$  versus  $B_{1\text{RMS}}^2$  over 9 animals. A similar  $\text{SAR}_{\text{app}}$  versus  $B_{1\text{RMS}}^2$  behavior was observed for each individual animal in the different coil configurations. However, depending on the fiber-optic probe position, the curves' offsets (i.e.  $Q_{\text{dec}}$ ) and slopes (i.e.  $\text{SAR}_{\text{RF}}/B_{1\text{RMS}}^2$ ) varied, as reflected by the high SD values across animals. To better visualize these spatial variations, we localized the extremity of the fiber-optic probes located in the brain and in the carotids and reported their position on anatomical slices. Then, the heating from the decoupling circuit ( $Q_{\text{dec}}$ ) and RF

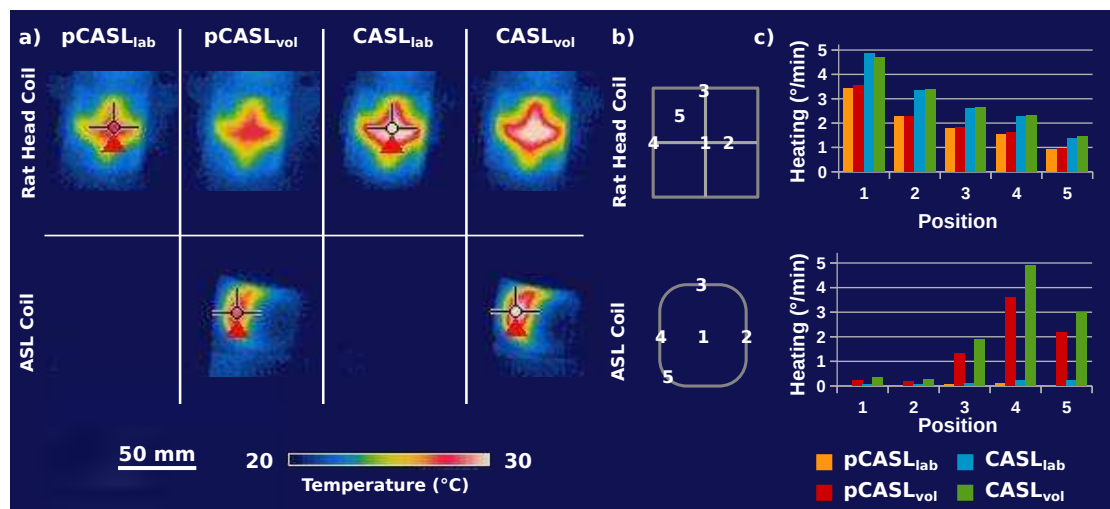


Figure 6.10.: Heating observed in absence of RF emission. (a) Images of the rat head coil (top row) and the ASL coil (bottom row) acquired with a thermal imaging camera at the end of 4-min pCASL and CASL scans. No RF power was sent. The baseline temperature was 21 °C. The cross indicates the warmest point for each applied sequence. (b) Illustrations of the array rat head coil (top row) and of the ASL coil (bottom row). (c) Heating (°/min) measured at the different coil locations shown on panel b during pCASL and CASL scans.

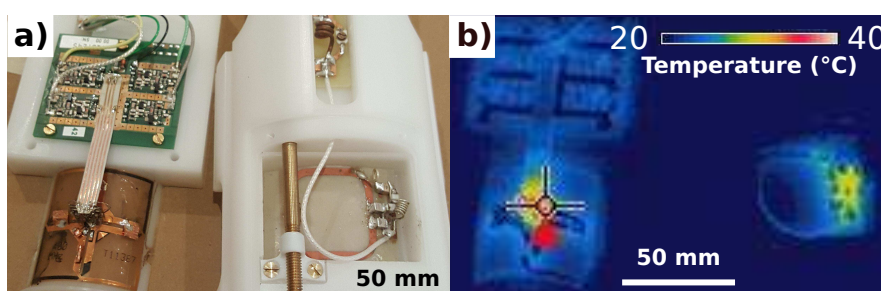


Figure 6.11.: (a) Opened coils with (b) corresponding thermal image acquired after a 4-minute CASL<sub>vol</sub> scan without RF emission. The baseline temperature was 21 °C. When comparing with Fig 6.10, note that the coils are turned around here and that the temperature scale, indicated in °C by the color bar, is different.

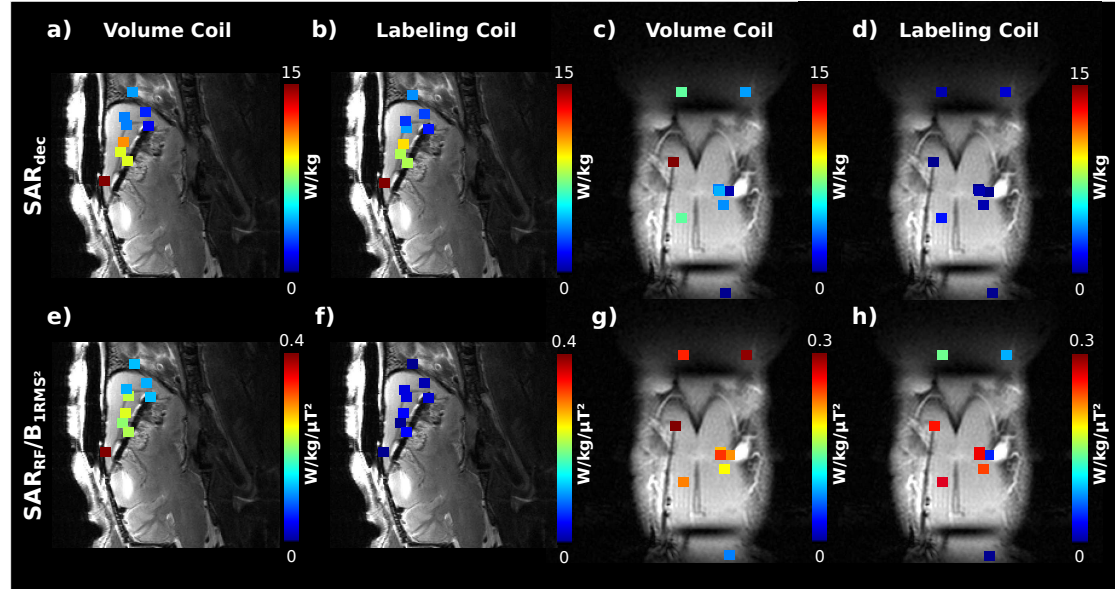


Figure 6.12.: SAR induced in absence of RF emission ( $Q_{dec}$ , top row) and generated by the emitted RF field normalized to  $B_{1RMS}^2$  ( $SAR_{RF}/B_{1RMS}^2$ , bottom row) in the brain (a, b, e and f) and in the neck (c, d, g and h) for pCASL. Each square represents the position of the fiber-optic probe of one particular animal. Note that the dark red squares on panels a and b represent values above the maximum of the color scale:  $Q_{dec} = 38$  W/kg (panel a) and  $Q_{dec} = 34$  W/kg (panel b). All other values are in the range of the color bars.

( $SAR_{RF}/B_{1RMS}^2$ ) for pCASL was color-coded and superimposed on these approximate temperature probe locations (Fig. 6.12).

The deeper the probe in the brain, the lower the  $Q_{dec}$ . A similar  $Q_{dec}$  distribution is observed in the brain when labeling with the volume (Fig. 6.12a) or the ASL coil (Fig. 6.12b). At the carotid's level, when labeling with the volume coil (Fig. 6.12c), the closer the probe's position to the left, the higher the heating induced by the contact with the coil ( $Q_{dec}$ ).

When labeling with the volume coil (Fig. 6.12e), the energy emitted by the RF field and absorbed by the brain is higher at positions close to the skull. Conversely, labeling with a separate coil induces negligible  $SAR_{RF}$  in the brain (Fig. 6.12f) and in the neck, the heating induced by the RF field is concentrated in the ASL coil's field of view (Fig. 6.12h).

If only  $SAR_{RF}$  is considered, i.e. if  $Q_{dec}$  values due to heating of the coils are removed, pCASL and CASL heat in the same way at equal  $B_{1RMS}^2$  (Figs. 6.13 a and b): for each probe and coil, the 8 points (3 for CASL and 5 for pCASL) are aligned. Note that in the carotids, when labeling with the ASL coil, no  $Q_{dec}$  was observed (no need to decouple the ASL coil when using it), which explains why  $SAR_{RF} = SAR_{app}$  in this particular case. Again, the benefit of labeling with a separate coil is clearly seen, since  $SAR_{RF}$  is

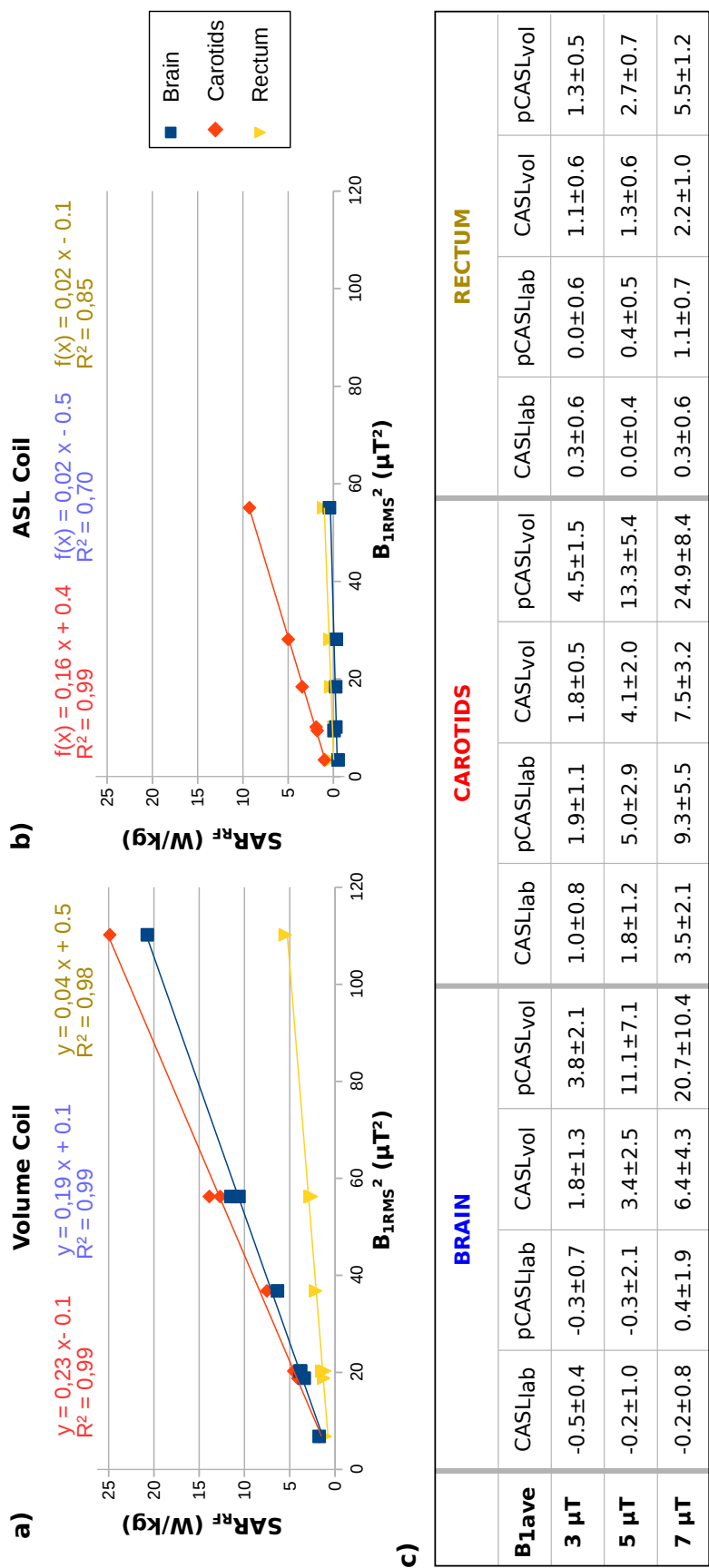


Figure 6.13.: Mean (9 animals) SAR<sub>RF</sub> versus B<sub>IRMS</sub><sup>2</sup> for CASL and pCASL in the brain (blue), the carotids (red) and the rectum (yellow) for a labeling with the volume coil (a) or the dedicated ASL coil (b). (c) Mean ± SD (9 animals) SAR<sub>RF</sub> in W/kg across B<sub>1ave</sub> for all sequences and temperature probes.

dramatically reduced.

### 6.3.6. CBF values

Fig. 6.14 shows a CBF map example for one animal. The strong hypo-perfused regions are due to the fiber-optic probe's presence. After animal positioning, CBF first increases from  $117 \pm 36$  mL/100g/min, the baseline CBF measured before the ASL and  $T_{2w}$  images, to a plateau value of  $174 \pm 31$  mL/100g/min, the mean  $\pm$  SD CBF value across animals and ASL sequences (Fig. 6.15). CBF is stable across ASL sequences and is hardly affected by the ASL sequence type, as shown on Figs. 6.7b and 6.15. For example, CBF is  $180 \pm 31$  mL/100g/min after a 4-min 5- $\mu$ T pCASL scan and stays at  $183 \pm 33$  mL/100g/min after the same, but 5 times longer 5- $\mu$ T pCASL scan, which induces much higher temperature increases. The CBF difference between the baseline and all 14 subsequent individual ASL scans was found significant, as determined with a paired t-test ( $P < 0.01$ ). No significant CBF differences were found for CASL<sub>Perfusion</sub> scans acquired after the 14 ASL scans.

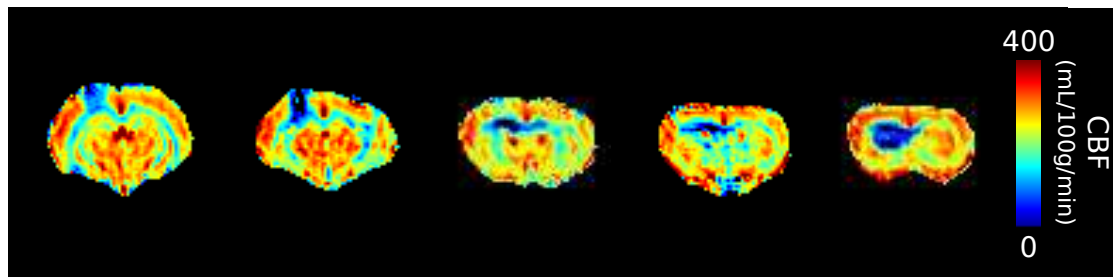


Figure 6.14.: CBF maps in mL/100g/min obtained with CASL<sub>Perfusion</sub>.

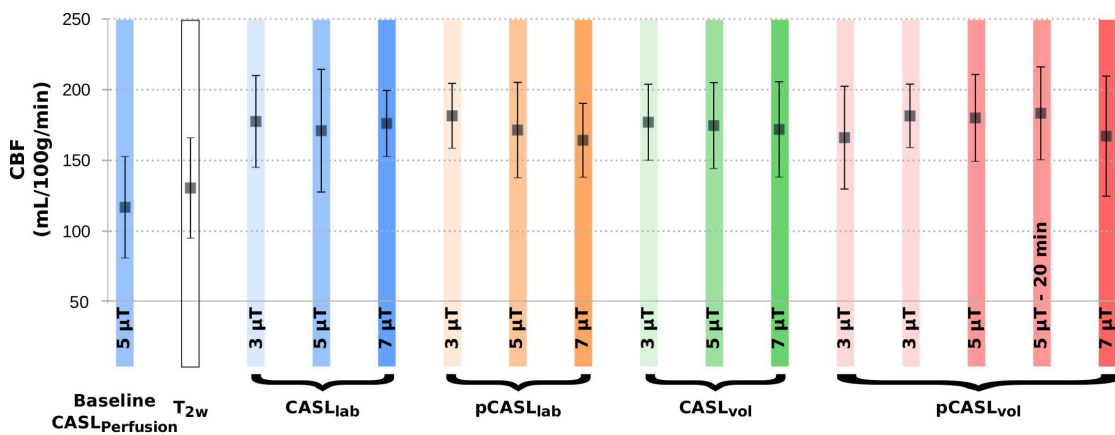


Figure 6.15.: Average CBF value  $\pm$  SD (9 animals) across sequences measured with the CASL<sub>Perfusion</sub> scans. The color boxes indicate the sequence type that preceded the CBF measurement: the box is red for pCASL<sub>vol</sub>, orange for pCASL<sub>lab</sub>, green for CASL<sub>vol</sub> and blue for CASL<sub>lab</sub>. The color's intensity reflects the amplitude of  $B_{1ave}$ : the stronger the color intensity, the higher the applied  $B_{1ave}$ .

### 6.3.7. Inversion efficiency

IE increases with  $B_{1\text{ave}}$  and thus with  $B_{1\text{RMS}}^2$  (Fig. 6.16a-b). Reducing  $B_{1\text{ave}}$  to less than  $3 \mu\text{T}$  led to lower IE ( $< 70\%$ ) for both  $\text{CASL}_{\text{vol}}$  and  $\text{CASL}_{\text{lab}}$  and asymmetrical labeling between carotids (Fig. 6.16c-d), especially when labeling with the ASL coil. For  $B_{1\text{ave}} \geq 5 \mu\text{T}$ , acceptable IE and low asymmetry were obtained for all sequences. Note that both pCASL sequences reached higher IE for lower  $B_{1\text{ave}}$  values than the CASL methods. However, they also yield higher  $B_{1\text{RMS}}^2$  and therefore higher  $\text{SAR}_{\text{RF}}$  at equal  $B_{1\text{ave}}$ .

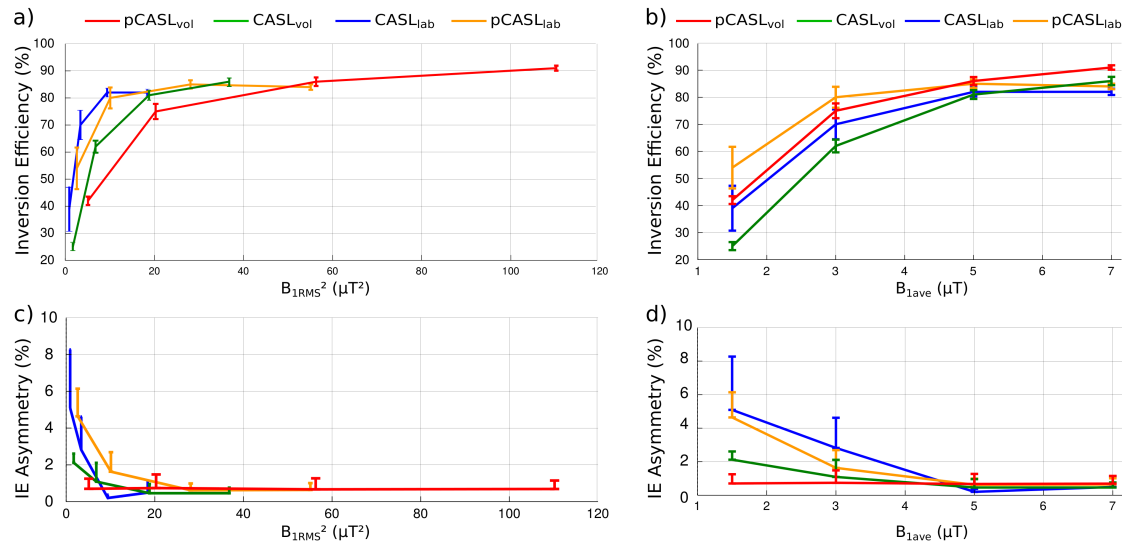


Figure 6.16.: (a, b) Inversion efficiency (mean  $\pm$  SD) and (c, d) IE asymmetry (mean  $\pm$  SD) between carotids as a function of  $B_{1\text{ave}}$  (a, c) and  $B_{1\text{RMS}}^2$  (b, d). IE was measured 5 mm downstream of the labeling plane for pCASL<sub>vol</sub> (red), CASL<sub>vol</sub> (green), CASL<sub>lab</sub> (blue), pCASL<sub>lab</sub> (orange).

## 6.4. Discussion

This study investigates the heating induced by pCASL and CASL scans. We observed that the measured  $\text{SAR}_{\text{app}}$  was, as expected, due to the RF energy absorbed in the sample ( $\text{SAR}_{\text{RF}}$ ) but was also partly due to  $B_1$ -independent heating induced by the surface receive and ASL coils ( $Q_{\text{dec}}$ ), with which the animal is in contact.

The different observed coil heating behaviors in absence of RF emission (cf. Fig. 6.10) allow to deduce that this heat (i.e.  $Q_{\text{dec}}$ ) is generated during the decoupling of the surface array and ASL coils: if one of the 3 coils is selected to emit RF pulses, DC current is sent to the 2 other non-selected coils to decouple, i.e. detune, them. Since labeling pulses or pulse trains are long (3 s), this heats some coil elements as shown in Fig. 6.3b. Contrary to the continuous pulse applied in CASL, a 3-s pCASL labeling train consists of thousands of short 400- $\mu\text{s}$  pulses repeated every 800- $\mu\text{s}$ . This difference in labeling

schemes explains why less  $Q_{\text{dec}}$  is generated during pCASL than during CASL (Figs. 6.9 and 6.10). The  $\sim 30\%$  pCASL/CASL difference may be explained by the fact that the DC current sent for decoupling is most probably lasting longer than the pulse duration itself and is therefore not absent during the entire time left in between 2 pCASL pulses (i.e. 400- $\mu\text{s}$ ). For all ASL experiments, the surface-array head coil was decoupled during labeling. This induced the observed  $Q_{\text{dec}}$  in the brain and explains the similar values obtained for a given labeling scheme when labeling with the volume or the ASL coil. Since heating in the brain due to the decoupling circuit in the surface coil is significant in all ASL scans and of the same order of magnitude as the heating due to RF, it might be useful to investigate the possibility of better adapting that circuit to the extreme duty cycles encountered in ASL. On the contrary, heating of the neck due to decoupling in the separate ASL coil should never be an issue. If the labeling is done with the ASL coil, no additional heat is measured ( $Q_{\text{dec}} = 0 \text{ W/kg}$ ), since the coil does not need to be decoupled. And the observed  $Q_{\text{dec}}$  in the carotids due to decoupling of the ASL coil when labeling with the volume coil should be absent in standard ASL experiments, since the user most probably will not install an ASL coil during the experiment if the labeling is done with the volume coil.

$\text{SAR}_{\text{RF}}$  is proportional to  $B_{1\text{RMS}}^2$  and since  $B_{1\text{RMS}}^2$  is 3 times higher for pCASL than for CASL at equal  $B_{1\text{ave}}$ , this explains the observed higher  $\text{SAR}_{\text{RF}}$  for pCASL compared to CASL at identical coil configuration and at equal  $B_{1\text{ave}}$  (Figs. 6.8 and 6.9). When labeling with a dedicated coil, negligible RF energy is absorbed in the brain ( $\text{SAR}_{\text{RF}}/B_{1\text{RMS}}^2 = 0.02 \text{ W/kg}/\mu\text{T}^2$  for (p)CASL<sub>lab</sub>), thanks to the small ASL coil coverage. Contrary to that, when labeling with the volume coil, a  $\text{SAR}_{\text{RF}}$  normalized to  $B_{1\text{RMS}}^2$  of  $0.19 \text{ W/kg}/\mu\text{T}^2$  is induced. In the neck, labeling with a dedicated coil reduces the  $\text{SAR}_{\text{RF}}/B_{1\text{RMS}}^2$  by  $56 \pm 7 \%$  compared to labeling with a volume coil.

The  $\text{SAR}_{\text{app}}$  derived from the two 3- and 5- $\mu\text{T}$  pCASL scans performed on each animal were comparable (Figs. 6.9 and 6.13), suggesting experimental stability.

Part of the standard deviations across animals in CBF is likely due to the variable positioning of the fiber-optic probe in the brain that damages the brain tissue and which leads to hypo-perfused regions variable in size and position. Moreover, the fact that the acquisition order was random and that the damaged brain area tends to shrink over time, is probably masking the CBF variations due to brain heating. Therefore, instead of considering a global brain ROI, local CBF could be studied to evaluate more precisely the temperature effect on CBF. Indeed, [Masamoto et al. \[2009\]](#) showed that exposing rats to RF during 7 minutes with a SAR of  $10.5 \text{ W/kg}$  was sufficient to increase the cortical CBF by 8 %. However, the rats in the latter study were anesthetized with a ketamine and xylazine mixture, known to induce lower basal CBF than isoflurane [[Lei et al., 2001](#)]. Therefore, in our study with isoflurane, we expect lower CBF variations elicited by temperature increase, since the baseline CBF is already higher.

Our data show that heating during ASL sequences can be significant. It is thus necessary to find a compromise  $B_{1\text{ave}}$  value that does not induce too much heat in the animals and still produces high enough labeling efficiency. IE values increase with  $B_{1\text{ave}}$  and are in agreement with the literature [Duhamel et al., 2012].  $B_{1\text{ave}}$  amplitudes around 4-5  $\mu\text{T}$  seem to be good compromise values between IE and  $\text{SAR}_{\text{RF}}$ . Using a separate ASL coil further reduces SAR while maintaining IE. Moreover, since CASL yields lower  $\text{SAR}_{\text{RF}}$  than pCASL at equal  $B_{1\text{ave}}$ , a  $\text{CASL}_{\text{lab}}$  sequence with a  $B_{1\text{ave}}$  of 5  $\mu\text{T}$  appears to be the best choice if an ASL coil is available. In this case the  $\text{SAR}_{\text{RF}}$  is  $0\pm 1$  W/kg in the brain and  $2\pm 1$  W/kg in the neck (Fig 6.13c). If no ASL coil is available, labeling is necessarily performed with the volume transmit coil and a pCASL sequence is the best option, despite the higher  $\text{SAR}_{\text{RF}}$  ( $11\pm 7$  W/kg in the brain and  $13\pm 5$  W/kg in the neck), since  $\text{CASL}_{\text{vol}}$  allows only a single slice measurement due to MT effects. However, depending on the total scan duration and on the animal's condition, the  $B_{1\text{ave}}$  amplitude, the labeling duration and/or the TR may need to be adapted to reduce the SAR to an acceptable value [Ghariq et al., 2012].

The observed asymmetries at lower  $B_{1\text{ave}}$ , especially when labeling with the ASL coil, are most probably due to the carotids position with respect to the labeling coil: if they are not located at the same distance from the ASL coil and low  $B_{1\text{ave}}$  is sent, resulting in lower penetration depth, the label pulse may not be adiabatic in one of the carotids, which leads to asymmetry. These asymmetry issues are lower when labeling with the volume coil, and become negligible when increasing  $B_{1\text{ave}}$  for all coil configurations and sequences (Figs. 6.16c and d).

The observed lower rectal temperature compared to that of the brain, is not in agreement with the literature [Wang et al., 2014]: small anesthetized animals have a high brain-surface-to-volume ratio compared to humans, that should result in a more favorable heat evacuation. However, the animal's fur and the current compact coil setup in which the animal is positioned hinders proper heat evacuation, which explains the observed results. Diseased animals (e.g. with stroke or TBI) may have locally reduced CBF, resulting in restricted blood circulation and reduced heat evacuation in the concerned regions. This could lead to higher temperature increases than the ones observed in the rats of this study, which may modify the animal's outcome and bias the obtained results as a consequence [Mrozek et al., 2012; Busto et al., 1989]. Care must therefore be taken in the development of RF coils for animals (both decoupling and coil packaging) to favor heat evacuation.

SAR estimations given by the MR system, as it is done on clinical scanners, could be of interest in preclinical studies to guide and warn the user.

The SAR values measured in this study are only local SAR estimations. Nevertheless, when reporting all local values from each of the nine animals on the same image, a more global view of the SAR distribution is obtained. To further investigate the presence of

possible hot-spots, this study may be completed by temperature maps and simulations.

## 6.5. Conclusion

This study shows that ASL experiments with standard parameters ( $B_{1ave} = 3 - 7 \mu\text{T}$ ) at 9.4 T can lead to increase in temperature. This should be taken into account especially when using ASL sequences for long scanning periods or with diseased animals such as stroke or TBI animal models. SAR can be dramatically reduced by using a dedicated ASL coil. A compromise must be found between SAR, inversion efficiency, acquisition time and/or coil configuration.

## 7. General conclusion & perspectives

### 7.1. Conclusion

The global objective of this PhD project was to increase the performance and to facilitate the use of continuous and pseudo-continuous ASL tools in preclinical studies. CBF quantification by means of ASL is one of the most challenging MRI modalities in terms of the workflow, since additional adjustment (MT correction or ASL coil reference RF power calibration), acquisition (inversion efficiency,  $T_1$  map) and post-processing steps (CBF map generation, outlier detection) are required. At higher magnetic field, problems, such as phase optimization in pCASL and SAR issues are added to this already complex method.

To render the workflow smoother for the user, we developed a CASL package in collaboration with Bruker. This workflow allows easier relative and absolute CBF measurements, thanks to the integration of automated adjustments and reconstruction steps. Inversion efficiency in chosen arteries can be easily retrieved, the optimal control frequency for residual MT effect correction is automatically calculated, and relative or quantitative CBF maps can be generated directly at the end of the CASL-EPI scan. Since in this manuscript, both manual and automatic steps were described in detail, the reader may have an impression of complexity. This is however not the case, since most steps are automatically performed. The developed prototypes have successfully been tested and Sascha Köhler integrated them as Bruker methods. This opportunity to spend one third of the allocated doctoral time in a company, was enriching for me by allowing me to experience both the industrial and the academic sides of research. The CASL package is the result of the successful collaboration between both parties. Several follow-up meetings took place and were useful to boost the interactions. In the frame of this collaboration, the ASL coil has been used for in-vivo experiments, which allowed feedback to Bruker. The coil is relatively large (22 mm) and its z-range to adapt its position limited. We also reported the heating issues due to the decoupling circuit. Moreover, when using this ASL coil with a surface coil, only small rats can be used (~200g) since bigger animals would have trouble breathing in such a tight setup. Bruker started the development of a smaller coil.

During this thesis, a robust unbalanced pCASL package was developed: after having transferred the existing pCASL code from Paravision 5 to Paravision 6, we developed a

prescan based phase correction strategy for unbalanced pCASL and tested its robustness towards sub-optimal shim conditions at 9.4 T *in vivo*. For all tested conditions, full ASL signal could be restored. Moreover, asymmetry between brain hemispheres, which could be as high as 100% without phase optimization, was dramatically reduced to  $1\pm 3\%$  when applying optimized label and control phases. This allows researchers now to routinely use second order shims in the brain, restoring optimal image quality without impairing inversion efficiency in the neck. In a second step, we attempted to correlate the measured phase corrections to the frequency in the carotids at the labeling plane. A strong correlation was found between both measured values, but additional offsets that depend on the applied pCASL parameters were observed as well. The origin of these phase offsets is still not identified. We highly suspect that the way off-resonance RF pulses are controlled on our MR systems leads to additional unwanted phase offsets as shown in Hennel [2014]. If the phase control is known, this would allow to predict the optimal label and control phases directly from the frequency measured in a voxel placed on the carotids.

This developed pCASL package has been shared with several other institutes worldwide (ten in total). Some of them led to abstracts presented at the international meeting on MRI (ISMRM). These collaborations were a unique opportunity to challenge the robustness of the pCASL package.

It also triggered a larger collaboration with groups in Leiden. The work presented in Chapter 5 was done in the frame of this collaboration, and especially with Leon Munting. Our different backgrounds (i.e. physics and biology) facilitated the project's progress. A Hadamard encoded pCASL sequence with its post-processing was developed. For the first time, ATT was mapped in mice, in which higher spatial and temporal resolution are required due to their smaller size and short transit times. The developed technique was applied in young and old mice. No CBF nor ATT variation was found with increasing age in these wild-type mice. A dynamic ASL scheme was also implemented with a 3D readout, and results are shown in Appendix B.3.

For the first time, we documented SAR induced by CASL and pCASL sequences in animals. Different heating sources were (surprisingly) observed: the measured SAR was not only due to the labeling RF emission, but a large part of it could be attributed to heat generated in the coils decoupling circuit. RF pulses that last several seconds are indeed not common and the standard coils are therefore not necessarily designed to be decoupled so long. We saw that a compromise between IE and reasonable SAR is obtained with a CASL sequence with a  $B_{1\text{ave}}$  of 5  $\mu\text{T}$  for which the labeling is performed with an ASL coil. In this case the induced  $\text{SAR}_{\text{RF}}$  is  $0\pm 1$  W/kg in the brain and  $2\pm 1$  W/kg in the neck. In absence of such an ASL coil, a pCASL sequence providing access to multi-slice acquisitions is the best option, despite the higher  $\text{SAR}_{\text{RF}}$  ( $11\pm 7$  W/kg in the brain and  $13\pm 5$  W/kg in the neck). A 4-minute pCASL acquisition leads to less

than 1°C temperature rise in the brain. However, how much RF heating a rat can be reasonably subjected to for longer acquisitions is not known and will also depend on the disease state of the animal. Hyperthermia has been shown to be detrimental in TBI, for example.

In summary, this thesis has produced a set of robust and validated ASL sequences and processing tools that render reproducible CBF measurement on Bruker preclinical MRI scanners straightforward and has raised important issues that merit further research, such as SAR constraints in preclinical imaging.

## 7.2. Perspectives

Concerning the industrial project, the robustness of the MT correction with respect to different imaging slice offsets and use of different gradient strengths should be evaluated and could also be compared to other MT correction techniques. To our knowledge, the initial comparison between frequency compensation and gradient reversal proposed by Pekar *et al.* in 1996 has not been further investigated. Implementation of an automatic outlier threshold calculation based on statistics and image registration could benefit the robustness of the current package. The developed CASL workflow could be strengthened based on user feedback.

Investigating whether the heating due to decoupling observed on our system is also present in other setups would be interesting. In this case, the reduction of this heating would be relevant, since it is not only present during ASL, but was also observed when running anatomical T<sub>2</sub>-TurboRARE scans or even during coil tuning and matching. If heating of the decoupling circuit could be avoided, this would provide significantly more headroom in terms of the acceptable ASL B<sub>1</sub> amplitude and scan duration, since currently heating due to RF accounts for only about half of the total heating observed in the brain when labeling using a volume transmit coil.

From a methodological point of view, the proposed strategy to optimize unbalanced pCASL could be tested on clinical high field scanners to evaluate whether additional phase offsets are observed as well. In this case, the proposed strategy to optimize both label and control phases separately could yield a robust pCASL sequence at higher magnetic fields in humans as well for the recommended unbalanced pCASL method. In absence of phase offset, an estimation of the resonance frequency on each carotid could become a robust optimization strategy, compatible with a clinical workflow.

It would be interesting to further investigate time-encoded ASL in animals. In the Hadamard-encoded study shown in this manuscript, the idea was to choose short subbolus durations to sample more accurately the labeled blood inflow. However, these short subboli also led to weak ASL signals that may question the sensitivity of the measurement method. Conversely, if we would have chosen longer subbolus durations, higher

ASL signal would have been measured, but then the accuracy of the retrieved ATT may have been questionable. This sub-bolus duration versus temporal resolution compromise could be further challenged by comparing the results from a Hadamard encoded labeling scheme with those obtained via a DASL scheme.

In rodents, the impact of ATT variations on CBF quantification is less pronounced than in humans: ATT values are shorter and magnetic fields are stronger, yielding longer blood  $T_1$  values. Therefore, in small animals, the interest when measuring ATT is more the ATT value in itself, since it can reflect underlying vascular pathologies [Hendrikse et al., 2004].

Regarding the pCASL package, several developments may be foreseen. Implementing crusher gradients would enable to measure tissue transit times and CBF values without vascular contamination, to be compared with the data from our study. Even better, a  $T_2$ -weighted, time-encoded ASL sequence, similar to Wells et al. [2013], could allow to simultaneously estimate arterial and tissue transit times. Using a pCASL labeling module instead of a FAIR technique would increase the rather low ASL SNR observed by the authors in that study.

We started to introduce background suppression pulses in the standard pCASL-EPI sequence to increase the ASL SNR when using the sequence with a 3D-EPI readout. In a next step, it would be interesting to implement other 3D-readout modules, such as GRASE or spiral, to reduce susceptibility artifacts.

Currently, only few 3D-ASL applications exist in rodents [Chugh et al., 2012]. Combining high field strength, i.e. 9.4 T, with a cryoprobe yields high quality images in mice anesthetized with isoflurane (cf. Appendix B.2). As a consequence, this opens the possibilities to characterize various pathological mouse models: e.g. in neurodegenerative disorders, psychiatric models or to study effects of pharmacological treatments [Bruns et al., 2015].

# APPENDICES



# A. CASL Reports

## A.1. Inversion efficiency report (CASL-FcFLASH)



Bruker BioSpin MRI

---

\$Revision: 1.4.2.2 \$Date: 2015/05/13 09:41:46 \$

## CASL FcFLASH Report

• 2016-02-29 17:05:00

## Table of Contents

1. CASL Parameters .....	2
2. Imaging Parameters .....	2
3. Reconstruction Parameters .....	3
4. Acquired Images .....	4

## 1. CASL Parameters

**Table 1. Labeling Parameters**

Display Name	Parameter	Value	Unit
Experiment Type	CASL_ExpType	Label_Control	
Acquisition Order	CASL_AcqOrder	Interleaved	
Control Images	CASL_ControlImages	1	
Label Images	CASL_LabelImages	1	
RF Power during Control	CASL_RFPowerYesNo	true	
B1 calculation mode	CASL_B1mode	Automatic	
Amplitude of B1 pulse	CASL_B1	5	$\mu$ T
Labeling Pulse Shape	CASL_PulseEnum	bp	
Labeling Pulse Power	CASL_RFPulAmpl.ppow	0.725	W
Labeling Pulse Amplitude	CASL_RFPulAmpl.pampl	6.021	V
Labeling Pulse Attenuation	CASL_RFPulAmpl.patt	1.396	dB
Labeling Position	CASL_LabelPos	Parallel	
Label Slice Offset	CASL_LabelSliceOffset	-20	mm
Labeling Time	CASL_LabelTime	200	ms
Post-Labeling Time	CASL_PostLabelTime	0	ms
Labeling Gradient	CASL_LabelGradient	10	mT/m
Labeling Gradient	CASL_LabelGradient	10	mT/m
Frequency list	CASL_FrequencyList	-8,515.28	Hz
Frequency list	CASL_FrequencyList	-4,257.64	Hz

## 2. Imaging Parameters

**Table 2. Imaging Parameters**

Display Name	Parameter	Value	Unit
Repetition Time	PVM_RepetitionTime	225	ms
Echo Time	PVM_EchoTime	6.168	ms
Dummy Scans	PVM_DummyScans	4	
Averages	PVM_NAverages	2	
Repetitions	PVM_NRepetitions	1	
Object Ordering Mode	PVM_ObjOrderScheme	Interlaced	
Read Offset	PVM_SPackArrReadOffset[0]	0	mm
Offset of Slices in Phase1 Direction	PVM_Phase1Offset[0]	0	mm
Slice Offset	PVM_SPackArrSliceOffset[0]	-15	mm

Display Name	Parameter	Value	Unit
Slices	PVM_SPackArrNSlices[0]	1	

### 3. Reconstruction Parameters

**Table 3. Reconstruction Options**

Display Name	Parameter	Value	Unit
Reconstruction Mode	RecoMethMode	Inversion_Eff	
Number of Carotids	CASL_NCarotids	2	
CASL mean inversion efficiency	CASL_IEMean	83.318	%
Mean IE ROI 1	CASL_IEAllCarotids[0].mean	84.301	%
SD IE ROI 1	CASL_IEAllCarotids[0].sd	3.554	
Adev IE ROI 1	CASL_IEAllCarotids[0].adev	2.877	
Min IE ROI 1	CASL_IEAllCarotids[0].min	78.449	
Max IE ROI 1	CASL_IEAllCarotids[0].max	92.078	
Number of voxels ROI 1	CASL_IEAllCarotids[0].nval	40	
Surface ROI 1	CASL_IEAllCarotids[0].surface	0.549	
Mean IE ROI 2	CASL_IEAllCarotids[1].mean	82.334	
SD IE ROI 2	CASL_IEAllCarotids[1].sd	3.219	
Adev IE ROI 2	CASL_IEAllCarotids[1].adev	2.642	
Min IE ROI 2	CASL_IEAllCarotids[1].min	73.996	
Max IE ROI 2	CASL_IEAllCarotids[1].max	86.599	
Number of voxels ROI 2	CASL_IEAllCarotids[1].nval	39	
Surface ROI 2	CASL_IEAllCarotids[1].surface	0.536	
ROI 1 Size	CASL_CarArrSize[0]	5	mm
ROI 1 Size	CASL_CarArrSize[0]	5	mm
ROI 1 Size	CASL_CarArrSize[0]	1	mm
ROI 2 Size	CASL_CarArrSize[1]	5	mm
ROI 2 Size	CASL_CarArrSize[1]	5	mm
ROI 2 Size	CASL_CarArrSize[1]	1	mm
ROI 1 Position	CASL_CarArrPosition[0]	6.393	mm
ROI 1 Position	CASL_CarArrPosition[0]	-10.656	mm
ROI 1 Position	CASL_CarArrPosition[0]	-15	mm
ROI 2 Position	CASL_CarArrPosition[1]	-5.574	mm
ROI 2 Position	CASL_CarArrPosition[1]	-9.344	mm
ROI 2 Position	CASL_CarArrPosition[1]	-15	mm
CASL_IECarotidMeanYN	CASL_IECarotidMeanYN	true	
CASL_IECarotidMeanYN	CASL_IECarotidMeanYN	true	
Remove Vessel Border	CASL_RemoveBorderYesNo	true	
Remove IE values lower than ...	CASL_AllowedIEDeviationYN	true	
Allowed deviation from maximum	CASL_AllowedIEDeviation	15	%
Store measured IE	StoreAfterReco	true	

## 4. Acquired Images

**Figure 1. Inversion Efficiency Map.**

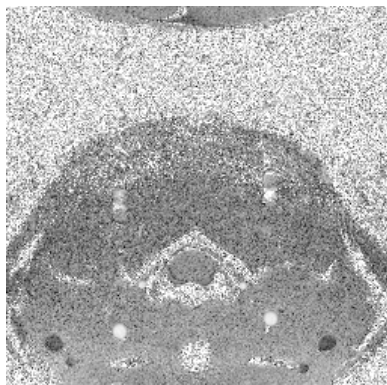
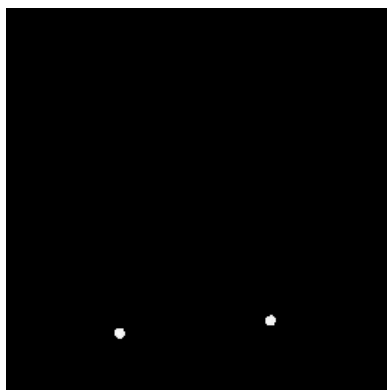


**Figure 2. Mask.**



## A.2. MT correction adjustment report (adjustement of CASL-EPI)



Bruker BioSpin MRI

---

\$Revision: 1.4.2.2 \$ \$Date: 2015/05/13 09:41:46 \$

## CASL EPI Report

- 2016-03-11 18:46:35

## Table of Contents

1. CASL Parameters .....	2
2. MT Correction .....	2
3. Imaging Parameters .....	3
4. Reconstruction Parameters .....	4
5. Acquired Images .....	4

## 1. CASL Parameters

**Table 1. Labeling Parameters**

Display Name	Parameter	Value	Unit
Experiment Type	CASL_ExpType	Label_Control	
Acquisition Order	CASL_AcqOrder	Dynamic	
Control Images	CASL_ControlImages	5	
Label Images	CASL_LabelImages	2	
RF Power during Control	CASL_RFPowerYesNo	true	
B1 calculation mode	CASL_B1mode	Automatic	
Amplitude of B1 pulse	CASL_B1	7	$\mu$ T
Labeling Pulse Shape	CASL_PulseEnum	bp	
Labeling Pulse Power	CASL_RFPulAmpl.ppow	1.421	W
Labeling Pulse Amplitude	CASL_RFPulAmpl.pampl	8.43	V
Labeling Pulse Attenuation	CASL_RFPulAmpl.patt	-1.527	dB
Labeling Position	CASL_LabelPos	Parallel	
Label Slice Offset	CASL_LabelSliceOffset	-20	mm
Labeling Time	CASL_LabelTime	3,000	ms
Post-Labeling Time	CASL_PostLabelTime	300	ms
Labeling Gradient	CASL_LabelGradient	10	mT/m
Frequency list	CASL_FrequencyList	-8,515.28	Hz
Frequency list	CASL_FrequencyList	-8,515.28	Hz
Frequency list	CASL_FrequencyList	6,812.224	Hz
Frequency list	CASL_FrequencyList	7,663.752	Hz
Frequency list	CASL_FrequencyList	8,515.28	Hz
Frequency list	CASL_FrequencyList	9,366.808	Hz
Frequency list	CASL_FrequencyList	10,218.336	Hz

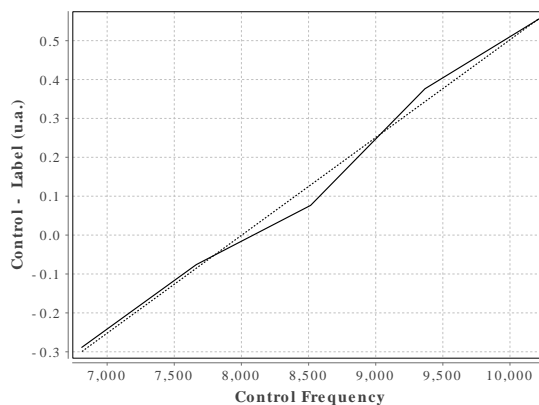
## 2. MT Correction

**Table 2. MT Correction Parameters**

Display Name	Parameter	Value	Unit
Control Frequency	CASL_OptControlFreq	8,524.127	Hz
Labeling Time MT	CASL_LabelTimeMT	3,000	ms
Control Images	CASL_ControlImagesMT	5	
CASL_ImagesMT	CASL_ImagesMT	7	

Display Name	Parameter	Value	Unit
Post-Labeling Time for MT adjustment	CASL_PostLabelTimeMT	300	ms
Labeling Time MT	CASL_LabelTimeMT	3,000	ms
MT correction frequency list	CASL_FrequencyListMT	-8,515.28	Hz
MT correction frequency list	CASL_FrequencyListMT	-8,515.28	Hz
MT correction frequency list	CASL_FrequencyListMT	6,812.224	Hz
MT correction frequency list	CASL_FrequencyListMT	7,663.752	Hz
MT correction frequency list	CASL_FrequencyListMT	8,515.28	Hz
MT correction frequency list	CASL_FrequencyListMT	9,366.808	Hz
MT correction frequency list	CASL_FrequencyListMT	10,218.336	Hz
CASL_GradMT	CASL_GradMT	0	mT/m
Control Frequency Step	CASL_MTcorrstep	10	%
CASL_MTcorrMap	CASL_MTcorrMap.prefix	/home/lydiane/ PV6.0.2.1/data/ lydiane	
CASL_MTcorrMap	CASL_MTcorrMap.study	20160309_162606	TestMT2_1_1
CASL_MTcorrMap	CASL_MTcorrMap.expno	25	
CASL_MTcorrMap	CASL_MTcorrMap.procno	1	
Dummy Scans MT correction	CASL_DummyScansMT	0	

Figure 1. MT Correction Results



### 3. Imaging Parameters

Table 3. Imaging Parameters

Display Name	Parameter	Value	Unit
Repetition Time	PVM_RepetitionTime	4,000	ms
Echo Time	PVM_EchoTime	0.375	ms
Dummy Scans	PVM_DummyScans	2	
Averages	PVM_NAverages	1	
Repetitions	PVM_NRepetitions	1	
Segments	NSegments	1	
Object Ordering Mode	PVM_ObjOrderScheme	Interlaced	

Display Name	Parameter	Value	Unit
Read Offset	PVM_SPackArrReadOffset[0]	0	mm
Offset of Slices in Phase1 Direction	PVM_Phase1Offset[0]	0	mm
Slice Offset	PVM_SPackArrSliceOffset[0]	0	mm
Slices	PVM_SPackArrNSlices[0]	1	

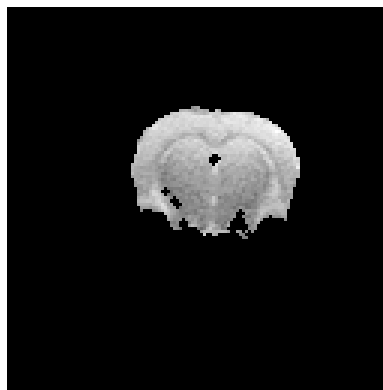
## 4. Reconstruction Parameters

**Table 4. Reconstruction Options**

Display Name	Parameter	Value	Unit
Reconstruction Mode	RecoMethMode	Default	
Repetition Averaging	CASL_RepetitionAveraging	false	
Outlier Detection	CASL_OutlierDetection	false	
Transit time	CASL_TransitTime	300	ms
Water partition coefficient (lambda)	CASL_lambda	0.9	mL/g
CASL inversion efficiency	CASL_IEMean	80	%
Take measured IE if calculated	RestoreAfterReco	true	
Longitudinal relaxation time for blood	CASL_T1b	2,430	ms
Longitudinal relaxation time for tissue	CASL_T1app	1,650	ms

## 5. Acquired Images

**Figure 2. Acquired Image 1/1.**



## A.3. CBF measurement report (CASL-EPI)



Bruker BioSpin MRI

\$Revision: 1.4.2.2 \$ \$Date: 2015/05/13 09:41:46 \$

## CASL EPI Report

- 2016-03-11 17:51:12

## Table of Contents

1. CASL Parameters .....	2
2. MT Correction .....	2
3. Imaging Parameters .....	3
4. Reconstruction Parameters .....	4
5. Acquired Images .....	5

## 1. CASL Parameters

**Table 1. Labeling Parameters**

Display Name	Parameter	Value	Unit
Experiment Type	CASL_ExpType	Label_Control	
Acquisition Order	CASL_AcqOrder	Interleaved	
Control Images	CASL_ControlImages	1	
Label Images	CASL_LabelImages	1	
RF Power during Control	CASL_RFPowerYesNo	true	
B1 calculation mode	CASL_B1mode	Automatic	
Amplitude of B1 pulse	CASL_B1	7	$\mu$ T
Labeling Pulse Shape	CASL_PulseEnum	bp	
Labeling Pulse Power	CASL_RFPulAmpl.ppow	1.421	W
Labeling Pulse Amplitude	CASL_RFPulAmpl.pampl	8.43	V
Labeling Pulse Attenuation	CASL_RFPulAmpl.patt	-1.527	dB
Labeling Position	CASL_LabelPos	Parallel	
Label Slice Offset	CASL_LabelSliceOffset	-20	mm
Labeling Time	CASL_LabelTime	3,000	ms
Post-Labeling Time	CASL_PostLabelTime	300	ms
Labeling Gradient	CASL_LabelGradient	10	mT/m
Frequency list	CASL_FrequencyList	-8,515.28	Hz
Frequency list	CASL_FrequencyList	8,524.127	Hz

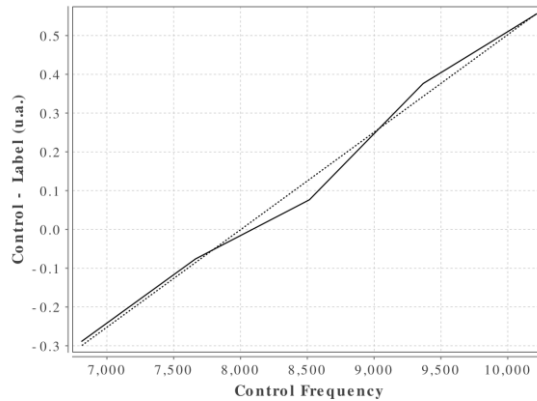
## 2. MT Correction

**Table 2. MT Correction Parameters**

Display Name	Parameter	Value	Unit
Control Frequency	CASL_OptControlFreq	8,524.127	Hz
Labeling Time MT	CASL_LabelTimeMT	3,000	ms
Control Images	CASL_ControlImagesMT	5	
CASL_ImagesMT	CASL_ImagesMT	7	
Post-Labeling Time for MT adjustment	CASL_PostLabelTimeMT	300	ms
Labeling Time MT	CASL_LabelTimeMT	3,000	ms
MT correction frequency list	CASL_FrequencyListMT	-8,515.28	Hz
MT correction frequency list	CASL_FrequencyListMT	-8,515.28	Hz
MT correction frequency list	CASL_FrequencyListMT	6,812.224	Hz

Display Name	Parameter	Value	Unit
MT correction frequency list	CASL_FrequencyListMT	7,663.752	Hz
MT correction frequency list	CASL_FrequencyListMT	8,515.28	Hz
MT correction frequency list	CASL_FrequencyListMT	9,366.808	Hz
MT correction frequency list	CASL_FrequencyListMT	10,218.336	Hz
CASL_GradMT	CASL_GradMT	0	mT/m
Control Frequency Step	CASL_MTcorrstep	10	%
CASL_MTcorrMap	CASL_MTcorrMap.prefix	/home/lydiane/ PV6.0.2.1/data/ lydiane	
CASL_MTcorrMap	CASL_MTcorrMap.study	20160309_162606	TestMT2_1_1
CASL_MTcorrMap	CASL_MTcorrMap.expno	21	
CASL_MTcorrMap	CASL_MTcorrMap.procno	1	
Dummy Scans MT correction	CASL_DummyScansMT	0	

**Figure 1. MT Correction Results**



### 3. Imaging Parameters

**Table 3. Imaging Parameters**

Display Name	Parameter	Value	Unit
Repetition Time	PVM_RepetitionTime	4,000	ms
Echo Time	PVM_EchoTime	0.375	ms
Dummy Scans	PVM_DummyScans	2	
Averages	PVM_NAverages	1	
Repetitions	PVM_NRepetitions	30	
Segments	NSegments	1	
Object Ordering Mode	PVM_ObjOrderScheme	Interlaced	
Read Offset	PVM_SPackArrReadOffset[0]	0	mm
Offset of Slices in Phase1 Direction	PVM_Phase1Offset[0]	0	mm
Slice Offset	PVM_SPackArrSliceOffset[0]	0	mm
Slices	PVM_SPackArrNSlices[0]	1	

## 4. Reconstruction Parameters

**Table 4. Reconstruction Options**

Display Name	Parameter	Value	Unit
Reconstruction Mode	RecoMethMode	CBF	
Repetition Averaging	CASL_RepetitionAveraging	true	
Outlier Detection	CASL_OutlierDetection	true	
Transit time	CASL_TransitTime	300	ms
Water partition coefficient (lambda)	CASL_lambda	0.9	mL/g
CASL inversion efficiency	CASL_IEMean	80	%
Take measured IE if calculated	RestoreAfterReco	true	
Longitudinal relaxation time for blood	CASL_T1b	2,430	ms
Longitudinal relaxation time for tissue	CASL_T1app	1,650	ms

**Table 5. Outlier Detection**

Display Name	Parameter	Value	Unit
Outlier threshold	CASL_OutlierThreshold	1.5	
Number of outliers Slice 1 (label)	CASL_OutlierCnt	3	
Number of outliers Slice 1 (control)	CASL_OutlierCnt	4	

Outlier Detection Results:

**Figure 2. Label Slice 1**

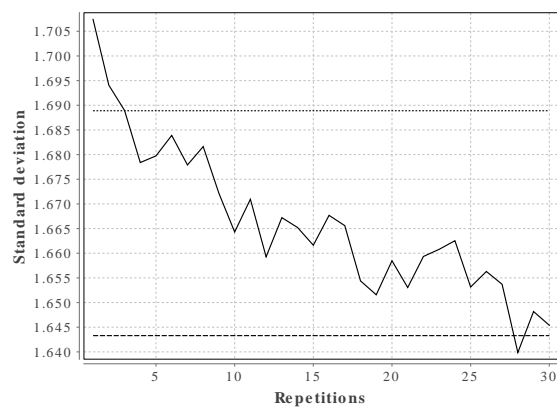
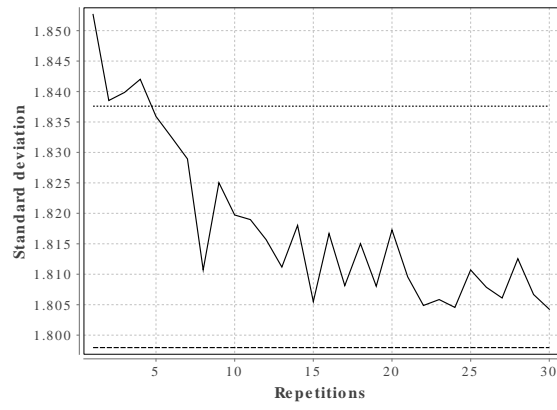
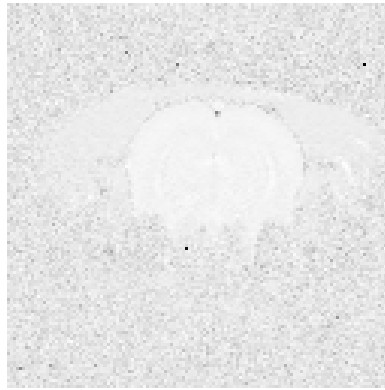


**Figure 3. Control Slice 1**



## 5. Acquired Images

**Figure 4. Acquired Image 1/1.**





## B. 3D Arterial Spin Labeling

### B.1. 3D Arterial Spin Labeling Optimization

This 3D ASL optimization is part of the master thesis of Agathe Leroux, who I had the opportunity to co-supervise. Here, the main optimization results are shortly summarized.

The 3D-pCASL has been optimized both on a water tube and in three rats. The imaging readout consisted in a 3D-EPI Bruker sequence and the tested volume contained 8 slices. Two saturation bands were positioned on either sides of the imaging area, to prevent aliasing of potential external signal, originating from imperfect slice excitation, into the volume of interest.

Different imaging and labeling parameters were tested, e.g. image slice thickness, readout bandwidth (BW), distance between saturation bands and image volume or pCASL labeling duration. 2D slices were acquired as well for comparison. During 2D acquisitions, the number of averages was chosen in order to compensate the fact that in 3D the labeling experiment is repeated for each phase step in the slice direction. 2D and 3D experiments had therefore a similar scan duration. To find the most adapted parameter set, the SNR and the perfusion SNR were calculated. Main results are shown in Fig. B.1.

Fig. B.1a shows the dependence of the SNR per slice across the distance between the saturation bands and the imaging area. The higher the distance, the higher the SNR. For saturation bands positioned at 0.625 mm from the imaging slice or lower, saturation bands cancel out the external signal due to imperfect slice excitation. However the border imaging slices are also partially saturated. Conversely, for bands positioned after this distance, the saturation bands cover less and less the external border signal and lose their anti-aliasing effect. The mean noise represented in pink, has an opposite behavior than SNR. Therefore, to combine the anti-aliasing effect and the best SNR, the chosen value is the threshold one since it delivers the highest SNR on the border slices without any aliasing effect on the central slices.

Fig. B.1b illustrates the perfusion SNR as a function of the readout bandwidth. We observe that perfusion SNR is proportional to  $1/\sqrt{BW}$ . The results are almost equivalent in 2D and 3D. However, the lowest BW values cause ghost apparitions and when increasing the BW, the echotime (TE) can be reduced, limiting the signal loss. A compromise value of 350 kHz has been chosen.

Concerning the evolution of the perfusion SNR with the labeling duration represented

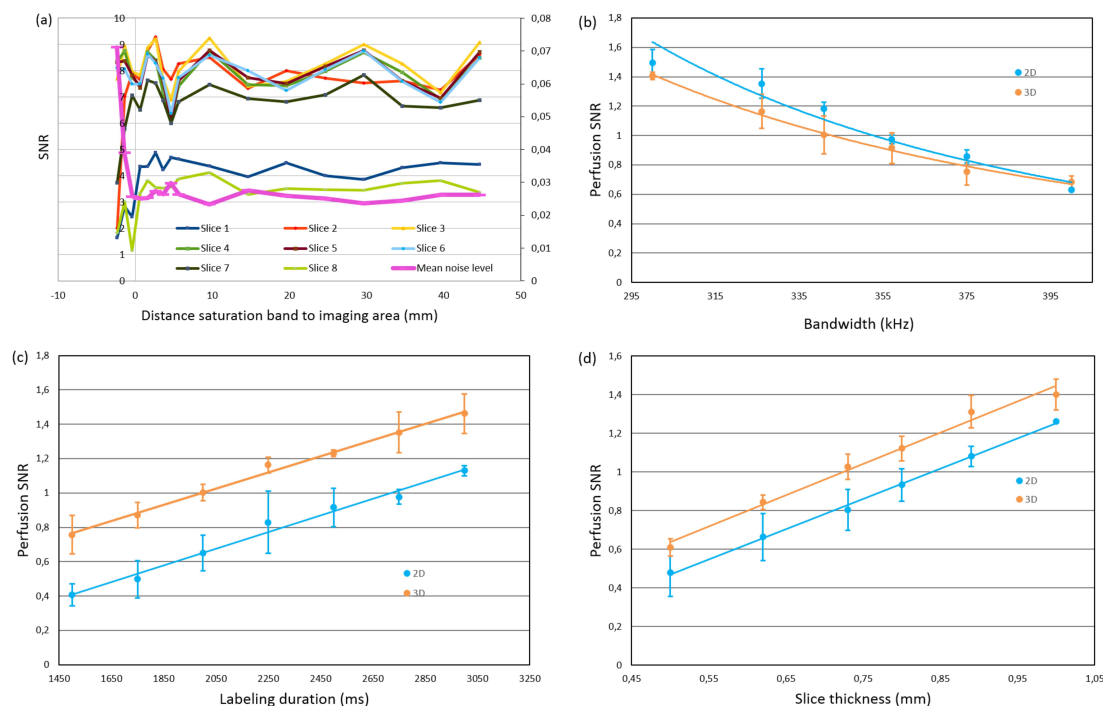


Figure B.1.: (a) SNR as a function of the distance between the saturation band and the imaging area for the 8 slices (slice1 = bottom and slice8 = top of the tube). The mean noise level is represented in pink. (b) Perfusion SNR as a function of the bandwidth for the 5<sup>th</sup> slice for 2D pCASL (blue) and 3D pCASL (orange) with a fixed echo time. (c) Perfusion SNR as a function of the labeling duration for the 5<sup>th</sup> slice in 2 (blue) and 3D (orange) pCASL. (d) Perfusion SNR as a function of the slice thickness for the 5<sup>th</sup> slice in 2D (blue) and 3D (orange) pCASL. In panels (b) (c) and (d), the markers show the mean values  $\pm$  SD and full lines represent a fit to the data.

in Fig. B.1c, as expected, a linear relation has been found with the labeling duration for both 2D and 3D in similar proportions, even if the 3D perfusion SNR is higher than 2D one. In 3D, all slices are acquired at the same post labeling time which is not the case for the 2D acquisitions: in 2D, slices are acquired the one after the other, leading to a signal loss between the first and last acquired slices. Since only the central slice has been studied here, this explains the difference between the 2D and 3D perfusion SNR values. A too long labeling duration causes an increase of the acquisition duration, therefore a compromise between high perfusion SNR and acquisition duration has to be made, which depends on the application. For standard pCASL measurements in rats, we chose a labeling duration of 3 s.

A linear relation between the perfusion SNR and the slice thickness is observed in Fig. B.1d with a higher 3D perfusion SNR. This can be explained by the fact that the 5<sup>th</sup> slice is considered here, leading to different PLDs in 2D and 3D. For standard pCASL application in rats, we chose the value yielding the best perfusion SNR, i.e. 1 mm, since the resolution stays acceptable for this value.

This 3D-EPI readout has been used in two studies in mice presented in the next sections. Some parameters were adapted to be suited to mouse brain imaging.

## B.2. Combined 3D perfusion and diffusion MRI to phenotype the mouse brain: Evaluation and application to a model of schizophrenia

This work was performed in collaboration with Ivy Uszynski, a PhD student working on diffusion imaging in mice, and has been presented as a poster and at the perfusion study group at the ISMRM 25<sup>th</sup> Annual Scientific Meeting in Honolulu, USA (Combined 3D perfusion and diffusion MRI to phenotype the mouse brain: Evaluation and application to a model of schizophrenia, Hirschler\* L, Uszynski\* I, Warnking J, Poupon C, Deloulme JC, Barbier EL).

### Purpose

To phenotype mouse model of brain diseases, perfusion and diffusion imaging both represent powerful tools: they do not require the use of contrast agent and provide quantitative, complementary, metrics. Indeed, imaging cerebral blood flow (CBF) may be seen as a surrogate marker of brain metabolism while diffusion imaging provides the structural aspects of brain wiring. To evaluate the potential of combined CBF and diffusion phenotyping, we first optimized this protocol on C57Bl6 mice and then evaluated the effect of knocking-out (KO) the microtubule-associated protein 6 (MAP6), which has been shown to play a critical role during the development of cerebral axonal tracts [Deloulme et al., 2015]. Experiments were performed on homogeneous C57Bl6/129Sv mice using 3D pseudo-continuous Arterial Spin Labeling (pCASL) and 3D diffusion tensor imaging (DTI) at 9.4T.

### Methods

**Protocol** Experiments were performed on a 9.4 T system (Bruker Biospec, AVIII-HD) with an 86 mm volume coil for excitation and a 4-channel cryoprobe surface coil for reception.

After anatomical images, we acquired one 3D diffusion weighted imaging sequence as follows: 4-shot SE-3D-EPI sequence ( $TR/TE = 500/17.3$  ms; 200  $\mu\text{m}$  isotropic resolution) with diffusion gradients characteristics  $\delta/\lambda = 3.3/6.5$  ms, 15 diffusion directions with a b-value of  $1000 \text{ s/mm}^2 + 3 \text{ b} = 0 \text{ s/mm}^2$  reference images for an acquisition time of 49 min.

Before and after the DTI sequence, a 3D pCASL-EPI sequence was performed: unbalanced pCASL-labeling pulses were applied in the mouse's neck (at -12 mm from the isocenter) during 3 s followed by a 300 ms post-labeling delay. The labeling consisted of Hanning-shaped RF pulses with an average amplitude of 5  $\mu\text{T}$ , duration of 400  $\mu\text{s}$ , repeated every 800  $\mu\text{s}$ , with optimized phases.  $G_{\text{max}}/G_{\text{ave}}$  was set to 90/10 mT/m instead

of the usual 45/5 mT/m (cf. Chapter 3). The reason for setting higher gradient amplitudes is that the 3D imaging volume in this study contains slices closer to the labeling plane than in our former studies. Therefore, by increasing the labeling gradient, the frequency difference between that of protons at the labeling plane and that of macromolecules in the brain tissue is increased, and MT effects are reduced as a consequence. Image acquisition was performed through single-shot EPI: TE/TR = 4000/22 ms, resolution =  $0.2 \times 0.2 \times 0.6$  mm<sup>3</sup>, 4 repetitions, acquisition time 15 min.

For CBF quantification, the labeling efficiency was measured 4 mm downstream the labeling plane with a flow-compensated, ASL-encoded FLASH. The total acquisition time per mouse was 2 h.

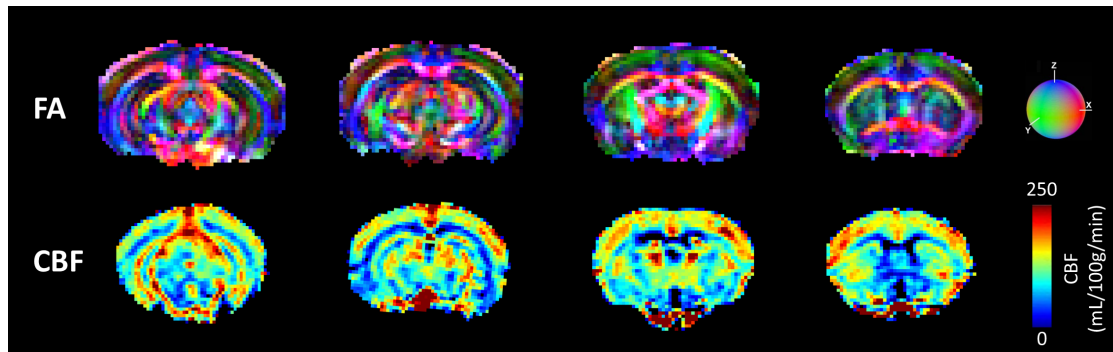


Figure B.2.: Selection of 4 axial CBF (mL/100g/min) and FA maps of a C57Bl6 mouse.

**Animals** The protocol was first adjusted on twelve C57Bl6 mice. Afterwards, it was applied on 12 wild type (WT) (age:  $22 \pm 2$  weeks) and 11 MAP6 KO (age:  $21 \pm 2$  weeks) male mice with a C57Bl6/129Sv genetic background. Mice were anesthetized using isoflurane (1.5-2%) in air:O<sub>2</sub> 70:30%.

**Post-processing** DTI data were processed using the Connectomist toolbox [Duclap et al., 2012]. Quantitative CBF maps were calculated (cf. post-processing in Chapter 4) with an assumed value of 300 ms for arterial transit time (ATT).

For all mice, the data were carefully registered to an atlas [Calabrese et al., 2015] after a skull-stripping step (Figure B.3), which allowed automatic segmentation of 148 regions. 11 grey- (GM) and white matter (WM) regions of interest (Figure B.6) were then particularly analyzed to better disentangle the results.

## Results

Fig. B.2 shows a slice selection of CBF and fractional anisotropy (FA) maps.

The mean CBF and DTI parameters values in C57Bl6 mice were calculated in 148 ROIs. A region-size weighted correlation between FA and CBF with  $R = 0.58$  ( $p < 0.05$ )

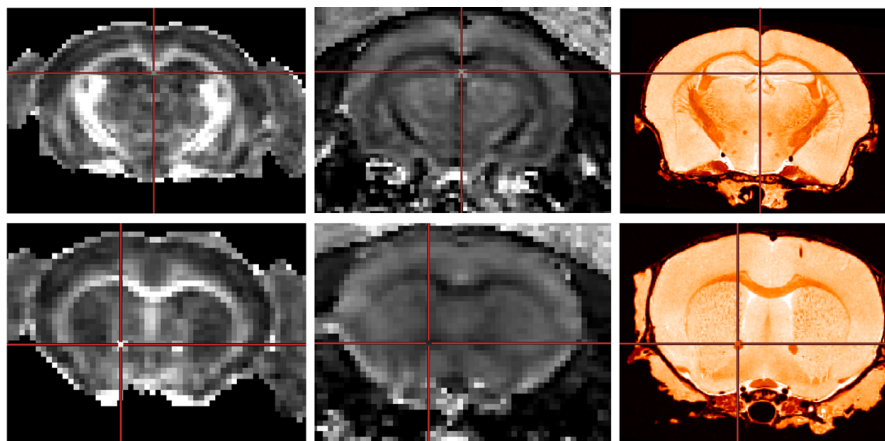


Figure B.3.: Selection of two slices (top and bottom rows) presenting the result of the registration for a WT mice. From left to right: FA map, CBF map and T<sub>2</sub>-weighted image of the atlas.

was found (Fig. B.4b): the higher the FA, the lower the CBF. Radial diffusivity (RD) follows an inverse trend (Fig. B.4d), whereas mean diffusivity (MD) appears to be CBF-independent (Fig. B.4d). Regions that show high FA and low CBF are predominantly white matter regions (red dots), whereas gray matter (blue dots; cf. atlas Fig. B.4a) show low FA and high perfusion. CBF remained globally stable during the diffusion scan (Fig. B.4e).

For the KO mice, the FA was significantly reduced in four regions (Fig. B.5 and B.6b), and the RD was increased in the fimbria. No significant CBF changes were observed between KO and WT mice. An average GM/WM CBF of  $(153 \pm 23)/(73 \pm 13)$  mL/100g/min and FA of  $(0.26 \pm 0.04)/(0.55 \pm 0.08)$  was found.

## Discussion and conclusion

This study shows the successful measurement of *in vivo* high-resolution whole-brain 3D perfusion and diffusion sequences in 20 mice.

A correlation between diffusion parameters and CBF was observed. The trends of FA-decrease in white matter regions that are not accompanied by significant CBF variations in MAP6-KO compared to WT mice may show that a white matter alteration does not necessarily induce vascular changes. This may be consistent with the fact that the MAP6-KO mouse model is known to show morphological and structural deficits but no neurodegenerative alterations [Deloulme et al., 2015], in which both CBF and white matter variations are expected [Wells et al., 2015]. Influence of ATT on the CBF quantification could also bias the CBF evaluations in the KO/WT mice [Alsop et al., 2015]. Mapping this parameter could allow for more reliable perfusion comparisons.

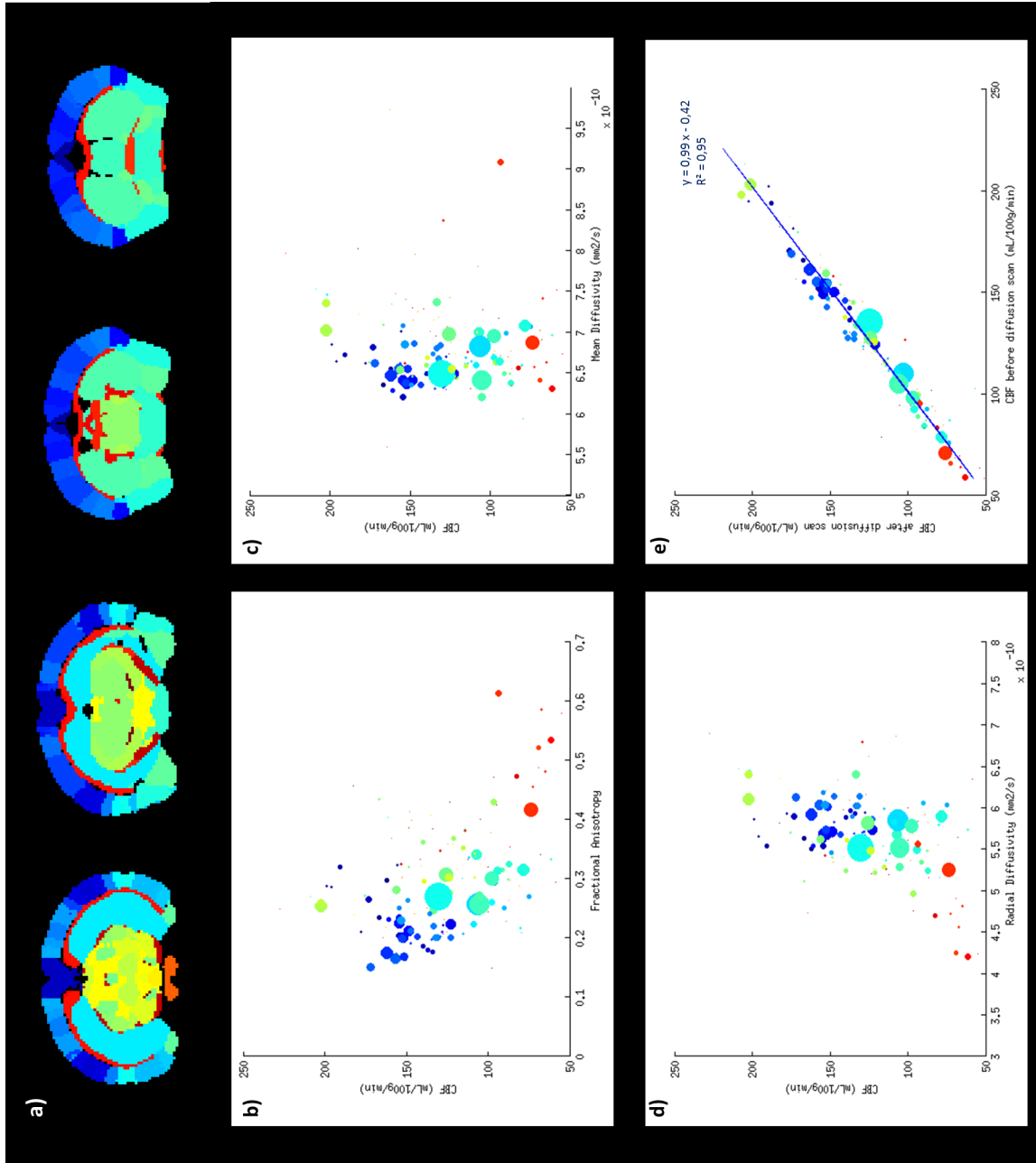


Figure B.4.: (a) Selection of 4 slices of the mouse brain atlas used for segmentation. Correlation between CBF and (b) FA, (c) MD and (d) RD on C57Bl6 mice for the segmented regions. CBF after vs. before the diffusion scan is plotted on panel (e). The blue line represents a linear regression. For all panels, the dot's size is proportional to the region's atlas color: dark blue colors represent gray matter regions and white matter regions are represented in shades of red.

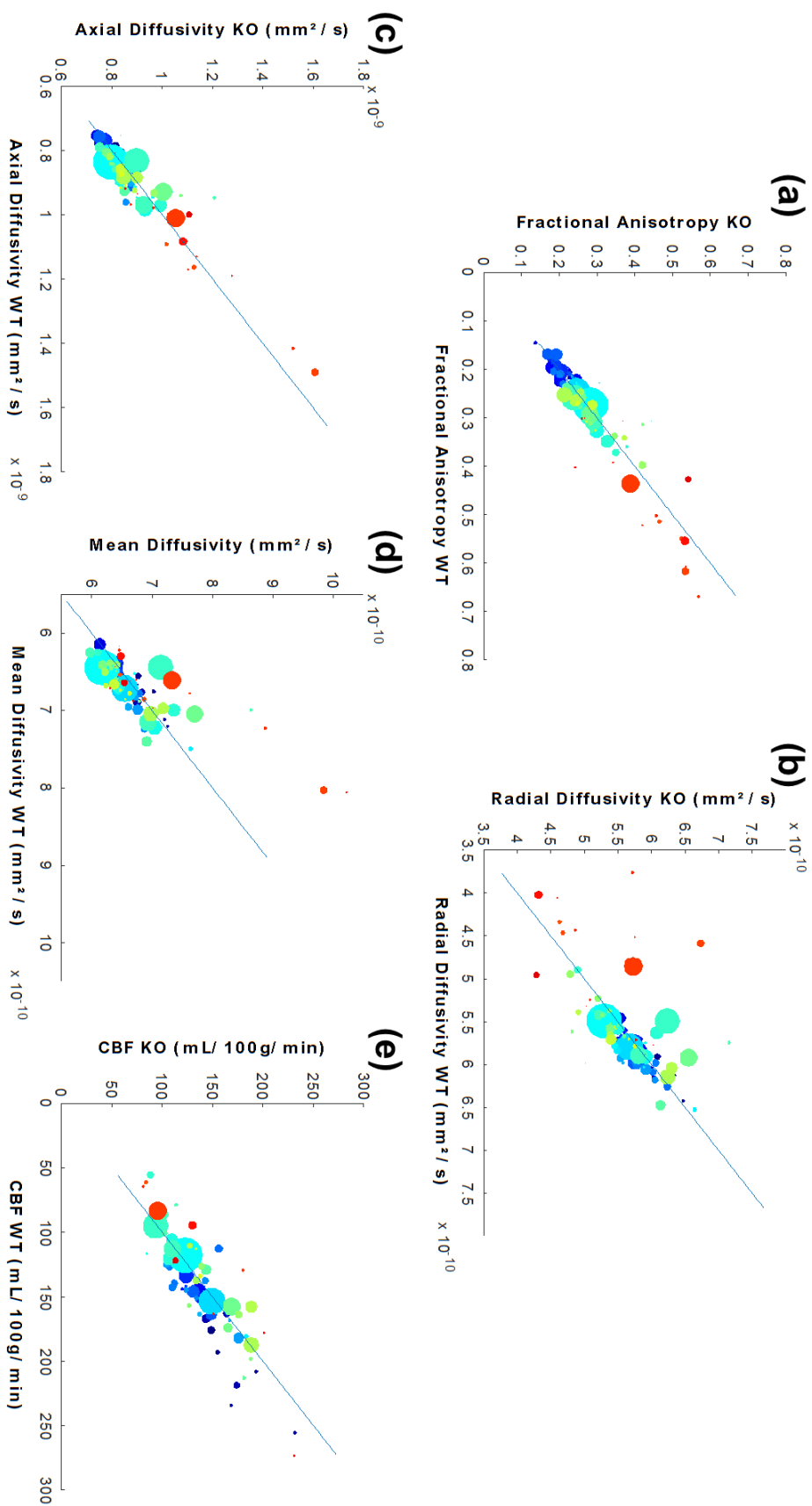


Figure B.5.: Comparison between WT and KO mice for (a) FA, (b) RD, (c) AD, (d) MD and (e) CBF in the 148 regions. The lines correspond to the identity function and the dots' color code is the same as that of Figure B.4.

B.2. Combined 3D perfusion and diffusion MRI to phenotype the mouse brain:  
Evaluation and application to a model of schizophrenia

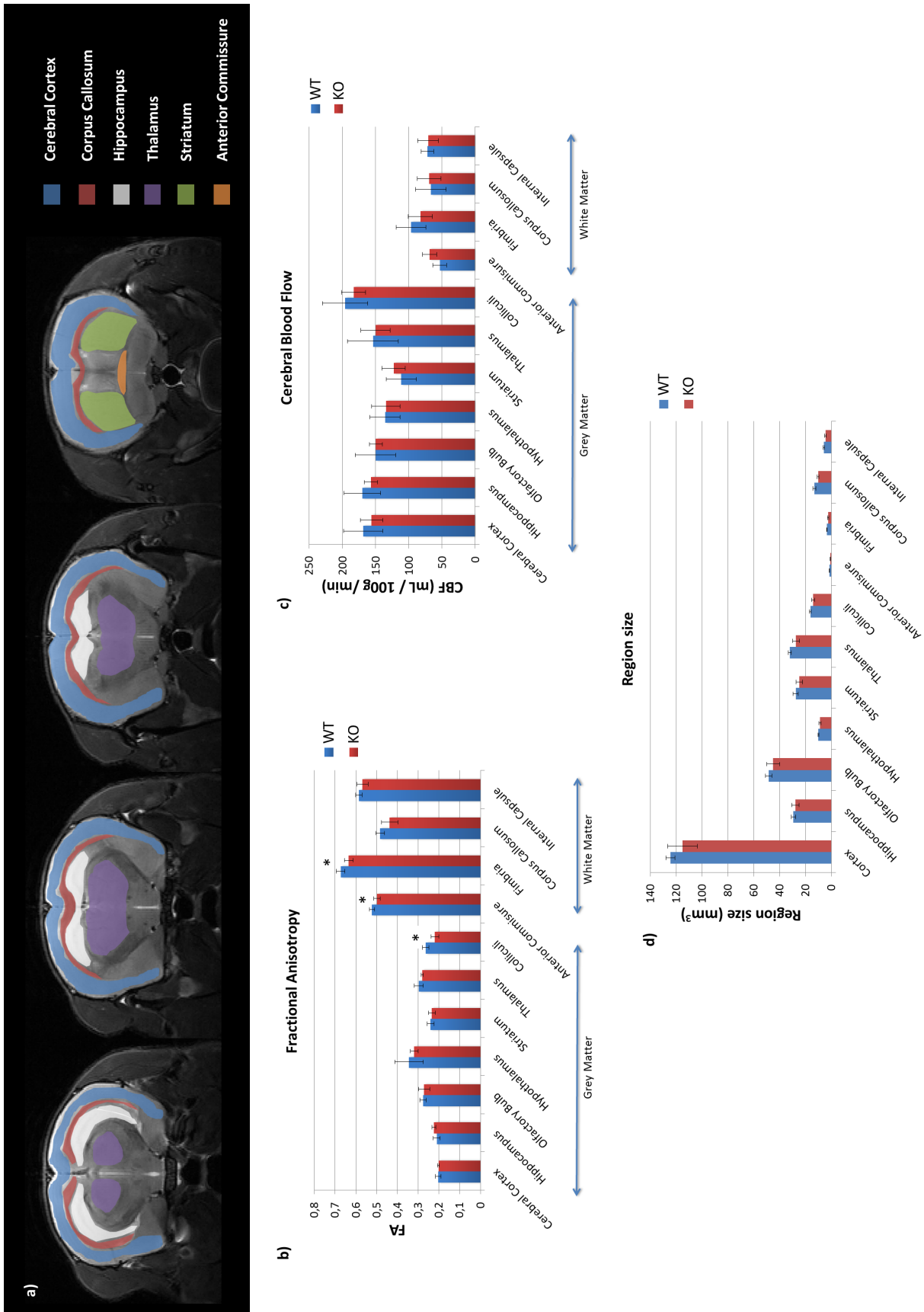


Figure B.6.: (a) Anatomical images of a WT mouse with 6 (out of 11) ROIs. Comparison between KO and WT mice in 11 regions for (b) FA and (c) CBF.



### B.3. 3D Dynamic Arterial Spin Labeling (DASL) in mice

A 3D dynamic pCASL was implemented and the obtained results in twenty mice are shown in this appendix. This work has been presented as a poster at the ISMRM 25<sup>th</sup> Annual Scientific Meeting in Honolulu, USA. (3D Dynamic Arterial Spin Labeling (DASL) in mice, Hirschler L, Uszynski I, Warnking J, Barbier EL).

#### Purpose

In preclinical perfusion studies, multiple 2D-slices are commonly acquired to measure perfusion [Duhamel et al., 2012; Debacker et al., 2016]. However, this readout limits the number of slices for which ATT can be measured accurately in rodents: the time it takes to acquire all slices (~30 ms per slice) rapidly exceeds the shortest ATTs, which are around 100 ms in healthy mice (cf. Chapter 5). Thus, accurate blood arrival sampling becomes difficult for the last acquired slices. A 3D-readout is therefore particularly interesting, since it allows for having the same postlabeling delay (PLD) for all acquired slices, without any additional delay due to the acquisition order.

In this study, we implemented and optimized a dynamic ASL labeling scheme [Barbier et al., 1999, 2001b] with a 3D echo planar imaging (EPI) readout to simultaneously map CBF, ATT and tissue  $T_1$  ( $T_{1t}$ ) in the mouse brain. Then, we applied the developed sequence on a mouse model of schizophrenia to evaluate the effect of knocking-out (KO) the microtubule associated protein 6 (MAP6) – a protein that has been shown to play a critical role during the development of cerebral axonal tracts [Deloulme et al., 2015]- on ATT and CBF.

#### Methods

Experiments were performed on a 9.4 T horizontal scanner (Bruker Biospec, AVIII-HD) with a 86 mm-volume coil for excitation and a 4-channel cryoprobe surface coil for reception. Mice were anesthetized using isoflurane (1.5-2%) in air:O<sub>2</sub> 70:30%. Two groups of C57Bl6/129Sv male mice (n = 10 per group) were studied: a wild type (WT) group and a group for which MAP 6 was knocked out (KO).

Unbalanced pCASL labeling pulses were applied in the mice's neck (at -12 mm from the isocenter) during 4 s following the DASL scheme shown on Fig. B.7. This scheme is optimized to sample the signal with high accuracy (50 ms temporal resolution) around the blood arrival time (i.e. between 0-0.4 s and 2-2.4 s) and with lower temporal resolution (200 ms) during the capillary blood filling (i.e. from 0.4-2 s and 2.4-4 s).

The labeling pulses consisted of Hanning window shaped RF pulses with an average amplitude of 5  $\mu$ T, duration of 400  $\mu$ s, repeated every 800  $\mu$ s, with optimized phases (cf. Chapter 4).  $G_{\max}/G_{\text{ave}}$  was set to 90/10 mT/m.

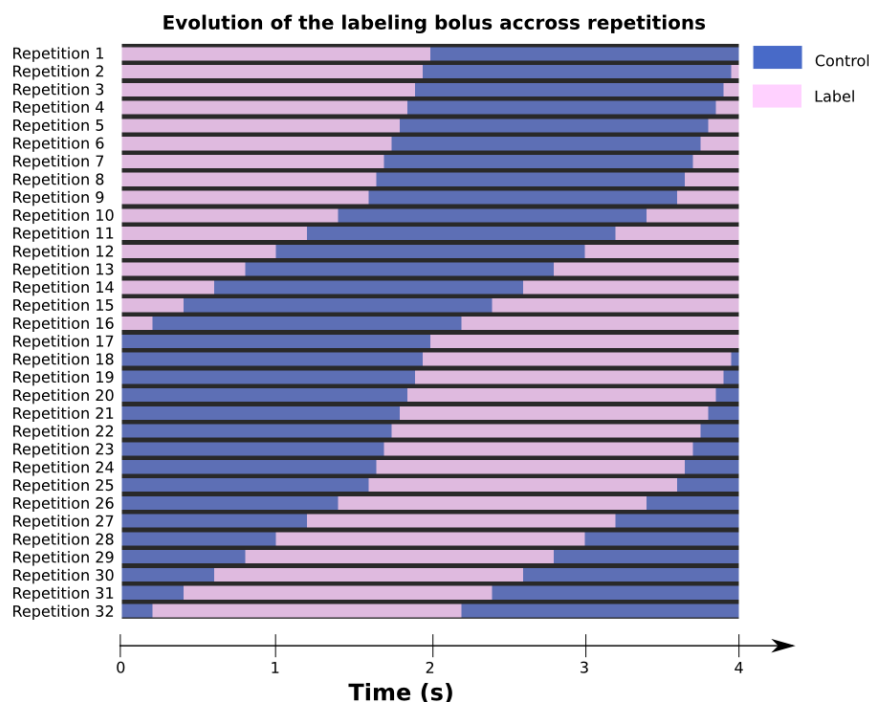


Figure B.7.: Dynamic pCASL labeling scheme. The labeling function changes at each repetition. The signal sampling frequency was increased between 0 and 0.4 s (i.e. from repetition 1 to 9) and from 2 to 2.4 s (i.e. from repetition 17 to 25) to sample more accurately the arterial transit time.

Image acquisition was performed through single-shot EPI:  $TE/TR = 4000/22$  ms, resolution =  $0.2 \times 0.2 \times 1.6$  mm<sup>3</sup>, 10 slices,  $T_{acq} = 22$  min. For CBF quantification, the labeling efficiency was measured 4 mm downstream the labeling plane with a flow-compensated, ASL-encoded FLASH. The signal time-course from the DASL experiment was fitted voxel-by-voxel to the model described by Barbier et al. [1999] (Fig. B.8) to obtain quantitative CBF, ATT and  $T_{1t}$  maps. ROIs were manually drawn in four brain regions.

## Results and discussion

Fig. B.9 shows examples of CBF, ATT and  $T_{1t}$  maps obtained from a 3D-DASL-EPI experiment. The observed contrast in the CBF maps is as expected, with higher cortical and thalamic perfusion values compared to white matter. Although the quantitative CBF values (Fig. B.10a) are much higher than that acquired with standard, 2D, pCASL [Duhamel et al., 2012; Hirschler\* et al., 2016], they are in the range of those measured with an Hadamard-encoded ASL scheme (cf. Chapter 5): in WT mice we measured an average brain CBF of  $323 \pm 95$  mL/100g/min. ATT values ( $236 \pm 68$  ms on average,

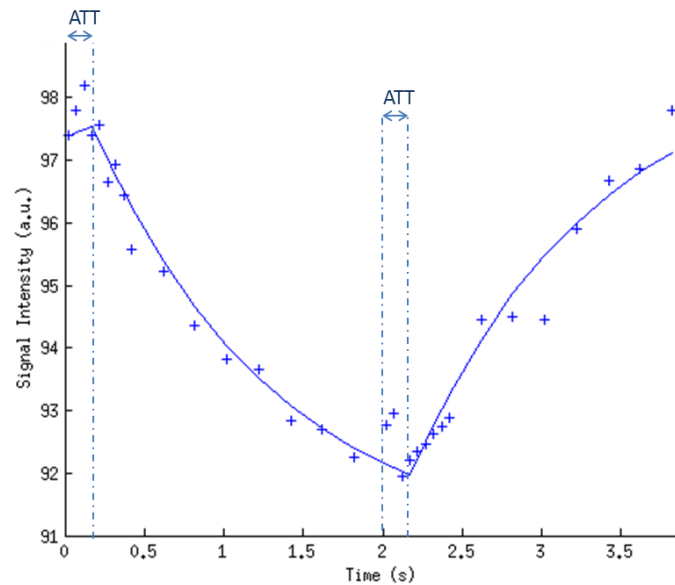


Figure B.8.: Example of the signal time-course from a single voxel as a function of time. Also plotted is the model fitted to the data. For this voxel, the estimated CBF was 220 mL/100g/min, the ATT 175 ms and the apparent  $T_{1t}$  1122 ms.

Fig. B.10b) are also in the same range as the one we previously measured in Chapter 5 and the regional variations are similar, with lower hippocampal transit times compared to other gray matter structures (cortex, thalamus and striatum).

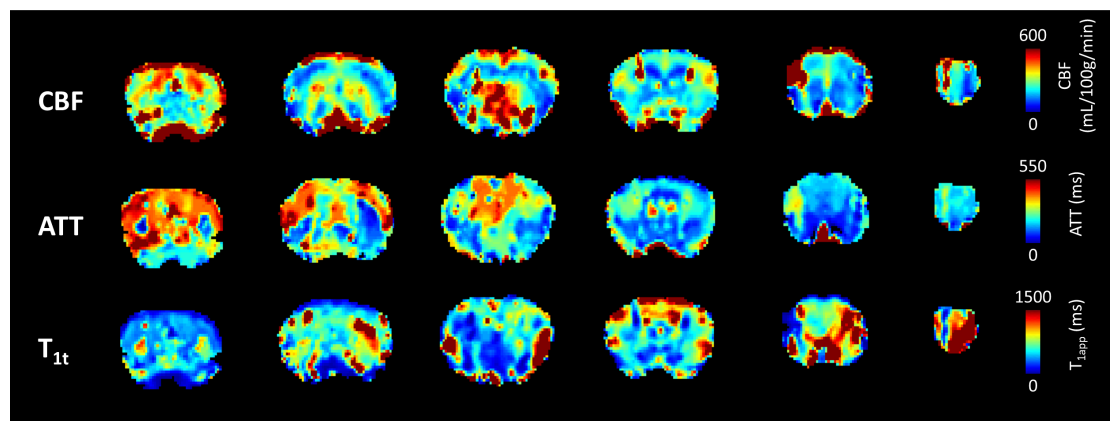


Figure B.9.: Selection of 6 axial CBF (mL/100g/min), ATT (ms) and  $T_{1t}$  (ms) maps obtained on a mouse at 9.4 T using dynamic ASL with a 3D-EPI readout.

For all slices,  $T_{1t}$  ( $811 \pm 282$  ms on average in the brain, Fig. B.10c) is lower than the expected tissue  $T_1$  (i.e. 1.7 s at 9.4 T). This low  $T_{1t}$  may be ascribed to the presence of intravascular signal in our time-encoded ASL approach (inflow and outflow effects). This intravascular signal and short  $T_{1t}$  may explain the high CBF values. Contrary to time-encoded measurements performed on humans (with longer transit times), short

ATT values in rodents induce more intravascular signal and require a finer temporal sampling.

In our study, the WT and KO mice showed similar CBF and ATT values (Fig. B.10a and b). The WT/KO variability (i.e. SD/mean) on CBF and ATT was 1 and 3%, respectively, suggesting a reproducible approach.

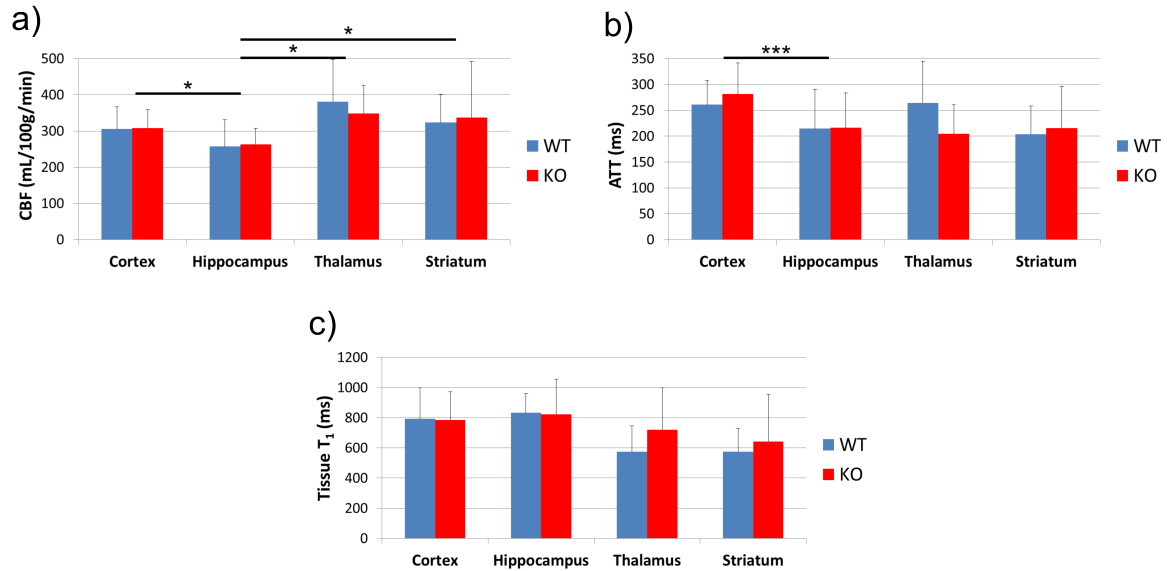


Figure B.10.: Comparison between WT and KO mice in 4 brain regions for (a) CBF, (b) ATT and (c)  $T_{1t}$ . \* (resp.\*\*\* ) indicate significant ( $p < 0.05$ , resp.  $p < 0.01$ ) differences between brain regions ( $n = 20$  animals in total).

## Conclusion

This study shows the successful implementation of 3D-DASL-EPI in mice. The obtained preliminary results are promising, since the ATT and CBF values are in good agreement with those previously observed in mice with Hadamard-encoded ASL.  $T_{1t}$  appears to be higher than expected. Therefore, the use of a separate  $T_1$  map could produce more precise and more robust CBF maps. Finally, the previous limitation to  $\sim 3$  2D-slices has been overcome with an optimized 3D-readout that allows for measuring the desired number of slices.

## C. Curriculum Vitae

LYDIANE HIRSCHLER

### Professional Experience

---

- 2014-2017 GRENOBLE INSTITUTE OF NEUROSCIENCE, GRENOBLE, FRANCE  
& BRUKER BIOSPIN MRI, ETTLINGEN, GERMANY  
**PhD in Physics - 3 years**  
Development of preclinical brain perfusion imaging using arterial spin labeling  
Supervisor: Emmanuel BARBIER, Co-supervisor: Jan WARNKING
- 2013 GRENOBLE INSTITUTE OF NEUROSCIENCE, GRENOBLE, FRANCE  
**Engineer assistant - 4 months**  
Diffusion tractography (data acquisition and processing) – Adaptation of a human tractography software (Connectomist) to animal studies.
- 2013 GRENOBLE INSTITUTE OF NEUROSCIENCE, GRENOBLE, FRANCE  
**Internship - 6 months**  
pCASL & CO<sub>2</sub> challenge: pCASL labeling parameter optimization and application on cerebral perfusion measurements during a CO<sub>2</sub> challenge on rats.
- 2012 BRUKER BIOSPIN MRI, RHEINSTETTEN & ETTLINGEN, GERMANY  
**Internship - 10 weeks**  
MRI and NMR applications, RF coil building for mouse imaging, development of visualization tools for diffusion tensor imaging data.
- 2011 MASTER-TECH, SCHNEIDER ELECTRIC, MOIRANS, FRANCE  
**Internship - 11 weeks**  
Creation of security training processes and questionnaires for operators (production unit).

### Education

---

- 2014-2017 **PhD in Physics**  
UNIVERSITE GRENOBLE ALPES, GRENOBLE, FRANCE  
& BRUKER BIOSPIN MRI, ETTLINGEN, GERMANY  
Development of preclinical brain perfusion imaging using arterial spin labeling. Grant from ANRT (French governmental agency).

- 2013      **Erasmus semester**  
ROYAL INSTITUTE OF TECHNOLOGY (KTH), STOCKHOLM, SWEDEN  
Medical Engineering: Medical Imaging, Radiotherapy, Anatomy, Physiology.
- 2013      **Engineering degree in biomedical engineering, with honors**  
PHELMA, ENGINEERING SCHOOL OF THE GRENOBLE INSTITUTE OF TECHNOLOGY, GRENOBLE, FRANCE  
Main subjects: Physics, Signal processing, Electronics, Molecular Biology.
- 2008-2010 **Classes préparatoires aux grandes écoles**  
LYCÉE KLÉBER, STRASBOURG, FRANCE  
Intensive 2-year program in Mathematics, Physics and Engineering.

## Skills

---

- Languages **French** - mother tongue.  
**English** - B2 level.  
**German** - C1 level: double diploma ABIBAC (Baccalauréat/Abitur).
- Informatics **OS** - Windows, Linux.  
**Software packages** - Paravision, Latex, Comsol Multiphysics, Labview, Microsoft Office.  
**Programming** - MATLAB, MRI sequence programming (Bruker course 2014), C (C++ basis), Python.
- Experimentation **Animal experimentation accreditation** (2014) - Level 1 (FELASA C).

## Conferences

---

- Oral      **L. Hirschler**<sup>1\*</sup>, L.P. Munting<sup>1\*</sup>, W.M. Teeuwisse, E. Suidgeest, J.M. Warnking, M.J.P. van Osch, E. L. Barbier, and L. van der Weerd. “Transit time mapping in the mouse brain using time-encoded pCASL”. *ISMRM 24<sup>th</sup> Annual Scientific Meeting, Singapore (Abstract No. 4654) - Power Pitch Presentation* – Magna Cum Laude Merit Award.
- L. Hirschler**, C. Debacker, J. Voiron, S. Köhler, J.M. Warnking, and E.L. Barbier. “Robust interpulse Phase Correction for Brain Perfusion Imaging at Very High Field using Pseudo-Continuous Arterial Spin Labeling (pCASL)”. *COST Action BM1103 Workshop on ASL, Les Diablerets, Switzerland*.
- L. Hirschler**, C. Debacker, J. Voiron, J.M. Warnking, and E. L. Barbier. “Dynamic pCASL acquisition for simultaneous multi-parametric perfusion quantification”. *SFRMBM 2<sup>nd</sup> Scientific Meeting, Grenoble, France*.

---

<sup>1\*</sup> both authors contributed equally

- 
- Poster **L. Hirschler**, I. Uszynski, J. Warnking, E.L. Barbier, "3-Dimensional cerebral blood flow and transit time mouse brain mapping using Dynamic Arterial Spin Labeling (DASL)", *ISMRM 25<sup>th</sup> Annual Scientific Meeting, Honolulu, USA (Abstract No. 4597)*.
- L. Hirschler**<sup>1\*</sup>, I. Uszynski<sup>1\*</sup>, J. Warnking, C. Poupon, JC Deloulme, and E.L. Barbier. "Combined 3D perfusion and diffusion MRI to phenotype the mouse brain: Evaluation and application to a model of schizophrenia", *ISMRM 25<sup>th</sup> Annual Scientific Meeting, Honolulu, USA (Abstract No. 5114)*.
- L. Hirschler**, J. Voiron, S. Köhler, N. Collomb, E. L. Barbier and J.M. Warnking. "SAR comparison between CASL and pCASL at high magnetic field (9.4T). Evaluation of the benefit of a separate labeling coil". *ISMRM 24<sup>th</sup> Annual Scientific Meeting, Singapore (Abstract No. 2748)*.
- L. Hirschler**, C. Debacker, J. Voiron, S. Köhler, J.M. Warnking, and E.L. Barbier. "Robust interpulse Phase Correction for Brain Perfusion Imaging at Very High Field using Pseudo-Continuous Arterial Spin Labeling (pCASL)". *ISMRM 23<sup>rd</sup> Annual Scientific Meeting, Toronto, Canada (Abstract No. 3168)*.

### Co-authored Conferences

---

- Oral C. Adams, M. Koletar, T. Beckett, L. Cahill, **L. Hirschler**, J.M. Warnking, E.L. Barbier, J. McLaurin, J.G. Sled, B. Stefanovic. "Long-term Cerebrovascular Dysfunction Following Repeated Mild Traumatic Brain Injury", *ISMRM 25<sup>th</sup> Annual Scientific Meeting, Honolulu, USA (Abstract No. 3098) - Power Pitch Presentation*.
- Poster L.P. Munting, **L. Hirschler**, E. Suidgeest, E. L. Barbier, M.J.P. van Osch, and L. van der Weerd. "Using time-encoded pCASL to study vascular function in a mouse model of Alzheimer's disease". *ISMRM 25<sup>th</sup> Annual Scientific Meeting, Honolulu, USA (Abstract No. 4312)*.
- S. Seramani, **L. Hirschler**, E. L. Barbier and K.J. Lee. "High Resolution Pseudo-Continuous Arterial Spin Labeling (pCASL) of mouse brain at 9.4 Tesla". *ISMRM 25<sup>th</sup> Annual Scientific Meeting, Honolulu, USA (Abstract No. 2947)*.
- S. Seramani, **L. Hirschler**, B. Ramasamy, S. Sekar, K. Bhakoo, E. L. Barbier and K.J. Lee. "Comparison of pCASL and FAIR for measuring Renal Blood Flow (RBF) of mouse kidney at 9.4T". *ISMRM 25<sup>th</sup> Annual Scientific Meeting, Honolulu, USA (Abstract No. 5271)*.
- L. Ciobanu, **L. Hirschler**, T. Tsurugizawa, D. Le Bihan, C. Debacker, and E.L. Barbier. "Cerebral perfusion measurements at 17.2 T using pCASL: a feasibility study." *ISMRM 23<sup>rd</sup> Annual Scientific Meeting, Toronto, Canada (Abstract No. 2249)*.

L. Boisserand, B. Lemasson, **L. Hirschler**, V. Hubert, A. Moisan, E.L. Barbier, C. Rémy, O. Detante. “Quantification of local blood oxygen saturation by MRI to distinguish ischemic core from penumbra in experimental stroke”. *ISMRM 23<sup>rd</sup> Annual Scientific Meeting, Toronto, Canada (Abstract No. 3595)* - Magna Cum Laude Merit Award.

## Publications

---

- **L. Hirschler**, C. Debacker, J. Voiron, S. Köhler, J.M. Warnking, and E.L. Barbier. Interpulse Phase Corrections for Unbalanced Pseudo-Continuous Arterial Spin Labeling at High Magnetic Field. *Magnetic Resonance in Medicine*. DOI: 10.1002/mrm.26767
- **L. Hirschler\***, L.P. Munting\*, W.M. Teeuwisse, E. Suidgeest, J.M. Warnking, M.J.P. van Osch, E. L. Barbier, and L. van der Weerd, Transit time mapping in the mouse brain using time-encoded pCASL (in preparation).
- **L. Hirschler**, S. Köhler, J. Voiron, N. Collomb, E.L. Barbier and J.M. Warnking, SAR comparison between CASL and pCASL at high magnetic field (9.4 T). Evaluation of the benefit of a separate labeling coil. (in preparation).
- L. Boisserand, B. Lemasson, **L. Hirschler**, A. Moisan, V. Hubert, E. L. Barbier, C. Rémy, O. Detante, Multiparametric MRI including oxygenation mapping of experimental ischaemic stroke. *Journal of Cerebral Blood Flow & Metabolism*. 2016:0271678X16662044.

## References

---

- Dr. Emmanuel Barbier, Grenoble Institute of Neuroscience, (emmanuel.barbier@univ-grenoble-alpes.fr).
- Dr. Jan Warnking, Grenoble Institute of Neuroscience, (jan.warnking@univ-grenoble-alpes.fr).
- Dr. Sascha Köhler, Bruker Biospin MRI (sascha.koehler@bruker.com).
- Dr. Jérôme Voiron, Bruker Biospin MRI (jerome.voiron@bruker.com).

## Bibliography

- Alsop, D. C., Detre, J. A., 1996. Reduced transit-time sensitivity in noninvasive magnetic resonance imaging of human cerebral blood flow. *Journal of cerebral blood flow and metabolism* 16 (6), 1236–1249. (Cited on pages 11, 20, 24, 93, and 105).
- Alsop, D. C., Detre, J. A., 1998. Multisection Cerebral Blood Flow MR Imaging with Continuous Arterial Spin Labeling. (Cited on page 19).
- Alsop, D. C., Detre, J. A., Golay, X., Günther, M., Hendrikse, J., Hernandez-Garcia, L., Lu, H., Macintosh, B. J., Parkes, L. M., Smits, M., Van Osch, M. J. P., Wang, D. J. J., Wong, E. C., Zaharchuk, G., 2015. Recommended implementation of arterial spin-labeled Perfusion mri for clinical applications: A consensus of the ISMRM Perfusion Study group and the European consortium for ASL in dementia. *Magnetic Resonance in Medicine* 73 (1), 102–116. (Cited on pages 15, 23, 25, 26, 31, 71, 76, 91, 97, 111, 119, and 160).
- Barbier, E. L., Lamalle, L., Décorps, M., 2001a. Methodology of brain perfusion imaging. *Journal of magnetic resonance imaging : JMRI* 13 (4), 496–520. (Cited on pages 1 and 15).
- Barbier, E. L., Silva, A. C., Kim, H. J., Williams, D. S., Koretsky, A. P., 1999. Perfusion analysis using dynamic arterial spin labeling (DASL). *Magn. Reson. Med.* 41 (2), 299–308. (Cited on pages 18, 30, 54, 74, 165, and 166).
- Barbier, E. L., Silva, A. C., Kim, S.-G. G., Koretsky, A. P., 2001b. Perfusion imaging using dynamic arterial spin labeling (DASL). *Magnetic resonance in medicine* 45 (6), 1021–1029. (Cited on pages 25, 30, 32, 104, 108, and 165).
- Barbier, E. L., St. Lawrence, K. S., Grillon, E., Koretsky, A. P., Décorps, M., 2002. A model of blood-brain barrier permeability to water: Accounting for blood inflow and longitudinal relaxation effects. *Magnetic Resonance in Medicine* 47 (6), 1100–1109. (Cited on page 6).
- Baskerville, T. A., McCabe, C., Weir, C. J., Macrae, I. M., Holmes, W. M., 2012. Noninvasive MRI measurement of CBF: evaluating an arterial spin labelling sequence with <sup>99m</sup>Tc-HMPAO CBF autoradiography in a rat stroke model. *Journal of cerebral blood flow and metabolism* 32 (6), 973–7. (Cited on pages 10, 32, and 33).

- Beaumont, M., Lamalle, L., Segebarth, C., Barbier, E. L., 2007. Improved k-space trajectory measurement with signal shifting. *Magnetic Resonance in Medicine* 58 (1), 200–205. (Cited on page 88).
- Berezcki, D., Wei, L., Otsuka, T., Hans, F. J., Acuff, V., Patlak, C., Fenstermacher, J., 1993. Hypercapnia slightly raises blood volume and sizably elevates flow velocity in brain microvessels. *The American journal of physiology* 264 (5 Pt 2), H1360–9. (Cited on page 32).
- Boisserand, L. S. B., Lemasson, B., Hirschler, L., Moisan, A., Hubert, V., Barbier, E. L., Rémy, C., Detante, O., 2016. Multiparametric magnetic resonance imaging including oxygenation mapping of experimental ischaemic stroke. *Journal of Cerebral Blood Flow & Metabolism*, 0271678X16662044. (Cited on pages 2 and 3).
- Borogovac, A., Asllani, I., 2012. Arterial spin labeling (ASL) fMRI: Advantages, theoretical constrains and experimental challenges in neurosciences. *Int. J. Biomed. Imaging* 2012. (Cited on page 13).
- Bouldi, M., 2014. Vers une application sure de l'IRM en présence d'implants actifs. Ph.D. thesis, Université Grenoble Alpes. (Cited on page 37).
- Bouzat, P., Millet, A., Boue, Y., Pernet-Gallay, K., Trouve-Buisson, T., Gaide-Chevronnay, L., Barbier, E. L., Payen, J.-F., 2013. Changes in brain tissue oxygenation after treatment of diffuse traumatic brain injury by erythropoietin. *Critical care medicine* 41 (5), 1316–24. (Cited on page 4).
- Bruns, A., Mueggler, T., Künnecke, B., Risterucci, C., Prinssen, E. P., Wettstein, J. G., von Kienlin, M., 2015. "Domain gauges": A reference system for multivariate profiling of brain fMRI activation patterns induced by psychoactive drugs in rats. *Neuroimage* 112, 70–85. (Cited on page 138).
- Busto, R., Dietrich, W. D., Globus, M. Y. T., Ginsberg, M. D., 1989. The importance of brain temperature in cerebral injury. *Stroke* 20, 1113–1114. (Cited on pages 111 and 133).
- Buxton, R. B., Frank, L. R., Wong, E. C., Siewert, B., Warach, S., Edelman, R. R., 1998. A general kinetic model for quantitative perfusion imaging with arterial spin labeling. *Magnetic resonance in medicine* 40 (3), 383–396. (Cited on pages 25, 27, 29, 31, 59, 75, 76, 97, and 119).
- Calabrese, E., Badea, A., Cofer, G., Qi, Y., Johnson, G. A., 2015. A Diffusion MRI tractography connectome of the mouse brain and comparison with neuronal tracer data. *Cerebral Cortex* 25 (11), 4628–4637. (Cited on page 159).

- Cantin, S., Villien, M., Moreaud, O., Tropres, I., Keignart, S., Chipon, E., Le Bas, J.-F., Warnking, J., Krainik, A., 2011. Impaired cerebral vasoreactivity to CO<sub>2</sub> in Alzheimer's disease using BOLD fMRI. *NeuroImage* 58 (2), 579–87. (Cited on page 8).
- Chao, L. L., Buckley, S. T., Kornak, J., Schuff, N., Madison, C., Yaffe, K., Miller, B. L., Kramer, J. H., Weiner, M. W., 2010. ASL perfusion MRI predicts cognitive decline and conversion from MCI to dementia. *Alzheimer disease and associated disorders* 24 (1), 19–27. (Cited on page 4).
- Chappell, M. A., MacIntosh, B. J., Donahue, M. J., Günther, M., Jezzard, P., Woolrich, M. W., may 2010. Separation of macrovascular signal in multi-inversion time arterial spin labelling MRI. *Magnetic resonance in medicine* 63 (5), 1357–65. (Cited on page 107).
- Chen, Y., Wang, D. J. J., Detre, J. A., apr 2011. Test-retest reliability of arterial spin labeling with common labeling strategies. *J. Magn. Reson. Imaging* 33 (4), 940–949. (Cited on pages 16 and 111).
- Chugh, B. P., Bishop, J., Zhou, Y.-Q., Wu, J., Henkelman, R. M., Sled, J. G., 2012. Robust method for 3D arterial spin labeling in mice. *Magn. Reson. Med.* 68 (1), 98–106. (Cited on page 138).
- Ciobanu, L., Hirschler, L., Tsurugizawa, T., Bihan, D. L., Debacker, C. S., Barbier, E. L., 2015. Cerebral perfusion measurements at 17.2 T using pCASL: a feasibility study. In: *Proceedings of the 23rd Annual Meeting of ISMRM, Toronto, Ontario, Canada, 2015*. Abstract 2964. (Cited on page 91).
- Coquery, N., Francois, O., Lemasson, B., Debacker, C. S., Farion, R., Rémy, C., Barbier, E. L., 2014. Microvascular MRI and unsupervised clustering yields histology-resembling images in two rat models of glioma. *J. Cereb. Blood Flow Metab.* 34 (8), 1354–1362. (Cited on page 9).
- Dai, W., Garcia, D., De Bazelaire, C., Alsop, D. C., 2008. Continuous flow-driven inversion for arterial spin labeling using pulsed radio frequency and gradient fields. *Magnetic Resonance in Medicine* 60 (6), 1488–1497. (Cited on pages 20, 21, 65, 66, 71, and 95).
- Dai, W., Lopez, O. L., Carmichael, O. T., Becker, J. T., Kuller, L. H., Gach, H. M., 2009. Mild cognitive impairment and Alzheimer disease: patterns of altered cerebral blood flow at MR imaging. *Radiology* 250 (3), 856–866. (Cited on page 4).
- Dai, W., Shankaranarayanan, A., Alsop, D. C., 2013. Volumetric measurement of perfusion and arterial transit delay using hadamard encoded continuous arterial spin

- labeling. *Magnetic Resonance in Medicine* 69 (4), 1014–1022. (Cited on pages 28 and 94).
- de Graaf, R. A., Brown, P. B., McIntyre, S., Nixon, T. W., Behar, K. L., Rothman, D. L., 2006. High magnetic field water and metabolite proton T1 and T2 relaxation in rat brain in vivo. *Magnetic Resonance in Medicine* 56 (2), 386–94. (Cited on pages 26, 76, and 119).
- de Senneville, B. D., Mougnot, C., Quesson, B., Dragonu, I., Grenier, N., Moonen, C. T. W., 2007. MR thermometry for monitoring tumor ablation. *European Radiology* 17 (9), 2401–2410. (Cited on page 112).
- Debacker, C. S., 2014. Développement de l'imagerie de perfusion cérébrale par marquage des spins artériels. Ph.D. thesis, Université Grenoble Alpes. (Cited on pages 18 and 32).
- Debacker, C. S., Daoust, A., Köhler, S., Voiron, J., Warnking, J. M., Barbier, E. L., 2016. Impact of tissue T1 on perfusion measurement with arterial spin labeling. *Magn. Reson. Med.* 00 (April), 1–9. (Cited on pages 17, 23, 50, 73, 76, and 165).
- Debacker, C. S., Warnking, J. M., Koehler, S., Voiron, J., Barbier, E. L., 2015. Comparison of ASL inversion efficiency and CBF quantification for 3 perfusion techniques at 3 magnetic fields. In: *Proc. Intl. Soc. Mag. Reson. Med.* 23. Toronto, Canada, p. 794. (Cited on pages 32, 34, and 91).
- Deloulme, J.-C., Gory-Fauré, S., Mauconduit, F., Chauvet, S., Jonckheere, J., Boulan, B., Mire, E., Xue, J., Jany, M., Maucler, C., Deparis, A. a., Montigon, O., Daoust, A., Barbier, E. L., Bosc, C., Deglon, N., Brocard, J., Denarier, E., Le Brun, I., Pernet-Gallay, K., Vilgrain, I., Robinson, P. J., Lahrech, H., Mann, F., Andrieux, A., 2015. Microtubule-associated protein 6 mediates neuronal connectivity through Semaphorin 3E-dependent signalling for axonal growth. *Nature communications* 6, 7246. (Cited on pages 158, 160, and 165).
- D'Esposito, M., Deouell, L. Y., Gazzaley, A., 2003. Alterations in the BOLD fMRI signal with ageing and disease: a challenge for neuroimaging. *Nature reviews. Neuroscience* 4 (11), 863–872. (Cited on page 7).
- Detre, J. A., Leigh, J. S., Williams, D. S., Koretsky, A. P., 1992. Perfusion imaging. *Magnetic Resonance in Medicine* 23, 37–45. (Cited on pages 11 and 31).
- Dixon, W. T., Du, L. N., Faul, D. D., Gado, M., Rossnick, S., 1986. Projection angiograms of blood labeled by adiabatic fast passage. *Magnetic Resonance in Medicine* 3 (3), 454–462. (Cited on page 14).

- Dobre, M. C., Ugurbil, K., Marjanska, M., 2007. Determination of blood longitudinal relaxation time (T1) at high magnetic field strengths. *Magnetic Resonance Imaging* 25, 733–735. (Cited on pages 26, 59, 66, 76, 98, 107, and 119).
- Dorr, A., Sled, J. G., Kabani, N., may 2007. Three-dimensional cerebral vasculature of the CBA mouse brain: a magnetic resonance imaging and micro computed tomography study. *NeuroImage* 35 (4), 1409–23. (Cited on pages 24, 91, 104, 106, and 107).
- Duck, F., 1991. *Physical Properties of Tissue. A Comprehensive Reference Book. Vol. 18.* (Cited on pages 37 and 38).
- Duclap, D., Lebois, A., Schmitt, B., Rigg, O., Guevara, P., Marrakchi-Kacem, L., Brion, V., Poupon, F., Mangin, J.-F., Poupon, C., 2012. Connectomist-2.0: a novel diffusion analysis toolbox for brainvisa. In: *Proceedings of the 29th ESMRMB, Lisbon, Portugal, 2012.* (Cited on page 159).
- Duhamel, G., Callot, V., Tachrount, M., Alsop, D. C., Cozzzone, P. J., may 2012. Pseudo-continuous arterial spin labeling at very high magnetic field (11.75 T) for high-resolution mouse brain perfusion imaging. *Magnetic resonance in medicine* 67 (5), 1225–36. (Cited on pages 34, 71, 104, 133, 165, and 166).
- Engel, O., Kolodziej, S., Dirnagl, U., Prinz, V., 2011. Modeling Stroke in Mice - Middle Cerebral Artery Occlusion with the Filament Model. *J. Vis. Exp.* 47, 2–5. (Cited on pages 16, 17, and 20).
- Esparza-Coss, E., Wosik, J., Narayana, P. A., 2010. Perfusion in rat brain at 7 T with arterial spin labeling using FAIR-TrueFISP and QUIPSS. *Magnetic Resonance Imaging* 28 (4), 607–612. (Cited on pages 32 and 81).
- Ferrara, L. A., Mancini, M., Iannuzzi, R., Marotta, T., Gaeta, I., Pasanisi, F., Postiglione, A., Guida, L., 1995. Carotid Diameter and Blood Flow Velocities in Cerebral Circulation in Hypertensive Patients. *Stroke* 26 (3), 418–421. (Cited on page 67).
- Franklin, K. B., Paxinos, G., 2007. *The Mouse Brain in Stereotaxic Coordinates*, 3rd Edition. (Cited on page 96).
- Ghariq, E., Teeuwisse, W. M., Webb, A. G., Osch, M. J. P. V., 2012. Feasibility of pseudocontinuous arterial spin labeling at 7 T with whole-brain coverage. *Magnetic Resonance Materials in Physics, Biology and Medicine* 25 (2), 83–93. (Cited on pages 34, 72, and 133).
- Grobner, T., 2006. Gadolinium – a specific trigger for the development of nephrogenic fibrosing dermopathy and nephrogenic systemic fibrosis? *Nephrology Dialysis Transplantation* 21 (4), 1104. (Cited on page 11).

- Gudbjartsson, H., Patz, S., dec 1995. The rician distribution of noisy mri data. *Magnetic Resonance in Medicine* 34 (6), 910–914. (Cited on page 108).
- Günther, M., 2007. Highly efficient accelerated acquisition of perfusion inflow series by cycled arterial spin labeling. In: *Proceedings of the 16th Annual Meeting of ISMRM*. Berlin. (Cited on pages 28, 94, 98, and 103).
- Haida, M., Yamamoto, M., Matsumura, H., Shinohara, Y., Fukuzaki, M., 1987. Intracellular and extracellular spaces of normal adult rat brain determined from the proton nuclear magnetic resonance relaxation times. *J Cereb Blood Flow Metab* 7 (5), 552–556. (Cited on page 26).
- Hansen, T. D., Warner, D. S., Todd, M. M., Vust, L. J., Trawick, D. C., 1988. Distribution of cerebral blood flow during halothane versus isoflurane anesthesia in rats. *Anesthesiology* 69 (3), 332–7. (Cited on page 81).
- Hendrich, K. S., Kochanek, P. M., Williams, D. S., Schiding, J. K., Marion, D. W., Ho, C., 1999. Early perfusion after controlled cortical impact in rats: Quantification by arterial spin-labeled MRI and the influence of spin-lattice relaxation time heterogeneity. *Magnetic Resonance in Medicine* 42 (4), 673–681. (Cited on page 32).
- Hendrikse, J., van Osch, M. J. P., Rutgers, D. R., Bakker, C. J. G., Kappelle, L. J., Golay, X., van der Grond, J., dec 2004. Internal carotid artery occlusion assessed at pulsed arterial spin-labeling perfusion MR imaging at multiple delay times. *Radiology* 233 (3), 899–904. (Cited on pages 25, 93, and 138).
- Henkelman, R. M., Stanisz, G. J., Graham, S. J., 2001. Magnetization transfer in MRI: A review. *NMR in Biomedicine* 14 (2), 57–64. (Cited on page 18).
- Hennel, F., 2014. The Effective Phase of Soft RF Pulses. *Concepts Magn. Reson.* 43A(4), 127–137. (Cited on pages 89, 90, and 136).
- Hernandez Tamames, J. A., -. ASL as replacement for PET.  
URL [www.aslindementia.org](http://www.aslindementia.org) (Cited on page 4).
- Herscovitch, P., Raichle, M. E., 1985. What is the correct value for the brain–blood partition coefficient for water? *Journal of cerebral blood flow and metabolism* 5 (1), 65–69. (Cited on pages 76, 97, and 119).
- Hirschler, L., Debacker, C., Voiron, J., Koehler, S., Warnking, J., Barbier, E., 2017. Inter-Pulse Phase Corrections for Unbalanced Pseudo-Continuous Arterial Spin Labeling at High Magnetic Field. *Magn Reson Med*. In press. (Cited on page 71).
- Hirschler\*, L., Munting\*, L. P., Teeuwisse, W. M., Suidgeest, E., Warnking, J. M., Van Osch, M. J. P., Barbier, E. L., van der Weerd, L., 2016. Transit time mapping in the

- mouse brain using time-encoded pCASL. In: Proceedings of the 24th Annual Meeting of ISMRM, Singapore, Singapore, 2016. Abstract 4654. (Cited on page 166).
- Holmes, W. M., Lopez-Gonzalez, M. R., Gallagher, L., Deuchar, G. A., Macrae, I. M., Santosh, C., 2012. Novel MRI detection of the ischemic penumbra: Direct assessment of metabolic integrity. *NMR in Biomedicine* 25 (2), 295–304. (Cited on page 3).
- Homan, P., Kindler, J., Hauf, M., Walther, S., Hubl, D., Dierks, T., 2013. Repeated measurements of cerebral blood flow in the left superior temporal gyrus reveal tonic hyperactivity in patients with auditory verbal hallucinations: a possible trait marker. *Frontiers in human neuroscience* 7 (June), 304. (Cited on page 4).
- Hrabe, J., Lewis, D. P., mar 2004. Two analytical solutions for a model of pulsed arterial spin labeling with randomized blood arrival times. *Journal of magnetic resonance (San Diego, Calif. : 1997)* 167 (1), 49–55. (Cited on page 108).
- Hua, J., Jones, C. K., Blakeley, J., Smith, S. A., van Zijl, P. C. M., Zhou, J. Y., 2007. Quantitative description of the asymmetry in magnetization transfer effects around the water resonance in the human brain. *Magnetic Resonance in Medicine* 58 (4), 786–793. (Cited on pages 18 and 19).
- International Electrochemical Commission, 2010. Medical electrical equipment: part 2-33. Particular requirements for the safety of magnetic resonance equipment for medical diagnosis. (Cited on page 39).
- Jahanian, H., Noll, D. C., Hernandez-Garcia, L., 2011. B<sub>0</sub> field inhomogeneity considerations in pseudo-continuous arterial spin labeling (pCASL): effects on tagging efficiency and correction strategy. *NMR Biomed* 24 (10), 1202–1209. (Cited on pages 34 and 95).
- Jauch, E. C., Saver, J. L., Adams, H. P., Bruno, A., Connors, J. J. B., Demaerschalk, B. M., Khatri, P., McMullan, P. W., Qureshi, A. I., Rosenfield, K., Scott, P. a., Summers, D. R., Wang, D. Z., Wintermark, M., Yonas, H., 2013. Guidelines for the Early Management of Patients With Acute Ischemic Stroke: A Guideline for Healthcare Professionals From the American Heart Association/American Stroke Association. *Stroke: A Journal of Cerebral Circulation* 44 (3), 870–947. (Cited on page 3).
- Jung, Y., Wong, E. C., Liu, T. T., 2010. Multiphase pseudocontinuous arterial spin labeling (MP-PCASL) for robust quantification of cerebral blood flow. *Magnetic resonance in medicine* 64 (3), 799–810. (Cited on pages 34 and 35).
- Kety, S. S., Schmidt, C. F., 1948. The Effects of Altered Arterial Tensions of Carbon Dioxide and Oxygen on Cerebral Blood Flow and Cerebral Oxygen Consumption of Normal Young Men. *Journal of Clinical Investigation* 27 (4), 484–492. (Cited on page 8).

- Kim, S.-G., 1995. Quantification of relative cerebral blood flow change by flow-sensitive alternating inversion recovery (FAIR) technique: Application to functional mapping. *Magnetic Resonance in Medicine* 34 (3), 293–301. (Cited on pages 11 and 16).
- Kim, T., Kim, S. G., 2005. Quantification of cerebral arterial blood volume and cerebral blood flow using MRI with modulation of tissue and vessel (MOTIVE) signals. *Magnetic Resonance in Medicine* 54 (2), 333–342. (Cited on page 81).
- Kimura, H., Takeuchi, H., Koshimoto, Y., Arishima, H., Uematsu, H., Kawamura, Y., Kubota, T., Itoh, H., 2006. Perfusion imaging of meningioma by using continuous arterial spin-labeling: Comparison with dynamic susceptibility-weighted contrast-enhanced MR images and histopathologic features. *Am. J. Neuroradiol.* 27 (1), 85–93. (Cited on page 3).
- Kleiber, M., 1932. Body size and metabolism. *Hilgardia: A Journal of Agricultural Science* 6 (11), 315–353. (Cited on page 39).
- Klein, S., Staring, M., Murphy, K., Viergever, M., Pluim, J., 2010. Elastix: a toolbox for intensity based medical image registration. *IEEE Transactions on Medical Imaging* 29 (1), 196–205. (Cited on page 97).
- Kreis, D., Schulz, D., Stein, M., Preuss, M., Nestler, U., 2011. Assessment of parameters influencing the blood flow velocities in cerebral arteries of the rat using ultrasonographic examination. *Neurological Research* 33 (4), 389–395. (Cited on pages 49, 65, 67, and 78).
- Kwong, K. K., Chesler, D. A., Weisskoff, R. M., Donahue, K. M., Davis, T. L., Ostergaard, L., Campbell, T. A., Rosen, B. R., 1995. MR perfusion studies with T1-weighted echo planar imaging. *Magnetic Resonance in Medicine* 34 (6), 878–887. (Cited on page 16).
- Lahti, A. C., Weiler, M. A., Holcomb, H. H., Tamminga, C. A., Carpenter, W. T., McMahon, R., 2006. Correlations between rCBF and symptoms in two independent cohorts of drug-free patients with schizophrenia. *Neuropsychopharmacology* 31 (1), 221–230. (Cited on page 4).
- Landau, W. M., Freygang, W. H. J., Roland, L. P., Sokoloff, L., Kety, S. S., 1955. The local circulation of the living brain; values in the unanesthetized and anesthetized cat. *Trans Am Neurol Assoc* 80 (125), 125–129. (Cited on page 10).
- Larkin, J. R., Simard, M. A., Khrapitchev, A. A., Ray, K. J., Meakin, J. A., Kinches, P., Smart, S., Jezard, P., Chappell, M. A., Sibson, N. R., 2016. Multiphase pCASL for imaging blood flow in rodent brains. In: *Proceedings of the ISMRM 24th Annual Meeting ISMRM, Singapore.* p. 1497. (Cited on pages 34 and 35).

- Lascialfari, A., Zucca, I., Asdente, M., Cimino, M., Guerrini, U., Paoletti, R., Tremoli, E., Lorusso, V., Sironi, L., 2005. Multiexponential T2-relaxation analysis in cerebrally damaged rats in the absence and presence of a gadolinium contrast agent. *Magnetic Resonance in Medicine* 53 (6), 1326–1332. (Cited on page 26).
- Leenders, K. L., Perani, D., Lammertsma, A. A., Heather, J. D., Buckingham, P., Jones, T., Healy, M. J. R., Gibbs, J. M., Wise, R. J. S., Hatazawa, J., Herold, S., Beaney, R. P., Brooks, D. J., Spinks, T., Rhodes, C., Frackowiak, R. S. J., 1990. Cerebral blood flow, blood volume and oxygen utilization: Normal values and effect of age. *Brain* 113 (1), 27–47. (Cited on page 108).
- Lei, H., Grinberg, O., Nwaigwe, C. I. I., Hou, H. G. G., Williams, H., Swartz, H. M. M., Dunn, J. F. F., 2001. The effects of ketamine-xylazine anesthesia on cerebral blood flow and oxygenation observed using nuclear magnetic resonance perfusion imaging and electron paramagnetic resonance oximetry. *Brain Res.* 913 (2), 174–179. (Cited on page 132).
- Li, C. H., Lee, C. K., 1993. Minimum cross entropy thresholding. *Pattern Recognition* 26 (4), 617–625. (Cited on page 55).
- Librizzi, L., de Curtis, M., Janigro, D., Runtz, L., DeBock, F., Barbier, E. L., Marchi, N., de Curtis, M., Janigro, D., Runtz, L., DeBock, F., Barbier, E. L., Marchi, N., 2017. Cerebrovascular heterogeneity and neuronal excitability. *Neurosci. Lett.* (Cited on pages 3 and 4).
- Liddle, P. F., Friston, K. J., Frith, C. D., Frackowiak, R. S., 1992. Cerebral blood flow and mental processes in schizophrenia. *Journal of the Royal Society of Medicine* 85 (April), 224–227. (Cited on page 4).
- Lin, A.-L., Qin, Q., Zhao, X., Duong, T. Q., 2012. Blood longitudinal (T 1) and transverse (T 2) relaxation time constants at 11.7 Tesla. *Magnetic Resonance Materials in Physics, Biology and Medicine* 25 (3), 245–249. (Cited on page 59).
- Lin, C.-M., Tseng, Y.-C., Hsu, H.-L., Chen, C.-J., Chen, D. Y.-T., Yan, F.-X., Chiu, W.-T., 2016. Arterial Spin Labeling Perfusion Study in the Patients with Subacute Mild Traumatic Brain Injury. *PloS one* 11 (2), e0149109. (Cited on page 3).
- Liu, P., Uh, J., Lu, H., 2011. Determination of spin compartment in arterial spin labeling MRI. *Magnetic Resonance in Medicine* 65 (1), 120–127. (Cited on pages 25, 26, 27, and 106).
- Liu, Y., Zhu, X., Feinberg, D., Guenther, M., Gregori, J., Weiner, M. W., Schuff, N., 2012. Arterial spin labeling MRI study of age and gender effects on brain perfusion hemodynamics. *Magnetic Resonance in Medicine* 68 (3), 912–922. (Cited on page 108).

- Lu, H., Clingman, C., Golay, X., Van Zijl, P. C. M., sep 2004. Determining the longitudinal relaxation time (T1) of blood at 3.0 tesla. *Magnetic Resonance in Medicine* 52 (3), 679–82. (Cited on pages 33 and 59).
- Luh, W. M., Li, T. Q., Wong, E. C., Bandettini, P. A., 2008. Pseudo-Continuous Arterial Spin Labeling at 7 T. In: 16th Annual Meeting of ISMRM. Toronto, Canada, p. 3339. (Cited on page 72).
- Luh, W. M., Talagala, S. L., Li, T. Q., Bandettini, P. A., 2013. Pseudo-continuous arterial spin labeling at 7 T for human brain: Estimation and correction for off-resonance effects using a Prescan. *Magnetic Resonance in Medicine* 69 (2), 402–410. (Cited on pages 34, 35, and 95).
- Maccotta, L., Detre, J. A., Alsop, D. C., 1997. The efficiency of adiabatic inversion for perfusion imaging by arterial spin labeling. *NMR in biomedicine* 10 (4-5), 216–221. (Cited on pages 19 and 65).
- Maier, F. C., Wehrl, H. F., Schmid, A. M., Mannheim, J. G., Wiehr, S., Lerdkrai, C., Calaminus, C., Stahlschmidt, A., Ye, L., Burnet, M., Stiller, D., Sabri, O., Reischl, G., Staufenbiel, M., Garaschuk, O., Jucker, M., Pichler, B. J., nov 2014. Longitudinal PET-MRI reveals  $\beta$ -amyloid deposition and rCBF dynamics and connects vascular amyloidosis to quantitative loss of perfusion. *Nature medicine* 20 (12), 1485–1492. (Cited on pages 108 and 109).
- Masamoto, K., Fukuda, M., Vazquez, A., Kim, S. G., 2009. Dose-dependent effect of isoflurane on neurovascular coupling in rat cerebral cortex. *European Journal of Neuroscience* 30 (2), 242–250. (Cited on pages 31 and 132).
- Masuda, H., Hirata, A., Kawai, H., Wake, K., Watanabe, S., Arima, T., Poullietier de Gannes, F., Lagroye, I., Veyret, B., jan 2011. Local exposure of the rat cortex to radiofrequency electromagnetic fields increases local cerebral blood flow along with temperature. *J. Appl. Physiol.* 110 (1), 142 LP — 148. (Cited on page 111).
- Matsumae, M., Oi, S., Watanabe, H., Okamoto, K., Suzuki, Y., Sato, K., Atsumi, H., Goto, T., Tsugane, R., 2003. Distribution of intracellular and extracellular water molecules in developing rat's midbrain: comparison with fraction of multicomponent T(2) relaxation time and morphological findings from electron microscopic imaging. *Child's nervous system : ChNS* 19 (2), 91–95. (Cited on page 26).
- McDonald, R. J., McDonald, J. S., Kallmes, D. F., Jentoft, M. E., Murray, D. L., Thielen, K. R., Williamson, E. E., Eckel, L. J., 2015. Intracranial Gadolinium Deposition after Contrast-enhanced MR Imaging. *Radiology* 000 (0), 150025. (Cited on page 11).

- McGehee, B. E., Pollock, J. M., Maldjian, J. A., 2012. Brain perfusion imaging: How does it work and what should i use? (Cited on pages 11 and 12).
- Mrozek, S., Vardon, F., Geeraerts, T., 2012. Brain temperature: Physiology and pathophysiology after brain injury. *Anesthesiology Research and Practice* 2012 (Figure 1). (Cited on pages 111 and 133).
- Nasrallah, F. a., Lee, E. L. Q., Chuang, K.-H., 2012. Optimization of flow-sensitive alternating inversion recovery (FAIR) for perfusion functional MRI of rodent brain. *NMR in biomedicine* 25 (11), 1209–16. (Cited on pages 26, 59, 76, and 119).
- Otsu, N., 1975. A threshold selection method from gray-level histograms. *Automatica* 11 (285-296), 23–27. (Cited on page 51).
- Pagani, M., Salmaso, D., Jonsson, C., Hatherly, R., Jacobsson, H., Larsson, S. A., Wägner, A., 2002. Regional cerebral blood flow as assessed by principal component analysis and (99m)Tc-HMPAO SPET in healthy subjects at rest: normal distribution and effect of age and gender. *European Journal of Nuclear Medicine and Molecular Imaging* 29 (1), 67–75. (Cited on page 108).
- Pannetier, N., Lemasson, B., Christen, T., Tachrount, M., Troprès, I., Farion, R., Segebarth, C., Rémy, C., Barbier, E. L., 2012. Vessel size index measurements in a rat model of glioma: Comparison of the dynamic (Gd) and steady-state (iron-oxide) susceptibility contrast MRI approaches. *NMR in Biomedicine* 25 (2), 218–226. (Cited on page 7).
- Pardridge, W. M., 2012. Drug Transport across the Blood–Brain Barrier. *Journal of Cerebral Blood Flow & Metabolism* 32 (11), 1959–1972. (Cited on pages 6 and 7).
- Parkes, L. M., Tofts, P. S., 2002. Improved accuracy of human cerebral blood perfusion measurements using arterial spin labeling: Accounting for capillary water permeability. *Magnetic Resonance in Medicine* 48 (1), 27–41. (Cited on page 107).
- Pekar, J., Jezzard, P., Roberts, D. A., Leigh, J. S., Frank, J. a., McLaughlin, A. G., 1996. Perfusion imaging with compensation for asymmetric magnetization transfer effects. *Magnetic Resonance in Medicine* 35 (1), 70–79. (Cited on pages 18, 54, and 137).
- Pennes, H. H., 1948. Analysis of tissue and arterial blood temperatures in the resting human forearm. *Journal of applied physiology* 1 (2), 93– 122. (Cited on page 36).
- Petrinovic, M. M., Hankov, G., Schroeter, A., Bruns, A., Rudin, M., von Kienlin, M., Künnecke, B., Mueggler, T., 2016. A novel anesthesia regime enables neurofunctional studies and imaging genetics across mouse strains. *Scientific reports* 6, 24523. (Cited on pages 31, 32, and 81).

- Pinkham, A., Loughead, J., Ruparel, K., Wu, W. C., Overton, E., Gur, R., Gur, R., 2011. Resting quantitative cerebral blood flow in schizophrenia measured by pulsed arterial spin labeling perfusion MRI. *Psychiatry Research - Neuroimaging* 194 (1), 64–72. (Cited on page 4).
- Pires, P. W., Dams Ramos, C. M., Matin, N., Dorrance, A. M., 2013. The effects of hypertension on the cerebral circulation. *American Journal of Physiology - Heart and Circulatory Physiology* 304 (12), H1598—H1614. (Cited on pages 7 and 8).
- Pizzini, F. B., Farace, P., Manganotti, P., Zoccatelli, G., Bongiovanni, L. G., Golay, X., Beltramello, A., Osculati, A., Bertini, G., Fabene, P. F., 2013. Cerebral perfusion alterations in epileptic patients during peri-ictal and post-ictal phase: PASL vs DSC-MRI. *Magnetic Resonance Imaging* 31 (6), 1001–1005. (Cited on page 4).
- Pohmann, R., Shajan, G., Balla, D. Z., 2011. Contrast at high field: Relaxation times, magnetization transfer and phase in the rat brain at 16.4 T. *Magn. Reson. Med.* 66 (6), 1572–1581. (Cited on page 20).
- Pollock, J. M., Tan, H., Kraft, R. A., Whitlow, C. T., Burdette, J. H., Maldjian, J. A., 2009. *Arterial Spin-Labeled MR Perfusion Imaging: Clinical Applications*. (Cited on page 11).
- Sabri, O., Erkwow, R., Schreckenberger, M., Owega, A., Sass, H., Buell, U., 1997. Correlation of positive symptoms exclusively to hyperperfusion or hypoperfusion of cerebral cortex in never-treated schizophrenics. *Lancet* 349 (9067), 1735–1739. (Cited on page 4).
- Sakurada, O., Kennedy, C., Jehle, J., Brown, J. D., Carbin, G. L., Sokoloff, L., 1978. Measurement of local cerebral blood flow with iodo [<sup>14</sup>C] antipyrine. *Am J Physiol* 234 (1), H59–66. (Cited on page 10).
- Scheef, L., Manka, C., Daamen, M., Kühn, K.-U., Maier, W., Schild, H. H., Jessen, F., 2010. Resting-state perfusion in nonmedicated schizophrenic patients: a continuous arterial spin-labeling 3.0-T MR study. *Radiology* 256 (1), 253–60. (Cited on page 4).
- Schlaug, G., Benfield, A., Baird, A. E., Siewert, B., Lövblad, K. O., Parker, R. A., Edelman, R. R., Warach, S., 1999. The ischemic penumbra: operationally defined by diffusion and perfusion MRI. *Neurology* 53 (April 1997), 1528–1537. (Cited on page 3).
- Schmid, S., Teeuwisse, W. M., Lu, H., van Osch, M. J. P., 2015. Time-efficient determination of spin compartments by time-encoded pCASL T2-relaxation-under-spin-tagging and its application in hemodynamic characterization of the cerebral border zones. *NeuroImage* 123, 72–79. (Cited on pages 27 and 106).

- Schwarzbauer, C., Morrissey, S. P., Deichmann, R., Hillenbrand, C., Syha, J., Adolf, H., Nöth, U., Haase, A., 1997. Quantitative magnetic resonance imaging of capillary water permeability and regional blood volume with an intravascular MR contrast agent. *Magnetic resonance in medicine* 37 (5), 769–777. (Cited on page 6).
- Shin, D. D., Liu, T. T., Wong, E. C., Shankaranarayanan, A., Jung, Y., 2012. Pseudocontinuous arterial spin labeling with optimized tagging efficiency. *Magnetic Resonance in Medicine* 68 (4), 1135–1144. (Cited on page 34).
- Silva, A. C., Zhang, W., Williams, D. S., Koretsky, A. P., 1995. Multi-slice MRI of rat brain perfusion during amphetamine stimulation using arterial spin labeling. *Magnetic resonance in medicine* 33 (2), 209–214. (Cited on page 19).
- Sotero, R. C., Iturria-Medina, Y., 2011. From Blood Oxygenation Level Dependent (BOLD) Signals to Brain Temperature Maps. *Bulletin of Mathematical Biology* 73 (11), 2731–2747. (Cited on page 118).
- Stanisz, G. J., Odobina, E. E., Pun, J., Escaravage, M., Graham, S. J., Bronskill, M. J., Henkelman, R. M., sep 2005. T1, T2 relaxation and magnetization transfer in tissue at 3T. *Magnetic resonance in medicine* 54 (3), 507–12. (Cited on page 59).
- Takagi, S., Ehara, K., Finn, R. D., 1987. Water extraction fraction and permeability-surface product after intravenous injection in rats. *Stroke; a journal of cerebral circulation* 18 (1), 177–183. (Cited on page 32).
- Talagala, S. L., Barbier, E. L., Williams, D. S., Silva, A. C., Koretsky, A. P., 1998. Multi-slice Perfusion MRI Using Continuous Arterial Water Labeling: Controlling for MT Effects with Simultaneous Proximal and Distal RF. In: *Proc. 6th Annu. Meet. ISMRM, Sydney*. p. 381. (Cited on page 19).
- Talagala, S. L., Ye, F. Q., Ledden, P. J., Chesnick, S., 2004. Whole-brain 3D perfusion MRI at 3.0 T using CASL with a separate labeling coil. *Magn. Reson. Med.* 52 (1), 131–140. (Cited on page 19).
- Tan, H., Maldjian, J. A., Pollock, J. M., Burdette, J. H., Yang, L. Y., Deibler, A. R., Kraft, R. A., may 2009. A Fast, Effective Filtering Method for Improving Clinical Pulsed Arterial Spin Labeling MRI. *Journal of magnetic resonance imaging* 29 (5), 1134–1139. (Cited on page 59).
- Tanaka, Y., Nagaoka, T., Nair, G., Ohno, K., Duong, T. Q., 2011. Arterial spin labeling and dynamic susceptibility contrast CBF MRI in postischemic hyperperfusion, hypercapnia, and after mannitol injection. *Journal of cerebral blood flow and metabolism* 31 (6), 1403–11. (Cited on page 32).

- Teeuwisse, W. M., Schmid, S., Ghariq, E., Veer, I. M., van Osch, M. J. P., 2014a. Time-encoded pseudocontinuous arterial spin labeling: Basic properties and timing strategies for human applications. *Magnetic Resonance in Medicine*, 1–11. (Cited on pages 28, 94, and 98).
- Teeuwisse, W. M., Schmid, S., Helle, M., van Osch, M. J. P., 2014b. 2-shim or not 2-shim, that is a question in pseudo continuous arterial spin labeling. In: *Proc. ISMRM 22rd Annu. Meet. Milan, Italy. Vol. 24. p. 4808.* (Cited on pages 34, 72, and 90).
- Teeuwisse, W. M., Webb, A. G., Van Osch, M. J. P., 2010. Arterial spin labeling at ultra-high field: All that glitters is not gold. *International Journal of Imaging Systems and Technology* 20 (1), 62–70. (Cited on pages 34 and 72).
- Telischak, N. A., Detre, J. A., Zaharchuk, G., 2015. Arterial spin labeling MRI: Clinical applications in the brain. (Cited on pages 2, 4, and 5).
- Thomas, D. L., Lythgoe, M. F., van der Weerd, L., Ordidge, R. J., Gadian, D. G., 2006. Regional variation of cerebral blood flow and arterial transit time in the normal and hypoperfused rat brain measured using continuous arterial spin labeling MRI. *Journal of cerebral blood flow and metabolism* 26 (2), 274–282. (Cited on pages 25, 32, 93, and 104).
- Thompson, W. R., 1935. On a Criterion for the Rejection of Observations and the Distribution of the Ratio of Deviation to Sample Standard Deviation. *Ann. Math. Stat.* 6 (4), 214–219. (Cited on page 64).
- Tofts, P. S., Kermode, A. G., 1991. Measurement of the blood-brain barrier permeability and leakage space using dynamic MR imaging. 1. Fundamental concepts. *Magnetic resonance in medicine* 17 (2), 357–367. (Cited on page 6).
- Touzani, O., Roussel, S., MacKenzie, E. T., 2001. The ischaemic penumbra. *Current opinion in neurology* 14, 83–88. (Cited on page 2).
- Troprès, I., Pannetier, N., Grand, S., Lemasson, B., Moisan, A., Péoc'h, M., Rémy, C., Barbier, E. L., 2015. Imaging the microvessel caliber and density: Principles and applications of microvascular MRI. *Magnetic Resonance in Medicine* 73 (1), 325–341. (Cited on page 7).
- Vaughan, J. T., Griffiths, J. R., 2012. RF Coils for MRI. (Cited on pages 36 and 37).
- Wang, H., Wang, B., Normoyle, K. P., Jackson, K., Spitler, K., Sharrock, M. F., Miller, C. M., Best, C., Llano, D., Du, R., 2014. Brain temperature and its fundamental properties: a review for clinical neuroscientists. *Front. Neurosci.* 8, 307. (Cited on pages 111 and 133).

- Wang, J., Alsop, D. C., Song, H. K., Maldjian, J. A., Tang, K., Salvucci, A. E., Detre, J. A., 2003. Arterial transit time imaging with flow encoding arterial spin tagging (FEAST). *Magnetic Resonance in Medicine* 50 (3), 599–607. (Cited on page 105).
- Warmuth, C., Günther, M., Zimmer, C., 2003. Quantification of Blood Flow in Brain Tumors: Comparison of Arterial Spin Labeling and Dynamic Susceptibility-weighted Contrast-enhanced MR Imaging. *Radiology* 228 (2), 523. (Cited on page 3).
- Warnking, J. M., Pike, G. B., 2006. Reducing contamination while closing the Gap: BASSI RF pulses in PASL. *Magnetic Resonance in Medicine* 55 (4), 865–873. (Cited on page 17).
- Wegener, S., Wu, W.-C., Perthen, J. E., Wong, E. C., 2007. Quantification of rodent cerebral blood flow (CBF) in normal and high flow states using pulsed arterial spin labeling magnetic resonance imaging. *Journal of magnetic resonance imaging : JMRI* 26 (4), 855–862. (Cited on pages 32 and 108).
- Wells, J. A., Lythgoe, M. F., Choy, M., Gadian, D. G., Ordidge, R. J., Thomas, D., 2009. Characterizing the origin of the arterial spin labelling signal in MRI using a multiecho acquisition approach. *J Cereb Blood Flow Metab* 29 (11), 1836–1845. (Cited on pages 23, 26, and 106).
- Wells, J. A., Lythgoe, M. F., Gadian, D. G., Ordidge, R. J., Thomas, D. L., 2010. In vivo Hadamard encoded Continuous arterial spin labeling (H-CASL). *Magnetic Resonance in Medicine* 63 (4), 1111–1118. (Cited on pages 25, 28, 32, 94, and 103).
- Wells, J. A., O’Callaghan, J. M., Holmes, H. E., Powell, N. M., Johnson, R. A., Siow, B., Torrealdea, F., Ismail, O., Walker-Samuel, S., Golay, X., Rega, M., Richardson, S., Modat, M., Cardoso, M. J., Ourselin, S., Schwarz, A. J., Ahmed, Z., Murray, T. K., O’Neill, M. J., Collins, E. C., Colgan, N., Lythgoe, M. F., may 2015. In vivo imaging of tau pathology using multi-parametric quantitative MRI. *NeuroImage* 111, 369–78. (Cited on page 160).
- Wells, J. A., Siow, B., Lythgoe, M. F., Thomas, D. L., 2013. Measuring biexponential transverse relaxation of the ASL signal at 9.4 T to estimate arterial oxygen saturation and the time of exchange of labeled blood water into cortical brain tissue. *Journal of cerebral blood flow and metabolism* 33 (2), 215–224. (Cited on pages 26, 27, 106, and 138).
- Willats, L., Calamante, F., 2013. The 39 steps: Evading error and deciphering the secrets for accurate dynamic susceptibility contrast MRI. *NMR in Biomedicine* 26 (8), 913–931. (Cited on page 11).

- Williams, D. S., Detre, J. A., Leigh, J. S., Koretsky, A. P., 1992. Magnetic resonance imaging of perfusion using spin inversion of arterial water. *Proceedings of the National Academy of Sciences of the United States of America* 89 (1), 212–216. (Cited on pages 11 and 14).
- Williams, R., Needles, A., Cherin, E., Zhou, Y. Q., Henkelman, R. M., Adamson, S. L., Foster, F. S., 2007. Noninvasive Ultrasonic Measurement of Regional and Local Pulse-Wave Velocity in Mice. *Ultrasound Med. Biol.* 33 (9), 1368–1375. (Cited on page 67).
- Wintermark, M., Sesay, M., Barbier, E., Borbely, K., Dillon, W. P., Eastwood, J. D., Glenn, T. C., Grandin, C. B., Pedraza, S., Soustiel, J.-F., Nariai, T., Zaharchuk, G., Caille, J.-M., Dousset, V., Yonas, H., 2005. Comparative Overview of Brain Perfusion Imaging Techniques. *Stroke* 36 (9), e83–99. (Cited on pages 1 and 10).
- Wolk, D. A., Detre, J. A., 2012. Arterial spin labeling MRI: an emerging biomarker for Alzheimer’s disease and other neurodegenerative conditions. *Current opinion in neurology* 25 (4), 421–8. (Cited on pages 4, 10, 93, and 108).
- Wong, E. C., Buxton, R. B., Frank, L. R., 1998. A theoretical and experimental comparison of continuous and pulsed arterial spin labeling techniques for quantitative perfusion imaging. *Magnetic resonance in medicine* 40 (3), 348–355. (Cited on page 20).
- Wong, E. C., Cronin, M., Wu, W.-C. C., Inglis, B., Frank, L. R., Liu, T. T., 2006. Velocity-selective arterial spin labeling. *Magnetic resonance in medicine* 55 (6), 1334–1341. (Cited on pages 22 and 23).
- Wu, R. H., Bruening, R., Noachtar, S., Arnold, S., Berchtenbreiter, C., Bartenstein, P., Drzezga, A., Tatsch, K., Reiser, M., 1999. MR measurement of regional relative cerebral blood volume in epilepsy. *Journal of Magnetic Resonance Imaging* 9 (3), 435–440. (Cited on page 4).
- Wu, W. C., Fernández-Seara, M., Detre, J. a., Wehrli, F. W., Wang, J., 2007. A theoretical and experimental investigation of the tagging efficiency of pseudocontinuous arterial spin labeling. *Magnetic Resonance in Medicine* 58 (5), 1020–1027. (Cited on pages 21, 34, 65, and 71).
- Ye, F. Q., Mattay, V. S., Jezzard, P., Frank, J. A., Weinberger, D. R., McLaughlin, A. C., 1997. Correction for vascular artifacts in cerebral blood flow values measured by using arterial spin tagging techniques. *Magnetic Resonance in Medicine* 37 (2), 226–235. (Cited on pages 26 and 105).
- Zhang, K., Herzog, H., Mauler, J., Filss, C., Okell, T. W., Kops, E. R., Tellmann, L., Fischer, T., Brocke, B., Sturm, W., Coenen, H. H., Shah, N. J., 2014. Comparison of

- cerebral blood flow acquired by simultaneous [(15)O]water positron emission tomography and arterial spin labeling magnetic resonance imaging. *J. Cereb. Blood Flow Metab.* (April), 1–8. (Cited on page 10).
- Zhang, W., Williams, D. S., Detre, J. A., Koretsky, A. P., 1992. Measurement of brain perfusion by volume-localized NMR spectroscopy using inversion of arterial water spins: Accounting for transit time and cross-relaxation. *Magnetic resonance in medicine* 25 (2), 362–371. (Cited on pages 18, 44, and 54).
- Zhang, W., Williams, D. S., Koretsky, A. P., 1993. Measurement of rat brain perfusion by NMR using spin labeling of arterial water: In vivo determination of the degree of spin labeling. *Magnetic Resonance in Medicine* 29 (3), 416–421. (Cited on pages 13 and 50).
- Zhang, Y., Cao, Y., Shih, G. L., Hecht, E. M., Prince, M. R., 2017. Extent of Signal Hyperintensity on Unenhanced T1-weighted Brain MR Images after More than 35 Administrations of Linear Gadolinium-based Contrast Agents. *Radiology* 282 (2), 516–525. (Cited on page 11).
- Zhao, L., Vidorreta, M., Soman, S., Detre, J. A., Alsop, D. C., 2016. Improving the robustness of pseudo-continuous arterial spin labeling to off-resonance and pulsatile flow velocity. *Magn. Reson. Med.* (July). (Cited on page 88).